THE UNIVERSITY
of EDINBURGH

The role of Blood Brain Barrier failure in progression of cerebral small vessel disease: A detailed Magnetic Resonance Imaging study

Xin Wang

Doctor of Philosophy

The University of Edinburgh

2014

Contents

List of Figures

List of Tables

Acknowledgements

First of all, I wish to express my profound gratitude and respect to my principle supervisor, Professor Joanna Wardlaw, who offered me the wonderful opportunity to work in her great research group and financial support, and constantly helped, supported, encouraged and inspired me over the past years. I admire her honesty and strictness in research greatly, since she asked me, from the first day of my PhD, to take clear experiment notes and to be honest in research even sometimes the results were not so promising. She is extraordinarily smart, I always feel cheerful and inspired after meeting with her who challenged me with lots of questions and highlighted different nodes in a very broad picture of this field, like viewing sparkling stars in a clear night sky. She taught me to look and think in various angles which I lacked in my previous study experiences. I would also like to thank her for all advices, encouragements, proofreading and suggestions on academic writing. I feel extremely lucky to have such a great supervisor as Joanna!

I am very thankful to my second supervisor, Dr. Maria Valdes Hernandez, who trained me in image segmentation and has always been there whenever I needed advice on any imaging analysis related subjects.

I am very grateful to our statistician Dr. Francesca Chappell who helped me and guided me with statistical analysis. Thanks a lot for her patience and kindness in teaching me statistical techniquesand professional expressions.

I would like to thank Dr. Fergus Doubal who recruited all the patients in the Mild Stroke Study, which I used in my PhD project. He also provided valuable help in patients' information and advice on analysis. I am very

grateful to Ms. Kirsten Shuler who verified the large database with all patients' characteristics in the Mild Stroke Study, and her effects in proofreading my work and finding publications which I needed but were not in our university database.

I am also thankful to Dr. Gillian Potter who explained her excellent and inspiring work relating to perivascular spaces to me. I would also like to thank Dr. Andrew Farrall for giving me suggestions on searching the blood brain barrier literature and Dr. Emma Bailey for showing me her blood brain barrier animal model work.

I wish to express my gratitude to Ms. Elaine Sandeman and Dr. Dominic Job for the valuable help with scanning information, image storage and retrieval, and to the IT department in the Division of Clinical Neurosciences for excellent support with computer and software.

I am also very grateful to the China Scholarships Council/University of Edinburgh Scholarships which provided me this PhD scholarship. Being an international student sometimes was not easy, I am indebted to Ms. Moira Henderson and Dr Duncan Martin for providing invaluable help with student attendance confirmation, a variety of letters for visa application, and contacting with other administrative offices in the university.

I am extremely grateful to my colleagues and friends in the lab for making the laboratory such a nice and friendly place to work, for helping me study British culture, and for their suggestions and proofreading in my studies. I would particularly thank Dr. Jehill Parikh, Dr. Simon Cox, Natalie Royle, Anna Jones, Islem Rekik, David Dickie, Andreas Glatz, Stewart Wiseman, Anna Heye and Shadia Mikhael. They were the sweet ones who cheered me

up on a variety of disappointing and panic occasions when things were going wrong.

I did pharmaceutical science and immunology in my previous studies, sometimes it was quite hard for me to understand many subjects relating to brain imaging of which I had little background. I am so lucky to have my wonderful friends Yu Song, Hao Shen, Weipeng Huang, Wei Cao, Sheng Qin, Uemoto Yoshinobu and some others who work in those areas. They encouraged me and shared with me their knowledge of physics, engineering, mathematics and other topics. I also want to express my gratitude to Shanshan Guo, Lei Han, Martina Cougiu, Yue Liu, Chungfen Tsai, Mengmeng Liu, Yao Ding and other friends who shared their life experiences with me and encouraged me during at my lowest ebb of PhD.

PhD is a special and wonderful experience in my life: I studied the inspiring topic I love, lived in a lovely city with warm smiles and beautiful colours, saw so many amazing things and people which broadened my view of this world. During the PhD, I found my faith, my dreams, had a clearer idea about what kind of person I want to be, and understood that in life pain is inevitable, but suffering is optional. Probably that is why people call this degree a 'Doctor of Philosophy'. I feel deeply grateful for this experience and sincerely hope my humble work could be useful to relieve patients' pain and benefit further research.

This thesis is dedicated to my parents, Mr. Naiqiang Wang and Ms. Chunlan Zhang for their unfailing love. Gratitude is beyond what I feel in the depths of my heart. I could not have done the PhD without their trust and support.

Declaration

I declare that I composed this thesis and that it is my own original work except where explicitly stated in the text. I have not submitted any part of this thesis for any other degree or professional qualification.

Xin Wang

1st Dec 2013

Publications relating to the work of this thesis

Papers in peer-reviewed journals (Appendix I)

1. Wang, X., Valdes Hernandez, M.C., Doubal, F., Chappell, F.M., Wardlaw, J.M., 2012. How much do focal infarcts distort white matter lesions and global cerebral atrophy measures? *Cerebrovasc Dis* 34, 336-342.

2.Wardlaw, J.M., Doubal, F.N., Valdes-Hernandez, M., Wang, X., Chappell, F.M., Shuler, K., Armitage, P.A., Carpenter, T.C., Dennis, M.S., 2013a. Blood-brain barrier permeability and long-term clinical and imaging outcomes in cerebral small vessel disease. *Stroke* 44, 525-527.

3. Hernandez, M.D., Piper, R.J., Wang, X., Deary, I.J., Wardlaw, J.M., 2013. Towards the automatic computational assessment of enlarged perivascular spaces on brain magnetic resonance images: A systematic review. *J Magn Reson Imaging* 38, 774-85.

Published abstracts for conference presentation (Appendix I)

1. Wang X, Hernandez MCV, Armitage PA, Doubal F, Wardlaw JM. Pilot study to assess white matter lesion progression in longitudinal studies:

preliminary findings from The Mild Stroke Study 1. International Society for Magnetic Resonance in Medicine 2010.

2. Wang X, Hernandez MCV, Armitage PA, Doubal F, Wardlaw JM. Effect of infarcts on the assessment of brain atrophy in longitudinal studies. European Stroke Conference 2011.

3. Wang X, Hernandez MCV, Doubal F, Chappell FM, Wardlaw JM. Development and validation of a computational method to quantify perivascular spaces on MRI in cerebral small vessel disease. European Stroke Conference 2013.

4. Wang X, Hernandez MCV, Doubal F, Chappell FM, Wardlaw JM. Computational quantification of perivascular spaces (count and volume) in ischemic stroke patients is associated with white matter hyperintensities and cerebral atrophy. European Stroke Conference 2013.

5. Wang X, Hernandez MCV, Wardlaw JM. Structure and function of perivascular spaces in the brain: a systematic literature analysis. European Stroke Conference 2014.

6. Wang X, Hernandez MCV, Sakka E, Wardlaw JM. Common white matter hyperintensity artefacts on fluid attenuated inversion recovery images: literature review and ischemic stroke patient study. European Stroke Conference 2014.

7. Wang X, Hernandez MCV, Doubal F, Chappell FM, Wardlaw JM. Basal ganglia perivascular spaces are associated with reduced von Willebrand Factor in patients with mild stroke – evidence of cerebral endothelial dysfunction. European Stroke Conference 2014 (Platform presentation).

Abstract

Small vessel disease (SVD) is an important cause of stroke, cognitive decline, and age-related disability. The cause of SVD is unknown, increasing evidence from neuropathology and neuroimaging suggests that failure of the blood-brain barrier (BBB) precipitates or worsens cerebral SVD progression and its failure is associated with SVD features such as white matter hyperintensities (WMH), perivascular spaces (PVS) and lacunar infarcts. The BBB change mechanism may also contribute to other common disorders of ageing such as Alzheimer's disease (AD).

Magnetic resonance imaging (MRI) has revolutionised our understanding of SVD features. The MRI contributes to better understanding of the SVD pathophysiology and their clinical correlates. The purpose of this project was to better understand the pathogenesis of SVD, which involves improved understanding of BBB structures and pathophysiology and accurate measurement of cerebral SVD imaging characteristics on MRI scans. We aimed to assess (1) structures related to the BBB and factors that affect the BBB; (2) efficient and consistent WMH measurement method; (3) effect of stroke lesions on WMH and cerebral atrophy progression; (4) development and optimisation of computational PVS measurement method; (5) the relationships between PVS and SVD, blood markers, and BBB permeability.

Section one describes structures and pathophysiology of the BBB. I reviewed the BBB structural and functional components from the view of neurovascular unit, PVS, and junctional proteins. The PVS part was done in a systematic search. I also reviewed some common stimuli for BBB permeability including inflammation and ischemia. Ischemic triggers for the

BBB permeability were summarized systematically. Based on the literatures above, I summarized changes in junctional proteins in ischemia, inflammatory pain and AD models.

Section two describes accurate measurement of WMH progression and atrophy. I used data from 100 patients who participated in a stroke study about BBB permeability changes in lacunar versus cortical stroke. To find a most efficient and consistent WMH measurement method, we tested several computational methods and effect of common processing steps including bias field correction and intensity adjustment. To avoid the effect of artefacts, I did a systematic search about artefacts and tested methods of image segmentation to avoid WMH artefacts as much as possible. To investigate the effect of stroke lesions on WMH and atrophy progression, I did the WMH, atrophy segmentation and stroke lesion measurements in a subgroup of 46 patients with follow-up scans, and showed that stroke lesions distorted measurement of WMH and atrophy progression and should be excluded.

Section three describes development and optimization of a computational PVS measurement method, which measures the count and volume for PVS based on a threshold method using Analyze™ software. We tested the observer variability and validated it by comparison with visual rating scores. We investigated the associations between PVS results with other SVD features (WMH, atrophy), risk factors (hypertension, smoking and diabetes), blood markers, and BBB permeability.

In conclusion, MRI is a valuable tool for the investigation of cerebral SVD features and BBB permeability. Exclusions of artefacts and stroke lesions are important in accurate measurement of WMH. PVS are important features of

BBB abnormalities, and they correlate and share risk factors with other SVD features, and they should be considered as a marker of SVD and BBB permeability. Further systematic histological and ultrastructural studies of BBB are desirable in understanding the BBB regarding to the different parts of the cerebral vascular tree.

List of abbreviations

(In each chapter all names are fully spelt out before being subsequently abbreviated, abbreviations within figures and tables are spelt out in the accompanying legend)

3D = three-Dimensional

3D-TSE-VFL = 3D imaging with a Turbo Spin-Echo sequence with Variable FLip-angle echo trains

AA = Amino Acid

Aβ = Amyloid-beta

ABC = ATP-Binding Cassette

ABCB1 = ABC subfamily B member 1

AD = Alzheimer's Disease

AIDS = Acquired Immune Deficiency Syndrome

AJ = Adherens Junctions

Ang = Angiopoietins

ApoE = Apolipoprotein E

AQP = AQuaPorin

ATP = Adenosine TriPhosphate

BBB = Blood Brain Barrier

BFC = Bias Field Correction

BG = Basal Ganglia

BG ROI = Basal Ganglia Regions Of Interest

BLADE = a PROPELLER equivalent implementation of the Siemens Medical System (Erlagen, Germany)

BM = Basement Membranes

CAA = Cerebral Amyloid Angiopathy

CADASIL = Cerebral Autosomal Dominant Arteriopathy with Subcortical Infarcts and Leukoencephalopathy

CFA = Complete Freund's Adjuvant

CCL2 = chemokine (C-C motif) Ligand 2

CD = Cluster of Differentiation

CI = Confidence Interval

CHS = Cardiovascular Health Study

CNS = Central Nervous System

COX-2 = CycloOXygenase 2

CRP = C-reactive protein

CS = Centrum Semiovale

CSF = CerebroSpinal Fluid

CT = Computed Tomography

CXCL12 = chemokine (C-X-C motif) Ligand 12

Da = Daltons

DC = Dendritic Cells

df = degrees of freedom

DWI = Diffusion-Weighted Imaging

DWMH = Deep White Matter Hyperintensities

E = Experiment

EAAT = Excitatory Amino Acid Transporter

EAE = Experimental Autoimmune Encephalomyelitis

EB = Evan's Blue

ELISA = Enzyme-Linked ImmunoSorbent Assay

F 1+2 = Fragments 1 and 2 of prothrombin

FAIS = Flow Artefact–InSensitive

Fib = Fibrinogen

FLAIR = FLuid Attenuated Inversion Recovery

FLIRT = FMRIB Linear Registration Tool

Gd = Gadolinium

Gd-DTPA = Gadolinium DiethyleneTriamine Pentaacetic Acid

GFP = Green-Fluorescent-Protein

GJ = Gap Junction

GLUT-1 = GLUcose Transporter-1

GM = Gray Matters

GRE = GRadient Echo

HIV = Human Immunodeficiency Virus

HIVE = Human Immunodeficiency Virus Encephalitis

HOCl = HypOChlorite

HRP = HorseRadish Peroxidise

HSPG = Heparan Sulfate ProteoGlycan

ICAM = IntraCellular Adhesion Molecule

ICH = intracerebral hemorrhage

IFN-γ = InterFeroN gamma

IgG = Immunoglobulin G

IL = InterLeukin

INPH = Idiopathic Normal Pressure Hydrocephalus

ISF = InterStitial FluidJAM = Junctional Adhesion Molecule

kDa = KiloDaltons

KHz = KiloHertz

KRISP = K-space Reordered by Inversion time at each Slice Position

LADIS = LeukoAraiosis and DIsability Study

LBC1936 = Lothian Birth Cohort 1936 study

LFA-1= Leukocyte Function associated Antigen-1

LM = Light Microscopy

LNAA = Large Neutral Amino Acids

LPS = LipoPolySaccharide

LRP-1 =Low-density lipoprotein Receptor-related Protein 1

MCAO = Middle Cerebral Artery Occlusion

MCMxxxVI method = Multispectral Coloring Modulation and Variance Identification

MCT-1 = MonoCarboxylate Transporter-1

MH = marginal homogeneity

MHC class II = Major Histocompatibility Complex class II

ml = millilitre

mm = millimetre

mm^3 = cubic millimetre

MMP = Matrix MetalloProteinases

MR = Magnetic Resonance

MRI = Magnetic Resonance Imaging

MRP = Multidrug Resistance-associated Proteins

ms = millisecond

MS = Multiple Sclerosis

MSS = Mild Stroke Study

MTC = Magnetisation-Transfer Contrast

N3 = Nonparametric Nonuniform intensity Normalization

NIHSS = National Institutes of Health Stroke Scale

Ninj1= Ninjurin1

NO = Nitric Oxide

Ob= Observer

OR = Odds Ratio

PD = Proton-Density

PDGF-B = Platelet-Derived Growth Factor subunit B

PDGFR-β = Platelet-Derived Growth Factor Receptor beta

PECAM = Platelet Endothelial Cell Adhesion Molecule

P-gp = P-glycoprotein

PVS = PeriVascular Spaces

PWMH = Periventricular White Matter Hyperintensities

RAGE = Receptor for Advanced Glycation End-products

RG = Red and Green

ROI = Regions Of Interest

RSS = Rotterdam Scan Study

S1P = Spingosine-1-Phosphate

S1P1 = Sphingosine-1-Phosphate receptor 1

SAH = SubArachnoid Hemorrhage

SAS = SubArachnoid Spaces

SD = Standard Deviation

SEM = Scanning Electron Microscopy

SENSE = SENSitivity Encoding

SH3 = Src Homology 3

SIV = Simian Immunodeficiency Virus

SMC = Smooth Muscle Cells

SPS = SubPial Spaces

SVD = Small Vessel Disease

T = Tesla

T1W = T1-weighted

T2W = T2-weighted

TAT = Thrombin-AntiThrombin complex

TBI = Traumatic Brain Injury

TEER = TransEndothelial Electrical Resistance

TEM = Transmission Electron Microscopy

TGF-β = Transforming Growth Factor beta

TJ = Tight Junction

TNFα = Tumor Necrosis Factor alpha

tPA = tissue Plasminogen Activator

VaD = Vascular Dementia

VE-cadherin = Vascular-Endothelial-cadherin

VEGF = Vascular Endothelial Growth Factor

VLA-4 = Very Late Activation Antigen-4

VRS = Virchow-Robin Spaces

vWF = von-Willebrand Factor

WM = White Matters

WMH = White Matter Hyperintensities

WML = White Matter Lesion

ZO = Zonula Occludens

Chapter 1 Introduction

1.1 The global burden of stroke

Stroke is a most common life-threatening neurologic disease and is a leading cause of death and disability worldwide. Stroke is the second commonest cause of death after ischemic heart disease worldwide, and is the fifth cause of death in low-income countries, the first cause of death in middle-income countries and the second cause of death in high-income countries in 2004 (Mathers et al., 2009). In 2005, approximately 16 million first-ever strokes occurred and stroke caused 5.7 million deaths, 87% of which were in low and middle-income countries. Numbers of first-ever stroke are predicted to rise to 18 million in 2015 and 23 million in 2013. Numbers of deaths caused by stroke are expected to rise be 6.5 million in 2015 and to 7.8 million in 2030 globally (Strong et al., 2007). Stroke is also a dominant cause of disability. The disability after stroke demands rehabilitation and long-term care. This huge economic burden is still increasing (Lopez et al., 2006; Strong et al., 2007).

The diagnosis of the pathological types and causes of stroke in clinical practice influences therapy efficiency and patient management. Population-based stroke incidence studies showed ischemic stroke is the most prevalent stroke type, approximately four fifths of all strokes are due to cerebral ischemia (ranged from 67% to 81%), followed by parenchymal hemorrhage (7% to 20%) and subarachnoid hemorrhage (1% to 7%), and there is still 2% to 15% for undetermined type. Ischemic stroke was categorised into four groups: large vessel disease, small vessel disease (SVD), cardioembolic stroke, and other ischemic types (including boundary strokes) (Feigin et al., 2003).

1.2 SVD imaging features

Cerebral SVD account for approximately a quarter of ischemic stroke and a fifth of all stroke worldwide, and it is also the most common vascular contributor to dementia (Wardlaw et al., 2013c; Warlow et al., 2003). The development of imaging techniques facilitates studies of the stroke and SVD mechanisms in humans and animals and helps the clinical diagnosis. X-ray computed tomography (CT) was first used as a pioneering imaging tool for clinical diagnosis and research in the early 1970s. Later in the 1980s, magnetic resonance imaging (MRI) was developed and used in clinics. CT remains widely used in stroke as it is quick and easy for routine imaging in patients presenting with possible stroke. It is very accurate in acute hemorrhagic stroke. Though the scanning time of MRI is longer than CT, it generates superior image quality for the display of detailed brain anatomical structures and detection of tiny lesions such as ischemic stroke and SVD.

The principle of MRI is based on the spin of atomic nuclei, which absorb and emit electromagnetic waves, and magnetic resonance (MR) scanners can therefore detect radio frequency signals emitted by excited atoms. Hydrogen (^{1}H) nuclei are commonly used in clinical MR imaging, due to their abundance that the human body is largely composed of water and each water molecule contain two hydrogen nuclei (Storey, 2006).

A routine structural MR brain examination for stroke and SVD commonly consists of multiple sequences, including: a) T1- and T2-weighted imaging (T1W and T2W); b) T2*-weighted gradient-recalled echo imaging (GRE); c) fluid attenuated inversion recovery (FLAIR) imaging; d) diffusion-weighted imaging (DWI). T1W imaging is normally used to depict the anatomical structures (Bitar et al., 2006), and T2W imaging is sensitive for disease

detection such as fluid, gliosis and demyelination because higher water content in pathological tissues appears more hyperintensive than normal tissues on T2W imaging, and T2W imaging is used for PVS detection (Mantyla et al., 1999a). The GRE sequence can help hemorrhage detection, while FLAIR is used to null the cerebrospinal fluid (CSF) signal (which made the lesions near the fluid-containing spaces such as sulci or ventricles more distinguishable). DWI sequences aid the diagnosis of recent strokes (Bitar et al., 2006).

Major SVD features on MRI (Wardlaw et al., 2013b; Wardlaw et al., 2013c) include (Figure 1.1)

- White matter hyperintensities (WMH)
- Perivascular spaces (PVS)
- Lacunes
- Recent small subcortical infarcts
- Cerebral microbleeds
- Atrophy

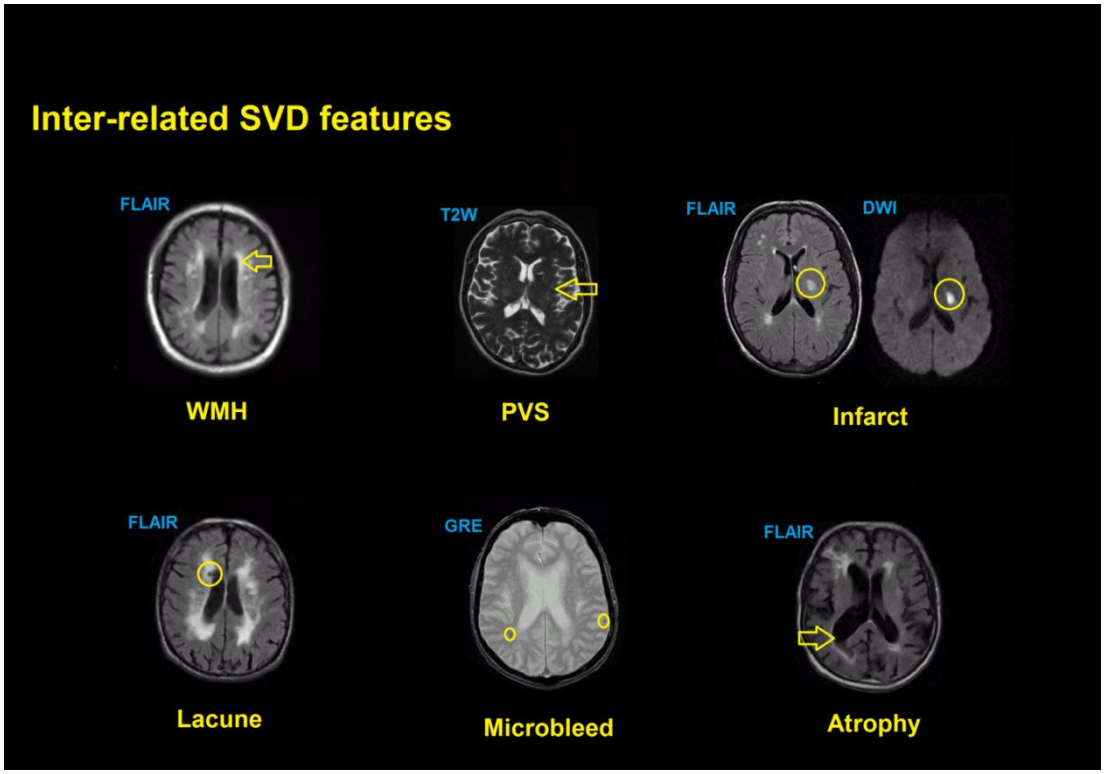

Figure 1.1 Inter-related SVD features.

Abbreviations:
SVD: small vessel diseases; WMH: white matter hyperintensities; PVS: perivascular spaces; FLAIR: fluid attenuated inversion recovery imaging; T2W: T2-weighted imaging; DWI: diffusion-weighted imaging; GRE: T2*-weighted gradient-recalled echo imaging. Because WMH are diffuse lesions, so an arrow points to a region with WMH intensity characteristics. Though PVS are focal lesions, there are too many of them, an arrow points to one PVS dot, all other dots having the same intensity, size and shape are also PVS. Other focal lesions such as infarct, lacune and microbleed features are highlighted within the circles. An arrow in the atrophy figure pointing to the enlarged ventricles which is a one of the features in cerebral atrophy.

1.2.1 WMH

WMH are signal abnormalities of variable size in the white matter that are of presumed vascular origin. They also occur in deep grey matter. WMH show low attenuated areas on CT (Mantyla et al., 1999b), appear as hyperintense on T2W, FLAIR (Gouw et al., 2008b; Haller et al., 2013; Jokinen et al., 2009; Wardlaw et al., 2004), and occasionally appear as hypointense on T1W MRI images (not as hypointense as CSF) but often are not visible on T1W images

(Mantyla et al., 1999a). This radiological description helps to distinguish the white matter lesions of presumed vascular origin from other causes such as multiple sclerosis or leukodystrophies. WMH are generally distributed symmetrically in the white matter of cerebral hemispheres, and they coalesce together to become diffuse lesions when the number of lesions is large. Lesions in the deep grey matter and brainstem can be included in WMH category, but this should be explicitly stated and it may be better to use the term 'subcortical hyperintensities' (Wardlaw et al., 2013b; Wardlaw et al., 2013c). Having more WMH at first presentation is also a predictor of worse WMH progression (Gouw et al., 2008a; Wardlaw et al., 2013a).

WMH presence or progression are related to other SVD features such as PVS (Doubal et al., 2010b; Potter et al., 2013), lacunes (Gouw et al., 2008a), microleeds (Cordonnier et al., 2007) and atrophy (Aribisala et al., 2012; de Leeuw et al., 2006), and the WMH burden is more severe in patients with lacunar stroke (Rost et al., 2010).

Presence and progression of WMH are also related to age-related vascular pathology, BBB permeability and ischemia (Brown et al., 2002; Pantoni and Garcia, 1997; Uh et al., 2010; Wardlaw et al., 2013a; Young et al., 2008). WMH on both T2W and FLAIR images correlate with myelin loss pathologically, though imaging overestimated periventricular and perivascular lesions but underestimated lesion in deep white matter (Haller et al., 2013). Increasing age is associated with WMH progression and is a risk factor for WMH (Longstreth et al., 2005; Wardlaw et al., 2013a). Hypertension is another risk factor for WMH, hypertension at baseline is significantly associated with severe WMH at follow-up (Dufouil et al., 2001).

Increased WMH are associated with structural and functional brain changes and cognitive and motor deficits, increased risk of stroke and death (Debette and Markus, 2010; Garde et al., 2005; Liou et al., 2010; Longstreth et al., 2005; Marquine et al., 2010; Silbert et al., 2008; van den Heuvel et al., 2006a).

Currently, various visual rating scores and automatic or semi-automatic quantitative methods are available to measure presence and progression of WMH (Gouw et al., 2008b; Hernandez et al., 2010; Kapeller et al., 2003; Prins et al., 2004; van den Heuvel et al., 2006b). When using the automatic or semi-automatic methods to measure WMH volume, observers should be aware of artefacts, focal infarcts and strokes which mimic the appearance of WMH, and the outputs need to be visually checked by an experienced rater.

In order to investigate the mechanisms and clinical relevance of WMH in large population based studies, it is crucial to measure WMH accurately without including artefact and WMH mimics like stroke lesions. We will discuss about our work in achieving these aims in later chapters: the quantitative method we selected for WMH (Chapter 3), a summary of common WMH artefact on MR images (Chapter 4) and the influence of stroke lesions on WMH progression measurement (Chapter 5).

1.2.2 PVS

PVS are fluid filled spaces around the vessels (arteries, arterioles, veins, and venules) in both the deep and superficial areas of the brain (Pollock et al., 1997; Zhang et al., 1990). PVS separate blood vessels from their surrounding brain parenchyma. Previously the presence of PVS was often dismissed as artefacts of tissue processing.

PVS are commonly microscopic. They are not visible on neuroimaging unless enlarged. The definition of PVS on MR images are structures with similar intensity as CSF on all MRI sequences. They appear as linear shape when imaged parallel to the course of the vessel they followed and they appear round (Di Costanzo et al., 2001; Rouhl et al., 2008), with a diameter less than 3 mm when imaged perpendicular to the course of the vessel (Descombes et al., 2004; Hernandez et al., 2013; Wuerfel et al., 2008). PVS had been considered as a benign sign in the brain because PVS also appear on MRI in young and healthy people. However, increasing evidence showed that enlarged PVS might reflect the immune cells accumulation in the PVS and fluid drainage dysfunction (Polledo et al., 2012; Roher et al., 2003; Sagar et al., 2012; Schley et al., 2006; Thal, 2009; Wuerfel et al., 2008). Increasing age and hypertension are two risk factors for PVS, and PVS are associated with SVD features WMH, lacunar infarct (Rouhl et al., 2008), lacune (Zhu et al., 2010), microbleeds (Martinez-Ramirez et al., 2013) and atrophy (Potter et al., 2013), inflammatory blood markers (Aribisala et al., 2014; Rouhl et al., 2011; Rouhl et al., 2010; Satizabal et al., 2013), increased BBB permeability (Wardlaw et al., 2009) and declining cognition (Maclullich et al., 2004; Roher et al., 2003). Increased PVS loads are considered as an important sign for active inflammatory disease such as MS (Wuerfel et al., 2008) and cognitive impairment such as AD (Thal, 2009).

Currently most studies assess the PVS by visual rating scales, the lack of quantitative PVS measurement restrain the comparisons in the studies of evaluating the pathophysiological importance of PVS. We will describe more about PVS in later chapters. We will describe the PVS structure and function based on current available literature (Chapter 2), will outline the

development and optimization process of a semi-automatic method we developed for PVS measurement (Chapter 6 and 7), and we also investigated the associations between PVS and SVD features (WMH and atrophy), blood markers, and blood-brain barrier permeability (Chapter 8).

1.2.3 Lacunes

Lacunes (derived from the French for 'holes') are subcortical CSF-filled cavities of presumed vascular origin with signal intensities the same as CSF on all MRI sequences, usually with a hyperintense rim when they appear hypointense on FLAIR (Potter et al., 2010b; Potter et al., 2011). They are larger than PVS, between 3 mm and about 15 mm in diameter in round or ovoid shape (Hernandez et al., 2013; Wardlaw, 2008).

Asymptomatic lacunes are seen on imaging in middle aged and elderly patients frequently with no history of stroke-like symptoms. The prevalence of lacunes increases with aging in population-based studies (Vermeer et al., 2007). Lacunes are associated with WMH and PVS (Choi et al., 2012; Zhu et al., 2010). Higher lacune scores are associated with an increased risk of post stroke depression (Santos et al., 2009), gait disorder, subsequent stroke and dementia (Snowdon et al., 1997; Vermeer et al., 2007) .

Most lacunes are presumed to result from small subcortical infarcts although some might be the end result of small deep hemorrhages (Franke et al., 1991) and sometimes striatocapsular infarcts (which are atherothromboembolic or cardioembolic in origin) can resolve to leave a lacune (Wardlaw et al., 2013b).

1.2.4 Recent small subcortical infarcts

Recent small subcortical infarcts, commonly previously called lacunar strokes, cause about 25% of all ischemic strokes. They appear in the

territories of perforating small arteries or arterioles in the internal parts of the brain, 'recent' indicating that they have occurred in the previous few weeks (Wardlaw et al., 2013c). On neuroimaging, recent small subcortical infarctions appear as low attenuation on CT scans, or increased signal on DWI, FLAIR and T2W images, and hypointense on T1W MRI compared with normal grey or white matter (Wardlaw et al., 2013b; Wardlaw et al., 2013c). However, for unknown reasons, a third of the patients with symptomatic lacunar stroke syndromes have negative DWI, which is an important alert for clinicians not to exclude the diagnosis of stroke even if DWI is negative (Doubal et al., 2010a).

Subcortical infarcts were once considered as a benign ischemic stroke subtype because they rarely lead to death in the acute phase, were generally mild and not physically disabling and had a low recurrent stroke rate. However longer term studies have shown that long term there is an increased risk of death, disability, cognitive dysfunction, dementia and stroke recurrence (Norrving, 2008). Acute subcortical infarcts commonly shrink to lacunes, presence of cavitation range from 28% to 94% (Loos et al., 2012; Moreau et al., 2012; Potter et al., 2010b) or smaller lesions of similar appearance of WMH or occasionally change to normal appearing tissues. Like other SVD features, the exact mechanisms underlying recent small subcortical infarcts are still debated (see later part 1.3 SVD pathological mechanisms).

1.2.5 Cerebral microbleeds

In the histopathology analysis, most cerebral microbleeds are believed to represent hemosiderin deposits in the perivascular tissues including in the PVS, hemosiderin-laden macrophages and leakage of blood cells containing

hemosiderin (Shoamanesh et al., 2011). Microbleeds are generally not visible on CT, FLAIR, T1W and T2W MRI images, but are seen as small hypointense lesions on GRE images, are generally 2–5 mm in diameter and are up to 10 mm (Cordonnier et al., 2007; Greenberg et al., 2009).

Cerebral microbleeds are most commonly located in the deep grey or white matter in the cerebral hemispheres, brainstem, and cerebellum (Shoamanesh et al., 2011; Wardlaw et al., 2013c). Microbleeds are associated with lacunar stroke and WMH (Wardlaw et al., 2006) and PVS (Martinez-Ramirez et al., 2013). They were considered to be asymptomatic SVD markers, however, increasing evidence showed the microbleeds correlated with cerebral amyloid angiopathy and cognitive impairment in patients with dementia (Shoamanesh et al., 2011).

1.2.6 Atrophy

Brain atrophy is a reduction in brain volume and occurs in many disorders. As a feature of SVD, atrophy is defined as decreased total brain volume not caused by various macroscopic focal injuries such as trauma, inflammation or infarction (Wardlaw et al., 2013c). Generally, cerebral atrophy is manifested by decreased grey or white matter volume, increased ventricular volumes and enlarged superficial sulci or affecting only particular lobes or specific brain regions.

On MRI of longitudinal studies, cerebral atrophy could be measured as decreased brain volume or increased CSF volume using serial registered MR imaging. It is a common accompaniment of ageing and is associated with SVD features such as WMH (Aribisala et al., 2012) and PVS (Chen et al., 2011; Doubal et al., 2010b; Potter et al., 2013). It is considered to be important in the

studies assessing the burden of vascular damage in the brain. Brain atrophy is also associated with cognitive decline and dementia. The global cerebral atrophy rate in Alzheimer's disease is higher than in healthy controls (Fox and Schott, 2004). Focal tissue loss caused by stroke lesions and lacunes should not be considered as part of brain atrophy, and the influence of stroke lesions on atrophy measurement will be described in later chapter (Chapter 5).

1.2.7 Inter-related SVD features

These main features of SVD visible on conventional MRI are now considered to be inter-related. Acute lesions with different causes may have similar late appearance in their chronic stages (Wardlaw et al., 2013b; Wardlaw et al., 2013c).

Stroke symptoms with no visible lesions might change to normal appearing tissues or WMH in their chronic stage. Small subcortical infarcts change to normal appearing tissues, WMH, cavitate or disappear sometimes. Most lacunes are thought to arise from small subcortical infarcts, although some might be from hemorrhages or striatocapsular infarcts (Wardlaw et al., 2013c).

1.3 SVD pathological mechanisms

There are few human SVD pathology studies because they rarely caused death in the acute phase. Increasing imaging evidence showed that all these SVD features are inter-linked, however, a common underlying mechanism explaining all these small vessel pathologies is not completely known.

Occlusion of small vessels is one widely acknowledged mechanism of SVD which is derived from the detailed pathological dissections along small deep

perforating vessels from Fisher's work (Fisher, 1968, 1979, 1982, 1998). The occlusion mechanism suggested that when a small arteriole occluded by fibrinoid necrosis which thicken the arteriolar wall and narrow the vascular lumen eventually lead to ischemia and tissue necrosis, which is called the lacunar hypothesis (Pantoni, 2010). Hypoperfusion was thought to be caused by vessel lumen restriction resulted in oligodendrocyte death and finally demyelination in the white matter (Pantoni, 2010; Pantoni et al., 1996; Petito et al., 1998). Vessel wall atheroma and vasospasm were two mechanisms thought to lead to narrowing of the arteriolar lumen and occlusion leading to reduced blood flow contributing to chronic and diffuse ischemia (Pantoni, 2010). These three possible mechanisms of vascular ischemia in the brain were useful in explaining some of the pathological and imaging features of infarcts and WMH in the past. However, they were poor for explaining the arteriolar wall changes and could not explain the PVS and microbleed features (Wardlaw et al., 2013b).

Stimuli in the brain such as ischemia, inflammatory cytokines, seizures and oxidative stress may induce vascular endothelium wall property changes. The blood brain barrier (BBB) which is a single layer of endothelial cells joined by junction proteins limits substance transport into and out of the brain and may become permeable to some molecules or cells in response to stimuli (details in Chapter 2). The failure of BBB leads to leakage of components into and through the cerebral small vessels walls, fluid accumulation in the PVS, and edema in the perivascular tissues that affects the neuronal and glial cells and damages the brain parenchyma (Figure 1.2). This BBB permeability mechanism could explain SVD features such as small subcortical infarcts, WMH, PVS and microbleeds (Wardlaw, 2010).

Many studies have found an association between failing BBB with normal ageing (Farrall and Wardlaw, 2007; Wardlaw et al., 2009) and worsening of BBB permeability in patients with lacunar stroke (Wardlaw et al., 2009; Wardlaw et al., 2008), increasing WMH (Rosenberg, 2009; Starr et al., 2003; Wardlaw et al., 2009), PVS (Wardlaw et al., 2009), cognitive impairment such as vascular cognitive impairment, dementia and Alzheimer's disease (AD) (Farrall and Wardlaw, 2007; Starr et al., 2009; Taheri et al., 2011; Zipser et al., 2007). Increased BBB permeability in normal appearing tissues at initial presentation with stroke also increased the risk of poor outcome and disability at long term follow-up after stroke (Wardlaw et al., 2009; Wardlaw et al., 2013a).

1.4 Techniques for assessing BBB permeability

Most of the studies previously used CSF:plasma albumin ratio to assess BBB permeability. Increase in CSF:plasma albumin ratio was used to assess increased BBB permeability which is based on the knowledge that albumin is a medium-sized protein of a molecular size of 67 kDa, with no specific active transport process related to its transport across the BBB. Although the brain could synthesis albumin, the majority of albumin is synthesised outside the brain, on the luminal side of the BBB (Farrall and Wardlaw, 2007; Wardlaw, 2010).

Increasing studies used MRI with intravenous contrast agent injection such as gadolinium contrast agents to examine BBB permeability. Signal enhancement data in different tissue types following contrast agent injection were used to estimate BBB failure (Armitage et al., 2011; Farrall and Wardlaw, 2007; Starr et al., 2009; Taheri et al., 2011; Topakian et al., 2009).

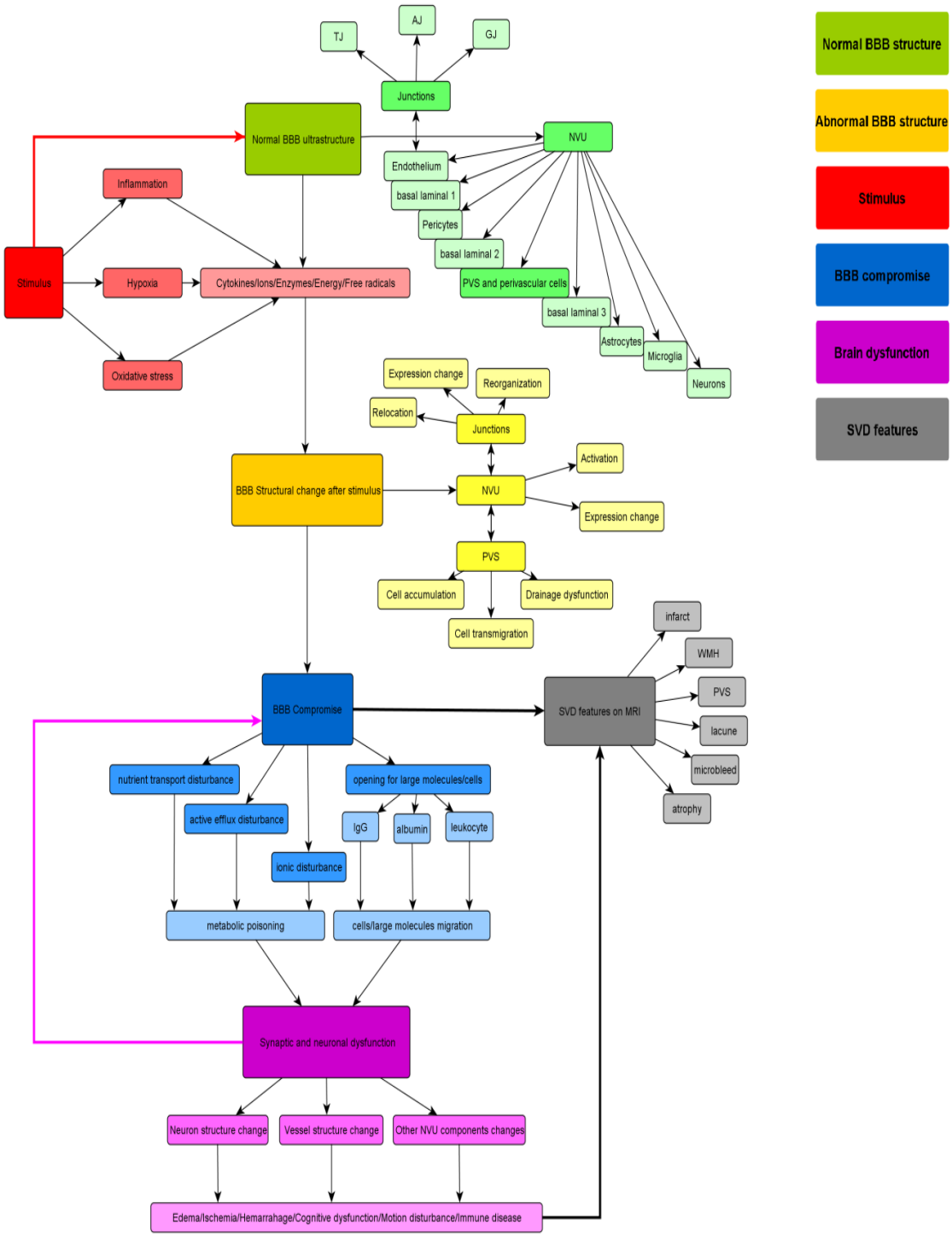

Figure 1.2 The SVD mechanism from the endothelium and BBB dysfunction hypothesis.

*Based on the hypotheses by Wardlaw and Zlokovic (Wardlaw et al., 2003; Zlokovic, 2008). SVD: small vessel diseases; BBB: blood brain barrier; TJ: tight junctions; AJ: adhesion junctions; GJ: gap junctions; NVU: neurovascular unit; PVS: perivascular spaces; WMH: white matter hyperintensities; IgG: Immunoglobulin G.

1.5 Unanswered questions

A number of questions remain about the mechanism of SVD and how individual SVD features progress and are related to each other. In this thesis, I will address the following topics:

(1) How does the BBB permeability influence SVD, is it the initiating mechanism of SVD?

(2) What stimuli influence the endothelium and BBB changes in the early stages?

(3) How should WMH volume, an SVD feature, be measured most accurately and efficiently on MRI using computational measures?

(4) Can and how should PVS, another SVD feature, be measured computationally on MRI accurately and efficiently?

(5) What are the associations between SVD features, blood markers of thrombosis, endothelial function and inflammation and BBB permeability?

1.6 Outline and Aims of the thesis

1.6.1 Section one: structure and pathophysiology of the BBB

(1) What are the BBB structural and functional components, from the perspective of the neurovascular unit (NVU), PVS, and junctional proteins?

(2) What are the stimuli for BBB permeability: where do ischemia and inflammation fit in?

(3) How do junctional proteins change in ischemia, inflammation and in AD models?

1.6.2 Section two: accurate measurement of WMH progression and atrophy

(4) Testing of computational methods and effect of common processing steps.

(5) Identification of common WMH artefacts.

(6) Testing the effect of stroke lesions on measurement of WMH and atrophy.

1.6.3 Section three: computational PVS measurement method and associations

(7) Development and optimization of a computational PVS measurement.

(8) Associations between PVS measures and other SVD features (WMH, atrophy), risk factors (hypertension, smoking and diabetes), blood markers, and BBB permeability.

Chapter 2 Blood brain barrier structures and changes under pathological conditions

2.1 Structures related to the blood brain barrier: from endothelium to neurons

This chapter will describe major structural components of the blood brain barrier (BBB) and their functions from the view of neurovascular unit (NVU), perivascular spaces (PVS), and junctional proteins. This chapter also includes information on two important stimuli for BBB malfunction which are ischemia and inflammation. The structure and function of PVS and ischemia stimulus were reviewed in systematic searches.

2.2 Neurovascular unit (NVU)

Cerebral vessel endothelial cells, pericytes, smooth muscle cells (diminished in the capillary level (Zhang et al., 1990)), glial cells (astrocytes, microglia and oligodendrocytes), perivascular spaces between endothelial cells and endfeet of glia limitans, and neurons together form a functional unit, which are involved in regulating the cerebral blood flow, often referred as the NVU (Abbott et al., 2006) (see Figure 2.1). The cross-talk among neighbouring cells is important in maintaining the endothelium and the BBB integrity and function (Nakagawa et al., 2007).

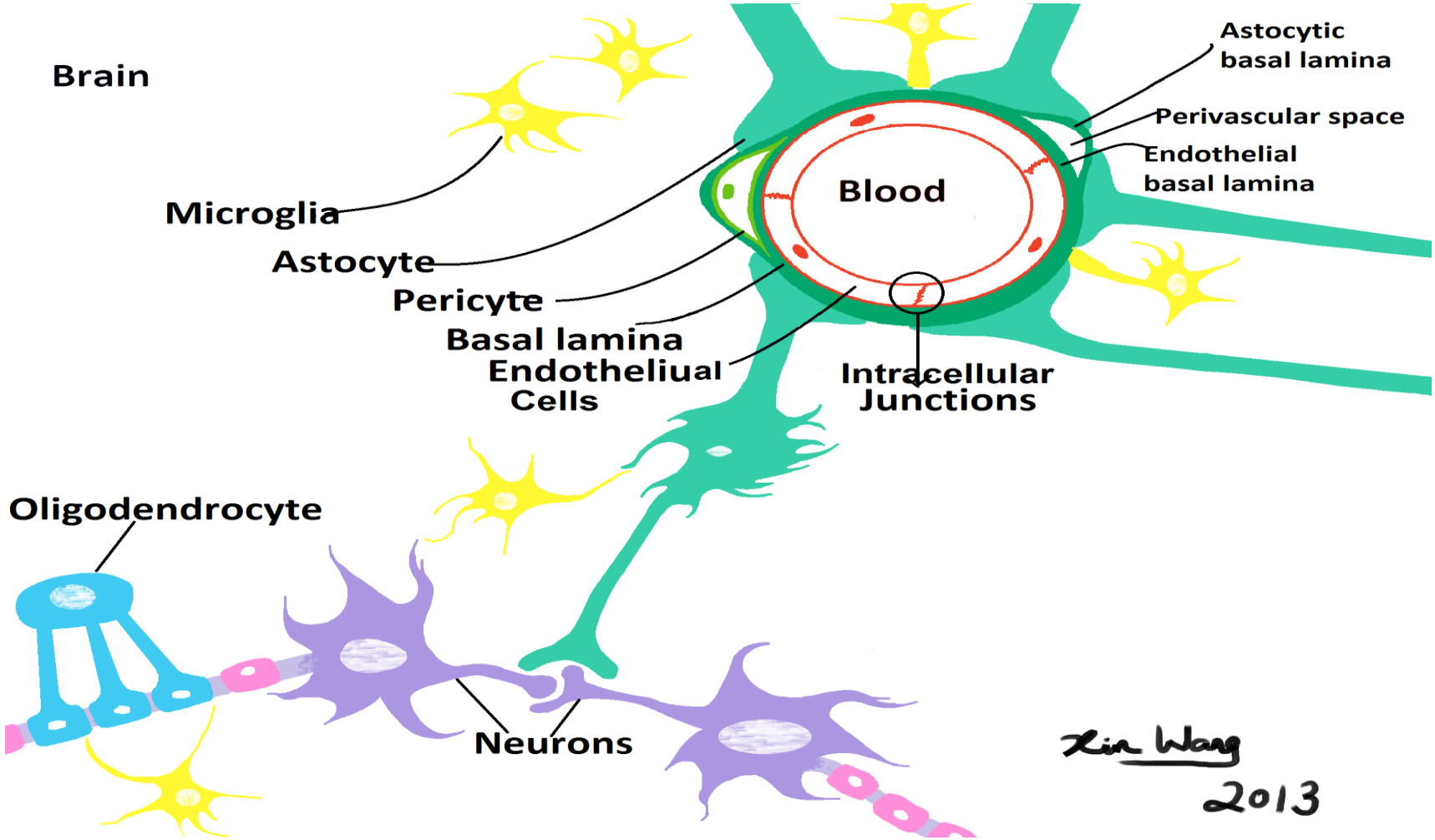

Figure 2.1 Neurovascular unit structure.

2.2.1 Endothelium

(1) Structures

The BBB is formed by a single layer of brain capillary endothelial cells, inducing high electrical resistance (Rubin and Staddon, 1999). These endothelial cells adhere tightly to each other through different types of transmembrane junctional proteins.

Two major categories of junctional proteins are called tight junctions (TJ) and adherens junctions (AJ) (Bazzoni and Dejana, 2004). They both function as a barrier which limits the paracellular permeability. TJ maintain cellular polarity and are formed by different types of TJ proteins, such as occludin, zonula occludens (ZO), claudins, and junctional adhesion molecules (JAM). AJ is involved in assisting leukocyte migration and intercellular signalling, and includes platelet endothelial cell adhesion molecule (PECAM), cadherins, catenins and actins. Detailed information about the structure and function for each TJ and AJ proteins, and their changes during pathological conditions, will be discussed in section '2.3 BBB junction proteins'.

The third major type of cellular junction is called gap junctions (GJ). Gap junctional complexes are channels built by connexins, which allow intercellular communication such as exchanges of ions and small molecules (Bazzoni and Dejana, 2004; Cuevas et al., 1984; Dbouk et al., 2009).

(2) Transport barrier

O_2 and CO_2 diffuse freely through the BBB along concentration gradients, and molecules with a molecular weight of less than 400 Daltons (Da) and with less than 8 hydrogen bonds can also cross the BBB via lipid-mediated diffusion (Pardridge, 2007). Transport of most nutrients or metabolic wastes is via active transport, which has a high energy demand and needs their

specialised transporters to facilitate the bidirectional transport through the barrier (Sa-Pereira et al., 2012; Zlokovic, 2011).

(2-1) Transporters for nutrients

Glucose is the main energy resource of the brain, and its transporter Glucose transporter-1 (GLUT-1, 55 kDa, kiloDaltons) mediates the glucose transport across the BBB (Cardoso et al., 2010). GLUT-1 is present on both the luminal and abluminal sides of the endothelium. The appearance of GLUT-1 is three times more on the abluminal side than on the luminal side (Simpson et al., 2007a). This asymmetrical distribution might prevent excess glucose accumulation in the brain (Zlokovic, 2008).

Monocarboxylate transporter-1 (MCT-1) is the transporter for lactate which is another important energy resource (Dienel, 2012; Wyss et al., 2011). MCT-1 is also present on both sides of the endothelium (Neuwelt et al., 2011; Zlokovic, 2011).

The amino acid (AA) transport systems L and y^+ facilitate the bidirectional transport of essential amino acids, which are present on both the luminal and the abluminal sides of the endothelium (Hawkins et al., 2006; Omidi et al., 2008). System L is a sodium-independent transporter, and mediates the transport of large essential neutral AA (i.e. histidine, threonine, methionine, valine, leucine, isoleucine, phenylalanine, and tyrosine). System y^+ facilitates the transport of essential cationic AA in the brain which is sodium-independent (i.e. lysine). With the presence of sodium, there is a weak interaction between system y^+ and large essential neutral AA (i.e. histidine, threonine, cysteine, methionine, and valine). Both systems also mediate the non-essential AA transport (Hawkins et al., 2006).

There are five sodium-dependent transporters which exist only on the abluminal side of the endothelium and help to remove larger or small neutral AA, nitrogen rich AA, and acidic AA from the brain. They are system A, system ASC, system N, transporter for large neutral amino acids (LNAA), and transporter for excitatory amino-acid (EAAT) (Hawkins et al., 2006). There are two sodium-independent transporters present exclusively on the luminal side. They are system n and system x_{G^-} which mediate the transport of glutamine and acidic AA (Hawkins et al., 2006).

(2-2) Transporters for metabolic waste

Metabolic wastes are continuously generated in the brain and need to be eliminated otherwise they are neuron toxic. The rapid removal of toxic products is through high energy demanding active efflux though the transporters on the luminal side of the membrane, which facilitates the transport towards vessels. Transporters assist this active efflux including: ATP-binding cassette (ABC); low-density lipoprotein receptor-related protein 1 (LRP-1), and EAAT (ElAli and Hermann, 2011; Zlokovic, 2008).

ABC subfamily B member 1 (ABCB1) is one of the ABC transporters, which is also known as P-glycoprotein (P-gp) and was previously called multidrug resistance-associated proteins (MRP). ABCB1 preferably locates on the luminal side of the endothelium and controls the removal of toxic lipophilic and amphipathic metabolites, prevents drug accumulation, and is involved in the amyloid-beta (Aβ) efflux (ElAli and Hermann, 2011; Hermann and Bassetti, 2007; Zlokovic, 2011).

The LRP-1 is a multiligand lipoprotein receptor. It is involved in the signalling pathways related to Aβ, apolipoprotein E (ApoE) and tissue plasminogen activator (tPA). It is the main efflux transporter for the Aβ

clearing across the BBB. The receptor for advanced glycation end-products (RAGE) mediates the influx of Aβ (Deane et al., 2004).

EAAT is one of the sodium-dependent transporters located on the abluminal side of the endothelium. It is responsible for clearing potentially neurotoxic amino acid glutamate (or glutamine) and keeping glutamate at low levels in the brain (Hawkins et al., 2006; Zlokovic, 2008).

(2-3) Transporters for ions

Levels of sodium and potassium could influence the neuronal and synaptic functions. They are mediated by the sodium pump also known as Na^+-K^+-ATPase located in the plasma membrane of all animal cells. At the level of BBB, the sodium pump on the abluminal side of the endothelium facilitates the sodium influx and potassium efflux across the BBB (Zlokovic, 2008, 2011).

(2-4) Transporters for large peptides and proteins

Larger peptides and proteins have their own specific transporters, such as transferrin receptor and insulin receptor. They cross the BBB through receptor-mediated transport system (Zlokovic, 2008, 2011). Albumin is eliminated by receptors on the membranes of caveolae which controls transcellular permeability by regulating signaling, endocytosis, and transcytosis of the BBB (Zlokovic, 2008).

(3) Transporter changes under pathological states

Pathological factors trigger the expression or structural changes of the transporters, which can result in secondary neurodegenerative changes.

(3-1) Ischemia

Under ischemia-hypoxia conditions, the sodium pump stops working (Simard et al., 2007) and expression of GLUT-1 increases. The low level of

glucose also augments the GLUT-1 expression (Boado and Pardridge, 2002). In ischemic stroke, the P-gp transporter expression is upregulated (ElAli and Hermann, 2011). The effect of ischemia stimulus on BBB junctional proteins and its association with BBB will be described in detail in later section.

(3-2) Neurodegeneration

Both ABCB1 and LRP-1 are related to active efflux in the BBB, and their downregulation may play a role in neurodegeneration. Decreased P-gp function or deficiency was found in the progression of Parkinson's disease, Alzheimer's disease, and white matter degeneration of ageing subjects (Bartels et al., 2009; Bartels et al., 2008; Cirrito et al., 2005). Both decreased expression of LRP1 and oxidized LRP1 were found in the Alzheimer's disease brains (Owen et al., 2010; Shibata et al., 2000). Suppression of P-gp and LRP1 could aggravate the Alzheimer disease progression though the mechanism of excess Aβ deposition.

2.2.2 Basement membrane

Cells and their extracellular matrix support one another to maintain the structural integrity and function. The basement membranes are thin sheets of extracellular matrix and are comprised of two layers (lamina): basal lamina and reticular lamina.

The basal lamina is derived from extracellular matrix and is a crucial component in the NVU. It supports the NVU structure and integrity by encircling the endothelium and pericyte. The adhesion receptors existing in the basal lamina establish the connections between endothelium and astrocyte. The basal lamina provides a complementary support for the BBB

barrier function, which is partially explained by the existence of TJ and AJ in the endothelium (del Zoppo and Milner, 2006; Garden and Moller, 2006).

(1) Structure and characters

The endothelium and astrocyte cooperate together to generate the basal lamina. The basal lamina consists of collagen type IV, heparan sulfate proteoglycans (HSPG), laminins, other types of extracellular matrix and matrix adhesion receptors (i.e. integrin and dystroglycan) (del Zoppo and Milner, 2006; Farkas and Luiten, 2001). Mixed combinations of these basal lamina make up a three layered structure: an endothelial layer, an astrocytic layer and a fused layer between these two layers. Both endothelial and astrocytic layers are composed of collagen type IV, HSPG and laminins, with the middle layer mainly consisting of collagen type IV (Farkas and Luiten, 2001).

(2) Functions

Besides potentiating the BBB barrier function, establishing the connections and providing the structural support for the NVU (del Zoppo and Milner, 2006; Sa-Pereira et al., 2012), the basal lamina is involved in matrix-endothelium signalling (Carvey et al., 2009) and a two steps leukocyte transport action through the BBB: (1) leukocytes migrate across endothelium and endothelial basal lamina into the perivascular spaces; (2) then pass across the astrocytic basal lamina into the brain (Bechmann et al., 2007). A detailed description of the leukocyte transmigration process and junction proteins involved in this process is outlined in section '2.4 Stimuli for the BBB compromise'.

(3) Changes in ischemic stroke

In ischemic stroke, the basal lamina rapidly loses integrin and dystroglycan matrix receptors. Matrix metalloproteinases (MMP) induces collagen IV degradation in the basal lamina and it is also associated with hemorrhagic transformation after stroke (del Zoppo, 2010a, b; Rosell et al., 2008). Tissue plasminogen activator (tPA) could exacerbate the outcome by activating MMPs (Adibhatla and Hatcher, 2008). Hyperbaric oxygen treatment reduces post ischemic damage by attenuating basal lamina degradation and decreasing MMP levels in a rat model (Veltkamp et al., 2006).

2.2.3 Pericyte

Pericytes are contractile cells encompassing the endothelial cells throughout the body and they have bidirectional contractile function in controlling capillary size and playing a major role in controlling cerebral blood flow (Peppiatt et al., 2006). They were first described as "contractile elements" by French scientist Rouget in 1874, and since then have been referred to as Rouget cells (Rouget, 1874). They were named as "pericyte" later to reflect their location: they are vascular mural cells embedded within the basal lamina layers on the abluminal side of capillaries. They have close associations with the endothelium through intercellular signalling (Armulik et al., 2005; Dore-Duffy, 2008).

(1) Structure and character

Pericytes are normally star-shaped cells with an oval cell body surrounding the abluminal side of the microvascular endothelium, with elongated and a cigar shaped nucleus. They are embedded between the endothelial and astrocytic basal lamina extracellular matrix (Dore-Duffy and Cleary, 2010; Krueger and Bechmann, 2009; Sa-Pereira et al., 2012).

Pericytes can synthesize and release a variety of factors which contribute to the BBB integrity, vessel stability and new vessel formation, hemostasis, contractile function and immune response (Dore-Duffy, 2008; Sa-Pereira et al., 2012).

(2) Functions

(2-1) Maintaining BBB integrity

Pericytes may play an important role in maintaining BBB integrity, the influence of the pericyte on the BBB integrity being as important as that of the astrocyte, which will be discussed in later section '2.2.4 (1) Astrocyte (A)'. In cell co-culture conditions, pericytes increased higher transendothelial electrical resistance (TEER) and there was lower permeability for small molecular weight markers than with astrocytes in separate co-culture conditions. In the triple co-culture conditions, when a pericyte was positioned in the middle of endothelial cells and astrocytes, they induced the tightest barrier (Nakagawa et al., 2007). The pericyte densities may also contribute to the BBB integrity: they are positively related to vessel density and negatively related to vessel diameter (Armulik et al., 2010). Interactions between pericyte and endothelial cells are central processes in the regulation of vascular formation, stabilization, and remodelling.

(2-2) Angiogenesis

New vessel formation can be initiated after strong stimuli such as brain injury and hypoxia (Sa-Pereira et al., 2012). Vascular endothelial growth factor (VEGF), transforming growth factor β (TGF-β), angiopoietins (Ang-1, Ang-2), platelet-derived growth factor and its receptors (PDGF-B, PDGFR-β), spingosine-1-phosphate and its receptors (S1P, S1P1), and Notch signalling

are involved in regulating endothelial and pericyte cell function and vascular stability (Dore-Duffy, 2008; von Tell et al., 2006; Wolfle et al., 2005).

VEGF is very important for initiating vessel formation and new vessel maturation (Jain, 2003). The expression of VEGF could increase production of PDGF-B which directs pericyte recruitment in the new vessels (Dore-Duffy, 2008; Jain, 2003). In endothelium-restricted Pdgfb knockout-mutants, the loss of PDGF-B signalling leads to impaired pericyte recruitment to blood vessels (Bjarnegard et al., 2004). Another example is in the pericyte-specific PDGFRb deficient signalling mouse model: the pericyte loss in this model lead to vessel leakage in the brain and also leads to increased BBB permeability and hypoperfusion caused by reduced blood flow and reduced vessel reactivity (von Tell et al., 2006). In ageing mice, progressive pericyte loss preceded neurodegenerative changes with neuronal loss, reduced vessel reactivity and density, and impaired learning and memory function (Bell et al., 2010; Quaegebeur et al., 2010).

(3) Immune potentials

Pericytes have immune potential in modulating inflammatory events. They respond to inflammatory cytokines and express cell surface molecules which might facilitate T-cell recruitment (Balabanov et al., 1999). They also express macrophage surface markers and are involved in leakage of plasma proteins (Balabanov et al., 1996; Sims, 2000).

(3) Changes in pathological states

(3-1) Changes in ischemic stroke

Under ischemic stimulus, pericytes become activated and degrade basal lamina to facilitate their migration into the central nervous system (CNS) (Duz et al., 2007).

(3-2) Changes during neurodegeneration

Deficiency and dysfunction of pericytes influence neurodegeneration by two possible pathways: (1) pericyte loss reduces efficient microcirculation, and it induces perfusion stress to neurons and neuronal injury. (2) BBB breakdown induces serum protein transmigration and accumulation in the CNS, which also triggers neuronal injury. Platelet-derived growth factor receptor beta (PDGFRβ) deficiency contributes to the pericyte loss (Bell et al., 2010). In Alzheimer's disease (AD), pericyte loss leads to reduced vessel density and reactivity, reduced blood flow and increased BBB permeability (Quaegebeur et al., 2010).

2.2.4 Glial Cells

Besides neurons, and vascular cells such as endothelium and pericytes, there is another important type of cell in the CNS: glial cells, which include astrocytes, microglia and oligodendrocytes. 'Glia' is a Greek word meaning 'glue' for its supporting function of surrounding neurons (Franklin and Bussey, 2013). The overall cerebral glia/neuron ratio is approximately 1.31 for female, 1.49 for male, and it varies across different brain structures (Azevedo et al., 2009; Pelvig et al., 2008). The cortical glial cells are comprised of approximately 75% oligodendrocytes, 20% astrocytes and 5% microglia. The number of oligodendrocytes decreases with age, and microglia increase with age in females, whereas the number of astrocytes is consistent through life (Pelvig et al., 2008).

Glial cells provide direct effect or signalling in a variety of neuronal functions: forming myelin sheaths around axons (Mathis et al., 2003); controlling neuron maturation (Purkinje cell (Mathis et al., 2003)); mediating cerebral blood flow (Attwell et al., 2010); contributing to the BBB tightness

and function; associated with metabolic and lipid synthetic pathways (Chang et al., 2008) and mediating inflammatory response (Mrak and Griffin, 2005). These functions of glial cells contribute to neuron maturation and maintain CNS homeostasis (Hansson and Ronnback, 2003).

Dysregulation of glial functions is involved in various injuries and diseases: ischemic stroke induces glial cell activation and inflammatory responses, which may contribute to neuron apoptosis (Stoll et al., 1998). Increased microglia activation, astrocyte and oligodendrocyte apoptosis are found in cerebral white matter lesions (Simpson et al., 2007a; Simpson et al., 2007b). Glial activation and cytokine expression-mediated inflammation contributes to neurodegenerative diseases such as AD, and BBB permeability (Mrak and Griffin, 2005; Salmina, 2009; Tomimoto et al., 1996).

(1) Astrocyte

Astrocytes contribute to the BBB integrity, water transport and dynamic signalling involved in the microcirculation control, metabolic and inflammation pathways (Cahoy et al., 2008; Zonta et al., 2003). The astrocyte endfeet generate the astrocytic basal lamina which surrounds the outer surface of the endothelium. The dysfunction of astrocytes leads to BBB permeability and neurodegenerative diseases.

(1-1) Functions of astrocytes

(1-1-1) Regulating water transport

Transmembrane proteins, located at the endfeet of astrocytes and which mediate cellular water movement, belong to the aquaporin (AQP) family. AQP4 is the primary water channel in the brain, highly expressed in astrocytic endfeet (Bloch and Manley, 2007). Another aquaporin, AQP1, conducts gas transport of CO_2 and NH_3 (Musa-Aziz et al., 2009). After the

breakdown of the BBB, the AQP4 water channel contributes to edema formation. The deletion of AQP4 can reduce brain edema accumulation when the BBB is broken, but also slows down the edema clearance when the BBB is restored (Bloch and Manley, 2007; Tomas-Camardiel et al., 2005).

(1-1-2) Maintaining BBB integrity

Astrocytes and their endfeet encircle the brain capillaries and provide signalling factors in the BBB development (Eugenin et al., 2011). The co-culture of brain endothelium and astrocytes greatly enhances TJ expression and reduces the gap junctions when comparing with separately cultured endothelium. This co-culture also increases the astrocyte assembly and concentration, reduces the BBB permeability to sucrose and elevates the TEER (Cohen-Kashi Malina et al., 2009; Tao-Cheng and Brightman, 1988). Both agrin and AQP4 in the astrocytic endfeet help maintain the BBB integrity, and their loss is related to BBB permeability (Wolburg et al., 2009; Zhou et al., 2008). After the BBB is disrupted, astrocytes help to restore the BBB integrity by directing TJ proteins (Willis, 2010).

(1-1-3) Signalling transduction

Astrocytes can secrete a range of neurotransmitters or cytokines which modulate synaptic transmission, and signalling or metabolic pathways (Abbott et al., 2006; Cahoy et al., 2008; Hansson and Ronnback, 2003; Zlokovic, 2008). Neuron-astrocyte signalling also plays a role in cerebral blood flow regulation (Koehler et al., 2009; Zonta et al., 2003).

(1-2) Changes under pathological conditions

Astrocyte dysfunction triggered by pathological stress leads to BBB leakage. There is a decrease in astrocyte expression under hypoxic stress. Loss of astrocytes leads to reduced TJ expression and loss of BBB integrity (Willis,

2011). Under human immunodeficiency virus (HIV) infection stress, HIV-infected astrocytes can trigger the signalling pathways to compromise BBB through a gap-junction-dependent manner (Eugenin et al., 2011).

(2) Microglia

Microglia were first described as a distinct glial cell type by del Rio Hortega in 1927 (del RÃ-o Hortega and Penfield, 1927). Microglia cells have surface antigens and are related to the phagocytic cell linage; they differentiate from circulating monocytes in the blood which enter the brain during embryonic development (Kim and de Vellis, 2005; Kreutzberg, 1996). Microglia are classified into two groups according to their activation status and morphology: (1) highly ramified resting/surveying microglia and (2) amoeboid activated microglia (Kim and de Vellis, 2005). The shift from one state to another needs cytokine release and surface antigen expression (Hanisch and Kettenmann, 2007; Kim and de Vellis, 2005; Kreutzberg, 1996; Zlokovic, 2008).

(2-1) Functions

(2-1-1) Immune sensors

Microglia cells are immune sensors in the brain. They continually screen the brain parenchyma tissue, and they are extremely sensitive guarders (Hanisch and Kettenmann, 2007; Hughes, 2012). The surface antigen expression and cytokine synthesis increased after various stimulus (Kim and de Vellis, 2005).

(2-1-2) Tissue repair

Activated microglia cells initiate tissue repair and promote injured tissue to return to homeostasis by secreting growth factors (Hanisch and Kettenmann, 2007; Kreutzberg, 1996).

(2-2) Changes under pathological conditions

In white matter lesions (WML), there are an increased number of microglia cells. Microglia cells become highly activated and express more surface molecules such as major histocompatibility complex II (MHC class II). There are more MHC class II in the normal appearing white matters around WML than the normal appearing WM from no lesion brains (Simpson et al., 2007a; Simpson et al., 2007b).

Activated microglia cells are involved in systemic inflammation and could contribute to chronic neurodegenerative disease, such as AD and PD (Perry et al., 2010).

Activated microglia cells could also induce BBB dysfunction by releasing proinflammatory cytokines (Abbott et al., 2006). After the stimulus of lipopolysaccharide (LPS), the release of tumor necrosis factor-α (TNF- α) was elevated by release from activated microglia which induces BBB permeability (Nishioku et al., 2010). Similar to astrocytes, microglia cells could help restore the BBB integrity after the BBB is disrupted by directing TJ proteins (Willis, 2010).

(3) Oligodendrocytes

Oligodendrocytes are responsible for synthesis of the myelin sheaths of axons (Aggarwal et al., 2011; Bradl and Lassmann, 2009; Mathis et al., 2003). The myelin and saltatory nerve conduction are the basis for fast information processing in a short distance (Aggarwal et al., 2011).

Oligodendrocytes play a crucial role in NVU signalling. Oligodendrocytes express growth factors influencing the function of neighbouring neurons, and are involved in lipid metabolism (Cahoy et al., 2008; Du and Dreyfus,

2002; Hansson and Ronnback, 2003). Neuroligands could induce Ca^{2+} signal which mediates oligodendrocyte development, myelination in white matter, and demyelination. Ca^{2+} signal could be influenced by growth factors (Soliven, 2001). Oligodendrocytes are connected with astrocytes through gap junctions (Aggarwal et al., 2011).

Deletion or dysfunction of oligodendrocytes can cause myelin loss and impair cerebellum development (Mathis et al., 2003; Watzlawik et al., 2010). Myelin attenuation and oligodendrocyte apoptosis are associated with WML (Simpson et al., 2007a).

2.2.5 Perivascular space (PVS)

The virtual spaces located between the endothelial basal lamina and the astrocytic basal laminas are called perivascular spaces (PVS) (Bechmann et al., 2007). PVS were firstly described and confirmed in detail by a German pathologist Rudolf Virchow and a French histologist Charles Philippe Robin more than a century ago, thus PVS are also known as Virchow-Robin spaces (VRS) (Hutchings and Weller, 1986).

PVS are fundamental structures around vessels in a variety of species, and increasing evidence shows PVS function as an important site for immune cell accumulation and reaction in inflammatory disease, and are related to fluid drainage in the brain which is associated with brain edema and cognitive dysfunction. PVS are also associated with cerebral small vessel disease (SVD) and BBB permeability. We systematically searched the literatures for structure and functions related to PVS using Medline© up to June 2013. After limiting the PVS search to the brain, 349 papers met our search criteria.

We included 96 papers regarding PVS structure, PVS cell origin, immune cell accumulation within PVS, immune cell transmigration through PVS, and also pathological changes related to PVS under a variety of stimuli and associations with SVD and inflammatory diseases. We excluded case reports, comments, review papers, non-translatable (not English or Chinese), duplicates, and where the full text was unavailable. We also excluded topics about vet disease, gene-related diseases, method or treatment comparisons, neurotoxic effect, non-cerebral disease (such as in the spinal cord) and non-vascular disease (such as cerebral metabolic disease). The number of included and excluded paper is summarized in Figure 2.2.

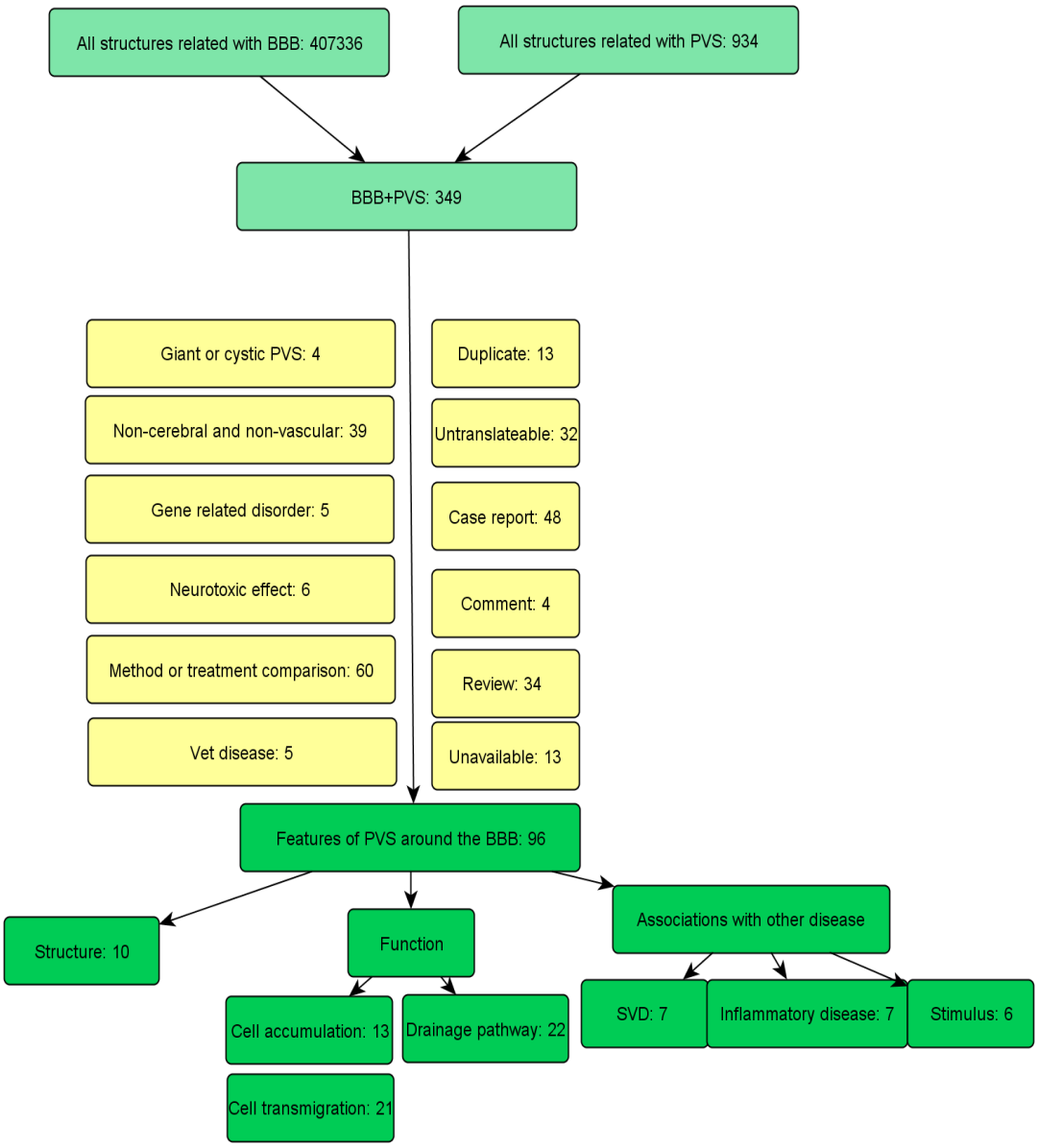

Figure 2.2 Inclusion and exclusion list for PVS systematic search.

(1) PVS Structures

In both the superficial and the deep areas of the brain, PVS are extracellular fluid filled spaces located between the vascular endothelial basement membrane and the glial basement membrane, and they separate blood vessels from the surrounding brain parenchyma (Abbott, 2004). They follow the course of cerebral arteries, arterioles, venules and veins, and eventually disappear around the capillaries when endothelial and glial basement

membranes fuse together (Owens et al., 2008). However those spaces might become expanded under pathological conditions influenced by inflammation or fluid drainage dysfunction. When expanded, these spaces can be seen on magnetic resonance imaging (MRI) especially T2-weighted sequences which have signal intensity similar to cerebrospinal fluid (CSF) and generally less than 3 mm. They appear linear, round or ovoid depends on the imaged direction to the course of the vessels (Wardlaw et al., 2013c).

PVS are fundamental structures located around vessels to maintain pressure, buoyancy and function as a drainage route in a variety of species such as avian, rodents, amphibians, reptiles and mammals (Table 2.1, all tables are in the last section of this chapter, 2.6 Tables).

Three ultrastructural studies illustrated human cerebral PVS by light microscopy (LM), scanning electron microscopy (SEM) and transmission electron microscopy (TEM) (Esiri and Gay, 1990; Hutchings and Weller, 1986; Zhang et al., 1990). It is accepted that PVS are more likely to be extensions of subpial spaces (SPS) (Esiri and Gay, 1990; Hutchings and Weller, 1986; Zhang et al., 1990) rather than the subarachnoid spaces (SAS), which was proposed to have a free communication with PVS proven by tracer studies for a long time. Layers of leptomeningeal cells (pia mater) separate the SAS from the SPS and PVS, and those cells are joined by desomosomes or nexus junctions (Hutchings and Weller, 1986; Zhang et al., 1990). Based on the information from the literatures (Table 2.2), generally a blood vessel is separated from neuropil by three layers of basement membranes (BM), pericyte, and sometimes complete layers of smooth muscle cells (SMC, no SMC layers in capillaries), PVS and limitans from the endfeet of glial cells. On the side of blood vessels, the first layer of BM is on top of the endothelial cells, and this

BM layer is surrounded by a pericyte and the second layer of BM. On the side of glial limitans, the third BM surrounded the glial limitans. PVS are the spaces between the second and third layer of BM, filled with extracellular fluid, perivascular cells and collagens. So we hypothesize typical PVS cell types array from blood vessel to neurons as **endothelial cells/1st BM/pericyte/2nd BM/PVS-cells/3rd BM/ limitans from the endfeet of glial cells** (Figure 2.3)**.** This PVS structure varies with vessel type and vessel location.

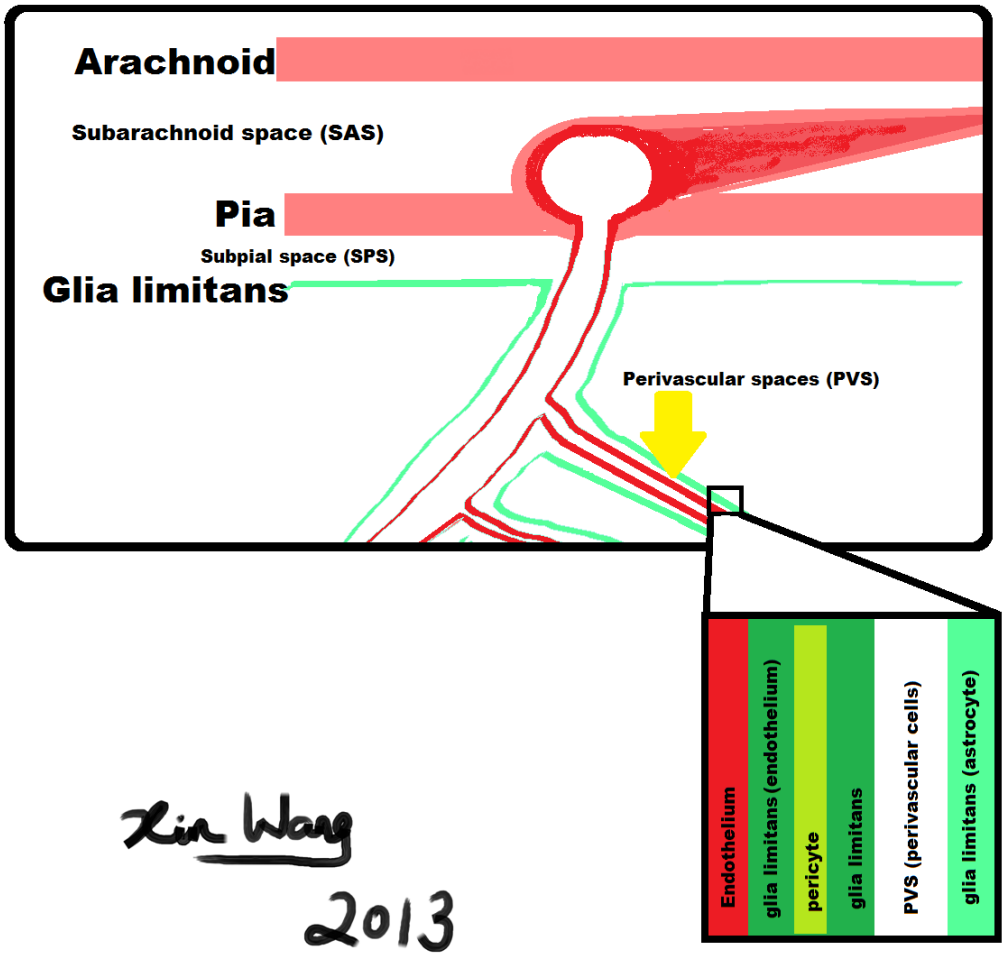

Figure 2.3 PVS structure.

In the basal ganglia regions, PVS around arteries are different from veins. PVS around arteries are like the typical PVS structure and location as described above (Figure 2.3), they are composed by two layers of leptomeningeal cells: arteries are firstly coated by 1st BM layer, pericyte, complete layers of SMC, 2nd BM and an inner layer of leptomeninges (L1), which forms the inner wall of the PVS; the outer layer of leptomeninges (L2) contact with basement membrane of glia limitans (3rd BM) in the brain. These two layers of leptomeningeal cells isolating the PVS from the arteries and glia limitans, and bundles of collagens fill the PVS. In comparison, PVS around veins are composed by one layer of leptomeninges and collagen sheets. Veins surrounded by 1st BM layer, pericyte, incomplete and atypical layer of SMC, 2nd BM layer and inner layer of leptomeninges (L1), but lack an outer layer of leptomeninges (L2), thus the PVS are encompassed by collagen sheets which are continuously overlying the basement membrane of the glia limitans (3rd BM layer) (Pollock et al., 1997).

The structure of PVS also varies according to vessel location. Unfortunately, PVS have not been studied systematically in regard to the different parts of the cerebral vascular tree. We found three original studies about PVS ultrastructure and summarized their findings in Table 2.2. In Zhang's research (Zhang et al., 1990), they examined the arteries and veins in the SAS, arterioles, metarterioles, small and large veins, and small venules in the SPS, and arterioles, venules and capillaries in the cerebral cortex and white matter; in Pollock's research (Pollock et al., 1997), they differentiate structural characteristics of the arteries in the basal ganglia and the arteries in the cerebral cortex, and veins in the basal ganglia. In Hutchings's research

(Hutchings and Weller, 1986), they did not distinguish the arteries and veins or arterioles and venules, and used a general word 'vessel'.

There is a need of systematic research of PVS ultrastructure in the different parts of the cerebral vascular tree in human and animal models. This kind of research would help us understand PVS function and eliminate the apparently contradictory findings in current studies, such as whether PVS are continuous with SAS or SPS, whether fluids within PVS have exchanges with CSF and PVS differences between arteries and veins, arterioles and venules.

(2) PVS cells

Cells located within PVS are addressed as perivascular cells by their location. Perivascular cells differ from pericytes and microglia by their location, morphology and immune phenotype (Bechmann et al., 2001). This population contained dense lysosomal bodies and have active phagocytic activities; they function as scavengers in the PVS (Bechmann et al., 2001; Kida et al., 1993). Perivascular cells express ED2 antigens and MHC class II antigens (Kida et al., 1993), and are able to present antigens to naïve $CD4^+$ T cells (Esiri and Gay, 1990; Walker, 1999). Perivascular cells share morphology and immune similarity with blood-borne macrophages, so they are also called perivascular macrophages (Bechmann et al., 2001; Guillemin and Brew, 2004).

The question of whether perivascular macrophages were a population of resident histiocytes or a migratory population from the blood monocytes has been debated. Researchers using tracer injection, green-fluorescent-protein (GFP)-transfected cells and monoclonal antibodies immune staining (Table 2.3) found conflicting evidence which support both a resident and a non-

resident origin of perivascular macrophages (Bechmann et al., 2001). Macrophages have a short life span (Mercier et al., 2006). The carbon injection experiment demonstrated that carbon particles were still within macrophages for at least 2 years (Kida et al., 1993) suggests that at least some are resident macrophages but is conflict with short life time span of macrophages (Hickey, 2001). A possible explanation for this phenomenon is the carbon particles could possibly be re-ingested by new macrophages after the death of old ones. Currently it is accepted that macrophages could be replaced by circulating hematopoietic stem cells from blood approximately every three weeks (Hess et al., 2004; Mercier et al., 2006). This extravasation process was activated by macrophage chemo-attracting protein-1 (Hess et al., 2004). After successful extravasation from vascular endothelium, the monocytes (or the stem cells) mature into perivascular macrophages (Mercier et al., 2006).

Tracer experiments showed that though blood-borne macrophages could infiltrate into PVS and mature into perivascular cells, those cells did not further migrate into brain parenchyma at least in normal rats' brain (Bechmann et al., 2001).

(3) PVS Cell accumulation and transmigration

CNS immune invasion is the entry of immune cells into the brain parenchyma in inflammatory conditions, and the invasion involves two steps: (1) immune cell accumulation within PVS; (2) after complete breakdown of BBB, immune cells transmigrated across the PVS and glia limitans and then invaded into the brain parenchyma (Owens et al., 2008). PVS functioned as an immune cell buffering site and reaction place responsible for immune cell accumulation (Table 2.4) and transmigration

(Table 2.5). In normal and in inflammatory conditions such as multiple sclerosis (MS), human immunodeficiency virus encephalitis (HIVE), encephalitis induced by other types of viruses and bacteria, and cerebral ischemia, a variety of immune cells such as macrophages, microglia, monocytes, T-lymphocytes, B-lymphocytes, and dendritic cells (DC) accumulated within PVS or infiltrated into the brain parenchyma through PVS. PVS were also involved in non-inflammatory pathological states, such as cerebral ischemia, traumatic brain injury (TBI), neurodegeneration and tumors (see Table 2.4 and 2.5).

Under inflammatory condition of MS, accumulation of immune cells such as macrophages, DC and lymphocytes in PVS are prominent features of acute MS plaques (Bogie et al., 2011; Esiri and Gay, 1990). Transmigration of DC, macrophages, monocytes, neutrophils and other leukocytes across the BBB into the brain were found in MS or the MS rodent model Experimental autoimmune encephalomyelitis (EAE) (Ahn et al., 2009; McCandless et al., 2008a; Sagar et al., 2012; Tsai et al., 1997). The very late activation antigen-4 (VLA-4) assisted the entry of $CD4^+$T cells into brain to cause EAE (Tsai et al., 1997). Chemokine (C-X-C motif) ligand 12 (CXCL12) mediated leukocytes infiltrating to PVS, but not into parenchyma. CXCL12 redistributed to the luminal sides of venules in active MS lesions and this altered expression was specifically associated with MS (McCandless et al., 2008a). Nerve injury-induced protein Ninjurin1 (Ninj1) facilitated the entry of myeloid cells, such as macrophages and monocytes across the BBB into the CNS in normal and EAE brains (Ahn et al., 2009). Chemokine ligand 2 (CCL2) facilitated transmigration of DC across the BBB (Sagar et al., 2012).

Under the inflammatory condition of HIVE, mononuclear cells, $CD3^+$ and $CD8^+$ T cells accumulated in the PVS. The accumulation of immune cells was an important biomarker for HIVE and associated with BBB permeability (Hawkins et al., 1993; Petito et al., 2006). Lymphocyte infiltration to the PVS had been found in all three stages after HIV infection: asymptomatic HIV infection, early stage of Acquired Immune Deficiency Syndrome (AIDS) and fully developed AIDS. It was a characteristic finding in asymptomatic HIV infection (Kibayashi et al., 1996). Zonula occluden-1 (ZO-1) disruption and BBB permeability was found in the brain of patients with HIVE, cyclooxygenase 2 (COX-2) and CD68 positive macrophages, T and B lymphocytes infiltrated the PVS and migrated into the brain parenchyma through a damaged BBB (Fiala et al., 2002). Very low numbers of B lymphocytes entered all parts of the healthy human brain, and the transmigration into the PVS and brain was increased in some AIDS and pre-AIDS brains (Anthony et al., 2003). In an animal model of HIV, researchers observed monocytes transmigrated from blood to CNS within 48 hours after simian immunodeficiency virus (SIV) infection. This monocyte infiltration was in the acute phase of SIV infection (Clay et al., 2007).

Beside HIVE, immune cell accumulation within PVS and transmigration through PVS were also observed in other types of encephalitis induced by viruses or bacteria. In sheep infected with visna/maedi virus, macrophages, $CD8^+$, $CD4^+$ T cells and B cells accumulated within PVS (Polledo et al., 2012). When mice were infected by West Nile virus, specific CD8 T cells infiltrated the PVS and entered the CNS which was mediated by CXCL12 (McCandless et al., 2008b). When interferon gamma (IFN-γ) gene knockout mice were infected with retrovirus, the mice showed distinct axon degradation and

leukocyte transmigration into PVS and ventricles. Infiltrated leukocytes were positive to inducible nitric oxide synthases staining (Koustova et al., 2000). In humans infected with Venezuelan equine encephalitis virus, infiltration of lymphocytes, mononuclear cells and neutrophils was present in the PVS and leptomeninges (de la Monte et al., 1985). Accumulation of mononuclear cells in the PVS and infiltration into the meninges was observed in chicken infected with Marek's disease virus (Barrow et al., 2003). In rats infected by *Trypanosoma brucei gambiense*, which causes African trypanosomiasis in humans, transmigration of plasma and T cells was found in the PVS and leptomeninges (Anthoons et al., 1989). Leukocytes infiltrated into PVS, choroid plexus and leptomeninges was observed in cats infected with *pneumoniae* (Hochwald et al., 1984). In cerebral malaria, another cerebral inflammatory disease, leukocytes, macrophages and lymphocytes accumulation in PVS was a hallmark (Lackner et al., 2006). AQP4 located around capillary endothelium and astrocyte endfeet which facilitated the water movement also contributed to leukocyte accumulation (Ampawong et al., 2011).

Under ischemic stimulus, infiltrating monocytes from the circulating blood, perivascular cells and parenchymal microglia increasingly expressed CD14, which functions as binding receptors for bacteria, viruses and apoptotic cells which activate monocytes and macrophages (Beschorner et al., 2002). $CD14^+$ cells significantly contributed to the post-ischemic inflammatory response (Beschorner et al., 2002).

Perivascular macrophages could produce cytokines and factors to enhance immune responses in collaboration with other immune cells and other factors accumulated in this space or facilitate immune cells transmigration

through this space into brain parenchyma (Galea et al., 2005; Staines et al., 2008).

(4) Fluid drainage through PVS

The PVS are filled with interstitial fluid (ISF) instead of CSF within brain parenchyma. ISF was derived from the fluid in the blood, grey matter and white matter presumably by diffusion through the extracellular spaces and bulk flow along PVS (Abbott, 2004; Schley et al., 2006; Zhang et al., 1992). Another kind of extracellular fluid CSF is produced by the choroid plexuses in the ventricles. CSF circulates in the ventricles and subarachnoid space (SAS) and drains into the blood via arachnoid granulations and villi in humans (Schley et al., 2006). There is a continuity between ISF and CSF (Tarnaris et al., 2011), both ISF and CSF systems function as supplements to the lymphatic circulation and protein clearance, and PVS is associated with ISF and CSF drainage in both physiological and pathological conditions (Table 2.6).

Tracers such as albumin (Bradbury et al., 1981; Yamada et al., 1991), horseradish peroxidise (HRP) (Gregory et al., 1985; Rennels et al., 1985; Wagner et al., 1974) and immunoglobulin G Fc receptor (Siegelman et al., 1987) entering the CNS were drained by the PVS around blood vessels to the arachnoid granulations and finally enter the lymphatic circulation in physiological conditions. Soluble antigens, but not cells, drain from the brain by perivascular pathways (Schley et al., 2006). Such drainage pathways play a protective role in the clearance of proteins (Siegelman et al., 1987).

The drainage efficiency of Aβ and tau proteins was associated with cerebral amyloid angiopathy (CAA) and AD (Carare et al., 2008; Roher et al., 2003;

Schley et al., 2006). The structure of the PVS in the basal ganglia region may facilitate effective Aβ drainage in this region (Pollock et al., 1997). In ageing vessels, the reduced amplitude of pulse could prolong Aβ attachment time on vessel walls, and induce its accumulation (Schley et al., 2006). The accumulated Aβ deposition in drainage pathways would further impede clearance of Aβ and ISF from the brain in AD (Carare et al., 2008). The myelin particle clearance in MS may follow the same particles elimination mechanism (Kooi et al., 2009). Dilation of PVS was a sign of ineffective ISF drainage which correlated with total Aβ load, ApoE ε4 genotype and CAA severity in AD patients (Roher et al., 2003; Thal, 2009).

In idiopathic normal pressure hydrocephalus (INPH), which is a condition of unknown causes that affects older people and results in enlarged ventricles, and problems of cognition, balance, gait and continence (Shprecher et al., 2008), alterations in CSF dynamics may trigger the abnormal bulk flow of ISF along the PVS (Tarnaris et al., 2011). The altered CSF dynamics also impaired the Aβ clearance in an INPH rat model (Silverberg et al., 2010). The INPH also showed associations with ischemia (Corkill et al., 2003) and SVD, such as infarction (Bradley et al., 1991), and White Matter Hyperintensities (WMH) on MRI (Krauss et al., 1996; Krauss et al., 1997) in humans.

In the rat model of intracerebral hemorrhage (ICH), spread of hematoma along perivascular spaces and perineural tracts was observed. The hematoma extension may involve lymphatic encephalopathy (He et al., 2012). PVS functioned as the route for edema fluid clearance in a tumor model in rats (Kida et al., 1994).

(5) PVS associate with inflammatory disease

Besides the pathological evidence associated with immune cells in PVS described in earlier part'(3) PVS Cell accumulation and transmigration', other studies (which did not describe from the direction of cells within PVS) also suggested the association between PVS and inflammatory disease such as MS (Gay, 2006), HIV (Gorantla et al., 2010), cryptococcosis in HIV infection (Klock et al., 2009) and trypanosomiasis (Rudin et al., 1984; Schmidt, 1983) within the CNS.

In addition to histology, PVS on MRI have been investigated as a prognostic tool for inflammatory disease, especially in MS. For example, two studies show associations between PVS enlargement and inflammation in MS, with comparison to healthy controls, PVS number and volume was a marker for inflammation in MS patients (Wuerfel et al., 2008). Another study shows PVS in the supraventricular region was a marker for MS (Al-Saeed et al., 2012). PVS on MRI could possibly be a convenient tool in detecting inflammatory disease in other studies.

(6) PVS associate with Small Vessel Disease (SVD)

PVS are not visible on MRI unless enlarged. Enlarged PVS have been considered as normal structures in the brain for a long time since they also appear in small numbers in young and healthy control volunteers. However, increasing age and hypertension are two risk factors for PVS (Potter et al., 2013). PVS rating score was independently associated with age, hypertension, WMH, and lacunar infarctions in basal ganglia regions (Martinez-Ramirez et al., 2013; Rouhl et al., 2008), and in both basal ganglia and white matters regions (Zhu et al., 2010). Also accumulating evidence shows that dilatation of PVS could be a potential marker for cerebral small

vessel disease (SVD), inflammation, BBB permeability and cognitive dysfunction (Doubal et al., 2010b; Potter et al., 2013; Zhu et al., 2010).

PVS associated with SVD: higher numbers of PVS in the basal ganglia region were associated with more severe silent lacunar infarcts and WMH (Rouhl et al., 2008). The severity of PVS was associated with the load of WMH and lacunes, as well as showing the association is stronger if the PVS are located in the basal ganglia rather than in the white matter (Zhu et al., 2010). The PVS in the white matter were associated with lobar microbleeds (Martinez-Ramirez et al., 2013). PVS rating scores in the basal ganglia region were significantly associated with lacunar stroke and PVS scores in the centrum semiovale region after adjusting for vascular risk factors and WMH (Doubal et al., 2010b; Potter et al., 2013). Total PVS rating scores (basal ganglia and centrum semiovale) were correlated with deep WMH and previous stroke (Potter et al., 2013).

PVS were also detected in the basal ganglia and temporal white matters in patients with cerebral autosomal dominant arteriopathy with subcortical infarcts and leukoencephalopathy (CADASIL), which is a single gene disorder form of SVD (Cumurciuc et al., 2006; Flossmann, 2006). PVS in the basal ganglia region were potential markers for cerebral microvascular angiopathy before WMH become apparent in subjects at risk of stroke (Selvarajah et al., 2009). PVS also associated with myotonic dystrophy, as PVS near vertex were more frequent and severer in patients with myotonic dystrophy than in controls (Di Costanzo et al., 2001). The PVS rating score was related to BBB permeability in patients with lacunar stroke (Wardlaw et al., 2009). Increased BBB permeability in the white matter was also suggested to be related to normal ageing, increasing WMH and vascular dementia. PVS

were correlated with worse cognitive function in healthy older people. PVS were more common in older adults and more severe in patients with AD or mild cognitive impairment than in cognitively normal controls (Chen et al., 2011).

2.3 BBB junction proteins

As mentioned in the earlier section describing the endothelium part of the NVU, tight junctions (TJ) and adherens junctions (AJ) are two major categories of junctional proteins in the BBB (Bazzoni and Dejana, 2004). The detailed description about the structure and function for each TJ and AJ proteins and their changes during pathological conditions will be discussed as follows. A junction proteins atlas of the BBB is depicted in Figure 2.4.

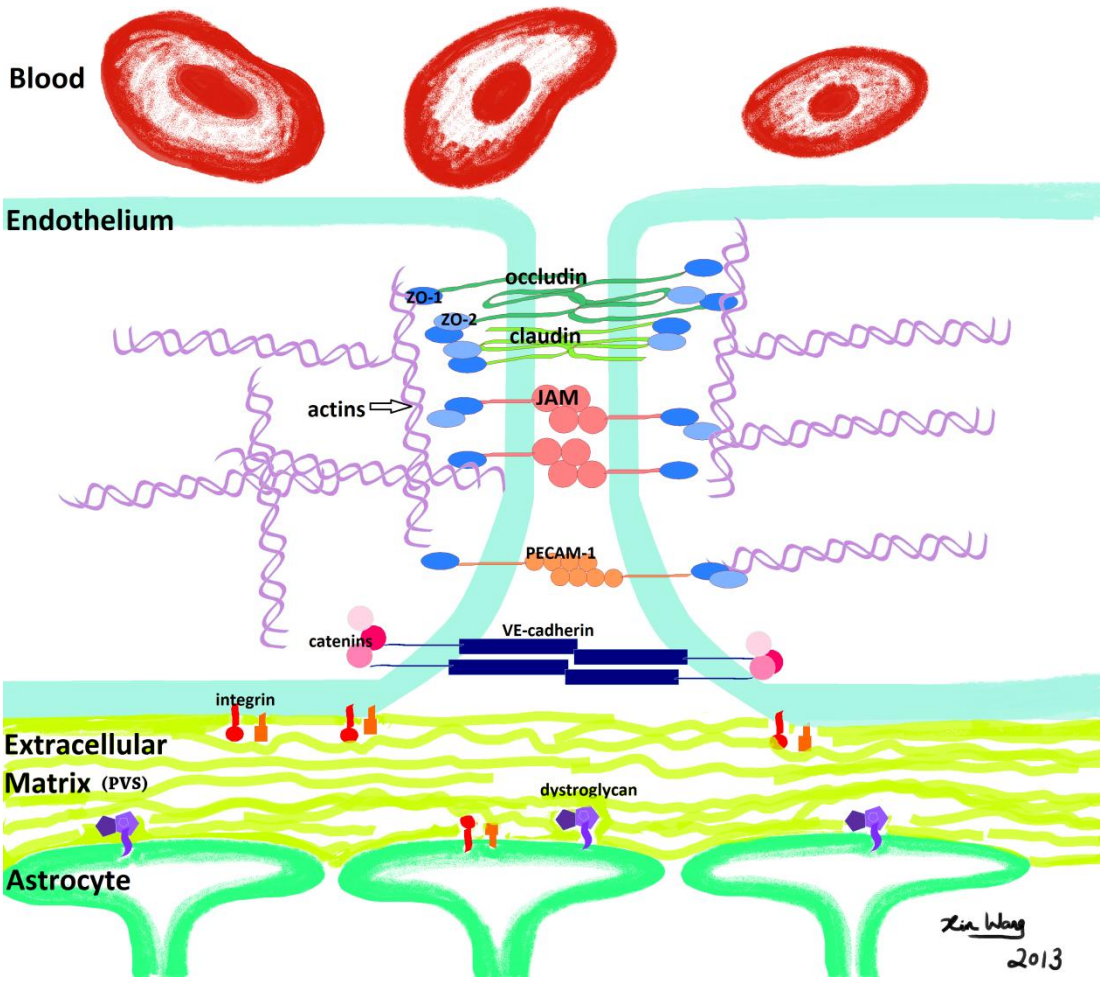

Figure 2.4 Junction proteins atlas of the BBB.

2.3.1 Tight junctions (TJ)

The TJs arrange as oligomeric proteins with transmembrane domains. In response to external stressors, such as hypoxia, inflammation and Aβ stresses, structure and phosphorylation states of TJ proteins alter rapidly. This may cause changes in BBB integrity and permeability (McCaffrey et al., 2007; Sakakibara et al., 1997).

(1) Occludin

Occludin is the most studied TJ protein. Studies have found that occludin is located in the TJ in both epithelial and endothelial cells. It is an approximately 65 kDa protein with hydrophilicity (Furuse et al., 1993).

Occludin is composed of four transmembrane domains and a COOH-terminal domain (domain E). The four transmembrane domains make up two extracellular loops which are rich in tyrosine and glycine residues. Domain E was found to be necessary to locate occludin at TJ (Furuse et al., 1994).

Occludin contributes to the electrical barrier function of TJ and probably the formation of aqueous pores. The increased expression of occludin was associated with the increase of transendothelial electrical resistance (TEER), which is an example of the occludin making the electrical paracellular barrier tighter (McCarthy et al., 1996). The TJ barrier function is also influenced by occludin phosphorylation status. Highly phosphorylated occludin is concentrated at TJ, and the use of protein tyrosine phosphatase inhibition induces occludin proteolysis and increases the paracellular permeability (Wachtel et al., 1999). Thus the phosphorylation is considered to be a key regulator of TJ assembly (Sakakibara et al., 1997). The occludin phosphorylation is regulated through RhoA-p160ROCK -dependent and -independent manners (Hirase et al., 2001). The oligomeric form of occludin (homodimers) is critical in TJ assembly at the BBB which associates with ZO-1 and caveolin-1 locate in plasma membrane (McCaffrey et al., 2007).

The occludin expression and phosphorylated status is altered in a variety of pathological states. In studies of inflammatory pain models, expression of occludin significantly decreased in inflammatory pain groups induced by the λ-carrageenan and complete Freund's adjuvant (CFA) (Huber et al., 2001). The total occludin expression was significantly decreased at 1h, 3h, 6h, 12h and 48h after the λ-carrageenan-induced inflammatory pain (Huber et al., 2002). In the CFA treated inflammatory pain groups, expression of occludin

significantly decreased by 60% (Brooks et al., 2005). Both stimuli increased BBB permeability. Studies have shown excessive occludin phosphorylation on tyrosine residuals increases transcellular permeability in epithelial and endothelial cells. Thus these studies suggested, using the inflammatory pain model, BBB permeability can be induced by decreased occludin expression secondary to inflammatory pain stimuli, which may be a consequence of increased tyrosine phosphorylation triggered by inflammation (Huber et al., 2001).

Hypoxic stress induced little change in occludin expression; however the expression increased significantly after hypoxia-reoxygenation (Mark and Davis, 2002). Further study of hypoxia stress has found that in the condition of hypoxia-reoxygenation there is more phosphorylated occludin (Witt et al., 2003). In cerebral ischemia, expression of occludin decreases which leads to BBB integrity disruption, which might be caused by MMP (Rosenberg and Yang, 2007). During ischemia, tPA and age independently increase occludin phosphorylation, which triggers early BBB permeability following ischemic stroke (Kaur et al., 2011).

In the experimental diabetic rats, occludin degradation was observed to coincide with increased MMP activity. This suggests that diabetes increases loss of TJ proteins which leads to BBB permeability, and MMP may contribute to this process (Hawkins et al., 2007). However, the combined stress of hypoxia and aglycemia, which is seen in ischemic stroke, induced increased occludin expression which was interpreted as a protection effect to minimize BBB permeability (Brown and Davis, 2005).

In neurodegeneration disease, such as AD and vascular dementia (VaD), neurons overexpress occludin in frontal cortex and basal ganglia as compared to ageing controls (Romanitan et al., 2010; Romanitan et al., 2007). ApoE is a major apolipoprotein in the brain, and its isoform ApoE4 is a major risk factor for AD. The BBB and TJ integrities are regulated by apoE in an isoform-dependent manner. For example, BBB was reconstructed with primary astrocytes from human apoE4-knock-in mice (apoE4-BBB model). The effects of occludin phosphorylation at tyrosine residuals, and the activation of protein kinase C eta, were more enhanced in the apoE4-BBB model, when compared with those effects in the apoE3-BBB model (Nishitsuji et al., 2011).

In EAE, an animal model of MS, the occludin dephosphorylation co-occurs with inflammation, which suggests occludin dephosphorylation could relate to immune cells migration and increased BBB permeability (Andrews et al., 2007).

In the human glioblastoma multiforme, occludin expression was significantly reduced in hyperplastic vessels, which may contribute to the microvascular permeability in human gliomas (Liebner et al., 2000).

The altered expression of occludin is related to BBB permeability and leukocyte trafficking into the endothelium cells, which will be discussed in detail in a later section.

In order to function properly and locate at TJ, occludin also needs cytoplasmic support from the family membrane-associated guanylate kinase (MAGUK) proteins which function as scaffolding proteins.

(2) Zonula Occludens (ZO)

Membrane-associated guanylate kinase (MAGUK) proteins are characterised by MAGUK domains: PDZ, Src homology 3 (SH3), and guanylate kinase-like domains. All of these domains can function as protein-protein interaction sites (Shin et al., 2000). Zonula occludens (ZO-1, ZO-2 and ZO-3) are members of the MAGUK protein family.

(2-1) ZO-1

ZO-1 is a protein with molecular mass of 220 kDa (Furuse et al., 1994; Itoh et al., 1993). It links transmembrane protein occludin with the cytoskeleton, which is directly required for occludin localization at TJ (Furuse et al., 1994).

ZO-1-associated nucleic acid-binding protein binds to ZO-1 through SH3 domain of ZO-1, which can regulate ErbB-2 expression and function in paracellular permeability (Balda and Matter, 2000). Gα12 can also bind to SH3 domain of ZO-1, which regulates barrier function of cultured Madin-Darby canine kidney epithelial cells (Meyer et al., 2002).

Altered expressions of ZO-1 are found in various pathological states. In the induced inflammatory pain model, ZO-1 expression is significantly increased in formalin, λ-carrageenan, and CFA pain models (Huber et al., 2001). It was confirmed in another λ-carrageenan induced inflammatory model that ZO-1 expression significantly increased at 1h, 3h, and 6h compared with controls, and it returned to control level by 12h (Huber et al., 2002). However, in contrast with the previous two studies, there was no significant increase in ZO-1 protein expression in CFA induced chronic inflammatory pain model (Brooks et al., 2005).

In the studies of MS, ZO-1 expression was found to be significantly different between different lesion types in MS, and also between MS lesions and normal appearing white matter. Further MS research found that ZO-1 is more frequent in active WML (Kirk et al., 2003; Leech et al., 2007). In experimental diabetes rats, expression of ZO-1 decreased compared with controls (Hawkins et al., 2007). One study of human HIV found that loss of ZO-1 was highly associated with monocyte transmigration in HIV infection, and was also highly correlated with HIV-1-associated dementia (Boven et al., 2000).

(2-2) ZO-2

Another protein from the MAGUK family is ZO-2, with a molecular mass of 160 kDa (Furuse et al., 1994). ZO-2 and ZO-1 are not functionally identical: it aid the anchoring of occludin to the cytoskeletal architecture (actin) (Mitic and Anderson, 1998) which functions redundantly as ZO-1 (Umeda et al., 2004).

Similar to hypoxia stress induced change in occludin, the expression of ZO-1 and ZO-2 are nearly the same after hypoxia, however, the expression of ZO-1 and ZO-2 increases significantly after post hypoxia reoxygenation (Mark and Davis, 2002).

(2-3) ZO-3

Another MAGUK protein related to TJ is ZO-3. Similar as ZO-1 and ZO-2, ZO-3 also concentrates at TJ. However, it is expressed in many types of epithelial cells instead of the endothelium (Ekre et al., 2003). Except for the important TJ proteins like occludin, ZO-1, and ZO-2 mentioned above, there is another family of proteins which has higher cell adhesion activity than occludin, called the claudin family.

The claudin family is another important component in maintaining the BBB integrity. Occludins and claudins are both good adhesion molecules functioning at TJ to compose the tight "kissing point of TJ" which completely removes the space between neighbouring cells. The cell-adhesion activity of occludin is negligible when compared with that of claudins (Kubota et al., 1999).

(3) Claudins

Claudins, named from the Latin claudere, means "to close" (Mitic et al., 2000). Claudin-1 and claudin-2 were first isolated from chicken liver junctional fractions, from which occludin was first identified (Furuse et al., 1998). They soon turned out to be a growing family of tight junction proteins (Mitic et al., 2000). Now, the claudin multigene family is composed of 16 transmembrane proteins with molecular weight of 20–28 kDa (Kubota et al., 1999; Romanitan et al., 2010). Claudins have high cell adhesion activity, concentrated at TJ and have an essential role in the formation of TJ strands. They appear to function as the primary seal at TJ in forming the TJ backbone (Romanitan et al., 2010). There are at least three types of claudin-claudin interactions: TJ type, disjunction type, and intracellular type; which can all be influenced by a single amino acid in the claudin extracellular loop 2 (Piontek et al., 2008).

Claudins are responsible for TJ specific cell adhesion activity. Here are some descriptions of the claudin TJ function features.

(3-1) Claudin-5

Of all the claudin proteins expressed by brain endothelial cells, claudin-5 is considered to be the most critical component in keeping the BBB integrity and is the most studied TJ protein in the claudin family. Claudin-5 is

expressed in all tissues, specifically localising in the endothelium of blood vessels, and functions importantly in regulating vascular and BBB permeability (Romanitan et al., 2010).

A study of claudin-5 deficient mice found that the BBB barrier function against small molecules (<800 Da) was selectively dysfunctional. The brains of these mice had no bleeding or edema showing the main vessel structure was not altered. Also, the BBB barrier function against large molecules (>800 Da) still remained. Therefore, the size-selective loosening of BBB in claudin-5 deficient mice proved that claudin-5 plays a role in BBB size selecting passage function (Nitta et al., 2003).

Similar to findings about occludin, the oligomeric form of claudin-5 is critical in TJ assembly at the BBB. Claudin-5 homodimers also associate with plasma membrane protein ZO-1 and caveolin-1 (McCaffrey et al., 2007).

Since occludin and claudin-5 were considered as two of the most important TJ proteins in keeping BBB integrity and barrier function, and increased phosphorylation states of both claudin 5 and occludin during ischemia were influenced by increased tPA level and age (Kaur et al., 2011). There is a hypothesis to distinguish their effects. It is hypothesised that the severity of BBB permeability relates to the disassembly of different TJ proteins, either occludin or claudin-5. In claudin-5 deficient mice, loss of claudin-5 leads to BBB dysfunction against small molecules (<800 Da) (Nitta et al., 2003) which was considered as a mild leakage, whereas decreased occludin expression was associated to albumin leakage (68 kDa) which was considered as a severe leakage and suggested that occludin disassembly predominates severe BBB permeability (Kaur et al., 2011).

(3-2) Other proteins in the claudin family

Similar to claudin-5, claudin-1 and claudin-3 also localize at the BBB and their expression levels were also altered in various pathological states (Romanitan et al., 2010). In addition, claudin-1, claudin-2, claudin-5 and claudin-11 were also found to localize at the choroid plexus where their expression is affected by protein kinase C activation (Romanitan et al., 2010; Wolburg and Lippoldt, 2002). Claudin-11 is concentrated in TJ and myelin, and it is also known as an oligodendrocyte-specific protein. It is proposed that claudin-11 plays a key role in the development and formation of oligodendrocytes and Schwann cells (Bronstein et al., 2000).

Claudin-1, -2, and -3 function as cell adhesion molecules in a Ca^{2+} independent manner (Kubota et al., 1999). Claudin-2, claudin-4 and claudin-7 regulate Na^{+} and Cl^{-} ion transportation (Romanitan et al., 2010). In contrast to other BBB gatekeeper claudins, introducing claudin-2 markedly decreased the tightness of individual claudin-1/4-based TJ strands (Furuse et al., 2001).

(3-3) Alterations of claudin proteins in pathological states

In cerebral ischemia, decreased expression of claudin-5 impairs BBB integrity, and this process involves MMP (Rosenberg and Yang, 2007). During ischemia after stroke, tPA and age enhance claudin-5 phosphorylation independently. The increase in claudin-5 phosphorylation triggers early BBB permeability following ischemic stroke (Kaur et al., 2011).

In the CFA-treated inflammatory pain rats' model, expression of claudin-3 increased 450% and claudin-5 increased 615%. The changes in transmembrane claudin proteins contribute to alteration in BBB function (Brooks et al., 2005). However, no differences were seen in claudin-1

expression in formalin, λ-carrageenan, and CFA pain models (Huber et al., 2001).

Claudin family proteins might respond to cellular stress, for example in AD and VaD brains there were altered expressions of claudin-2, claudin-5 and claudin-11 in neurons, astrocytes and oligodendrocytes. There was a significant increase of claudin-2, claudin-5 and claudin-11 in the neurons from both AD and VaD brains as compared to aged controls. Claudin-2 and claudin-11 expressed significantly higher in astrocytes from AD and VaD brains as compared to controls. For the oligodendrocytes, claudin-11 was significantly higher in AD and claudin-2 was significantly higher in VaD as compared to controls (Romanitan et al., 2010).

In the human glioblastoma, expression of claudin-1 was totally lost in the majority of tumor microvessels and claudin-5 expression decreased significantly in hyperplastic vessels, which may contribute to the microvascular permeability and edema seen in human gliomas (Liebner et al., 2000).

(4) Junctional adhesion molecule (JAM)

Junctional adhesion molecule (JAM) proteins belong to the immunoglobulin superfamily (Del Maschio et al., 1999). JAM proteins facilitate leukocyte migration into the CSF and brain parenchyma, and also function in albumin influx into CSF. The monocyte and neutrophil infiltration, and albumin influx were strongly reduced after using JAM inhibitor (Del Maschio et al., 1999). JAM has been found to colocalize with TJ molecules such as occludin, ZO-1 and cingulin and also initiate actin assembly (Bazzoni et al., 2000;

Sobocka et al., 2004). These data indicate that JAM may be a component in facilitating junction protein assembly.

JAM-A, also known as platelet adhesion molecule 1 (PAM-1; F11 Receptor: F11R; a.k.a; JAM-1), is a protein with a molecular weight of 32-35 kDa (Sobocka et al., 2004). It is expressed in endothelial and epithelial cells and is also expressed on leukocytes, neutrophils, monocytes, erythrocytes and platelets (Bazzoni et al., 2000; Sobocka et al., 2004).

Localization of JAM-A is thought to be initiated by homophilic interactions on adjacent cells. Leukocyte function associated antigen-1 (LFA-1) is a receptor for JAM-A. The binding of JAM-A to the β2-integrin LFA-1 facilitates leukocyte migration. Thus JAM-A is a counter-receptor for LFA-1 for leukocyte migration and recruitment (Ostermann et al., 2002).

Abnormal JAM-A expression was found frequently in active white matter lesions areas of MS and the JAM-A staining was less intense and more diffuse in these areas. The abnormal JAM-A expression was observed from small capillaries to large vessels and influenced leukocyte trafficking (Padden et al., 2007).

2.3.2 Adherens junction (AJ)

The key interaction in adherens junction (AJ) is between cadherin and catenin. The cadherin-catenin complex is essential for strengthening cell–cell adhesion and for transferring signals between neighbouring cells. The cell signaling can be transferred in three different ways: firstly, by localising signaling molecules directly; secondly, by controlling catenins in the cytoplasmic level; and thirdly, by the releasing and binding of growth factors and cytokines.

(1) Platelet endothelial cell adhesion molecule (PECAM)

Platelet endothelial cell adhesion molecule 1 (PECAM-1), which is also known as CD31, is a 130 kDa protein (DeLisser et al., 1994), which belongs to the immunoglobulin superfamily (Del Maschio et al., 1999), which is expressed on the surface of endothelial cells, leukocytes (e.g. monocytes and neutrophils), platelets, and selected T cell subsets (Newman, 1997).

PECAM-1 promotes cell adhesion events involving endothelial cells, leukocytes and platelets (DeLisser et al., 1994). In some cell types, PECAM-1 is also involved in signal transduction processes. It may function as an agonist receptor which initiates signal pathways leading to secondary adhesion by non–PECAM-1 receptors (Newman, 1997).

PECAM-1 is a major participant in leukocyte recruitment and extravasation during inflammatory process and Aβ-related cerebrovascular disorders (DeLisser et al., 1994; Giri et al., 2000; Newman, 1997). In one EAE (animal model of MS) study, they fused PECAM-1 to human IgG-Fc. This fused sPECAM-Fc protein impaired leukocyte migration through the BBB and reduced autoimmunity (Reinke et al., 2007). Aβ mediates monocytes migration during cerebrovascular disorders like AD. Inhibitors of PECAM- 1 and Aβ receptor RAGE decrease the migration of monocytes (Giri et al., 2000). PECAM-1 inhibitors may bring a promising method in reducing leukocyte trafficking in both cerebral inflammatory and degenerative diseases with therapeutic benefits.

(2) Cadherin

Cadherin is a large family of single chain transmembrane adhesion proteins. Like other adhesion junction proteins, cadherin has adhesion functions of homophilic binding which contributes to maintaining the endothelial cell

permeability. Cadherin also contributes to scaffolding cellular morphology, signaling transduction, and angiogenesis (Dejana, 1996; Dejana et al., 2000).

Vascular-endothelial-cadherin (VE-cadherin, also called 7B4, cadherin-5) is a major cadherin in mediating adhesion junctions, which mediates cell adhesion through homophilic and calcium-dependent manners (Breviario et al., 1995). VE-cadherin collocates with α-catenin (Breviario et al., 1995) and links to p120 and β-catenin (Dejana, 1996) and is highly phosphorylated in tyrosine when there are weak and unstabilized junctions (Dejana, 1996).

VE-cadherin plays an important role in maintaining vessel endothelial integrity; it is required for both quiescent vessels and new vessels. VE-cadherin regulates vessel integrity through three mechanisms: the first mechanism is directly activating signaling molecules; the second one is regulating gene transcription; and the third may be through forming complexes together with growth factor receptors, and modulating signaling properties (Lampugnani and Dejana, 2007). VE-cadherin functions as a scaffolding protein which is able to regulate gene transcriptions, associate vascular endothelial cell growth factor receptor and promote signaling (Dejana et al., 2000).

(3) Catenin

There are three types of catenins which function as junctional cytoplasmic plaque proteins: α-; β-; and γ-catenin. Cadherin-catenin interactions are necessary for strengthening adhesion between neighbouring cells and in transferring signals between cells (Dejana, 1996).

Cadherin is bound to actin filaments, directly through interaction with α-catenin and indirectly through α-actinin, vinculin, and radixin (Mitic and

Anderson, 1998). The interactions between VE-cadherin and catenins are important in maintaining endothelial paracellular permeability (Dejana, 1996). Binding of catenins to ZO-1 weakens their interactions with VE-cadherin, which may block the formation of tight junctions (Rajasekaran et al., 1996).

(4) Actin

Actin functions as cytoskeletal architecture, to which TJ complexes are all anchored (e.g. claudin-1, occludin, ZO-1 and ZO-2) (Mark and Davis, 2002). Actin is involved in regulating paracellular permeability, and it binds to cadherin indirectly (Mitic and Anderson, 1998).

The expression of actin alters in response to extracellular stress. After the stress of hypoxia and reoxygenation, the expression of actin increased (Mark and Davis, 2002). However, in the condition of hypoxia and aglycemia, actin expression was dramatically reduced (Brown and Davis, 2005). Actin expression increased significantly in the inflammatory pain rat models induced by λ-carrageenan and CFA (Huber et al., 2001).

2.3.3 Colocalization of junction proteins

TJ and AJ proteins are highly colocalized (Figure 2.4, Table 2.7). From Table 2.7 it can be seen that TJ protein ZO-1 appeared 7 times in colocalization with other junction proteins. Another TJ protein JAM occurred 5 times, whereas VE-cadherin, occludin and claudin-5 occurred 3 times. These colocalizations suggest that ZO-1, JAM, occludin and claudin-5 are important junctional proteins in cytoskeleton structure, and may be involved in facilitating TJ and AJ assembly in order to maintain the BBB.

2.4 Stimuli for BBB compromise

2.4.1 Leukocyte transmigration

(1) Two steps of leukocyte transport across the BBB into brain parenchyma

(1-1) Migration across endothelium and endothelial basal lamina into PVS.

In this step, leukocytes have not entered the CNS yet. The PVS provides a buffering zone of pro-inflammatory cytokines and immune cells for further leukocyte trafficking.

(2-2) Passage across the astrocytic basal lamina into the brain.

Though both endothelial and astrocytic layers are built from collagen type IV, HSPG and laminin, the laminin isoforms are different. Endothelial basal lamina contains laminins 8 and 10, which are essential for T cell recruitment and adhesion. Laminins 1 and 2 are found in the astrocytic layer and are not capable of T cell adhesion (Sixt et al., 2001). The laminin isoform differences might explain why immune cells accumulate in the PVS: immune cells are able to migrate into the PVS but not out of the NVU: the second transport step out of the PVS needs assistance from MMP and their interactions with dystroglycan matrix receptors to digest the astrocytic basal lamina (Agrawal et al., 2006; Bechmann et al., 2007; Carvey et al., 2009), see Figure 2.5.

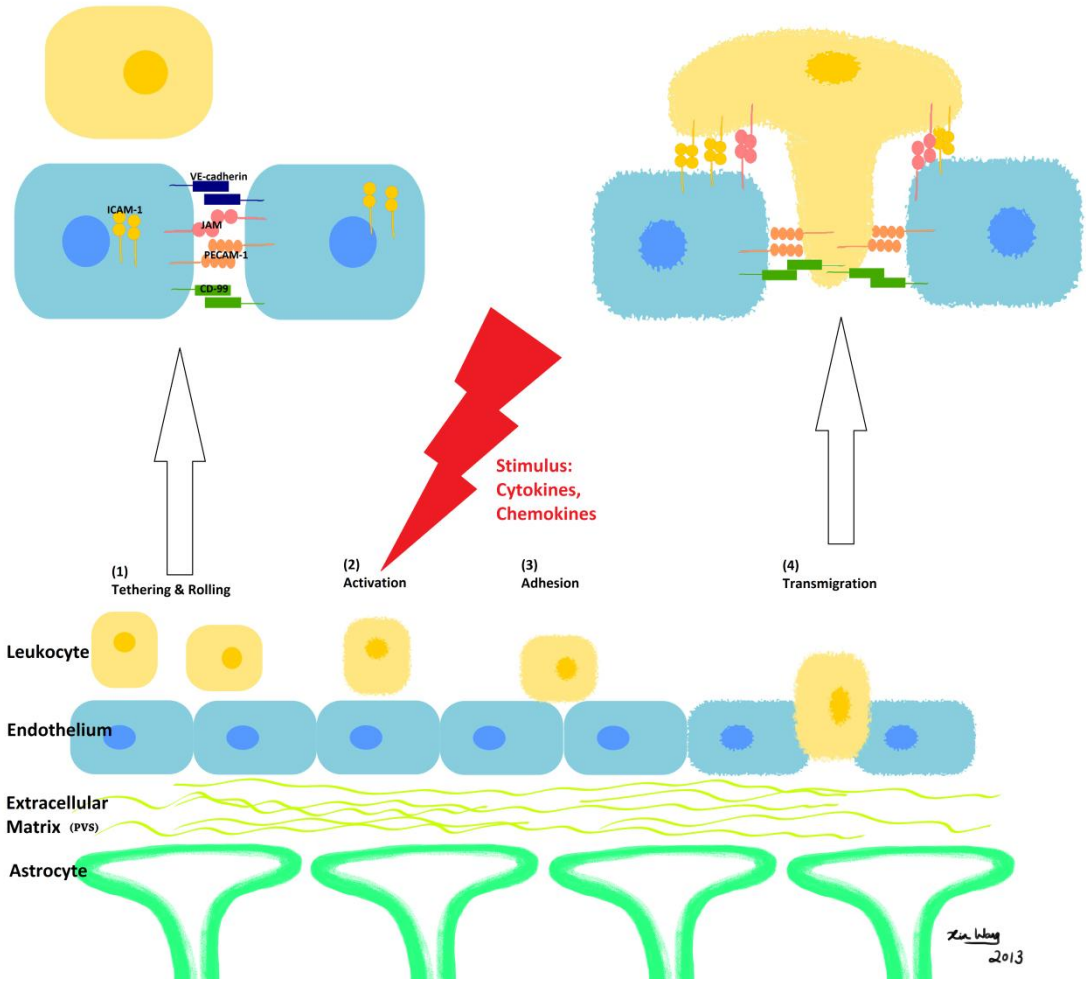

Figure 2.5 Leukocyte transmigration steps.

(2) General leukocyte transmigration steps

Many studies have demonstrated that leukocytes extravagate from vessels via a transmigration mechanism through opening of interendothelial junctions. A four-step model for this transmigration of circulating leukocytes has been proposed (Figure 2.5):

(2-1) Rolling: leukocyte rolling on endothelial cells

Leukocyte rolling is generally mediated by interaction between selectins, which enables leukocytes to detect more signals from the endothelium. Leukocyte-selectin, platelet-selectin, and endothelial-selectin are three adhesion molecules belonging to the selectin superfamily. L-selectin is found only on non-activated leukocytes, whereas P-selectin and E-selectin are expressed on inflammatory endothelium.

(2-2) Stimulation of the leukocytes

The activation of leukocytes is stimulated by chemokines.

(2-3) Tight adhesion to endothelial cells

After leukocytes are stimulated by chemokines, the activity of integrin increases and the adhesion ability of leukocytes to endothelial surface proteins also increases. These proteins are present on the endothelial cell surface and belong to the immunoglobulin superfamily. This enhanced binding affinity increases leukocyte stability on the endothelial cell surface.

(2-4) Transmigration

The leukocyte transmigration through the endothelium induces opening between adjacent cells to facilitate its passage between them. PECAM-1 and JAMs are adhesion junction proteins involved in this process.

(3) Junction proteins involved in the leukocyte transmigration

Table 2.8 gives a summary of a variety of TJ and AJ proteins involved in leukocyte transmigration. Many TJ and AJ proteins are involved in leukocyte transendothelial migration, such as JAM, ZO-1, VE-cadherin and PECAM-1 (Dejana et al., 2000; DeLisser et al., 1994; Muller, 2003; Ostermann et al., 2002) (Boven et al., 2000) (Figure 2.5). JAM-A and PECAM-1 are the most studied proteins in leukocyte diapedesis, functioning in leukocyte recruitment, adhesion and transmigration. Antibodies to JAM-1 and PECAM-1 inhibit their expression and are also efficient in inhibiting the leukocyte extravasation through endothelial junctions (Dejana et al., 2000; Del Maschio et al., 1999; Giri et al., 2000; Muller, 2003; Newman, 1997; Schenkel et al., 2002). Moreover, JAM-1 is a counter-receptor for LFA-1. JAM-1 contributes to LFA-1-dependent transmigration of T cells and neutrophils; it supports arrest of T cells by LFA-1−mediation; and it guides and controls leukocytes during leukocyte recruitment and adhesion (Ostermann et al., 2002).

Leukocyte transmigration can be triggered by inflammatory stress such as TNF-α, IFN-γ or HIV infection (Muller, 2003), which induces changes of junctional proteins' expression and distribution. Increased Aβ deposition related to disorder such as AD is another stimulus for leukocyte migration through transendothelial junctions by increasing the presence of monocytes (Giri et al., 2000).

2.4.2 Ischemic stimulus

We undertook a systematic search for studies of the influence of ischemic stroke on changes in BBB permeability. We searched the published literature using Medline© including literatures from 1st January 1966 up to 11th April

2013. We used exploded headings relating to Blood–brain barrier, Permeability, and Stroke with the Boolean operator AND.

From 44 papers describing the associations between BBB permeability and stroke, 12 assessed the association between BBB permeability and ischemic stroke stress and were eligible for inclusion. We excluded duplicates, reviews, comments and papers without full text. We also excluded non-stroke studies (renal hypertension; possible stroke; before ischemic stroke; vascular disruption model; relation with obesity) and excluded other types of strokes and combined ischemic and hemorrhage stroke (hemorrhage stroke or hemorrhage transformation; hyperglycemic stroke). Two studies focusing on the effect of ischemic stroke are not suitable for our study (edema and vascular density). Five studies describing permeability measurement methods were excluded. Figure 2.6 summarized the inclusion and exclusion numbers of papers in the systematic search.

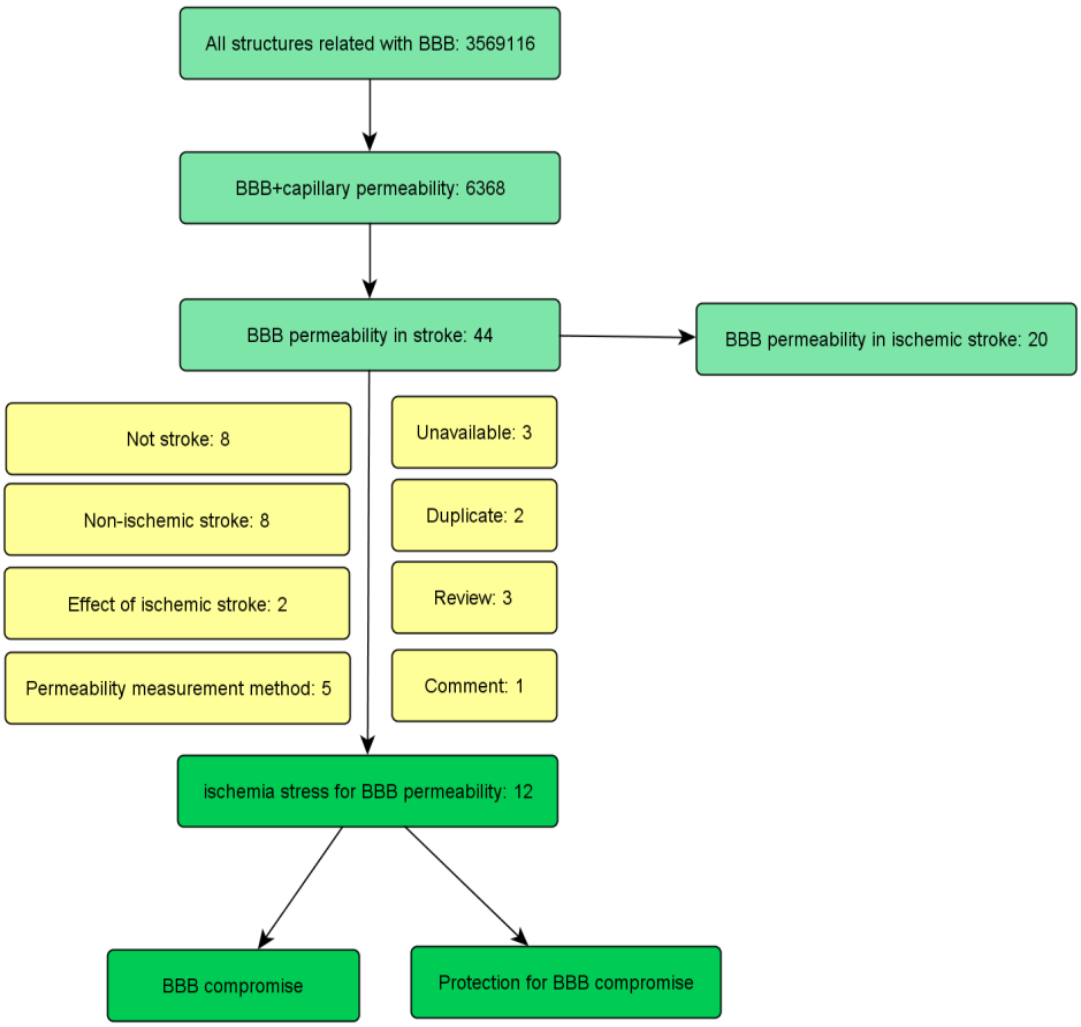

Figure 2.6 Systematic searching of ischemic stress for the BBB permeability.

From the 12 papers that appeared relevant for full assessment, we extracted data for animal type, ischemic stroke type, and permeability type and permeability markers used (details in Table 2.9). All 12 studies used animal models as the BBB permeability model induced by ischemia stimulus, five studies used mice and seven used rats (Sprague–Dawley rats are most frequently used animal model). Middle cerebral artery occlusion (MCAO) is the most common method in inducing experimental ischemia (8 of the 12 studies). They used tracers or MRI to assess the BBB permeability, and several tracers were used such as Evan's blue labelled albumin, horseradish peroxidise and sodium fluorescein.

From the information of these 12 papers, we generated the following figure (Figure 2.7) describing how the effect of cytokines, enzymes, drugs and other stimuli act individually or in combination to increase or decrease BBB permeability after the ischemic stimulus (information details used in generating Figure 2.7 figure is in Appendix A, Table A1).

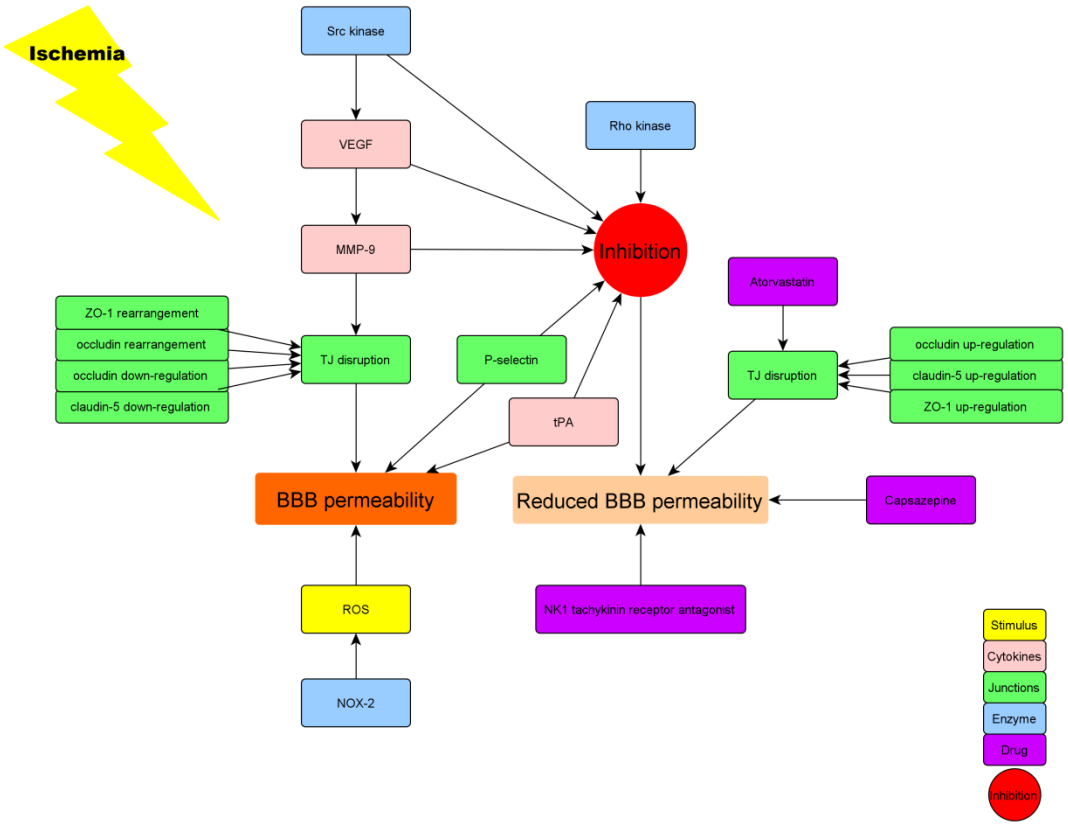

Figure 2.7 Summary of factors involved in the BBB permeability triggered by ischemia.

Abbreviations:
VEGF: Vascular endothelial growth factor; MMP: Matrix metalloproteinase; tPA: Tissue plasminogen activator; NOX2: NADPH oxidase; ROS: reactive oxygen species; TJ: tight junctions; ZO-1: Zonula occluden-1.

Cytokines MMP-9, VEGF and tPA disrupt BBB under ischemic stimulus (Abu Fanne et al., 2010; Paul et al., 2001; Wang et al., 2009; Wang et al., 2005). Inhibition of cytokines VEGF and MMP-9, Rho-kinase, and surface protein P-selectin are effective in reducing BBB permeability induced by ischemia (Jin et al., 2010; Paul et al., 2001; Satoh et al., 2010; Wang et al., 2009). However, inhibitor of NOX2 worsen ischemic stroke outcome and is not effective in reducing BBB permeability in ageing rats (Kelly et al., 2009). The NK1 tachykinin receptor antagonist reduces BBB permeability and the combination treatment with it and tPA also decreases BBB permeability (Abu Fanne et al., 2010). The use of capsazepine reduces BBB permeability (Gauden et al., 2007). High does anti-cholesterol drug atorvastatin decreased BBB permeability may through may be through up-regulation of claudin-5, occludin and ZO-1 (Cui et al., 2010).

2.4.3 Contributions of junction proteins to the BBB permeability

Pathological stresses influence the expression and phosphorylation status of TJ and AJ proteins which lead to BBB permeability. Here is an overview of TJ and AJ expression and phosphorylation changes in different pathological states.

The BBB permeability can be detected by decreased transendothelial electrical resistance measurement and the increased passage of molecular tracers such as Evan's blue labelled albumin, horseradish peroxidise and sodium fluorescein. The BBB permeability can also be determined by constant transfer for contrast agent (e.g. gadolinium compounds) on MRI.

There are three well-developed disease models for the mechanism of BBB permeability and cerebral vascular diseases, which are the inflammatory pain model, the hypoxia model and the AD model (Romanitan et al., 2010; Romanitan et al., 2007). The AD model is included here because of vascular changes rather than the neurodegenerative effects. The junction proteins changes in these three models are summarized in Table 2.10.

All inflammatory pain models (acute, short term and chronic) induced down regulation of occludin (Brooks et al., 2005; Huber et al., 2002; Huber et al., 2001). The expression of claudin-1 did not change in any of these inflammatory pain models (Huber et al., 2001), and the expression of claudin-3 and claudin-5 increased in the chronic inflammatory pain model (Brooks et al., 2005).

Hypoxia and reoxygenation stress triggered increased or decreased change expression of occludin (Brown and Davis, 2005; Kaur et al., 2011; Mark and Davis, 2002; Rosenberg and Yang, 2007; Witt et al., 2003). The expression

difference might be caused by different hypoxic conditions used by the researchers when inducing hypoxia. The phosphorylation of occludin increased triggered by ischemic stimulus (Kaur et al., 2011; Witt et al., 2003). During hypoxia, expression of claudin-5 was reduced, together with an increasing phosphorylation pattern (Rosenberg and Yang, 2007). Expression of ZO-1 and claudin-3 stayed almost the same during hypoxia and reoxygenation (Witt et al., 2003).

In AD and VaD brains, the expression of occludin, claudin-2, claudin-5 and claudin-11 increased significantly in neurons. However, most of the claudin-expressing neurons were pyramidal type, which are involved in cognition and are typically affected by AD pathology (Romanitan et al., 2010; Romanitan et al., 2007). The increased levels might reflect an autophagy of occludin and claudins proteins by neighbouring cells after the BBB breakdown (Zlokovic, 2008).

Changes in occludin under inflammatory pain and hypoxia stress are similar, and changes in claudin-5 under inflammatory pain, AD and VaD stress are mostly the same. The similar changes of TJ proteins may reveal analogous pathological mechanisms under these pathological states.

Apart from these three disease models, decreased expression, disorganisation or phosphorylation change of TJ proteins were also found in other disease such as tumor, HIV related dementia, MS tissue and apoE-4 knock-in mice model (Boven et al., 2000; Liebner et al., 2000; Nishitsuji et al., 2011; Padden et al., 2007).

2.5 Conclusion

The BBB is an important and complex structure which is involved in various cerebral diseases. Systematically reviewing the literature is useful to understand the structure and function of PVS, which are fundamental structures around vessels in a variety of species and important in immune function and fluid drainage in the brain. Changes in PVS are related to BBB permeability, and enlarged PVS are important imaging markers for cerebral small vessel disease.

Various stimuli could trigger BBB permeability such as inflammatory pain, ischemia, cytokines, chemokines and infections by bacteria and viruses. The ischemia stimulus to BBB permeability was analysed and summarised systematically. We also systematically searched other important effects on BBB such as oxidative stress, nitric oxide levels and Apolipoprotein E phenotypes, however, we did not manage to analyse them all limited by time. A further literature review of these topics would be beneficial in understanding triggers for BBB permeability.

Some results from the literature seem to contradict each other, maybe reflecting different models, methods and disease phase (such as acute and chronic) used in the studies.

2.6 Tables

Table 2.1 PVS structures in different species.

Spices	Model	Observation method	PVS place	PVS function	Study
Human	Normal	MRI, histology	whole cerebral hemispheres and connect the cerebral convexity, basal cistern, and ventricular system.	drainage, buoyancy, pressure maintenance	Tsutsumi, 2011
Rats	Normal	electron-microscopy	silver deposition, blood brain barrier	barrier	Van Breemen, 1955
Rat; Necturus	Normal	particle injection	Mammal: PVS is bounded by an inner arachnoid coat and an outer pia-glial, till arterioles and venules. Amphibian: PVS was found in intrapial vessels, capillary.	fluid flow; continuity between SAS, intrapial PVS, intracerebral PVS and pericapillary space	Brightman, 1953
Duck	Normal	electron-microscopy	Capillaries, wide PVS	tracer flow from blood to the PVS	Hirunagi, 1994
Necturus; Ambystoma	Normal	electron-microscopy	Necturus (capillaries): surrounded by a collagen-containing space, delimited by an endothelial and a glial basement membrane. In Ambystoma (capillaries): PVS (some other capillaries: a single basement membrane shared by endothelium and glia).	extracellular fluid	Bodenheimer,1968

Abbreviations:
PVS: perivascular spaces; SAS: subarachnoid spaces; MRI: magnetic resonance imaging.

Table 2.2 The ultrastructure of PVS in relation to vessels in different regions of human brains.

Observation method	Vessel type	Vessel location	PVS location and related structures	Study
TEM	vessel	Enter the cortex	SAS/pia/SPS SPS↔PVS Vessel/SPS-PVS(collagens)/BM (brain)	Hutchings,1986
LM	vessel	not described	BM/artefactual space (brain)	
TEM	Artery	SAS	Artery/lamina/SMC/space /pia (trabecula)	Zhang,1990
TEM	Arteriole	SPS	Arteriole/SMC/pia (nexus junctions)	
TEM	Vein	SAS	Vein/SMC/PVS(collagens)/pia (desmosomes)	
TEM	Vein	SPS	Vein/thick collagens	
TEM	Vein	SAS	Vein/collagen and flattened cells(SMC)/pia (desmosomes, nexus junctions)	
TEM	Arteriole	SPS	Arteriole/SMC/SMC/pia (nexus junctions)/space /pia	
TEM	Metarteriole	SPS	Metarteriole/incomplete SMC/collagens/pia(nexus junctions)/space/glia limitans (brain)	
TEM	Venule	SPS	Venule/atypical SMC/collagens/space /pia or glia limitans	
TEM	Venule	leave SPS enter trabecula	Venule/collagens/pial cells	
TEM	Large Arteriole	cerebral cortex	Artery/SMC/SMC/SMC/space/pia(nexus junctions/glia limitans	
TEM	Venule	WM	Venule/atypical SMC/space (collagens)/BM of glia limitans	
SEM	Artery	BG (GP)	Artery/cells/PVS/cells/space/BM (brain)	Pollock,1997
SEM	Vein	BG (GP)	Vein/cells/PVS/BM (brain)	
SEM	Artery	BG	Artery/cells/PVS/cells/collagens/BM (brain)	
TEM	Artery	BG	Artery/SMC/cells/PVS/cells(direct contact)/collagens/BM (brain)	
SEM	Vein	BG	Vein/cells/collagens (brain)	
TEM	Vein	BG	Vein/cells/PVS/collagens/BM (brain)	
paraffin block	Artery	SAS to brain	SAS Artery/cells/PVS/cells-pia/(brain)	

'/': the separation symbol we used to differentiate cell layers. 'space': consistent with the structure of PVS in other publications .

Abbreviations:
PVS: perivascular spaces; SAS: subarachnoid spaces; SPS: subpial spaces; BM: basement membrane; SMC: smooth muscle cells; L: a layer of cells (leptomeningeal cell layer in (Pollock et al., 1997)); SEM: Scanning electron microscopy; TEM: Transmission electron microscopy; LM: Light microscopy; BG: basal ganglia; GP: globus pallidus; WM: white matters.

Table 2.3 Studies about perivascular cells origins.

Observation method	Tissue type	Origin	Cell type	Immune characters	Study
Carbon label	Rats	Two types: resident, emigrate	Macrophages	Not mentioned	McKeever, 1978
Ink injection	Rats	Resident (2 years)	Phagocyte	$ED2^+$, $ED1^+$, MHC class II^+	Kida, 1993
Monoclonal antibodies	Mice	separate macrophages and microglia	Macrophages, microglia	MHC class II^+, CD 4^+T Not for microglia	Walker, 1999
Tracer injection	Rats	6% of blood-borne	Macrophages	ED-2	Bechmann, 2001a
transplanted, GFP	Mice	migratory	Macrophages	[GFP]	Bechmann, 2001b
Review	Not mention	migratory	Macrophages	similar to blood-borne macrophages	Guillemin, 2004

Abbreviations: GFP: green-fluorescent-protein; MHC: major histocompatibility complex.

Table 2.4 Immune cell accumulation within PVS.

Human or Animal	Disease Model	Cell type related	Accumulation place	Mechanisms	Study
Human	Ischemia	Monocyte, macrophages, (microglia)	PVS and brain parenchyma	Effect of CD14 in the acute inflammatory response following stroke. Resting microglia lack CD14	Beschorner, 2001
Rats	MS	macrophages, lymphocytes	PVS and CNS-draining lymph nodes	myelin phagocytosing macrophages inhibit TCR-triggered lymphocyte proliferation by producing NO	Bogie, 2011
Human	HIVE	CD3+, CD8+ T cells, CTL	PVS and inflammatory nodules (PVS: CD3+, CD8+ T)	parenchymal CD3+, CD8+T cells and CTLs are sensitive biomarkers for HIVE; CD8+ T cells and CTLs could mediate brain injury in HIVE	Petito, 2006
Human	HIV infection	mononuclear cell	Perivascular cuffing	perivascular cuffing associate with increased permeability of the BBB	Hawkins, 1993
Sheep	VM encephalitis	macrophages, CD8+, CD4+ T cells and B cells	Perivascular cuffs and sleeves	[Different stages of viral invasion] mild lymphocytic lesions: CD8+ T cells severe lymphocytic lesions: CD8+, CD4+ T cells histiocytic lesions: macrophages, CD8+, CD4+ T cells and B cells	Polledo, 2012
Mice	cerebral malaria	leukocytes, macrophages lymphocytes	PVS	Ultrastructural hallmarks of cerebral malaria	Lackner, 2006
Mice	Acute inflammatory; neurodegeneration	macrophages	PVS; brain-CSF and CSF-blood interfaces	Mannose receptor for macrophages	Galea, 2005
Rats	TBI	endostatin, collagen XVIII+ microglia, macrophages	lesion parenchyma and PVS	These cells as main cellular source of the antiangiogenic factor endostatin/collagen XVIII in areas of processing vascular regression	Mueller, 2007

Abbreviations:
CSF: brain-cerebrospinal fluid; T, T-lymphocytes; B: B-lymphocytes; CTL: cytotoxic T lymphocyte; TCR: T cell receptor; MS: multiple sclerosis; HIVE: human immunodeficiency virus type 1 encephalitis; VM: visna/maedi; TBI: traumatic brain injury; SIDS: sudden infant death syndrome; NO: nitric oxide; CD: cluster of differentiation.

Table 2.5 Immune cell transmigration through PVS.

Human or Animal	Disease Model	Cell type related	Migration place	Mechanisms	Study
Mice	EAE (MS)	dendritic cells	recruitment in PVS; across BBB	CCL2 facilitate CD11 labeled DC transmigration across the BBB in an ERK1/2-dependent manner; DC more efficient transmigration than T cell in BBB model	Sagar, 2012
Rats	EAE (MS)	macrophages/monocytes and neutrophils	PVS, across BBB	Ninj1 may mediate the entry of myeloid cells into the CNS across the BBB in normal and EAE brains	Ahn, 2009
Human	MS	leukocytes	across PVS	CXCL12 localize infiltrating leukocytes to PVS, preventing CNS parenchymal infiltration. Altered patterns of CXCL12 expression at the BBB were specifically associated with MS.	McCandless, 2008a
Mice	EAE (MBP injection)	leukocytes	PVS, across BBB	leukocytes infiltration in PVS and cerebral cortex; VLA-4 important for CD4+T entry into brain; ICAM-1,VCAM-1,LFA-1 expression in the brain after stimulation	Tsai, 1997
rhesus macaques	SIV (HIV)	monocytes	blood to CNS (within 48h)	proinflammatory cytokine IFN-r and the chemokine CXCL9 were rapidly induced in plasma in the SIV-infected group. IFN-inducible chemokine CCL2 (monocyte CNS trafficking)	Clay, 2007
Human	HIV	B, T cells	PVS, enter brain	B very low in normal brain Most AIDS brains lack B lymphocytes. Increased accumulation of B cells some AIDS and in pre-AIDS brains in the PVS and brain.	Anthony, 2003
Human	HIV, AD	Macrophages, T and B cells	PVS and neuropil	COX-2 and CD68 positive macrophages infiltrate AD and HIVE brains. ZO-1 disruption and fibrinogen leakage in AD and HIVE brains. Amyloid-β-containing macrophages infiltrate amyloid-β plaques and vessels in AD.T and B lymphocytes also infiltrate AD and HIVE.	Fiala, 2002
Human	HIV	lymphocyte	leptomeninges and PVS	Lymphocyte infiltration, found in all stages and characteristic finding in asymptomatic HIV infection.	Kibayashi, 1996
Mice	West Nile virus	WNV-specific CD8 T	PVS, enter CNS	CXCL12 localizes lymphocytes within CNS PVS in both humans	McCandless,

	encephalitis	lymphocytes		and mice with WNV. Inhibition of CXCR4 would promote T lymphocyte entry into the CNS parenchyma and increase viral clearance.	2008b
Chicken	Marek's disease virus	monocyte	PVS, meninges	blood monocytosis may be contributory factor in mononuclear infiltration into the meninges and PVS	Barrow, 2003
Mice	transgenetic, retrovirus infection	iNOS-positive leukocytes	PVS and ventricles	IFN-γ is necessary to protect against neurodegeneration in the inflammatory process	Koustova, 2000
Human	Venezuelan equine encephalitis	lymphocytes, mononuclear cells, neutrophils	PVS and adjacent tissue parenchyma	CNS infection	de la Monte, 1985
Rats	T. b. gambiense	IgM-producing plasma, morular, T	PVS, leptomeninges	T-dependent B-cell immune response with a chronic T. b. gambiense infection; Ia-positive neuroglial: antigen presenting cell	Anthoon, 1989
Cats	meningitis infected by bacteria	leukocytes	infiltration of the PVS, choroid plexus, and leptomeninges	hypoglycorrhachia of bacterial meningitis is the result of metabolism of the bacteria with little contribution from the leukocytes	Hochwald, 1984
Human	NMDAR encephalitis	antibody-secreting cells; T and B	antibody-secreting cells: PVS & interstitial space; B and T cells: PVS	antibody-secreting cells: intrathecal synthesis of antibodies	Martinez-Hernandez, 2011
Human	TBI	CD14+ macrophages, CD 14+ microglia	PVS, brain parenchyma	early CD14 expression: essential part of the acute inflammatory CNS response following trauma	Beschorner, 2002
Rats	Normal and tumor	activated lymphocytes	PVS	efflux and influx of activated lymphocytes	Kruse, 1994

Abbreviations:
PVS: perivascular spaces; BBB: blood brain barrier; T, T-lymphocytes; B: B-lymphocytes; DC: dendritic cells; MS: multiple sclerosis; EAE: Experimental autoimmune encephalomyelitis; SIV: simian immunodeficiency virus; HIV: human immunodeficiency virus; HIVE: human immunodeficiency virus type 1 encephalitis; AD: Alzheimer's disease; NMDAR: N-methyl-D-aspartate receptor; WNV: West Nile virus; T.b. gambiense: Trypanosoma

brucei gambiense; TBI: traumatic brain injury; NO: nitric oxide; iNOS: inducible Nitric oxide synthases; MBP: myelin basic protein; LFA-1: lymphocyte function-associated antigen-1; VLA-4: very late activation antigen-4; ICAM-1: intercellular adhesion molecule-1; VCAM-1: vascular cell adhesion molecule-1; CD: cluster of differentiation; CCL2: Chemokine ligand 2; CXCL9: chemokine (C-X-C motif) ligand 9; CXCL12: chemokine (C-X-C motif) ligand 12; CXCR4: C-X-C chemokine receptor type 4; ERK: extracellular-signal-regulated kinases; Ninj1: Ninjurin1, nerve injury-induced proteinCOX-2: Cyclooxygenase 2; ZO-1: Zonula occluden-1; IFN-γ: interferon-γ; IgM: Immunoglobulin M.

Table 2.6 Fluid drainage function involved PVS in normal and pathological conditions.

Human or Animal	Model related	components of fluid	drainage route	Mechanisms	Study
Rats	Normal	ISF, CSF	spread selectively along PVS outlining both arteries and veins and extending to surround capillaries	through cerebral white matter, grey matter, SAS to the cribriform plate and nasal lymphatics	Zhang, 1992
Rats	Normal	[14C]sucrose	[14C]sucrose was retained longer within the walls and PVS of pial arteries and arterioles than in other subarachnoid tissues	Rapid ventricle-to-cistern flow of CSF; CSF delivered factors and agents to these pial blood vessels.	Ghersi-Egea, 1996
Rabbits	Radioactive albumin injection	Albumin	CSF to deep cervical lymph	draining by bulk flow via PVS and passage SAS and to lymph	Brandbury, 1981
Rabbits	Albumin	Albumin	drainage from brain via PVS	Outflow through lymph	Yamada, 1991
Rats	HRP injection	HRP	ventricles to PVS of blood vessels	foreign protein removement	Wagner, 1974
Cats	HRP injection	HRP	HRP in the SAS enters the PVS around penetrating arterioles and rapidly permeates the gliovascular basal laminae surrounding capillaries	PVS and capillary basal laminae offer preferential 'paravascular' routes for fluid/solute influx from the SAS to the extracellular spaces	Gregory, 1985
Cats, Dogs	HRP injection	HRP	PVS around large vessels and in the BM around capillaries; over 4 min, in arterioles, venules and capillaries	exchange of solutes between the CSF and the cerebral extracellular spaces	Rennels, 1985
Human, Rabbits	IgG Fc receptor outflow	IgG Fc receptor	CSF pathway from the PVS to the arachnoid granulations	CSF outflow system has important lymphatic functions	Siegelman, 1987
Rats	hypoxic–ischemic injury	IGF-1	IGF-1 was detected predominantly in the pia mater, PVS and subcortical white matter tracts	The subcortical white matter tracts and perivascular pathways were the two major routes for IGF-1 movement	Guan, 2000
Rats	ICH	hematoma; blood	PVS and the spaces around the nerve fibers; lymph sinuses in the bilateral deep cervical	perivascular and perineural extension of hematomas widespread	He, 2012

		elements labelled dye	lymph nodes		
Human	MS	Myelin particles	extracellular myelin: leptomeningeal tissue and PVS	myelin debris was drained from sub-cortical or cortical lesions to PVS, the meninges	Kooi, 2009
Mice	CAA	Tracers;	tracers drained out of the brain along BM of capillaries and arteries	Soluble antigens, but not cells, drain from the brain by perivascular pathways.	Carare, 2008
mathematical model	Aβ elimination in AD and CAA	Aβ	PVS drainage of ISF and solutes out of brain was driven by pulsations of the blood vessel walls, reverse direction to the flow	Reduction in pulse amplitude prolonged attachment time, and impaired elimination of Aβ from the brain	Schley, 2006
Human	INPH	CSF, ISF	continuity of ISF and CSF	Abnormal bulk flow of ISF along PVS may be a consequence of the underlying alteration of CSF dynamics in INPH	Tarnaris, 2011
Rats	NPH	Aβ,Tau	Aβ42 in CSF clearance pathways also increase in PVS and cortical parenchyma; Aβ42 retention: along ISF and CSF outflow pathways (SAS,PVS) and BBB	Hydrocephalus in the elderly rat can induce Aβ and p-Tau accumulation. Altered CSF dynamics appears to impair Aβ clearance in this NPH model	Silverberg, 2010
Rats	Experimental Hydrocephalus	HRP, MP, $LaCl_3$	HRP and MP: intercellular spaces and PVS, restricted by tight junctions. La^{3+} penetrated tight junctions	the tight junctions may constitute for the transendothelial movement of small solutes	Nakagawa, 1985
Rats	lymphatic encephalopathy	lymph	model: PVS dilation; loosen tissues around PVS	partial ligation of cerebral superficial artery induced lymphatic encephalopathy	Xiao, 2011
Human, Rats	Tumor	edema	PVS were fluid drainage pathway of edema	PVS especially in grey matters	Kida, 1994
Rats	Edema	Albumin	toward ventricles and cortical surface	CSF pathway: protein-rich edema clearance	Ohata, 1990

Abbreviations:
ICH: intracerebral hemorrhage; INPH: Idiopathic Normal Pressure Hydrocephalus; NPH: normal pressure hydrocephalus; CAA: cerebral amyloid angiopathy; AD: Alzheimer's disease; CSF: cerebrospinal fluid; ISF: interstitial fluid; BM: basement membranes; SAS: subarachnoid space; Aβ: Amyloid-β; IGF-1: insulin-like growth factor; HRP: horseradish peroxidise; MP: microperoxidase; LaCl3: lanthanum chloride; IgG: immunoglobulin G.

Table 2.7 Colocalization of junction proteins in the BBB.

Junction type		Junction type		Interaction type	Reference
AJ	VE-cadherin	**AJ**	α-catenin	Antibody immunostained	Brevioria 1995
AJ	VE-cadherin	**AJ**	β-catenin	Immunoprecipitation	Rajasekaran 1996
TJ	ZO-1	**AJ**	α-,β-, γ-catenin		
TJ	JAM	**TJ**	occludin	Coprecipitation	Muraki 2000
TJ	JAM	**TJ**	ZO-1		
TJ	JAM	**TJ**	cingulin		
TJ	claudin-5	**TJ**	ZO-1	Immunocytochemical double labeling	Zaretski 2004
TJ	occludin	**TJ**	ZO-1		
TJ	JAM-A	**TJ**	ZO-1		
TJ	JAM-A	**AJ**	VE-cadherin		
TJ	claudin-5	**TJ**	ZO-1	Ultrastructural and immunofluorescent localization	McCaffrey 2007
TJ	claudin-5	**AJ**	caveolin-1		
TJ	occludin	**TJ**	ZO-1		
TJ	occludin	**AJ**	caveolin-1		

Abbreviations:
AJ: adherens junctions; TJ: tight junctions; JAM: junctional adhesion molecule; ZO: Zonula Occluden-1; VE-cadherin: vascular endothelial-cadherin.

Table 2.8 TJ and AJ involvement in leukocyte transmigration.

Type of leukocyte	TJ or AJ facilitate trafficking	antibody or stress to TJ or AJ	TJ or AJ Expression change	Influence to leukocyte	Ref
leukocyte	PECAM-1	-	-	Direct leukocyte recruitment; transendothelial migration	DeLisser, 1994
monocyte neutrophil	PECAM-1	antibodies	↓	inhibits transendothelial migration	Newman, 1997
monocyte	JAM	BV11 (mAb)	↓	inhibits monocyte transmigration	Del Maschio, 1999
monocyte	ZO-1	HIV	↓	monocyte infiltration	Boven, 2000
leukocyte	JAM	mAb	↓	inhibits leukocyte extravasation	Dejana, 2000
monocyte	RAGE	antibody	↓	inhibits amyloid peptide deposition, inhibits Aβ-mediated migration of monocytes	Giri, 2000
	PECAM-1	antibody	↓	inhibits Aβ-mediated migration of monocytes	
leukocyte	JAM-A	-	-	contributes to LFA-1-dependent transendothelial migration of T cells and neutrophils	Ostermann, 2000
monocyte	CD99	hec2 (mAb)	↓	inhibits diapedesis of monocytes across endothelial cells by >90%; arrested monocytes where they were partially through the junction	Schenkel, 2002
	PECAM-1	mAb	↓	arrests leukocytes on the apical surface of endothelium	
leukocyte	JAM-A	TNF-α+IFN-γ	redistribution	redistributes to the endothelial apical surface	Muller, 2003
	PECAM-1	IFN-γ	↓; redistribution	redistributes to the apical surface	
during migration	VE-cadherin	-	↓		
	JAM-A	-	↑		
	PECAM-1	-	↑		
	CD99	antibody	↓	Blockade of monocytes diapedesis.	

"-": not mentioned; "↓": down-regulated; "↑": upregulated

Abbreviations:

mAb: monoclonal antibody; RAGE: Aβ receptor; LFA-1: lymphocyte function−associated antigen 1; TNF-α: tumor necrosis factor-α; IFN-γ: interferon-γ.

Table 2.9 BBB permeability triggered by ischemia.

Animal	Type of ischemia	permeability type	permeability marker	**Study**
Male C57Bl/6 mice	Permanent MCAO	vascular permeability	EB	(Paul et al., 2001)
SHRSP rats	Transient forebrain ischemia	BBB permeability	sodium fluorescein; EB-labeled albumin	(Abraham et al., 2002)
VEGF-overexpressing mice	MCAO	BBB permeability	sodium fluorescein	(Wang et al., 2005)
Wistar rats	microsphere injection	vascular permeability	HRP	(Gauden et al., 2007)
Female Sprague–Dawley rats	MCAO-2h-reperfusion	BBB permeability	[14C] radioactivity	(Kelly et al., 2009)
Male 129S6/SvEvTac mice	Filamentous MCAO	BBB permeability	EB	(Wang et al., 2009)
Male Sprague–Dawley rats	Microthrombosis	endothelial permeability	bovine serum albumin	(Satoh et al., 2010)
Male NMRI mice	hypoxia at 8% oxygen-48h	vascular permeability	sodium fluorescein	(Bauer et al., 2010)
Sprague-Dawley rats	MCAO	BBB permeability	EB	(Abu Fanne et al., 2010)
Male C57/BL 6 wild type mice/ 29 P-selectin-deficient or knockout mice	MCAO-30min	BBB permeability	Gd contrast injection	(Jin et al., 2010)
Male Sprague–Dawley rats	MCAO	BBB permeability	IgG (Confocal microscope)	(Cui et al., 2010)
Male Sprague–Dawley rats	MCAO-2h-reperfusion	BBB permeability	EB	(Turner and Vink, 2012)

Abbreviations:
SHRSP: Stroke-prone spontaneously hypertensive rats; MCAO: middle cerebral artery occlusion; HRP: Horseradish peroxidise; EB: Evan's blue.

Table 2.10 Expression and phosphorylation changes on TJ and AJ in pathological conditions.

Pathological states	Stimulus	TJ or AJ	expression change	Phosphorylation change	BBB change	Study
Inflammatory pain	Acute; Short term; Long term	occludin	↓	p↑ tyrosine	[$_{14}$C]sucrose	Huber, 2001
		Claudin-1	↔	-		
		ZO-1	↑	-		
		actin	↑	-		
	Short term	occludin	↓	-	Evan's blue	Huber, 2002
		ZO-1	↑	-		
	Long term	occludin	↓60%	-	Evan's blue-	Brooks, 2005
		claudin-3	↑450%	-	labelled	
		claudin-5	↑615%	-	albumin	
		ZO-1	↔	-		
		actin	↔	-		
Hypoxia	1% O_2-99% N_2	occludin	↔↑*	-	[$_{14}$C]sucrose	Mark, 2002
	Hypoxic VS	ZO-1	↔↑*	-		
	Post-hypoxic	ZO-2	↔↑*	-		
	reoxygenation	claudin-1	↔↔	-		
		actin	↑*↑*	-		
	O_2-controlled hypoxia	occludin	shift in bands	p↑	[$_{14}$C]sucrose	Witt, 2003
		claudin-3	↔	-		
		ZO-1	↔	-		

		actin	↔	-		
	ischemia-RP	occludin	↓*RP	-	-	Rosenberg, 2007
	rt-PA; MMP	claudin-5	↓*RP	-		
	ischemia-RP	occludin	↓	p↑	Gd-DTPA	Kaur, 2011
	t-PA	claudin-5	↓	p↑	MRI	
Hypoxia and	SKF 96365	occludin	↑	localization	TEER	Brown, 2005
aglycemia		actin	↓	-		
Diabetes	insulin-	occludin	↓	-	[^{14}C]sucrose	Hawkins, 2007
	intervention	ZO-1	↓	-	Evan's blue	
	MMP-2,9	claudin-5	↔	-	albumin	
AD and VaD	post-mortem human brains	occludin	↑N;A;O	-	-	Romanitan, 2007
	post-mortem human brains	claudin-2	↑N;A;O (VaD)	-	-	Romanitan, 2010
		claudin-5	↑N;A	-	-	
		claudin-11	↑N;A;O (AD)	-	-	
Phosphorylation	Rho-p ROCK160 kinase	occludin	shift in bands	p↑	horseradish peroxidase	Hirase, 2001

↑: upregulated; ↓: down regulated; ↔: unchanged; p: phosphorylation; -: not mentioned; * significant change.
[Inflammatory pain]
Acute: formalin; Short term: λ-carrageenan; Long term (chronic): complete Freund's adjuvant (CFA)
[Hypoxia]
RP: reperfusion
Gd-DTPA: gadolinium- diethylenetriaminepentaacetic acid, contrast agent for MRI
[AD and VaD]
N: neurons; A: astrocytes; O: oligodendrocytes

Chapter 3 Patient Recruitment and Image Segmentation Main Methods

This chapter describes the methods used for evaluating the best method for analysing white matter hyperintensities (WMH) and other tissue volumes (such as cerebral atrophy and stroke lesions) in cross-sectional and longitudinal studies and trials of patients with small vessel disease (SVD) – either lacunar stroke or silent SVD features. The analysis used data from a longitudinal study of lacunar stroke mechanisms, the Mild Stroke Study (MSS). A brief description of the patient recruitment and selection into the MSS is given here, followed by the image processing steps that were tested.

3.1 Patient recruitment into MSS and subgroups

The recruitment for the MSS was prospective and as consecutive as possible. We prospectively recruited 275 patients with clinical features of acute lacunar stroke and mild cortical stroke (as controls) in a large academic teaching hospital between January 2005 and July 2007 for a study of stroke mechanisms, the Mild Stroke Study. Cortical stroke patients were chosen as controls because they have a different stroke mechanism (mostly), and control for having a stroke, risk factor profiles, and secondary stroke prevention medications (Doubal et al., 2010b; Wardlaw et al., 2009).

We included patients who had a definite diagnosis of lacunar or mild cortical stroke within three months of symptom onset. We classified the subtypes of lacunar and cortical strokes based on the clinical sympotoms and signs, then on the imaging findings, using risk factor free stroke subtyping (see below). All patients underwent usual investigations for stroke cause (carotid Doppler ultrasound, electrocardiogram, blood tests, brain imaging and so forth).

Diagnostic magnetic resonance imaging (MRI) at presentation was performed on a 1.5-Tesla magnetic resonance scanner (Signa LX; General Electric, Milwaukee, WI) with 22mTm^{-1} maximum-strength gradients. Sagittal T1-weighted (T1W) and axial T2-weighted (T2W), diffusion-weighted imaging (DWI), fluid-attenuated inversion recovery (FLAIR), and gradient-recalled echo (GRE) sequences were performed (parameters shown in Table 3.1).

Table 3.1 MRI scan parameters used in the Mild Stroke Study (baseline)

Sequence	TE	TR	Slice thickness (mm)	Slice gap (mm)	Matrix	Field of view	Flip angle
T_2W	102	6300	5	1.5	256 x 256	24 x 24	-
T_1W	Min	450	5	1.5	256 x 224	24 x 24	-
FLAIR	140	9000	5	1	256 x 224	24 x 24	-
GRE	15	625	5	1.5	256 x 192	24 x 24	20°

TE, time to echo; TR, time to repetition; T_2W, T_2-weighted imaging; T_1W, T_1-weighted imaging; FLAIR, fluid attenuated inversion recovery; GRE, gradient-recalled echo.

A trained stroke physician assessed all patients and defined the clinical stroke subtypes according to the Oxfordshire Community Stroke Project classification (Bamford et al., 1991). Lacunar stroke was defined as pure motor disorder and/or sensory loss, or ataxic hemiparesis and mild cortical stroke was defined as being equivalent to a partial anterior circulation stroke, including cortical symptoms or signs. The definition did not take account of risk factors. Following initial clinical classification, radiological classification of stroke subtype was defined by location of the recent infarct using diagnostic MRI; primarily diffusion imaging than the other sequences. Both the clinical and radiological classifications were used to decide the final stroke subtype classification. When its clinical characteristics subtyped 'lacunar' but its MRI DWI clearly showed a 'cortical' infarct, the final

diagnosis was 'cortical', and vice versa. This misdiagnosis that about 20% of cortical infarcts are misdiagnosed clinically as lacunar infarcts and vice versa, probably accounts for 'noise' in previous clinical-imaging dissociation studies (Potter et al., 2010a).

We recorded patients' age, gender, weight, race, vascular risk factors (history of hypertension, smoking, diabetes, alcohol use and so forth), severity of stroke (National Institutes of Health Stroke Scale), ischemic heart disease, peripheral vascular disease, or transient ischemic attack and drug treatment before the stroke. All patients included in the study have stable blood pressure, hypertensive patients have their blood pressure well controlled with antihypertensive medication and patients with unstable or untreated hypertension were excluded. Patients with unstable medical conditions or contraindications to MRI, and severe stroke or hemorrhagic stroke were excluded. Further details of patients' clinical characteristics related to each topic in Chapter 5 and 8 will be provided in these chapters.

The study was approved by the Lothian Research Ethics Committee (2002/W/RA/03) (Wardlaw et al., 2013a) and all participants gave written informed consent.

A subset of 100 patients without impaired renal function agreed to take part in a study using contrast enhanced MRI to assess blood brain barrier (BBB) permeability changes in lacunar versus cortical stroke. This second scan (permeability scan) was taken between at least one and three months after the diagnostic scans mentioned above to avoid any possible permeability alterations caused by the acute effects of the stroke. The T10 sequence with flip angles of 2° and 12° was run before contrast agent injection and the 12°

acquisition was repeated 26 times with acquisition time of 69s after injection sequentially after intravenous injection of 40 ml gadodiamide (Omniscan; GE Healthcare AS, Oslo, Norway) (Armitage et al., 2011; Wardlaw et al., 2009). For the 100 patients, the acquisition of permeability images failed for three patients for the following reasons: (1) Injector problem: injected 15ml of contrast agent rather than 40ml; (2) Contrast didn't enter blood stream for unknown reason; (3) Images missed the bottom of the brain due to radiographic error.

From the 97 patients who had successful contrast enhanced MRI BBB sequences (51 lacunar stroke and 46 with cortical stroke), 46 of them returned after a median of 39 months (IQR 30–45 months, between July and September 2009) for follow-up scanning (22 with the original diagnosis of lacunar stroke and 24 with the original diagnosis of cortical stroke). We performed MRI on the same 1.5-T Magnetic Resonance (MR) scanner with sagittal T1W and axial T2W, FLAIR and GRE sequences as obtained at baseline (parameters in the Table 3.2, slight differences were due to MR scanner upgrade that occurred in intervening period).

Table 3.2 MRI scan parameters used in the Mild Stroke Study (follow-up)

Sequence	TE	TR	Slice thickness (mm)	Slice gap (mm)	Matrix	Field of view	Flip angle
T_2W	140	5000	5	1.5	384 x 384	24 x 24	-
T_1W	Min	560	5	1	384 x 224	24 x 24	-
FLAIR	140	9000	5	1	384 x 224	24 x 24	-
GRE	15	625	5	1	384 x 224	24 x 24	20o

TE, time to echo; TR, time to repetition; T_2W, T_2-weighted imaging; T_1W, T_1-weighted imaging; FLAIR, fluid attenuated inversion recovery; GRE, gradient-recalled echo.

Eight of these 46 patients that had follow-up scans were selected to represent a full range of WMH and brain structural changes for a pilot study of image processing methods for this thesis (described in Chapter 5). In this pilot study, we explored seven different ways to find a reliable method that could measure the WMH at both time points consistently, and would be suitable to measure the longitudinal WMH change in the 46 patients with follow-up scans. By analysing and comparing the results, we were seeking the most accurate and least time-consuming method which could be applied to larger samples.

The patient recruitment process and patient subgroups in image analysis described above is shown in the flowchart below (Figure 3.1).

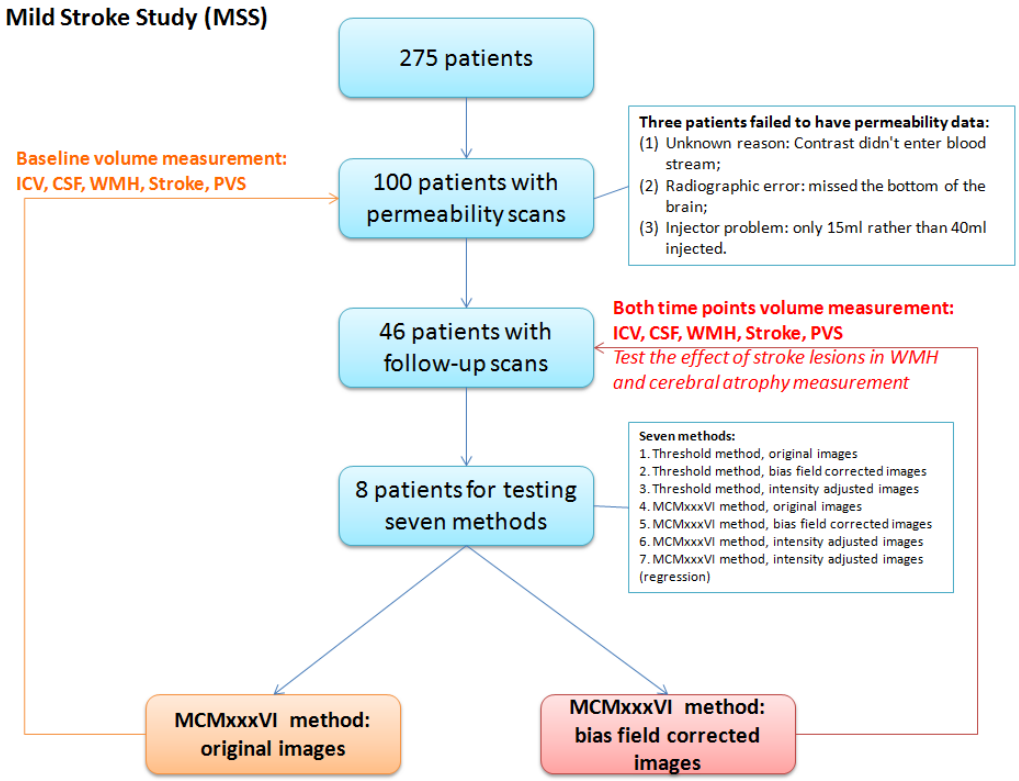

Figure 3.1 Summary of MSS patient recruitment process and patient subgroups in imaging analysis.

ICV: Intracranial volume, CSF: cerebrospinal fluid, WMH: white matter hyperintensities, PVS: perivascular spaces.

3.2 Basic imaging processing steps

All image processing was performed blind to all clinical and other imaging data. Baseline and follow-up images were analyzed separately and blind to each other's results. The intracranial volume (ICV), index stroke lesions, any old infarcts including lacunes at baseline and new cortical or subcortical stroke lesions appearing at follow-up were manually outlined (masked) in Analyze™ 9.0 software (Wang et al., 2012).

3.2.1 ICV segmentation

The ICV segmentation includes extracting the brain mask using the 'Object Extractor' module and modifying it using the 'Region of Interest' module in Analyze™ 9.0 software, based on GRE images (Figure 3.2).

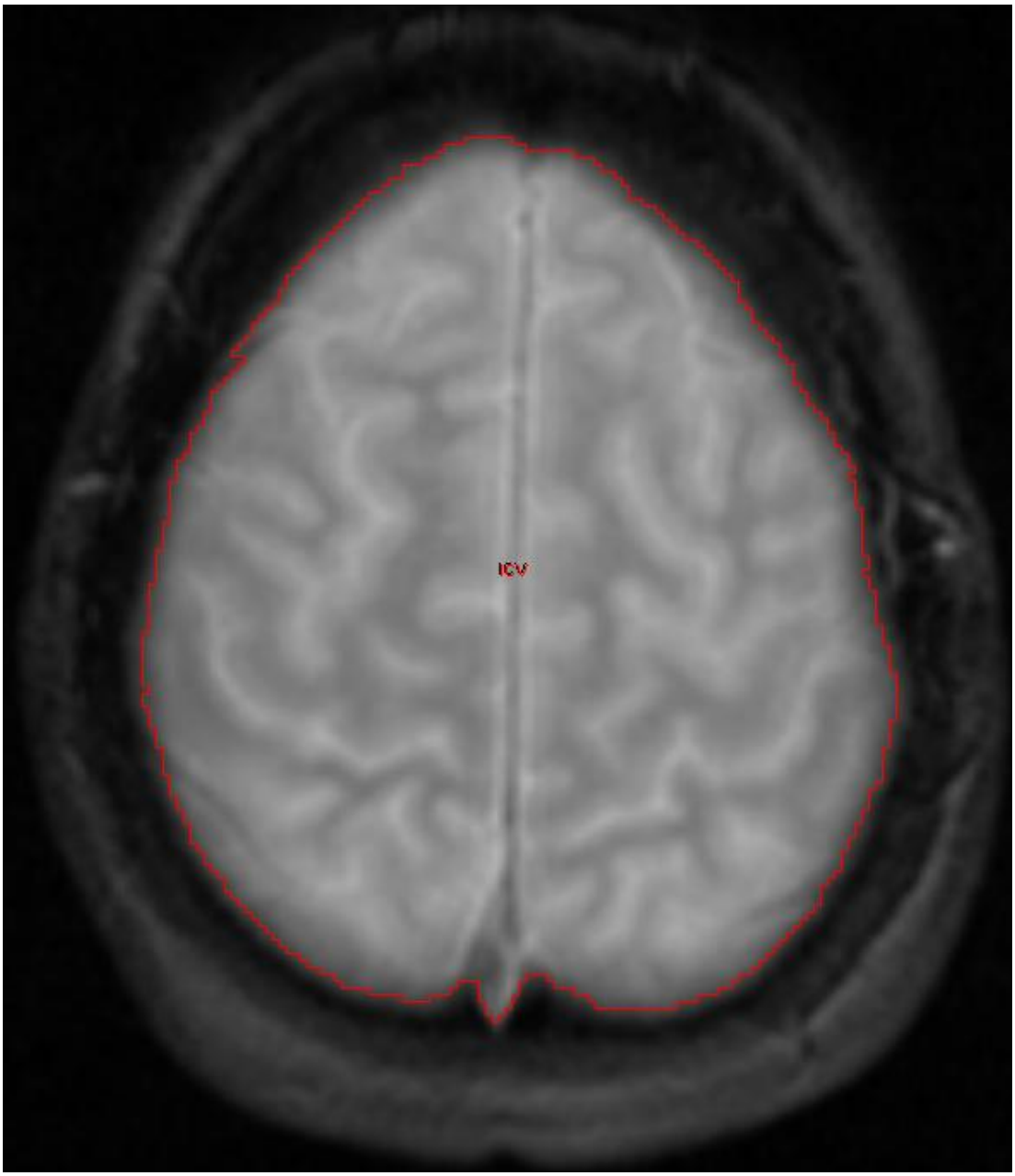

Figure 3.2 An example of ICV mask segmentated in the Analyze™ 9.0 software.

The ICV segmentation process includes:

(1) Slice selection
(2) Threshold selection
(3) Brain mask extraction
(4) Save brain mask object map
(5) Load image and brain mask
(6) Change the name and colour (name: ICV; colour: red)
(7) Edit and save the ICV mask
(8) Calculate the volume of the ICV mask
(9) Save the ICV mask in the AnalyzeImage (7.5) format

A detailed ICV segmentation manual is in the Appendix (B-1).

3.2.2 Stroke Segmentation

We manually outlined the stroke mask on the FLAIR image using the 'Image Edit' module, guided by DWI and T2W images based on the region-growing algorithm based in Analyze™ 9.0 software. The stroke segmentation included:

(1) Slice selection
(2) Adjust threshold in the 'Auto Trace' tool
(3) Select 'Delayed Flood Fill' tool
(4) Check visually for accuracy, edit if required and save the stroke mask

3.3 Testing seven MRI image processing methods for measuring WMH in eight patients

We systematically searched and reviewed the literature seeking reliable methods for segmenting WMH. Most studies used multiple sequences and semi-automatic segmentation. Although the criteria for selecting the optimum threshold varied, in general, the use of descriptive statistics of the signal intensity in lesions as opposed to normal-appearing regions was a common approach. Semi-automatic methods used two or more sequences and a clusterisation algorithm. Some studies considered intensity adjustment and correction of inhomogeneities in the magnetic field as pre-processing steps before the actual segmentation while others did not.

We grouped these alternatives into seven approaches using the method described in Ferguson's paper (Ferguson et al., 2005) for thresholding and the technique described in Hernandez's paper (Hernandez Mdel et al., 2010) as the semi-automatic clustering method – as we had found it performed better than other clustering methods in previous analysis (Valdes Hernandez Mdel et al., 2011). We tested these seven methods (Figure 3.3) in eight representative patients to find the most accurate method visual inspection and least time-consuming alternative for measuring WMH volumes on the baseline and follow-up scans, and for determining the longitudinal WMH change. The stroke lesions (including the acute lacunar or cortical stroke lesions and any old stroke lesions) were excluded from the WMH lesion volume to avoid changes in stroke lesions distorting the WMH volume measurement at both time points and the WMH change (Results in chapter 5) (Wang et al., 2012).

The following section would describe the technical aspects of different approaches and imaging processing steps we compared.

Thresholding Method

The thresholding method was implemented using FLAIR images and Analyze™ 9.0 software (Mayo Clinic, Rochester, MN). Thresholds for WMH and stroke lesion masks were obtained separately using a region-growing algorithm based on the pixel intensity in the FLAIR images. The threshold was achieved by placing four regions of interests (ROI) squares in the normal appearing white matters anterior to the frontal horn of the lateral ventricles on two consecutive slices (5mm X 5mm per each square; two squares bilaterally on one slice; the other two squares bilaterally on the consecutive slice). The mean intensity and standard deviations (SDs) of those four ROI squares was measured.

*Threshold= mean intensity + 6*SDs* *equation 1*

Previous studies of Framingham Offspring Cohort determined their effective thresholds in WMH measurements as 3.5 SDs in pixel intensity plus the mean intensity of brain parenchyma based on the summed images of first and second echo images from T2 sequences (Atwood et al., 2004; Jeerakathil et al., 2004). We modified it into 6 SD based on tests of WMH intensity on FLAIR images (equation 1). Thresholds obtained from this equation suited most cases. Because the threshold increased with severity of WMH loads, in cases with high WMH loads, signal heterogeneity increased in normal appearing white matter which we used to calculate the threshold. So in cases with high WMH loads, increased thresholds sometimes led to an

underestimation in lesion volumes, so for those cases we needed to adjust the threshold.

MCMxxxVI Method

The multispectral method (MCMxxxVI), all the hyperintense lesions (WMH and any old or new stroke lesions) were selected in the combined FLAIR and GRE images based on colour fusion technique (Hernandez Mdel et al., 2010), and the stroke lesions and the false positive WMH (see Chapter 4, WMH artefacts) were manually removed from the total hyperintensive volume as a post-processing step. WMH masks were saved in the Analyze image format and the lesion volumes were saved in a spreadsheet. We segmented WMH at both time points using each of the seven methods. WMH volume differences were calculated by subtracting the baseline WMH volume from the follow-up WMH volume.

The seven tests of MRI image processing methods for measuring WMH was based on thresholding and MCMxxxVI method mentioned above. We tested the efficiency of thresholding and MCMxxxVI methods using original images (Experiment 1 and 4), bias field corrected images (Experiment 2 and 5) and intensity adjusted images after histogram equalization (Experiment 3 and 6). Intensity adjusted images after regression analysis was also tested using MCMxxxVI method (Experiment 7). We summarized images, methods and the name of the seven testing experiments in the figure below (Figure 3.3) and detailed steps in each experiment as follows:

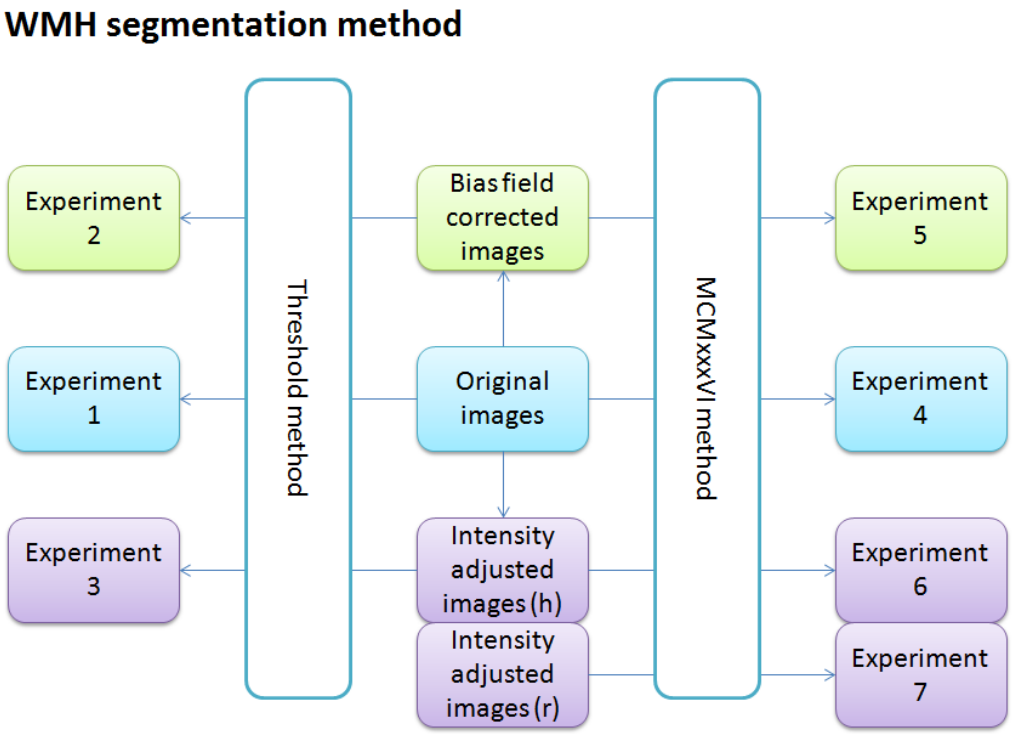

Figure 3.3 Testing of seven WMH segmentation experiments.

h: histogram equalization; r: regression analysis.

Experiment 1: testing the original images (Thresholding method)

We measured the WMH and stroke lesion volume at baseline and follow-up using Analyze 9.0 independently. The WMH segmentation steps in the threshold method include:

(1) Load original FLAIR image in Analyze™ 9.0 software workspace

(2) Place four ROI squares in the normal appearing white matters anterior to the frontal horn of the lateral ventricles on two consecutive slices (details were described in the 'Thresholding Method' above).

(3) Calculate mean intensity and SDs of those four ROI squares.

(4) Add seed in the WMH lesions and set the intensity of "Threshold= mean intensity + 6*SDs" for each slice

(5) Create a WMH object map and measure the WMH volume in all slices

(6) Save the WMH object map

Steps for stroke lesion segmentation are similar to the measurement of WMH segmentation, the only difference being to add the seeds in stroke lesion in step (4).

Experiment 2: testing the bias field corrected images (Thresholding method)

In order to test the effect of bias field correction algorithm in the threshold method, we used the method described in the paper (Guillemaud and Brady, 1997) to remove the bias field influence on the original FLAIR images and saved the parameters. We then changed the original FLAIR images into the bias field corrected FLAIR images, and repeated WMH segmentation steps in the threshold method listed in Experiment 1.

Experiment 3: testing the intensity adjusted images after histogram equalization (Thresholding method)

We adjusted the intensity of the original FLAIR images using MATLAB 'histogram equalization' algorithm script (Seul et al., 2000) by eliminating 1% data near the minimum intensity and 1% data near the maximum intensity, and stretching the rest of the intensity values of input image to new values. Therefore, we increased the output image contrast (Seul et al., 2000). We then repeated the WMH segmentation steps in the threshold method listed in the Experiment 1 using intensity adjusted images after histogram equalization.

Experiment 4: testing original images (MCMxxxVI method)

We need to register images, fuse FLAIR and GRE images, segment intracranial volume (ICV) mask and stroke lesions (Stage I to IV) using

Analyze™ 9.0 software before the WMH segmentation using the MCMxxxVI method.

Stage I-Image Registration

We registered FLAIR and GRE images to the permeability image using the ANALYZE 9.0 '3-D Voxel Registration' module, which allowed us to spatially register two volume images based on the Normalized Mutual Information algorithm. For the 3 cases which failed in the permeability scan, we registered FLAIR and GRE to T2W image (Figure 3.4).

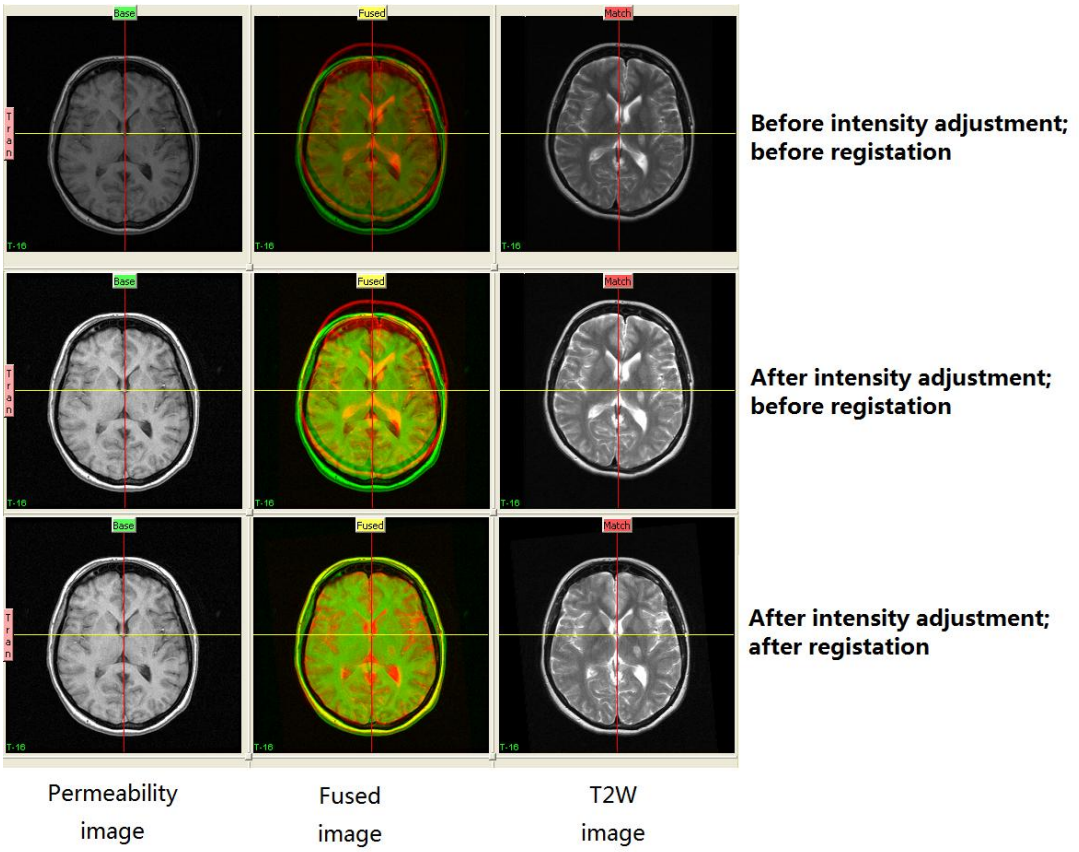

Figure 3.4 Image registration in Analyze™ 9.0 software.

The volume registration process is as follows:

(1) Intensity adjustment
(2) 3D-voxel registration
(3) Save transformed image
(4) Manual registry for unsuccessful automated registration

A detailed manual of image registration are in the Appendix (B-2).

Stage II-Fuse images

We fused FLAIR and GRE images using the '3-D Surface Registration' module in Analyze™ 9.0 software, the image combination includes following steps:

(1) Intensity adjustment
(2) 3D-surface registration
(3) Save the combined images of FLAIR and GRE as input images for MCMxxxVI method (Figure 3.5).

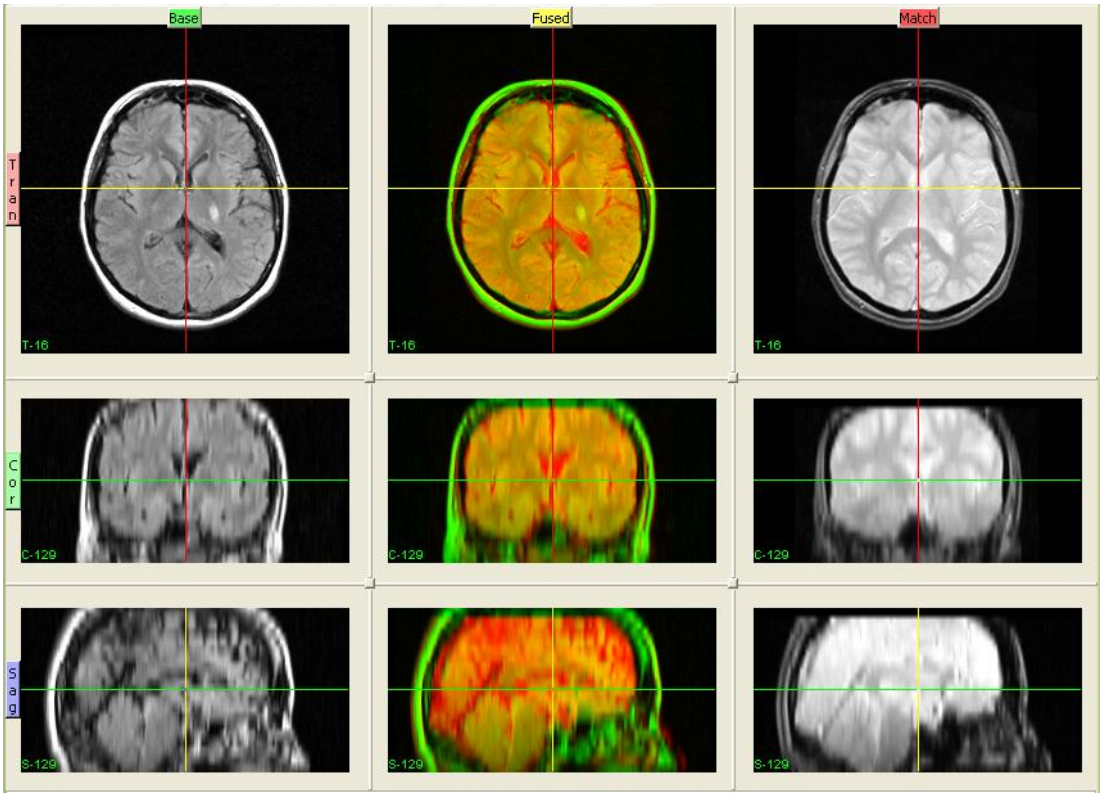

Figure 3.5 Image combination of FLAIR and GRE images using Analyze™ 9.0 software.

Base image: FLAIR image (Left), Match image: GRE image (Right), Combined image of FLAIR and GRE images (Middle).

Stage III-ICV Segmentation

Refer to the ICV segmentation steps in the previous section '3.2 Basic imaging processing steps-ICV segmentation'.

Stage IV-Stroke Segmentation

Refer to the ICV segmentation steps in the previous section '3.2 Basic imaging processing steps-Stroke segmantation'.

Stage V-CSF Segmentation

We segmented the CSF mask using the MCMxxxVI method, the segmentation process included:

(1) Load fused images saved and ICV mask generated from from previous steps (Figure 3.6 graphical interface of MCMxxxVI method)

(2) Press 'Load and Segment'

(3) Change the 'Red' from '1' to '255' and adjust the 'Green' from '1' to 'n' (n is the threshold selected)

(4) Press 'Extract tissue'

(5) Remove false positive CSF in the brain tissue (Figure 3.7)

(6) Save the final CSF and brain parenchyma binary masks and numerical results

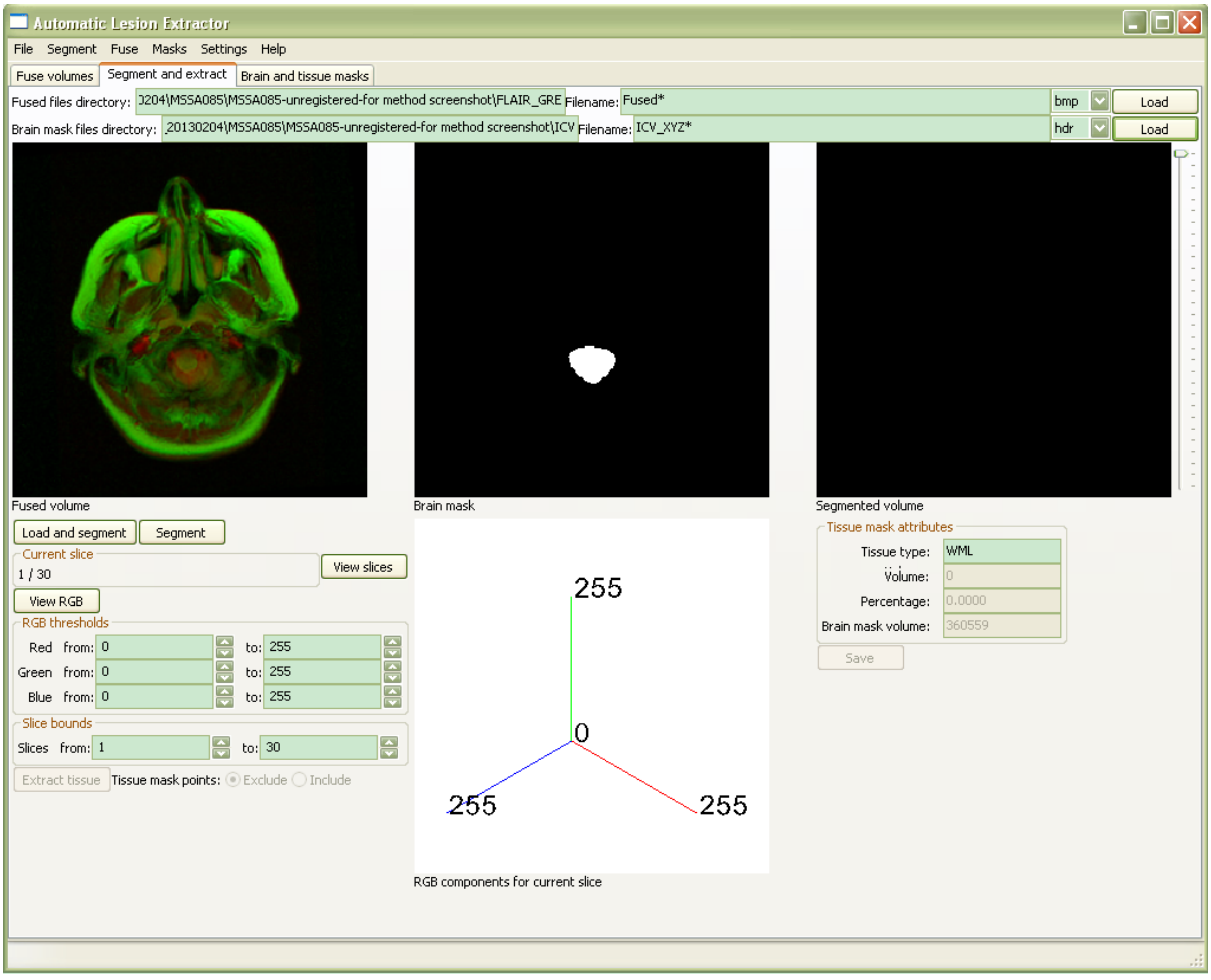

Figure 3.6 Graphical user interface of CSF segmentation in the MCMxxxVI software.

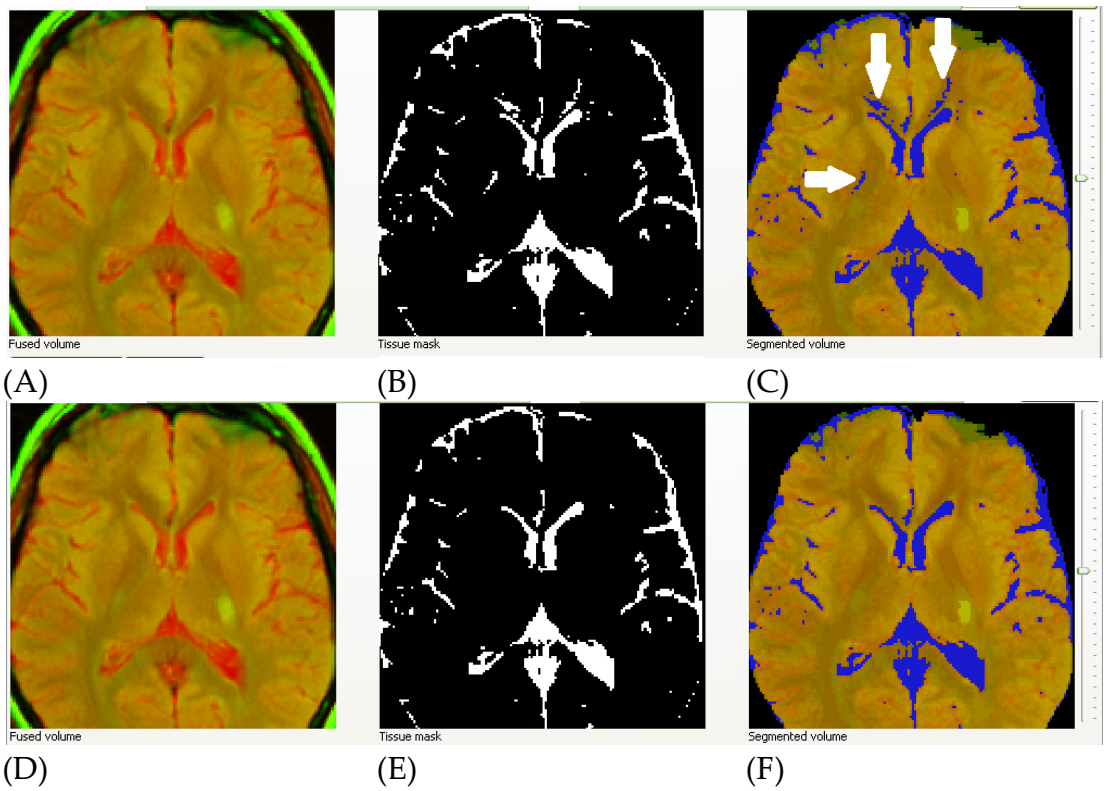

Figure 3.7 Removing of false CSF in MCMxxxVI method.

Upper row: CSF mask before false CSF removement. (A) Fused image of FLAIR and GRE; (B) Binary mask of CSF mask; (C) CSF mask on fused image, white arrows point to false CSF regions. Lower row: after the removement. (D) Fused image of FLAIR and GRE; (E) Binary mask of CSF mask; (F) CSF mask on fused image.

Stage VI-WMH Segmentation

We segmented the WMH mask using the MCMxxxVI method, the segmentation process includes:

(1) Load fused images saved from Stage II and brain parenchyma mask generated from Stage V
(2) Press 'Load and Segment'
(3) Adjust the 'Red' and 'Green' values
(4) Press 'Extract tissue'
(5) Remove false positive WMH and the stroke lesions
(6) Save the WMH mask

The whole multi-stage image processing (Figure 3.8) was performed blind to all clinical data. Baseline and follow-up images were analyzed separately and blind to each other's results.

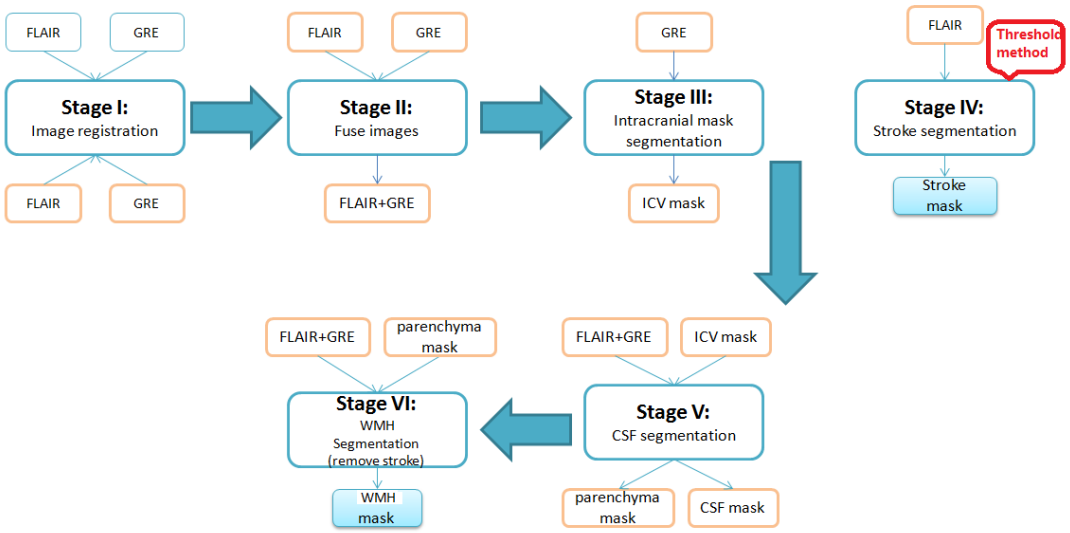

Figure 3.8 Flow process diagram of a multi-stage segmentation.

Abbreviations: FLAIR, fluid attenuated inversion recovery image; GRE: gradient echo image; ICV: intracranial volume; CSF: cerebrospinal fluid; TL: total lesions; WMH, white matter hyperintensities.

Experiment 5: testing the bias field corrected images (MCMxxxVI method)

We fused the bias field corrected FLAIR and GRE images (described in Experiment 2) and repeated the WMH segmentation steps in the MCMxxxVI method listed in Experiment 4.

Experiment 6: testing the intensity adjusted images after histogram equalization (MCMxxxVI method)

We fused the FLAIR and GRE images after histogram equalization (described in Experiment 3) and repeated the WMH segmentation steps in the MCMxxxVI method listed in Experiment 4.

Experiment 7: testing the intensity adjusted images after regression analysis (MCMxxxVI method)

Colour fusion was thought to be dependent on the relative contrasts of the fused sequences rather than on the parameters of the acquisition protocols. We aimed to test this hypothesis in a pilot study of 100 scan sets randomly selected from the LBC1936 participants (Deary et al., 2007) in The Disconnected Mind Study (http://www.disconnectedmind.ed.ac.uk), we did a regression analysis to derive the relationship between the initial and final intensity ranges after visually adjusting the intensity range in the FLAIR and GRE images. As a result, we found that the final FLAIR intensity range (equation 2) depends on the initial GRE intensity range, and that the final GRE intensity range (equation 3) depends on the final FLAIR intensity range. The associations are expressed in the following equations:

*FLAIR final=545.3365+0.8158*GRE initial* *equation 2*

*GRE final=674.5948+0.4061*FLAIR final* *equation 3*

After automatically adjusting the intensities of the FLAIR and GRE images, we fused the intensity adjusted FLAIR and GRE images and repeated the WMH segmentation steps in the MCMxxxVI method listed in Experiment 4.

3.4 Comparison of results from seven WMH measurement experiments

We had two image analysts testing our seven experiments. Analyst 1 performed all seven experiments, and analyst 2 repeated experiments 4 and 6. Though eight patients were not powerful enough to do a statistical analysis, the aim of this pilot study using eight patients was to find a sensible and reasonable method for analysing WMH longitudinal change which was the most accurate and least time-consuming method. Since there was no gold standard method we could refer to, we mainly evaluated the efficiency of method by segmentation time and visual inspection of image and segmentation results.

The WMH segmentation by the MCMxxxVI method (Experiment: E, E4 to E7) took 20 to 30 minutes per case, and this method used less time than the thresholding method (E1 to E3), which took approximately 40 to 90 minutes per case.

By visual inspection, the overall image appearance after intensity adjustment (E6 and E7) did not show as good resolution and contrast as original image or image after bias field correction (E4 and E5) and brought more difficulties in the process of WMH segmentation.

Moreover, by visual inspection, all of eight patients had obvious WMH longitudinal progression when comparing WMH loads between baseline and follow-up scans. However, after subtracted baseline WMH volume from follow-up volumes, some of results from the five experiments (expect E4 and E5) were negative appeared as WMH shrinkage (Figure 3.9).

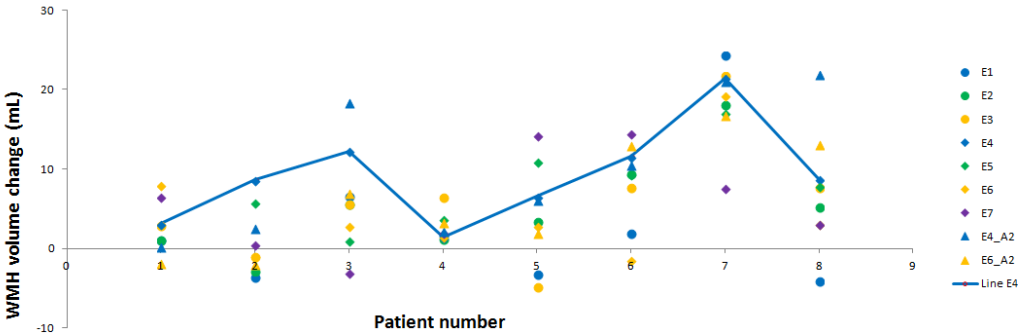

Figure 3.9 WMH volume change results from seven experiments, by two analysts.

E: experiment, A: analyst. Blue: experiments using original images; Green: experiments using bias field corrected images; Orange: experiments using intensity adjusted images after histogram equalization; Purple: after regression analysis. Both round dots and diamonds were the results from analyst 1, round dots presented the results of thresholding method (analyst 1, E1-E3), and diamonds were results from MCMxxxVI method (analyst 1, E4-E7). Triangles are the results from analyst 2 (analyst 2, E4 and E6).

Based on the results shown in Figure 3.9 and considering time consummation for each experiment, we decided to take forward the methods used in E4 and E5 for further testing to explain more about measuring WMH volumes in a large number of cases and to analyze the longitudinal WMH change.

3.5 Longitudinal image analysis of 46 cases with follow-up scans

The method testing experiments above (Figure 3.9) showed that the MCMxxxVI method was effective and consistent for WMH segmentation, using both original images (E4) and bias field corrected images (E5). Thus, we measured the CSF and WMH volume of the 46 patients who had follow-up scans using the MCMxxxVI method (E4 and E5) at both time points.

In order to assess the effect of stroke lesions on WMH and brain atrophy progression we also needed the intracranial volume (ICV) mask and stroke lesion mask (any old infarcts including lacunes at baseline and new stroke lesions appearing during follow-up). Both the ICV and stroke lesion masks were manually outlined based on the threshold method on FLAIR in Analyze 9.0 software, guided by FLAIR, diffusion-weighted and T2-weighted images. The whole multi-stage image processing (Figure 3.8) was performed blind to all clinical data. Baseline and follow-up images were analyzed separately and blind to each other's results. We segmented both baseline and follow-up scans for the 46 cases, using the MCMxxxVI method with both the original images (as in E4) and bias field corrected images (as in E5). We analyzed the effect of stroke on WMH and atrophy progression using the results from E5 (Results in Chapter 5). We also summarised the locations and frequencies of WMH artefacts appearing in the FLAIR images for the 46 cases at baseline using bias field corrected images (Results in Chapter 4).

3.6 Image analysis of the 100 patients baseline scans

The image preprocessing step of bias field correction (BFC) helped to compress noise and uniform tissue density which theoretically helps WMH segmentation. The old version of the BFC software did so (Figure 3.10 A); E5 was easier than E4 when doing the WMH segmentation. However, when we planned to use E5 to do WMH segmentation in the rest 54 patients of the 100 patients who participated in the BBB permeability study and had the baseline diagnostic and permeability scans only, we found the BFC software had been updated and the new version caused image display problems. The new version BFC software included a smoothing effect which explicitly eliminated hyperintensitive lesions, both WMH and focal infarcts, which distorted the essence of image characteristics. Because of this problem, we decided to avoid using bias field corrected images in our further studies for the present time. So we chose to use E4 (original image) to segment the remaining 54 cases. If better bias field correction software becomes available in future, its use could be rethought.

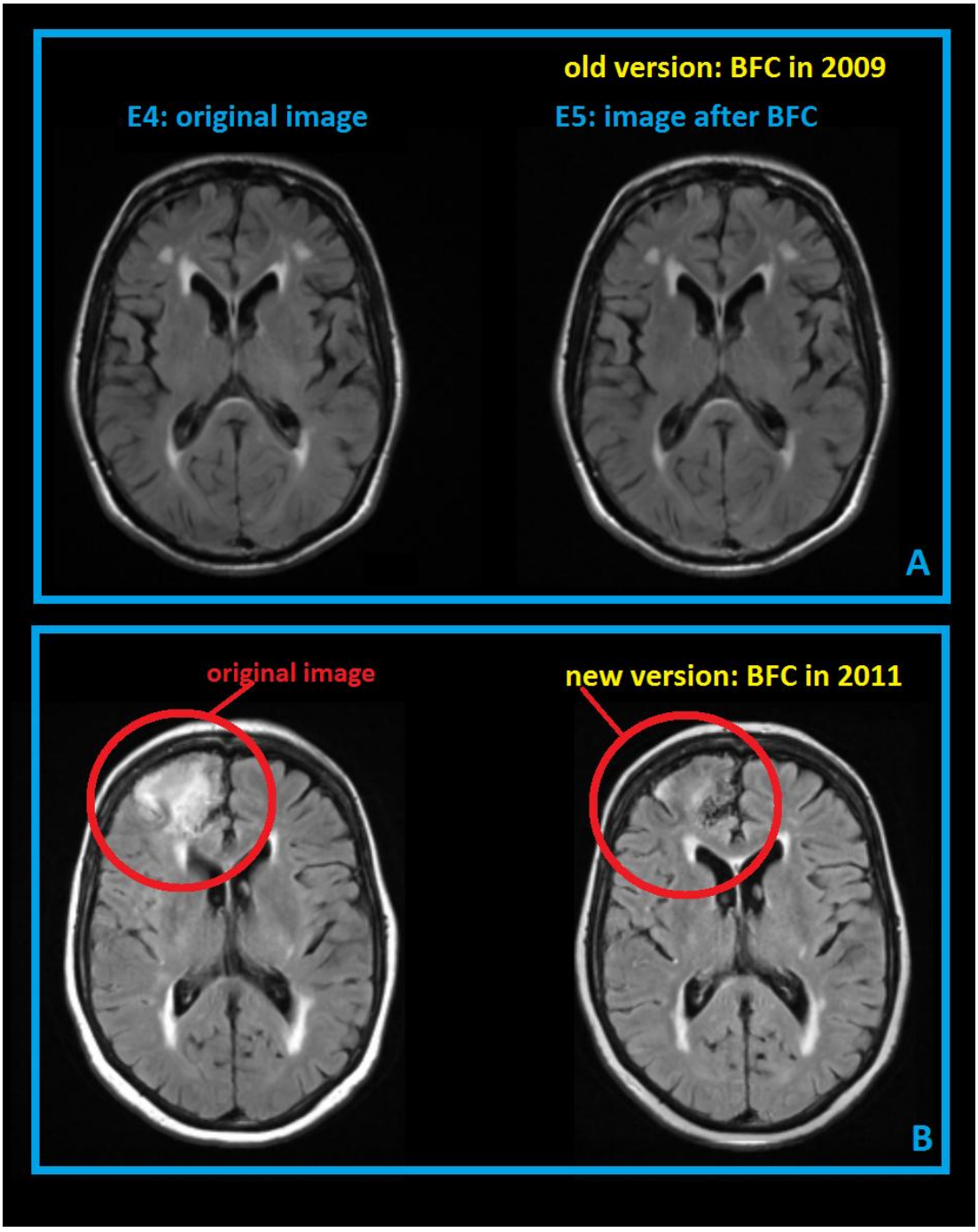

Figure 3.10 Comparison of old and new versions of bias field correction (BFC) software.

A: old version BFC software compressed noise and "uniformed" tissue signal. B: new version BFC software included smoothing effect and eliminated focal hyperintense lesions. E: experiment.

From prior experience of image segmentation (above), we found it was redundant to segment the stroke mask in Stage IV using the Analyze software and to remove the stroke lesion as false positive in Stage V. Moreover, the stroke lesion mask segmentation by threshold method in the Analyze software is very time consuming (o.5h~1.5h per case). Therefore we optimized the steps in the segmentation process (Figure 3.11).

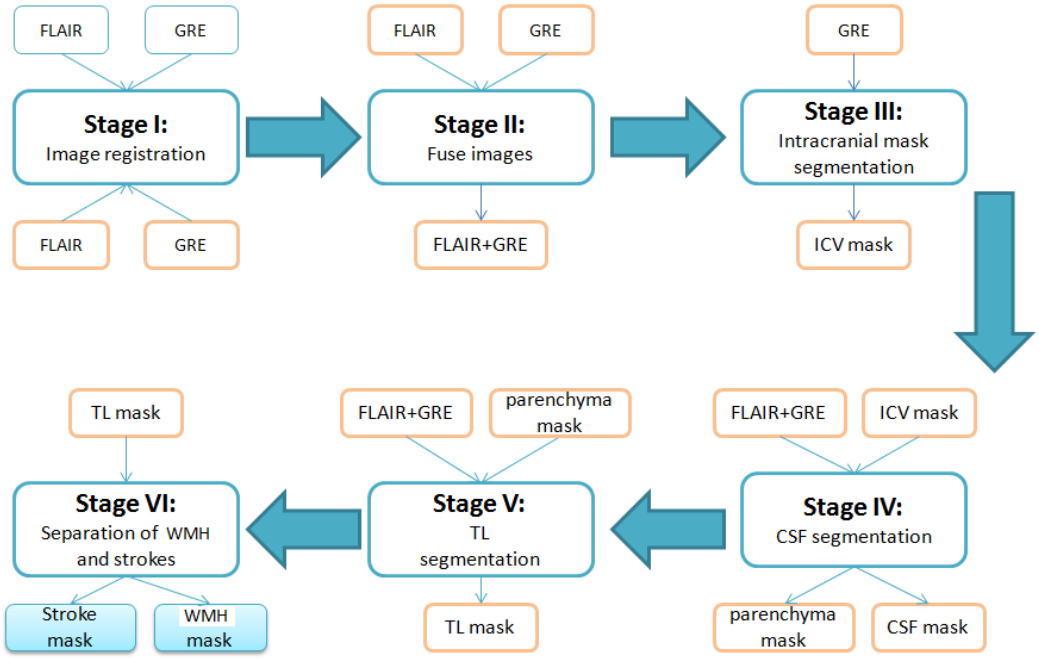

Figure 3.11 Flow process diagram of an optimized multi-stage segmentation developed in the MSS suitable for analysis of WMH and brain tissues in patients with stroke.

Abbreviations: FLAIR, fluid attenuated inversion recovery image; GRE: gradient echo image; ICV: intracranial volume; CSF: cerebrospinal fluid; TL: total lesions; WMH, white matter hyperintensities.

The first three steps (Image Registration; Fuse images; ICV segmentation) were the same, with the optimization occurring in the last three steps. Instead of obtaining stroke mask and WMH mask separately (as described above), in the MCMxxxVI method, we included all voxels with hyperintensity in the fused images, and named it as total lesion (TL) mask

(new Stage V). We then separated and modified the TL mask to a stroke mask and a WMH mask in the Analyze software (new Stage VI). The changes are as follows:

new Stage IV-CSF Segmentation

The same as Stage V described above, which we segmented the CSF mask using the MCMxxxVI method.

new Stage V-TL Segmentation

We segmented all the hyperintense areas (TL mask) using the MCMxxxVI method. The TL segmentation process included:

(1) Load fused images and parenchyma mask generated above
(2) Press 'Load and Segment'
(3) Adjust the 'Red' and 'Green' values
(4) Press 'Extract tissue'
(5) Save the TL mask

new Stage VI-Separation of WMH and strokes

We separated the TL mask into a WMH mask and a stroke mask using the 'Region of Interest' and 'Image Calculator' modules in the Analyze 9.0 software. We used the FLAIR, diffusion-weighted and T2-weighted images as references while doing the separation. The separation process included:

(1) Load FLAIR image and TL mask
(2) Remove the stroke lesions in the 'Region of Interest' module, edit and save the WMH mask
(3) Subtract WMH mask from TL mask in the 'Image Calculator' module
(4) Edit as required for accuracy by visual inspection and save stroke mask

The results for the 100 patients in the BBB permeability study with baseline imaging are in chapter 5 (Results in Chapter 5).

Chapter 4 White matter hyperintensities (WMH) artefacts

4.1 Introduction

The fluid attenuated inversion recovery (FLAIR) magnetic resonance image (MRI) is sensitive to subtle white matter hyperintensities (WMH), and is commonly used in WMH studies. However, the artefacts caused by cerebrospinal fluid (CSF) and blood flow, patient movement, inhomogeneity of magnetic field, and magnetic susceptibility sometimes mimic pathological conditions, could distort the accurate measurement of WMH and further misrepresent WMH progression, associations with risk factors and other cerebral small vessel disease features.

The history of studying WMH artefacts on MRI images is not long, only since 1992, when MRI started to be used more for studies in ageing, dementia and stroke. There is a need for a focused summary of the types of WMH artefacts and methods to avoid them in the WMH segmentation process, which would be a useful guide in the future training of WMH segmentation and facilitate accurate WMH measurements.

We aimed to summarize guidance in differentiating the white matter (WM) artefacts from WMH based on the published literature, especially on the FLAIR sequence which is commonly used to identify WMH. We also summarized the locations and frequencies of WMH artefacts in a cohort of 46 patients with stroke and WMH, and we compared them with artefacts based on the literature. The summary of location and frequency of WMH artefacts in the literature and stroke patients would be a useful guidance for future studies of stroke and WMH.

4.2 Method

4.2.1 Search strategy and study selection

We searched the published literature from PubMed© and Medline© up to 23rd January 2013. We searched the terms "Artefact FLAIR" and "Artefact FLAIR" using PubMed©; and we used exploded headings relating to WMH and Artefact using Medline©. We used a two-part search strategy: initially for artefacts seen on FLAIR images; then for artefacts specifically related to WMH. We also checked paper reference lists and comments for these papers.

4.2.2 Inclusion and exclusion criteria

We included full papers in English about human brain studies which assessed a variety of MRI artefacts (mainly on the FLAIR images) in various cerebral disease models, with high image qualities.

We excluded studies published only in abstract, not published in English and duplicates. We excluded studies that only included animals as well as non-cerebral disease studies because we wished to focus on studies of artefacts related to pathological changes in human brains. We excluded studies which used FLAIR image as a control evaluate a novel sequence, algorithm, diagnostic or measurement protocols which might mention artefact but not on FLAIR sequence. We also excluded studies used MRI images having low resolution, because their conclusions might be compromised by the poor image quality.

4.2.3 Data extraction

Firstly, I screened all papers' titles and abstracts, and extracted data into an assessment spreadsheet, which include authors' name, published year,

sequences used in studies, whether the study was about cerebrovascular disease, the main results and conclusion of the study.

Based on the main results and conclusion, studies focusing on the appearance of image artefacts were included for further full paper assessment. Artefacts types and locations, study aim, disease type and patients number of were extracted after reading through full papers. For those studies evaluating a specific sequence to reduce the image artefacts, whether the sequence was successful in reducing specific type of artefact, or contrarily increased the extent of artefacts was noted. We summarized artefact frequencies in the included literature.

4.2.4 Summary of common artefacts in a cohort of stroke patients with WMH

Independent of the literature searching described above, we summarized types and frequencies of WMH artefacts seen on the baseline scans of 46 stroke patients who returned for follow-up scans in the Mild Stroke Study permeability study (recruitment details in Chapter 3). We used baseline and follow-up images from these 46 patients to assess the effect of stroke lesions on WMH progression in the following chapter (Chapter 5).

All slices on FLAIR sequences in each patient were reviewed, and images of tissues with doubtful artefacts were saved into several categories (such as hyperintensities near ventricles, bilateral corticospinal tract hyperintensities, and patient movement) mainly based on their location. These WMH artefacts categories were reviewed and advised by an experienced neuroradiologist. The frequency of WMH artefacts in each category was calculated.

We compared types, locations and frequencies WMH artefacts in the 46 stroke patients with the results from our literature searching, and summarized types of artefacts mentioned in the previously published literature which also appeared in our study into a training guide for WMH segmentations.

4.2.5 Feedback from WMH segmentation training

Two image analysts have been trained with aid from our WMH artefacts guide in their WMH segmentation training (see Appendix C: WMH artifacts training guide). They provided feedback on the usability and comprehensibility of the guide.

4.3 Results

4.3.1 Artefact characteristics from the included literature

In addition to the 26 studies fitting our criteria, we included two more studies found from searching the reference lists of the literature, thus in total we included 28 studies (Figure 4.1) exploring the FLAIR artefacts in a variety of brain diseases, such as white matter lesions in multiple sclerosis (Bachmann et al., 2006; Sled et al., 1998), stroke (Willinek et al., 2003), subarachnoid hemorrhage (Wiesmann et al., 2002), epilepsy (Phal et al., 2008) and tumors (Oatridge et al., 2001; Von Kalle et al., 2010), as well as healthy and normal brains. In the 28 studies, four studies did not specify their patient characters such as number or disease type; the other 24 studies in total included 1044 participants, with a minimum sample size of four patients, a maximum of 377 patients, and a median of 25 patients (Table 4.1).

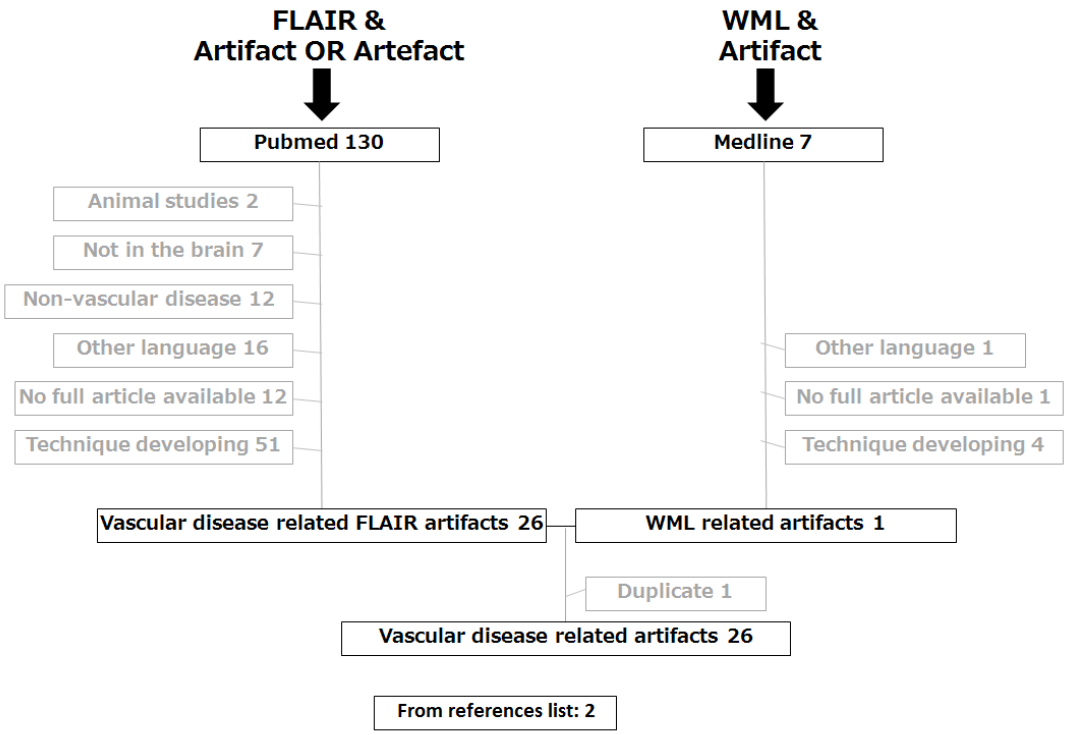

Figure 4.1 Flowchart of artefact searching strategy.

Grey lines and boxes indicate excluded studies and primary reasons. Black lines and boxes indicate studies included.

Table 4.1 Descriptions of 28 included studies arranged by published date.

In the results column "↓" means artefacts decreased, "↑" means increased, and "↔" means no change.

Author, year	Artefacts mentioned	Sequence detail	Effect on artefacts	Patient type	Patient Number
Gawne-Cain, 1997	CSF flow	FLAIR: normal and disease	appearance	normal brain	40
Sled, 1998	Inhomogeneity	N3:bias field correction	↓	MS (WML)	12
Bakshi, 2000	CSF flow	Ventricles artefacts	appearance	normal brain	100
Tanaka, 2000	CSF flow	FAIS	↓	posterior fossa disease	20
Hajnal, 2001	CSF flow	adiabatic inversion	↓	Not mentioned	4
Oatridge, 2001	Patient movement	KRISP	↔	gliomas	14
	CSF flow & Blood flow	KRISP	↓		
Herlihy, 2001	CSF flow & Blood flow	KRISP	↓	a variety of brain disease	20
	Patient movement	KRISP	↑		
Curati, 2001	CSF flow & Blood flow	KRISP & adiabatic KRISP	↓	established disease	10
Herlihy, 2001	CSF flow & Blood flow	KRISP	↓	suspected disease	10
Kallmes, 2001	CSF flow	3D	↓	healthy	7
Wu, 2002	CSF flow	Fast	↓	Not mentioned	377
Wiesmann, 2002	CSF flow	PD-weighted	↓	SAH	13
Willinek, 2003	Patient movement	SENSE	↓	cerebral ischemia (stroke)	62
	Inhomogeneity	SENSE	↓		
Aprile, 2003	CSF flow	MTC	↓	a variety of brain disease	50
Naganawa, 2004a	CSF flow	3D	↓	healthy; MS; tumor	11
Naganawa, 2004b	CSF flow	3D-TSE-VFL	↓	a variety of brain disease	Not mentioned
	Metal	3D-TSE-VFL	↓		
Bachmann, 2006	CSF flow	3T	↑	MS (WML)	22
Cianfoni, 2006	Patient movement	SS-FSE-FLAIR	↓ free	healthy; SAH patients	32
Bailey, 2007 (Review)	CSF flow & Metal	FLAIR artefacts	summary	a variety of brain disease	Not mentioned

Lisanti, 2007(Lisanti et al., 2007)(Lisanti et al., 2007)(Lisanti et al., 2007)	CSF flow	CSF artefact mechanism	Not mention	a variety of brain disease	Not mentioned
Stuckey, 2007	CSF flow & Blood flow	subarachnoid space	Not mention	a variety of brain disease	Not mentioned
	Metal				
	Patient movement				
Phal 2008	Patient movement	3T	↔	epilepsy	25
Neema, 2009	CSF flow	normal findings 3T	appearance	healthy	22
Alkan, 2009	Patient movement	BLADE	↓	tumor	50
	CSF flow	BLADE	↓ free		
Von Kalle, 2010	Patient movement	BLADE	↓	white matter abnormalities in tumor	26
	CSF flow	BLADE	↓		
Lummel, 2011	CSF flow	3D-Cube	↓	healthy; epilepsy; SAH	25
Nyberg, 2012	Patient movement	BLADE	↓	Not mentioned	25
Lavdas, 2012	Patient movement	BLADE	↓	uncooperative;	67
	CSF flow	T2 FLAIR BLADE	↓	cooperative	

Abbreviations

CSF: cerebrospinal fluid; SAH: Subarachnoid hemorrhage; MS: multiple sclerosis; WML: white matter lesions. FLAIR: fluid attenuated inversion recovery; N3: as nonparametric nonuniform intensity normalization; FAIS: flow artefact–insensitive; KRISP: k-space reordered by inversion time at each slice position; 3D: three-dimensional; PD: proton-density; SENSE: sensitivity encoding; MTC: magnetisation-transfer contrast; 3D-TSE-VFL: 3D imaging with a turbo spin-echo sequence with variable flip-angle echo trains; BLADE: a PROPELLER equivalent implementation of the Siemens Medical System (Erlagen, Germany).

The terms for describing the same type of artefact varied substantially between studies. For example, the CSF flow artefact used in Table 4.1 is also named as artefact caused by CSF inflow (Naganawa et al., 2004b), CSF motion (Aprile et al., 2003), CSF pulsation (Bakshi et al., 2000), pulsatile CSF flow (Cianfoni et al., 2006), pulsative flow (Lavdas et al., 2012) and motion-related phenomena of CSF (Lisanti et al., 2007) in the studies. And the patient movement artefact used in Table 4.1 is also named as motion artefact (Lavdas et al., 2012), artefact caused by patient motion (Cianfoni et al., 2006; Curati et al., 2001; Herlihy et al., 2001a), head movement (Cianfoni et al., 2006) and eye movement (Stuckey et al., 2007). This amount of variation inhibits cross-study comparisons, so we unified terms after as terms we used in Table 4.1. We avoided using the word 'motion' alone to describe artefact, because this word causes confusion, it could either be the artefact caused by patient movement and by CSF or blood movement, so we specify these different types of artefacts as 'Patient movement', 'CSF flow' and 'CSF and blood flow'.

There is a high interest (23/38) in studying the methods to reduce the artefacts. Twenty-two studies tried different imaging techniques to reduce flow artefacts, movement artefacts, inhomogeneity of magnetic field and metal artefacts. And one study improved the image processing algorithm to reduce the inhomogeneity artefacts.

Sequences such as flow artefact–insensitive (FAIS) (Tanaka et al., 2000), adiabatic inversion (Hajnal et al., 2001), k-space reordered by inversion time at each slice position (KRISP) (Curati et al., 2001; Herlihy et al., 2001a; Herlihy et al., 2001b; Oatridge et al., 2001), three-dimensional (3D), Fast, proton density-weighted (PD), magnetisation-transfer contrast (MTC), 3D

imaging with a turbo spin-echo sequence with variable flip-angle echo trains (3D-TSE-VFL) (Naganawa et al., 2004a), a PROPELLER equivalent implementation of the Siemens Medical System (BLADE) and 3D-Cube techniques have all shown the benefits in reducing CSF/blood flow artefacts. When the magnetic field is increased to three teslas (3T), the flow artefacts increased as well. SENSE, BLADE and SS-FSE-FLAIR techniques reduce patient movement artefact, whereas the movement artefact remains the same or even get worse with the KRISP technique. Increasing the magnetic field to 3T instead of 1.5T did not influence patient movement artefacts. 3D-TSE-VFL technique is useful in reducing the magnetic susceptibility caused by metal, and SENSE technique is useful in reducing the inhomogeneity of magnetic field. The N3 (nonparametric nonuniform intensity normalization) method is useful to eliminate the bias field.

The most frequent artefact was CSF flow artefacts, in 23 of the total 28 studies, and the second most frequent artefact is caused by patient movement (details in Table 4.2). Blood flow artefact, inhomogeneity artefact, and metal artefact are also included.

Table 4.2 Artefact frequency in the included literature.

Artefact Type	Number of studies (frequency)
CSF flow	23/28 (82.14%)
Blood flow	5/28 (17.86%)
Patient movement	10/28 (35.71%)
Metal	3/28 (10.71%)
Inhomogeneity	2/28 (7.14%)

4.3.2 Frequencies of artefacts in the 46 patients

As we found in Table 4.1 and 4.2, most literature described WMH artefact by mechanisms. However, we did not know the reasons underlying each

artefact type during WMH segmentations, but we feel it is generally harder to distinguish the WMH from normal appearing white matter tissues near ventricles, insular cortex and white matter tracts, so we summarized WMH artefacts by their locations in the 46 stroke patients following the sequence from the bottom to the vertex of the brain.

In order to describe each artefact type without confusion, we combined the information of both the type and location of artefact, and number them separately for convenience of artefact frequency analysis (Table 4.3). For example, CSF flow artefacts are numbered as N1 to N4 according to their locations in the fourth ventricle, bilateral sylvian fissures, third ventricle and lateral ventricles. And patient movement have been divided into head movement (N7) and eye movement (N8). The artefact in the white matter tracts only appeared in one article (Neema et al., 2009), but it is quite frequent in our analysis, so we number it as N5.

Table 4.3 WMH artefact number used in 46 patients.

Artefact type	Artefact Location	Artefact number (N)	Reference
CSF flow	fourth ventricle; aqueduct; cistern ventral to mesencephalon	N1	(Alkan et al., 2009; Bailey, 2007; Bakshi et al., 2000; Kallmes et al., 2001; Lummel et al., 2011; Stuckey et al., 2007)
CSF flow	bilateral sylvian fissures and insular cortex	N2	(Naganawa et al., 2004b; Neema et al., 2009)
CSF flow	third ventricle	N3	(Bakshi et al., 2000; Lummel et al., 2011; Neema et al., 2009)
CSF flow	lateral ventricles	N4	(Bakshi et al., 2000; Lummel et al., 2011; Neema et al., 2009)
Bilateral corticospinal tract hyperintensity	white matter tracts	N5	(Neema et al., 2009)
Inhomogeneity	inhomogeneity of magnetic field	N6	(Willinek et al., 2003)
Patient movement	eye movement	N7	(Stuckey et al., 2007)
Patient movement	head movement	N8	(Alkan et al., 2009; Nyberg et al., 2012; Willinek et al., 2003)

Within the 46 patients, artefacts N1 to N5, which are located in ventricles, cisterns, sylvian fissures and white matter tracts appeared frequently, in more than half of the patients. The artefacts in third ventricle and lateral ventricles showed in all 46 patients. The artefacts N6 and N7, which were caused by inhomogeneity of magnetic fields and eye movement occurred in less than two patients, so were infrequent artefacts. The artefact caused by patient head movement (N8) did not appear frequently, but could have large influence of all MR slices. A whole group and individual patient artefact frequency summary, for the artefacts with high frequency or high influence in the 46 patients are summarized below (Table 4.4).

Table 4.4 Frequencies of highly frequent or influential artefacts in the cohort of 46 patients and in individual patient, and the frequencies of real lesions in common place of artefacts.

TYPE	Frequency in 46 patients (pts)	Frequency in individual patient (number of slices)	Frequency of real lesions
N1 fourth ventricle; aqueduct; cisterns	40/46 (pts) 86.96%	1/30~6 /30 (slices) 3.33%~20.00%	1/46 (pts) 2.17%
N2 fissures	45/46 (pts) 97.83%	3/30~9/30 (slices) 10.00%~30.00%	1/46 (patients) 2.17%
N3 third ventricle	46/46(pts) 100.00%	4/30~10/30 (slices) 13.33%~33.33%	hard to distinguish: need a consistent standard
N4 lateral ventricles	46/46 (pts) 100.00%	1/30~6/30 (slices) 3.33%~20.00%	hard to distinguish: need a consistent standard (reference: Q3)
N5 WM tracts	24/46 (pts) 52.17%	1/30~7/30 (slices) 3.33%~23.33%	7/46 (pts) 15.22%
N8 head movement	6/46 (pts) 13.04%	5/30~30/30 (slices) 16.67%~100.00%	hard to distinguish, limited by image quality

Ventricles, fissures and white matter tracts are frequent places for artefacts, but real lesions also occur in these places, and need to be distinguished from artefact by reference to DWI, other sequences, and going through each individual slice, to decide whether the lesion is real or not (Figure 4.2).

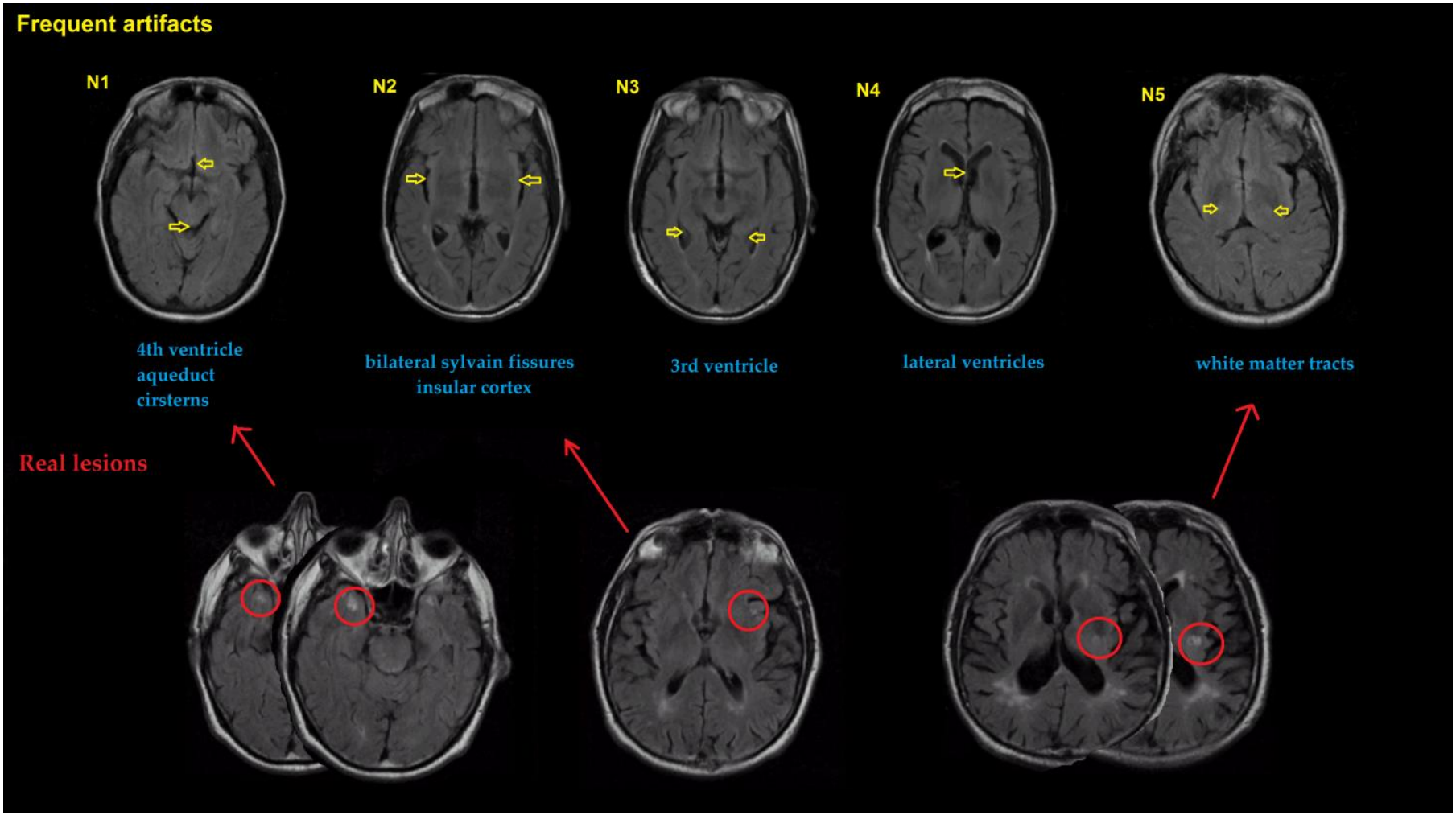

Figure 4.2 High frequent CSF flow and white matter tracts artefacts and real lesions.

Real lesions appeared in the cisterns, sylvian fissures and white matter tracts. For the third ventricle and lateral ventricles, there is no standard to distinguish artefacts from real lesions; we kept excluding the hyperintensities in those two places consistently (Table 4.4).

4.3.3 Three kinds of artefact-linked image features not mentioned in previous studies

There were three kinds of artefact-linked image features (Figure 4.3): Q1, hyperintensive circle around the whole skull; Q2, 'dirty white matter', are diffuse white matter lesions which are highly influenced by subtle changes in threshold applied; Q3, hyperintensive dots above the lateral ventricles. Q2 appeared frequently in more than half of the patients, and Q1 could influence more than half of the slices, details summarized in Table 4.5.

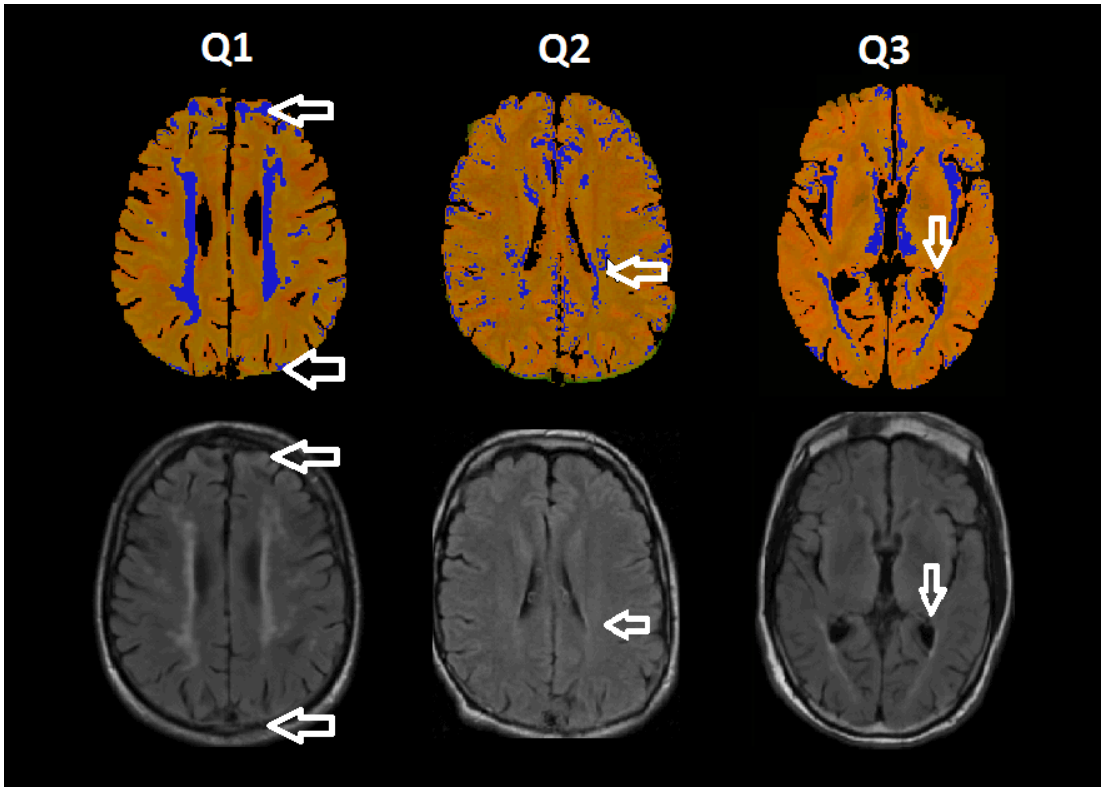

Figure 4.3 Three kinds of artefact-linked image features (Q1-Q3) showing in the 46 patients which have not been mentioned in previous publications.

Table 4.5 Frequencies of three kinds of artefact-linked image features in the cohort of 46 patients and in individual patient.

TYPE	Frequency in 46 patients	Frequency in individual patient (number of slices)
Q1	4/46 (pts)	3/30~ 15/30 (slices)
bright skull circle	8.70%	10.00%~50.00%
Q2	29/46 (pts)	1/30~11/30 (slices)
dirty white matter	63.04%	3.33%~36.67%
Q3	9/46 (pts)	3/30~8/30 (slices)
bright dots above lateral ventricles	19.57%	10.00%~26.67%

4.3.4 Feedback of WMH segmentation training guide

Two image analysts found this WMH artifacts training guide (Appendix C) very illuminating and helpful to decide about the WMH and artefacts especially when they found similar cases as the examples we gave in the guide. They also found it quite hard to decide about what to include when facing hyperintensities on the edges of the brain and dirty WM (Q1 and Q2).

4.4 Discussion

In the systematic searching and literature summary, I found it hard to extract information when different research group used slightly different terms to describe what appeared to be the same artefact, as there were at least seven different terms in describing the CSF flow artefacts and five for patient movement. We need to be consistent in the WMH artefact terminology and definitions. The term 'motion' should be avoided if used alone, because it could be either be artefacts caused by CSF or blood flow or patient movement, and people should make which of these they meant clear when using 'motion'. The term 'ghosting effect' also appeared quite often in the published literature and (while in common use to mean for example an image of the eyes outside the skull due to eye movement) should be avoided in the future since it lacks specificity of artefact origins or characteristics.

One literature by Gawne-Cain (Gawne-Cain et al., 1997) suggested standards to differentiate WMH from artefacts in the posterior internal capsule and posterior cerebral peduncles; pons and posterior centrum semiovale; anterior caps; periventricular lines; posterior caps and occipital white matter. However, we still need to investigate more in order to set a gold standard in excluding artefacts, for example in Gawne-Cain's paper, they considered hyperintensities less than 5 mm in anterior ventricular caps as artefacts even when they are asymmetrical. It was doubtful that in Bailey et al. (Bailey, 2007) considered WMH in the posterior horns of the lateral ventricles as 'shine through' artefact, which seemed to be real lesions from the example figure they provided in the paper. In the literature, Erasmus et al. (Erasmus et al., 2009) included partial volume as another kind of artefact, but we did

not include it since it is one of the common scenario on MRI and could not be avoided, and we need to stay as consistent as possible in tissue decision.

A variety of sequences and algorithms had been developed to deal with CSF and blood flow artefacts, movement artefacts, inhomogeneity of magnetic field and metal artefacts, and not all of them were successful. For example, though high magnetic field was successful in increasing image quality and improving some details on MRI, the acquisition time was longer and the artefacts were more pronounced which lead to little net benefit on diagnosis (Bachmann et al., 2006; Wardlaw et al., 2012).

Our WMH artefact results are consistent with the published literatures; CSF flow artefacts were the most frequent artefacts, which influenced large areas in the brain such as ventricles, cisterns, sylvian fissures and white matter tracts. Patient movement is another huge influencing factor in image quality and further distinguishing WMH.

We had a fairly large sample size, larger than the median of the sample size in the literature. It is a representative cohort of stroke patients with WMH, which would be useful in identifying the WMH artefacts in the studies of SVD.

Based on our WMH artefacts imaging summary generated in the 46 stroke patients, we selected examples of typical artefacts referring to previous published literatures (N1 to N8) and we added examples of real lesions which appeared in the same locations as typical artefacts. We also summarized three types of artefacts which had not been mentioned in previous publications (Q1 to Q3). We combined those image examples into a common WMH artefacts guide and we used it as a complementary guide in

the WMH segmentation training. We suggested that new image analysts should use a reference image (e.g. the same FLAIR slice) when doing the segmentation, and they should check 'tissue' through slices and compare with the common artefacts in the guide when they were doubtful about the artefacts. We had generally positive feedbacks from analysts who used this WMH artefact guide, they found very it helpful. They also found the same experience that "hyperintensities on the edges of the brain" and "dirty WM" were hard to decide.

Our literature review and artefact guide still has limitations and still needs improvements, because we only included the literature from the systematic search; other papers which describe WMH segmentation methods may also include some descriptions of artefacts, but were not included due to restricted time. However we think that we found the main artefacts and these were consistent with our own data.

Chapter 5 Effect of stroke lesions on WMH and cerebral atrophy measurement

5.1 Introduction

White matter hyperintensities (WMH), lacunar strokes, lacunes and atrophy are all features of cerebral small vessel disease (SVD). They are related to cognitive impairment and dementia. Accurate volumetric measurement is essential when using these SVD features as outcome measures in clinical trials and observational studies relating to SVD mechanisms and clinical consequences such as cognition.

As described in Chapter 1, 3 and 4, WMH have increased signal on T2-weighted (T2W) and fluid attenuated inversion recovery (FLAIR) magnetic resonance imaging (MRI), and decreased signal on T1-weighted (T1W) relative to normal white and grey matter (Wardlaw et al., 2013c). Stroke lesions may have similar signal characteristics to WMH on several MR sequences. The similar signal characteristics of WMH and stroke lesions mean that the latter may accidentally be included when measuring the burden of SVD in the form of WMH volume using image processing algorithms, resulting in distortion of the WMH volume.

Brain atrophy is associated with cognitive decline and dementia. Cerebral atrophy rates could be used as a surrogate marker to predict cognitive decline or monitor disease progression, and can be measured as brain volume decrease, or cerebrospinal fluid (CSF) increase, using serial registered MRI. Lacunes are subcortical rounded or ovoid cavities between 3 and 15 mm in diameter with the same intensity as CSF on all brain scan sequences (Wardlaw et al., 2013c). Brain atrophy rate measurement could be

distorted by tissue loss caused by focal tissue loss following stroke, either cortical or subcortical, by formation of, where replacement of damaged tissue by CSF, if included in the global brain volume measurement, would artificially inflate the brain atrophy measurement.

In this study, we measured WMH, CSF, stroke lesions and lacunes separately and evaluated the effect of stroke lesions on baseline measurement of WMH volume and CSF, and the influence of stroke lesions on longitudinal progressions of WMH and cerebral atrophy.

5.2 Methods

We used imaging data from 100 patients described in Chapter 3, who were recruited prospectively in a study of stroke mechanisms with clinical features of a lacunar or mild cortical stroke and also participated in blood brain barrier (BBB) permeability study (Wardlaw et al., 2009). From the 100 patients (51 lacunar stroke and 49 cortical stroke) who were recruited into the original study soon after presenting to hospital with an acute stroke, 46 patients (22 with the original diagnosis of lacunar stroke and 24 with the original diagnosis of cortical stroke) returned after a median of 39 months (IQR 30 to 45 months) for follow-up scanning. All patients were assessed by a trained stroke physician and underwent diagnostic MRI with T1W, T2W, FLAIR, gradient recalled echo (GRE), and diffusion weighted imaging (DWI) as described in Chapter 3. About three years later, we repeated MRI on the same 1.5 T MR scanner.

5.2.1 Image Processing and rating

All image processing was performed blind to all clinical and other imaging data. Baseline and follow-up images were analysed separately. The intracranial volume (ICV), stroke lesions, old infarcts including lacunes at baseline and new cortical or subcortical stroke lesions appearing at follow-up were manually outlined (masked) on FLAIR, guided by DWI and T2W images using a region-growing algorithm in Analyze 9.0 software, and CSF and WMH volumes (millilitre: ml) were measured using an image processing algorithm (MCMxxxVI) (Hernandez et al., 2010) (detailed segmentation steps were described in the segmentation section of Chapter 3).

Brain volume was obtained by subtracting CSF from ICV and cerebral atrophy was assessed by brain volume decrease or CSF increase between the

two time points. WMH progression is the volume difference between follow-up and baseline scans. The tissue loss due to stroke lesions was calculated by combining the baseline stroke lesion mask with the follow-up CSF mask, the overlapping tissue between those two masks was considered as tissue change due to stroke.

A neuroradiologist coded WMH using Fazekas score, for periventricular (PWMH) and deep lesions (DWMH) separately in the left and right hemispheres (Wardlaw et al., 2011). Brain atrophy were coded using a validated template (Farrell et al., 2009), with superficial and deep atrophy coded separately.

5.2.2 Statistical Analysis

In the baseline 100 patients, the distribution of ICV and brain tissue volume expressed as a percentage of ICV were normal, and the distribution of CSF, WMH, stroke lesion volumes and lacunes were not normal. All the volumes in the 46 patients with follow-up were not normal for both time points (from inspection of histograms). We expressed absolute lesion volumes in ml and also adjusted for inter-subject differences in head size using the ICV.

Numeric variables were expressed as mean (Standard deviation: SD) and median (interquartile range: IQR). For baseline 100 patients, we adjusted measures of WMH, atrophy and stroke lesions for factors such as stroke type, age, sex, hypertension, smoking and diabetes using multivariable regression. We compared WMH volume excluding stroke lesions with including stroke lesion using non-parametric tests (Wilcoxon Signed Rank Test), and considered $P<0.05$ as statistically significant. For the 46 patients with follow-up, we did more comparisons: we compared WMH excluding stroke

lesions/lacunes with WMH including stroke /lacunes (to test if the lacunes, a part of SVD, made a material difference to the WMH volume), and cerebral atrophy excluding versus including tissue loss due to stroke lesions/lacunes, using Wilcoxon Signed Rank Test. We also tested the effect of stroke lesions on sample size estimation for a clinical drug trial using WMH as an outcome measure using G power test.

Multivariable linear regression was performed with Minitab (Minitab Inc, version 16). Wilcoxon Signed Rank Test was performed with the Statistical Package for the Social Sciences, Version 16.0 (SPSS, Chicago, Illinois). The G power test was used for sample size calculations (Erdfelder et al., 1996) done by Dr Francesca Chappell in G* Power 3.

5.3 Results

5.3.1 Cross-sectional results of baseline 100 patients

In the 100 patients with stroke, the mean age was 66.81 years (SD, 11.3 years; range, 37 to 92 years), median National Institutes of Health Stroke Scale (NIHSS) score was 1 (interquartile range, 0 to 1), 77% were male, and there were 51 patients with lacunar stroke and 49 patients with cortical stroke.

The patients with cortical stroke were older (70 versus 64 years) and had a higher prevalence of hypertension and lower prevalence of smoking and diabetes than the patients with lacunar stroke (Table 5.1). Seventy-one patients (71%) had index stroke lesions visible on MRI. A third of the patients with symptomatic lacunar stroke syndromes did not show any lacunar infarct on DWI image and a quarter of the patients with cortical stroke also showed negative DWI. The result was consistent with a larger study of 246 patients that included these 100 patients (Doubal et al., 2010a).

At baseline (Table 5.2), the median WMH volume was 11.0 ml (IQR: 4.5 to 26.4), periventricular WMH rating was 1 (IQR: 1 to 2) and deep WMH rating was 1 (IQR: 1 to 1). Patients with cortical stroke had slightly higher WMH volume. The mean brain tissue volume was 79.7 ml (SD= 4.2), the median of deep atrophy rating was 1 (IQR: 0 to 2) and superficial atrophy rating 1 (IQR: 0 to 1). Patients with cortical stroke had less brain tissue volume. For 71 patients with index stroke lesion, the median of stroke lesion volume was 2.3 ml (IQR: 1.1 to 12.1), cortical stroke patients had larger stroke lesion volume than patients with lacunar stroke.

Table 5.1 Baseline characteristics of 100 patients.

Characteristic	Total (n=100)	Lacunar (n=51)	Cortical (n=49)	Difference (95% CI) and P Value Between Lacunar and Cortical Groups
Age	66.8 (SD=11.3)	64.1 (SD=11.7)	69.6 (SD=10.3)	mean difference=-5.5, (95% CI -9.9 to -1.1, p=0.014*)
Gender (Male)	77 (77.0%)	32 (62.7%)	45 (91.8%)	Chi-Square=11.9, df=1, p=0.001*
History of hypertension	62 (62.0%)	30 (58.8%)	32 (65.3%)	Chi-Square=0.4, df=1, p=0.504
History of smoking (n=99)	53 (53.5%)	28 (54.9%)	25 (51.0%)	Chi-Square=0.2, df=1, p=0.619
History of diabetes	15 (15.0%)	10 (19.6%)	5 (10.2%)	Chi-Square=1.7, df=1, p=0.188
Visible stroke on MRI	29 (29.0%)	17 (33.3%)	12 (24.5%)	Chi-Square=0.9, df=1, p=0.330

SD: standard deviation; IQR: interquartile range; df: degree of freedoms

Table 5.2 Volumetric and rating results of WMH, atrophy and stroke lesions of baseline 100 patients (unadjusted).

Measures	Total (n=100)	Lacunar (n=51)	Cortical (n=49)	Difference (95% CI) and P Value Between Lacunar and Cortical Groups
WMH				
WMH volume (ml)	11.0 (IQR: 4.5 to 26.4)	10.8 (IQR: 3.9 to 25.9)	11.5 (IQR: 4.7 to 27.8)	mean difference=-3.6, (95% CI -14.2 to -6.9, p=0.497)
PWMH rating	1 (IQR: 1 to 2)	1 (IQR: 1 to 2)	1 (IQR: 1 to 2.5)	Chi-Square=5.8, df=3, p=0.121
DWMH rating	1 (IQR: 1 to 1)	1 (IQR: 1 to 1)	1 (IQR: 1 to 1)	Chi-Square=0.7, df=3, p=0.879
Atrophy				
ICV (ml)	1428.4 (SD= 122.5)	1394.5 (SD=121.0)	1463.6 (SD=115.0)	mean difference=-69.1, (95% CI -115.9 to -22.2, p=0.004*)
CSF (ml)	279.4 (IQR: 231.5 to 343.1)	264.1 (IQR: 228.1 to 314.1)	321.9 (IQR: 256.5 to 356.7)	mean difference=-39.7, (95% CI -65.8 to -13.5, p=0.003*)
Brain tissue volume (%)	79.7 (SD= 4.2)	80.5 (SD=3.4)	78.7 (SD=4.8)	mean difference=1.8, (95% CI 0.2 to 3.4, p=0.032*)
Deep rating	1 (IQR: 0 to 2)	1 (IQR: 0 to 2)	1 (IQR: 0 to 2)	Chi-Square=4.1, df=3, p=0.249
Superficial rating	1 (IQR: 0 to 1)	1 (IQR: 0 to 2)	1 (IQR: 0 to 1)	Chi-Square=4.9, df=3, p=0.179
Stroke				
Stroke volume (ml)	2.3 (IQR: 1.1 to 12.1, n=71)	1.3 (IQR 0.7 to 2.0, n=34)	8.9 (IQR: 2.8 to 27.5, n=37)	mean difference=-11.7, (95% CI -17.1 to -6.4, p<0.001*)
Median NIHSS score	1 (IQR: 0 to 2)	1 (IQR: 0 to 2)	1 (IQR: 0 to 2)	Chi-Square=2.7, df=6, p=0.841

SD: standard deviation; IQR: interquartile range; NIHSS indicates National Institutes of Health Stroke Scale; brain tissue volume (%): brain tissue volume expressed as a percentage of intracranial volume.

We adjusted for stroke type, age, sex, hypertension, smoking and diabetes (Table 5.3), increasing age significantly associated with worse WMH, atrophy and stroke volume. Smoking correlated with higher PWMH rating scores ($p=0.018$) and male gender had worse deep atrophy ($p=0.003$). Patients with lacunar stroke had significant smaller stroke lesions than patients with cortical stroke ($p<0.001$).

Table 5.3 Influence of stroke type, age, sex, hypertension, smoking and diabetes on WMH, atrophy and stroke lesions (adjusted for stroke type, age, sex, hypertension, smoking and diabetes).

Coefficient/odds ratio (95%CI, p)	Stroke type (lacunar)	Age (increase per year)	Sex (male)	Hypertension (Yes)	Smoking (Yes)	Diabetes (Yes)
WMH						
WMH volume	1.154 (-10.247 to 12.555, p=0.841)	0.777 (0.283 to 1.272, p=0.002*)	2.390 (-10.906 to 15.685, p=0.722)	6.964 (-4.144 to 18.072, p=0.216)	7.441 (-3.150 to 18.032, p=0.166)	2.279 (-12.634 to 17.192, p=0.762)
PWMH rating	1.754 (0.719 to 4.167, p=0.219)	1.099 (1.053 to 1.149, p<0.001*)	1.205 (0.431 to 3.333, p=0.727)	1.587 (0.676 to 3.704, p=0.288)	2.778 (1.190 to 6.250, p=0.018*)	1.724 (0.535 to 5.556, p=0.365)
DWMH rating	1.613 (0.658 to 4.000, p=0.295)	1.099 (1.042 to 1.136, p<0.001*)	1.754 (0.602 to 5.000, p=0.304)	2.174 (0.885 to 5.263, p=0.090)	1.639 (0.709 to 3.704, p=0.250)	1.667 (0.524 to 5.263, p=0.386)
Atrophy						
Brain tissue (%)	0.556 (-0.915 to 2.028, p=0.455)	-0.253 (-0.317 to -0.189, p<0.001*)	0.248 (-1.468 to 1.964, p=0.775)	0.983 (-0.450 to 2.417, p=0.176)	-0.417 (-1.784 to 0.950, p=0.546)	-1.092 (-3.017 to 0.833, p=0.263)
Deep rating	1.818 (0.787 to 4.348, p=0.159)	1.124 (1.075 to 1.176, p<0.001*)	5.000 (1.754 to 14.286, p=0.003*)	1.389 (0.606 to 3.226, p=0.435)	0.943 (0.431 to 2.083, p=0.887)	1.563 (0.505 to 4.762, p=0.442)
Superficial rating	1.124 (0.474 to 2.703, p=0.788)	1.099 (1.053 to 1.149, p<0.001*)	2.174 (0.763 to 6.250, p=0.144)	1.389 (0.592 to 3.226, p=0.446)	1.282 (0.571 to 2.857, p=0.547)	0.746 (0.230 to 2.439, p=0.628)
Stroke						
Stroke volume	-10.581 (-16.342 to -4.820, p<0.001*)	0.291 (0.042 to 0.541, p=0.023*)	-1.230 (-7.948 to 5.488, p=0.717)	-2.274 (-7.887 to 3.339, p=0.423)	4.717 (-0.635 to 10.069, p=0.083)	-2.199 (-9.734 to 5.337, p=0.564)
NIHSS	1.020 (0.459 to 2.273, p=0.965)	0.971 (0.935 to 1.000, p=0.073)	1.010 (0.398 to 2.564, p=0.991)	0.935 (0.433 to 2.041, p=0.866)	0.901 (0.429 to 1.887, p=0.777)	0.448 (0.154 to 1.299, p=0.140)

PWMH: periventricular white matter hyperintensities; DWMH: deep white matter hyperintensities; brain tissue (%): brain tissue volume expressed as a percentage of intracranial volume; NIHSS indicates National Institutes of Health Stroke Scale.

We assessed the effect of stroke lesion volumes on baseline WMH volume by comparing volumes of WMH with and without stroke lesion volumes (Table 5.4). In all 100 patients, the median baseline WMH volume was 10.97 ml (IQR 4.48 to 26.38) excluding, and 17.96 ml (IQR 5.23 to 39.35) including stroke lesions (Z=-7.323, p<0.001). Restricting the analysis to just the 71 patients with visible stroke lesions on MRI, the median WMH volume was also smaller when excluding stroke lesion volumes (16.16 ml, IQR 6.29 to 33.19) than including stroke lesions (26.47 ml, IQR 12.23 to 53.21) (Z=-7.323, p<0.001). The results showed that failure to exclude stroke lesion volumes from WMH volume measurement in these patients resulted in both larger apparent WMH volumes and larger IQRs which added substantial noise to WMH baseline measurements, meaning that WMH volume would be significantly distorted.

Table 5.4 The effect of the stroke lesions on WMH volume (ml) interquartile range (IQR) at baseline in all 100 patients and 71 patients with visible stroke lesions on MRI.

	WMH	WMH + stroke	Significance level
100 patients			
Median (ml)	10.97	17.96	Z=-7.323, p<0.001
IQR	4.48 to 26.38	5.23 to 39.35	
Length of IQR	21.90	34.14	
71 patients with visible stroke lesion on MRI			
Median (ml)	16.16	26.47	Z=-7.323, p<0.001
IQR	6.29 to 33.19	12.23 to 53.21	
Length of IQR	26.91	40.97	

5.3.2 Longitudinal changes of 46 patients with follow-up

Amongst the 46 patients with follow-up scans, their baseline mean age was 68 (standard deviation: SD+/-11) years, 30 (66%) had hypertension, 4 (13%) had diabetes, 23 (50%) were lacunar subtype, median baseline National Institutes of Health Stroke Scale (NIHSS) was 2 (IQR 1-3). The median time to follow-up MR was 39 months (IQR 30 to 45 months).

Stroke lesions

At baseline, 33 (72%) had stroke lesions visible on MRI, median volume was 2.05 ml (IQR 0.88 to 8.88). Three patients had new stroke lesions on follow-up imaging. The stroke lesion volume decreased in 11 and increased in 22 patients between baseline and follow-up to give a median follow-up total stroke lesion volume of 2.43 ml (IQR 0.66 to 13.42). However the volume change ranged from 39.14 ml smaller to 79.97 ml larger than the baseline stroke lesion volume (Figure 5.1, Table 5.5).

Seven of the 33 patients (15% of total patients) had stroke lesions plus one or more lacunes at baseline. The median baseline lacune volume was 0.30 ml (IQR 0.17 to 0.47). Lacune volume decreased in 2 patients and increased in 5 patients during follow-up to give a median follow-up lacune volume of 0.43 ml (IQR 0.16 to 0.54) (Table 5.5).

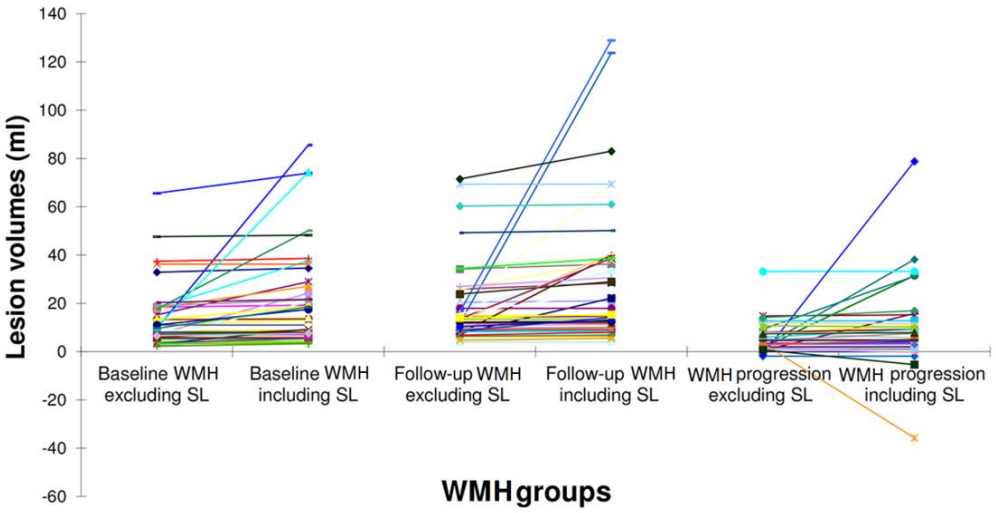

Figure 5.1 Variation in WMH volume at baseline, follow-up and progression due to excluding/including stroke lesions (SL) at baseline and new lesions appearing at follow-up.

Table 5.5 In all 46 patients with follow-ups, the results of median, minimum, maximum and IQR of stroke lesions (SL) volume (ml). SL progression is the volume difference between follow-up and baseline scans.

Patient Group	Median	Minimum	Maximum	IQR
SL at baseline				
All patients (n=46)	1.08	0.00	76.02	0.00 to 6.22
SL (n=33)	2.05	0.20	76.02	0.88 to 8.88
SL no lacunes (n=26)	2.23	0.20	76.02	0.93 to 10.09
SL and lacunes (n=7)	1.33	0.33	64.18	0.76 to 8.88
SL at follow-up				
All patients (n=46)	0.85	0.00	112.52	0.00 to 6.49
SL (n=33)	2.43	0.00	112.52	0.66 to 13.42
SL no lacunes (n=26)	2.26	0.00	112.52	0.70 to 14.79
SL and lacunes (n=7)	4.14	0.33	25.04	0.38 to 12.18
SL progression				
All patients (n=46)	0.00	-39.14	79.97	-0.01 to 1.29
SL (n=33)	0.12	-39.14	79.97	-0.32 to 2.75
SL no lacunes (n=26)	0.16	-6.11	79.97	-0.27 to 2.50
SL and lacunes (n=7)	0.05	-39.14	3.30	-0.43 to 3.17
SL relative change (%)				
All patients (n=46)	0.00	-100.00	356.11	-2.51 to 39.16
SL (n=33)	19.89	-100.00	356.11	-22.44 to 49.19
SL no lacunes (n=26)	20.58	-100.00	356.11	-18.43 to 51.81
SL and lacunes (n=7)	14.89	-60.99	211.38	-56.68 to 38.21

Effect of stroke lesions on WMH volume

Among all 46 patients with follow-ups, the median baseline WMH volume was 8.54 ml (IQR 5.86 to 15.80) excluding, and 10.98 ml (IQR 6.91 to 24.86) including stroke lesions (difference Z=-5.012, p<0.001). At follow-up, the median WMH volume was 12.17 ml (IQR 8.54 to 19.86) excluding and 14.87 ml (IQR 10.02 to 38.03) including the baseline and any new stroke lesions (difference Z=-4.937, p<0.001). Including/excluding just lacunes alone at baseline or follow-up also made small but significant differences (Table 5.6).

Restricting the analysis to just the 33 patients with stroke lesions at either time point, or the 26 patients with a stroke lesion but no lacunes, or the 7 patients with lacunes (who all also had stroke lesions) gave similar results for the proportional difference in WMH volume between including and excluding stroke lesions and lacunes as for all 46 patients (Table 5.7-5.9). However, the absolute true WMH volumes were larger in patients with a stroke lesion (e.g. baseline WMH volume 10.15 ml, IQR 6.51 to 18.13, Table 5.7) than in those without (e.g. baseline WMH volume 6.63 ml, IQR 4.62 to 9.47, Table 5.10). When we adjusted for inter-subject differences in intracranial volume, the pattern of results was the same.

Amongst all 46 patients, WMH volume increased in 43 and decreased in 3 patients between baseline and follow-up (range -1.94 ml to 33.16 ml) when stroke lesions were excluded. When stroke lesions were included, 40/46 patients had an increase and 6 had a decrease in WMH volume although the median WMH volume progression excluding stroke lesions did not differ significantly from that including stroke lesions (difference Z=-1.831, p=0.067, Table 5.6). However, the WMH progression was considerably different from patient to patient whether including or excluding stroke lesions, with the

potential difference in WMH volume progression being huge, ranging from -35.78 ml to 78.79 ml (Figure 5.1, 5.2) or between -208.75% to 163.83% of the baseline WMH volume, as shown in the increasing length of the IQRs, from WMH volume excluding stroke lesions (e.g. 11.77, Table 5.7) to including stroke lesions in the WMH volume (e.g. 23.47, Table 5.7). Thus including the stroke lesions adds substantial noise to the measurement of baseline, follow-up and progression of WMH volume.

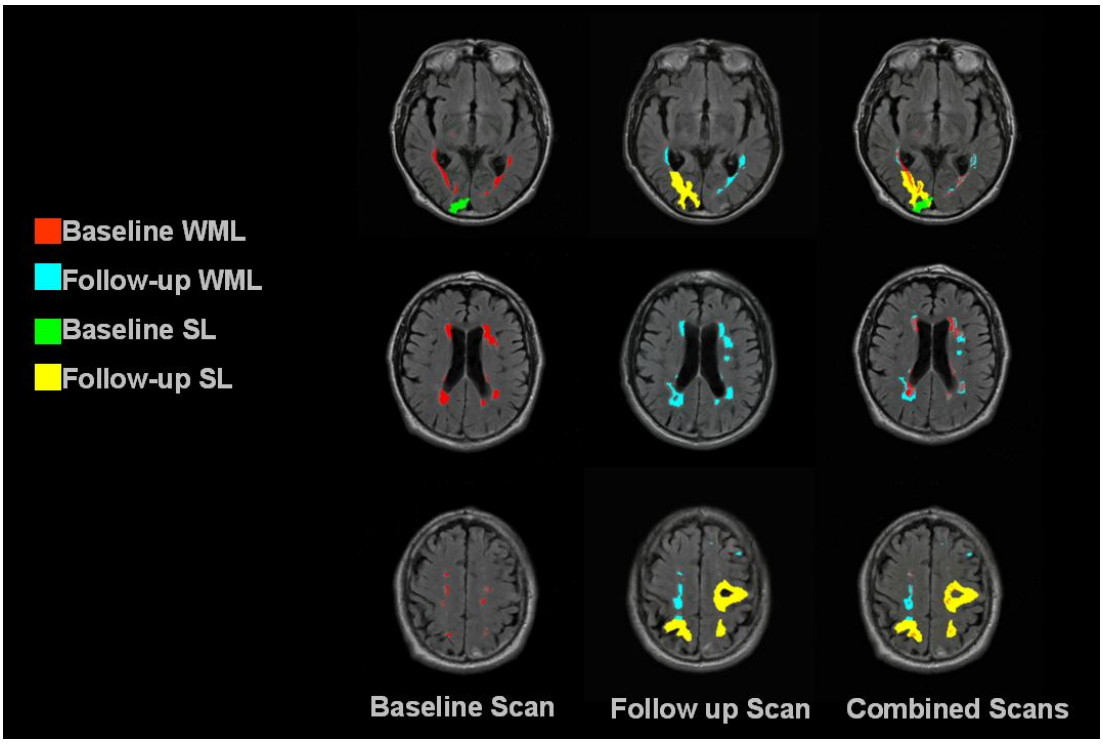

Figure 5.2 Three slices from the same patient showing the influence of stroke lesions (SL) at baseline and new stroke lesions appearing during follow-up on WMH volume measurements at baseline, follow-up and combined scans.

Table 5.6 In all patients with follow-ups (n=46), the results from non parametric tests (Wilcoxon Signed Rank Test) for differences in WMH volume (ml) according to inclusion/exclusion of lacunes or stroke lesions (SL).

Measurement (n=46)	Median	IQR	Length of IQR	Signed Rank for difference with WMH only	p-value
WMH only					
Baseline	8.54	5.86 to 15.80	9.94	-	-
Follow-up	12.17	8.54 to 19.86	11.32	-	-
Progression	3.25	1.22 to 7.59	6.37	-	-
WMH + lacunes					
Baseline	8.54	5.86 to 15.80	9.94	-2.371	0.018
Follow-up	12.19	8.54 to 19.86	11.32	-2.366	0.018
Progression	3.27	1.22 to 7.69	6.47	-1.690	0.091
WMH + SL					
Baseline	10.98	6.91 to 24.86	17.95	-5.012	<0.001
Follow-up	14.79	10.02 to 38.03	28.01	-4.937	<0.001
Progression	4.71	1.17 to 10.86	9.69	-1.831	0.067
WMH + lacunes + SL					
Baseline	10.98	6.91 to 25.00	18.09	-5.012	<0.001
Follow-up	14.87	10.02 to 38.67	28.65	-4.937	<0.001
Progression	4.69	1.17 to 10.92	9.75	-1.885	0.059

Table 5.7 In 33 patients with visible stroke lesions (SL) on MRI, the results of non parametric tests (Wilcoxon Signed Rank Test) for differences in WMH volume (ml) according to inclusion/exclusion of lacunes or SL.

Measurement (n=33)	Median	IQR	Length of IQR	Signed Rank for difference with WMH only	p-value
WMH only					
Baseline	10.15	6.51 to 18.13	11.62	-	-
Follow-up	13.93	9.93 to 24.74	14.81	-	-
Progression	3.36	1.35 to 7.64	6.29	-	-
WMH + lacunes					
Baseline	10.61	6.51 to 18.28	11.77	-2.371	0.018
Follow-up	14.04	9.93 to 24.83	14.9	-2.366	0.018
Progression	3.43	1.35 to 7.70	6.35	-1.690	0.091
WMH + SL					
Baseline	18.46	8.30 to 31.77	23.47	-5.012	<0.001
Follow-up	24.87	12.49 to 39.25	26.76	-4.937	<0.001
Progression	5.13	1.71 to 12.18	10.47	-1.831	0.067
WMH + lacunes + SL					
Baseline	18.46	8.31 to 31.77	23.46	-5.012	<0.001
Follow-up	24.87	12.51 to 39.52	27.01	-4.937	<0.001
Progression	5.13	1.71 to 12.24	10.53	-1.885	0.059

Table 5.8 In 26 patients with no lacunes but with visible stroke lesions (SL) on MRI, the results of non parametric tests (Wilcoxon Signed Rank Test) for differences in WMH volume (ml) according to inclusion/exclusion of SL.

Measurement (n=26)	Median	IQR	Length of IQR	Signed Rank for difference with WMH only	p-value
WMH only					
Baseline	9.06	6.02 to 15.80	9.78	-	-
Follow-up	12.30	8.54 to 19.86	11.32	-	-
Progression	2.74	1.30 to 7.45	6.15	-	-
WMH + SL					
Baseline	15.77	7.82 to 25.34	17.52	-4.557	<0.001
Follow-up	21.56	12.06 to 37.16	25.1	-4.373	<0.001
Progression	4.95	1.74 to 13.38	11.64	-1.867	0.062

Table 5.9 In seven patients with lacunes (who all also had stroke lesions: SL), the results of non parametric tests (Wilcoxon Signed Rank Test) for differences in WMH volume (ml) according to inclusion/exclusion of lacunes or SL.

Measurement (n=7)	Median	IQR	Length of IQR	Signed Rank for difference with WMH only	p-value
WMH only					
Baseline	18.14	10.15 to 37.39	27.24	-	-
Follow-up	25.67	13.51 to 49.18	35.67	-	-
Progression	5.93	3.36 to 11.80	8.44	-	-
WMH + lacunes					
Baseline	18.70	10.61 to 37.68	27.07	-2.371	0.018
Follow-up	26.35	14.04 to 49.61	35.57	-2.366	0.018
Progression	5.94	3.43 to 11.93	8.50	-1.690	0.091
WMH + SL					
Baseline	27.01	13.57 to 73.88	60.31	-2.366	0.018
Follow-up	38.55	14.61 to 50.14	35.53	-2.366	0.018
Progression	9.10	1.04 to 11.60	10.56	-0.338	0.735
WMH + lacunes + SL					
Baseline	27.57	13.74 to 74.05	60.31	-2.366	0.018
Follow-up	39.08	14.77 to 50.57	35.8	-2.366	0.018
Progression	9.12	1.03 to 11.73	10.70	-0.338	0.735

Table 5.10 In the 13 patients without visible stroke lesions (SL) on MRI, who all did not have lacunes, the results of Median, Minimum (Min) Maximum and IQR of WMH volume (ml).

WMH only (n=13)	Median	Minimum	Maximum	IQR
Baseline	6.63	3.10	36.22	4.62 to 9.47
Follow-up	9.19	4.00	69.38	6.35 to 12.57
Progression	3.13	-1.94	33.16	0.16 to 6.46
WMH relative change	61.34	-17.68	155.98	2.64 to 100.82

Effect of stroke lesions on atrophy

Among 46 patients, median brain tissue volume excluding the stroke lesions was 1155.16 ml (IQR 1069.97 to 1250.78) at baseline and 1127.66 ml (IQR 1054.82 to 1204.77) at follow-up; including the stroke lesions was 1154.35 ml (IQR 1069.97 to 1250.63) at baseline and 1127.66 ml (IQR 1052.26 to 1204.76) at follow-up. Expressed in terms of brain atrophy, the median brain atrophy volume was 24.49 ml (IQR 12.87 to 54.01) excluding and 24.61 ml (IQR 15.54 to 54.04) including the stroke lesions (Wilcoxon Signed Rank test, $Z=-3.915$, $p<0.001$).

When expressed as a percentage of ICV, the median percentage of brain tissue volume in the ICV excluding the stroke lesions was 81.04% (IQR 79.16% to 83.25%) at baseline and 78.45% (IQR 76.04% to 81.87%) at follow-up; including the stroke lesions was 81.03% (IQR 79.15% to 83.25%) at baseline (Wilcoxon Signed Rank test, $Z=-3.724$, $p<0.001$) and 78.32% (IQR 75.63% to 81.83%) at follow-up (Wilcoxon Signed Rank test, $Z=-4.372$, $p<0.001$).

For 46 patients, the median stroke lesions volume change between baseline and follow-up was 0.00 ml (IQR 0.00 to 0.81). Twenty-two patients had tissue loss due to stroke lesions, the median baseline tissue loss due to stroke lesions was 0.011 ml (IQR 0.00 to 0.24), and this decreased in 3 patients and increased in 19 patients during follow-up to give a median follow-up volume of 0.96 ml (IQR 0.07 to 2.95). For the 22 patients, the median stroke lesions volume change was 0.90 ml (IQR 0.05 to 2.89), with volume differences between true brain atrophy volume (excluding effect of stroke lesions) and apparent brain atrophy volume (including effect of stroke lesions) ranging from 0.05 ml less to 21.25 ml more than the true brain atrophy volume. This

represents up to 1.65% of the baseline brain tissue volume, or up to 4-fold more than true brain atrophy (Figure 5.3).

For all 46 patients, the median progression of brain atrophy as a percentage of ICV was 1.73% (IQR 0.92% to 3.55%) excluding versus 1.77% (IQR 1.03% to 3.56%) including the stroke lesions. For the 22 patients with tissue loss due to the stroke lesions, the median brain atrophy as a percentage of ICV was 2.03% (IQR 1.35% to 4.50%) excluding versus 2.03% (IQR 1.44% to 4.94%) including the ISL.

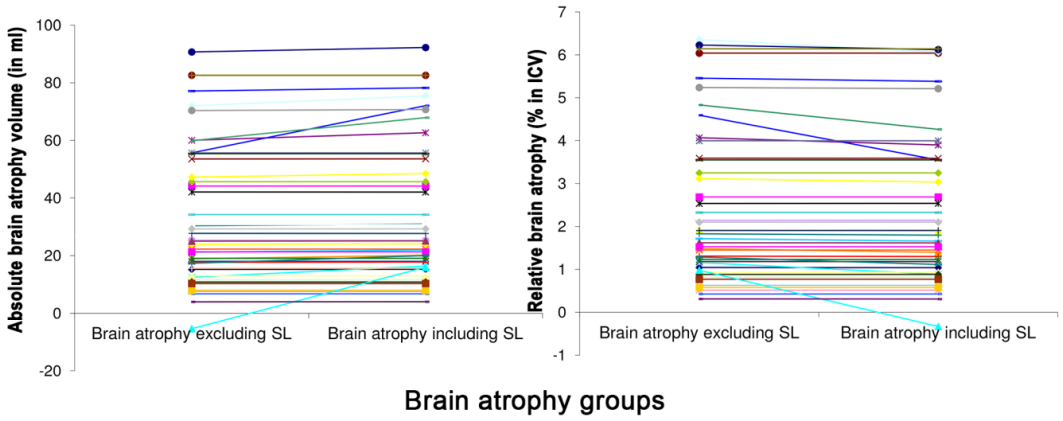

Figure 5.3 Estimation of absolute and relative brain atrophy excluding and including the stroke lesions (SL).

Effect of stroke lesions on sample size in studies of WMH as an outcome measure

We estimated sample size for a trial of the effect of a drug on WMH progression, assuming a 20% reduction in WMH progression with active drug, from 30% in the control group to 24% in the treated group. At 80% power and alpha of 0.05, the trial would require 1730 patients based on WMH volume excluding stroke lesions and 3623 patients if the stroke lesions were included in the WMH volume, this difference being largely driven by the larger IQR of WMH volume when including the stroke lesions.

5.4 Discussion

WMH and brain atrophy are of increasing interest in studies of ageing, stroke and dementia. In this fairly typical cohort of patients who had originally presented with an acute lacunar or cortical mild stroke, we demonstrated that failure to account for stroke lesions when measuring WMH volume could increase significantly both median baseline and follow-up WMH volume by about 20% and added substantial noise to the measurement of WMH progression. Similarly, for individual patients, failing to consider the stroke lesions when measuring brain atrophy could increase apparent brain volume loss by up to 21.25 ml more than true brain atrophy volume, representing 1.65% of baseline brain volume, or up to 4 times more than true brain atrophy.

As WMH and atrophy are commonly present together in brains of older people (Appelman et al., 2009) as are clinically apparent and silent infarcts (Liou et al., 2010), so failure to exclude stroke lesions from measures of both WMH and atrophy could confound substantially any studies assessing any correlation between risk factors for or treatments to prevent stroke, WMH and delay atrophy. For example, one might think that a drug to prevent cardioembolic stroke was reducing WMH progression when in fact it was preventing recurrent ischaemic stroke but not influencing WMH progression at all.

We demonstrate an important consideration for both cross-sectional and longitudinal studies of WMH, longitudinal studies of brain atrophy and randomised trials of treatments to prevent WMH progression or brain atrophy, by showing that failure to exclude the stroke lesions, even though for example the median stroke lesions volume was small (2.05 ml at baseline,

2.43 ml at follow-up), could lead to very misleading estimates of WMH volumes and brain atrophy. Including the stroke lesions in the WMH volumes adds noise to the WMH data at baseline, follow-up and estimates of progression, resulting in loss of statistical power. Acute or old stroke lesions may be present at entry to a study, may shrink in size or increase and new stroke lesions may appear during follow-up. Thus, for the individual patient, the effect of stroke lesions on WMH volume progression is huge and impossible to predict on an individual basis if stroke lesions are included because of the large negative or positive effects of the stroke lesions change. Reassuringly, the specific effect of lacunes alone on the longitudinal WMH measurements was small and can probably be ignored unless present in large numbers. Including the stroke lesions in measurement of atrophy also adds noise to the brain tissue volume at baseline, follow-up and estimation of progression.

This has important implications for design and in particular for sample size calculations for observational studies and randomised trials using WMH volume, WMH volume progression or brain atrophy as an outcome measure. Statistical power is driven by the IQR, a measure of "noise" in the system, as well as by the absolute difference between groups that one is trying to detect. The added noise from stroke lesions and consequent more than doubling of the sample size would substantially increase trial duration and costs. Failing to exclude stroke lesions from WMH volume measurement could obscure the effect of treatment on WMH progression and mean that potentially effective treatments would be missed in error or make ineffective treatments look as if they were beneficial. Visual WMH rating scales avoid the problem of infarcts contaminating the WMH volume. However, they are less sensitive to small

changes in WMH burden than are WMH volume measures, assuming that the latter are accurate. Use of both WMH visual scores and volumes in a study would help identify discordant volume values that might help avoid confounding of WMH volume by stroke lesions.

The strengths of this study include the use of a representative cohort of patients with a wide range of severities of WMH. The analyst was blinded to all clinical information. We used a carefully tested WMH and CSF volume measurement method (MCMxxxVI) (Hernandez et al., 2010) that combines information from two sequences to reduce errors in WMH and CSF detection. A neuroradiologist identified the infarcts, lacunes and distinguished them from WMH for image processing.

The study limitations include the results may not apply to patients with multiple lacunes as only seven patients had a few lacunes. Our population had more stroke lesions than in similarly-aged subjects without history of stroke, although silent cortical and subcortical stroke lesions and lacunes occur in up to 75% of otherwise asymptomatic older volunteers (Gorelick et al., 2011; Morris et al., 2009). It was difficult sometimes to distinguish the edge of the stroke lesions from the WMH but we performed the analysis blind to all other factors so any bias is likely to be minimal.

Further studies are needed to determine the full magnitude of the effect that stroke lesions and lacunes could have on WMH and cerebral atrophy measurement, find better ways of discriminating between stroke lesions and WMH, and between tissue loss due to stroke lesions and true brain atrophy.

Chapter 6 Development and optimization of a Perivascular spaces measurement method

Perivascular spaces (PVS), or Virchow-Robin spaces are pial extensions of the subarachnoid space that surround the walls of arteries, arterioles, veins and venules as they course into the brain parenchyma (Etemadifar et al., 2010; Kwee and Kwee, 2007). PVS function as drainage and fluid circulation pathways for soluble and insoluble material through the central nervous system (Rennels et al., 1985). Many inflammatory processes take place in the PVS, for example they are specific sites for immune cell accumulation, reaction and transmigration into the brain parenchyma (e.g. leukocytes, dendritic cells, T-cells, B-cells and macrophages (Polledo et al., 2012; Sagar et al., 2012; Wuerfel et al., 2008)). We had described the PVS ultrastructure, fluid drainage through PVS, immune cells accumulation and transmigration in the PVS, and inflammatory diseases or small vessel diseases (SVD) related to PVS in detail in Chapter 2 (2.1.5 perivascular space).

The appearances of PVS on imaging may provide evidence of vascular or inflammatory changes in the brain. PVS are round or linear delineated structures seen on magnetic resonance imaging with intensities close to cerebrospinal fluid (CSF) and less than 3mm (Kwee and Kwee, 2007) diameter in cross section (Wardlaw et al., 2013c). PVS on MRI are associated with increasing age, cognitive impairment, cerebral SVD (lacunar stroke and white matter hyperintensities: WMH), multiple sclerosis (MS), and may be related to altered blood brain barrier (BBB) permeability (Doubal et al., 2010b; Maclullich et al., 2004; Potter et al., 2013; Wardlaw, 2010; Zhu et al., 2010). We mentioned the definition of PVS on MRI and their associations with other SVD features in Chapter 1 (1.2.2 PVS).

In following three chapters, we will present the development and optimization processes of a computational method applied to quantify PVS count and volume using 16 test cases (Chapter 6). In Chapter 7, we validated the computational method in 100 mild stroke study cases (the patients' information in given Chapter 3) and compared PVS count/volume generated in the PVS computational method with the visual rating results from a validated visual rating scale (Maclullich et al., 2004). In Chapter 8 we will explore the associations between PVS and other SVD features (e.g. WMH and atrophy), blood markers, and BBB permeability.

6.1 Introduction

Perivascular spaces (PVS) on magnetic resonance imaging (MRI) are commonly assessed using visual rating scales, and several different rating scales have been proposed (Chen et al., 2011; Doubal et al., 2010b; Maclullich et al., 2004; Patankar et al., 2005; Potter, 2011; Rouhl et al., 2008; Zhu et al., 2010). These scales differ in how they score the anatomical location or range of PVS, as summarized in Table 6.1 (all tables in this chapter are in section 6.6 Tables). Potter (Potter, 2011) reviewed and evaluated the ambiguities and advantages in these existing PVS visual rating scales and combined their strengths to develop a more comprehensive visual rating scale (available at http://www.bric.ed.ac.uk/documents/epvs-rating-scale-user-guide.pdf). This new scale used standard T2-weighted (T2W) structural brain MRI to assess the severity of the PVS located in three major anatomical regions (midbrain: MB, basal ganglia: BG and centrum semiovale: CS) and tested its observer variability (Potter, 2011).

All existing rating scales have similar limitations: limited range of PVS, ceiling and floor effects, subjective and are therefore prone to intra- and

inter-observer differences. These limitations could be overcome by the use of computational methods, which may provide more precise PVS number and also allow their size/volume to be measured. Such methods could be useful for more subtle measurements and analyses, for example calculating the percentage of PVS volume in the total brain volume and investigating an association between PVS volume and white matter hyperintensities (WMH) volume.

To our knowledge, few studies have described any computational methods suitable for PVS quantification (Descombes et al., 2004; Uchiyama et al., 2008; Wuerfel et al., 2008). Our systematic review found six studies that used computational methods to assess PVS and four studies that presented approaches with potentials for quantifying PVS (Hernandez et al., 2013). Though these computational methods were promising, they have not been widely used in the target population of patients with small vessel disease, and maybe computational intense and time consuming for large clinical studies.

In this chapter, we present a user-friendly computational method for counting the number and measuring the volume of PVS useful in large clinical research studies. This method was based on the best knowledge from a validated visual rating scale regarding standard slice selection in the BG and the CS regions (Potter, 2011). We developed the method and tested the intra- and inter-observer agreement of this computational method. We describe thresholds that work in most cases, and describe refinements for assessing more difficult cases.

6.2 Methods

6.2.1 Sample selection

For developing and testing the computational approach, the imaging datasets for 16 subjects were randomly chosen from The Lothian Birth Cohort 1936 (LBC1936) Study (http://www.lothianbirthcohort.ed.ac.uk/) to represent a full range of PVS, WMH, lacunes, and brain atrophy based on previous analyses (Deary et al., 2007).

6.2.2 Brain MRI acquisition

All MRI acquisition was conducted in the Brain Research Imaging Centre, University of Edinburgh (http://www.bric.ed.ac.uk). A GE Signa Horizon HDx 1.5T clinical scanner (General Electric, Milwaukee, WI), equipped with a self-shielding gradient set and manufacturer-supplied eight-channel phased-array head coil, was used to acquire T2W, T1-weighted (T1W), gradient echo (GRE) and fluid attenuation inversion recovery (FLAIR) datasets amongst other sequences. Full details of the MRI protocol for this study had been published previously (Wardlaw et al., 2011). The characteristics of the sequences relevant for assessing PVS in this chapter are summarised in Table 6.2.

6.2.3 Standard image preprocessing steps

Registration

PVS on MRI are defined as 'sharply delineated round or linear structures of intensity similar to that of cerebrospinal fluid (CSF) and less than 3mm in axial diameter' (Kwee and Kwee, 2007; Wardlaw et al., 2013c). The main sequence used to identify PVS was T2W images (Kwee and Kwee, 2007). T1W and FLAIR images were also used as references to differentiate PVS

from other lesions such as WMH, infarcts and lacunes (Groeschel et al., 2006). The base sequence for our technique was the T2W sequence. T1W and FLAIR, were rigidly registered to the corresponding T2W volumes using FLIRT software (FMRIB Linear Registration Tool) (Jenkinson et al., 2002) from the FMRIB Software Library (FSL, University of Oxford, UK), available at http://fsl.fmrib.ox.ac.uk/fsl/fslwiki/.

Generation of intracranial volume (ICV) mask

In order to reduce the intensity difference between non-brain tissue and brain tissue, the ICV was manually masked out from the skull on the GRE images using the Object Extraction Tool based on a region-growing algorithm in Analyze™ 10.0 (Analyze Direct, Inc. Overland Park, KS, USA). False positives were removed manually. The steps in the ICV segmentation had been described in Chapter 3 and a detailed ICV segmentation manual is in the appendix (see Appendix B1 Intracranial volume segmentation Manual).

6.2.4 Development and optimization of the multi-stage PVS segmentation method

We used 'Object Counter' function in the Analyze™ 10.0 software to develop our segmentation technique. Figure 6.1 (all figures in this chapter are all in section 6.5 Figures) schematically represented all the steps that we applied in the method development and optimizations: the steps with solid outline were ultimately included in the final procedure for general PVS segmentation and full details of each step in Figure 6.1 are in the Appendix E1 (Detailed perivascular spaces segmentation steps in Figure 6.1).

PVS are commonly seen in the BG and CS (Kwee and Kwee, 2007) as these regions are highly vascularised. Based on a carefully developed and

evaluated clinical PVS visual rating scale (Potter, 2011), we selected a representative slice in the BG and CS. In the BG, we chose the slice that contains at least one characteristic BG structure (i.e. caudate nucleus, internal capsule, thalamus, lentiform nucleus, external capsule and insular cortex) and also usually shows the most PVS. In the CS, we chose a slice between the superior aspect of the bodies of the lateral ventricles and the subcortical white matter near the vertex (see Figure 6.2). Tests of intra- and inter-observer reliability (both visual rating and computational identification) showed high variability in the identification of the elongated PVS that are common in the CS and outer regions of the BG slice (Figure 6.3). Therefore, we restricted our assessment to bilateral ovoid regions on the BG slice, one in each hemisphere, delineated by the vertical ramus of the lateral fissures and the posterior segment of the lateral fissures as shown in Figure 6.2.

Analysis of the intensity distribution in the T2W images revealed that PVS have intensity levels ranging from 0.3 to 0.9 that vary even within the same subject, presumably due to factors such as partial volume averaging (Hernandez et al., 2013), making it unfeasible to assess PVS using a single threshold without any intensity adjustment. Therefore we performed a linear intensity adjustment in 3 stages: normalisation, gamma correction and linear mapping. The general equation for the gamma correction is:

$$i'_{(x,y,z)} = I_{\max} * \left(\frac{i_{(x,y,z)} - I_{\min}}{I_{\max} - I_{\min}} \right)^{(gamma + I_{\min})} \qquad (1)$$

where I_{max} and I_{min} are the maximum and minimum intensity levels and $i'_{(x,y,z)}$ and $i_{(x,y,z)}$ are the resultant and initial intensity levels for a voxel identified by the coordinates (x,y,z). Initially we used a linear intensity transformation (gamma equal 1) saturating the 1% of the lowest and highest intensities at the

minimum and maximum values respectively. However, it was necessary to transform the intensity levels quadratically to successfully apply one threshold on each of the test cases. This was achieved doing a voxelwise product of the intensity-adjusted-T2W image with itself, or, as I_{min} was zero, using a gamma correction factor of 2.

We performed additional tests to try to improve PVS segmentation such as combining T1W and T2W images and manually excluding lacunes (steps outlined by dotted lines in Figure 6.1).

6.2.5 Observers and analysis

Two observers (Ob1, Ob2) measured the PVS count and volume using Analyze™ 10.0 software. I'm the Ob1 had worked with clinical brain imaging for more than 2 years and designed and tested each step in this method , and Ob2 is an undergraduate medical student worked with brain imaging for 6 weeks and helped to test Step 2, 3 and 5 in this method (Figure 6.1). We both did the PVS measurement twice but on two separate occasions. I used the same standard slices both times. Ob2 was blinded to the standard slice number chosen by me for the first measurement, and was unblinded for the second measurement. Ob1 was a more experienced analyst; Ob2 did not have long time image analysis training. Bland-Altman plots (Bland and Altman, 1986) were used to estimate the agreement within or between observers on each stage.

6.3 Results

In the results section, we will show how we managed to increase method consistency and reduce numbers of thresholds. We summarized the work flow for the final optimized method.

6.3.1 Observer variability and optimization

Observer variability

After we applied multiple thresholds in step 2, we visualized the locations for intra- and inter- observer variability in the Figure 6.3. Three different PVS masks were selected as an example. This method was helpful in picking up the dots in the two ovoid regions of the BG, but was not effective in picking up the linear-shaped PVS in the CS.

For comparing the observer variability, we also calculated the mean and standard deviation (SD) of the PVS results and generated the Bland-Altman plots. Both observers had higher intra- and inter-observer variability on the PVS volume and count measurements in the BG regions than in the CS regions (large SD). Ob2 tended to measure less than Ob1 in the BG region, and more in the CS region for PVS volume and count measurements, tables of observer variability, Bland-Altman plots and locations for observer variability are in the Appendix F (Observer agreement in the PVS method development and validation).

In order to diminish the observer variability and increase the consistency, we restricted the regions of interest (ROI) to the bilateral ovoid regions in the BG regions for further method optimization (Figure 6.2).

Efficiency of restricting ROI into BG regions

For the PVS count measurements, after restricting the regions of interests specifically to the two BG ovoid regions (BG ROI), both intra- and inter-observer variability were less (smaller SD, Table 6.3) and the discrepancy range were smaller compared with measuring the whole BG slice (Appendix F).

6.3.2 Threshold optimization

We used intensity adjusted T2W image (T2W-ia) in the optimization step. We aimed to use only one threshold rather than multiple thresholds for each patient in the PVS segmentation and find a pattern of thresholds.

Tests such as combining T1W-ia and T2W-ia images and manually excluding lacunes were not successful in reducing numbers of thresholds (steps outlined by dotted lines in Figure 6.1, results in the Appendix G: Results from unsuccessful steps in the PVS method development and optimization).

A voxelwise product of the T2W-ia image with itself was able to reduce number of threshold into one. We also identified a general pattern that involved the use of three optimum thresholds, each one to be applied according to the T2W image characteristics of the individual patient as follows:

(1) Low Threshold (7.5% of maximum intensity) was suitable for a patient that had scattered PVS, a uniform, visually normal intensity background, and few focal lesions such as WMH or lacunes (1/16 case).
(2) High Threshold (15% or above of maximum intensity) was suitable for patients that either had grouped PVS, or a high background signal, or many

other lesions (WMH, lacunes, mineral deposits), or with poor scan quality, for example from patient movement (8/16 cases).

(3) Medium Threshold (11.25% of maximum intensity) was suitable for patients that did not have the characteristics requiring use of either low or high thresholds (7/16 cases).

6.3.3 Final optimized PVS segmentation method

The final procedure for general PVS segmentation was determined to be:

1. Chose the standard slice in the BG region.
2. Apply intensity adjustment to the T2W image.
3. Combine two T2W intensity adjusted images.
4. Set the region of interests into two BG ovoid regions (BG ROI).
5. Apply one threshold (Low, Medium or High) according to the image characters. T1W and FLAIR images would be used as reference image.
6. For difficult and complicated cases, another threshold or the same threshold plus manual editing should be applied.

For most of the cases, the final PVS segmentation would take 8 to 13 minutes per case in total, and for complicated cases, it might need 5 to 20 more minutes including the application of multiple thresholds or further manual editing (Figure 6.4).

6.4 Discussion

This semi-automatic threshold-based method was promising for measuring BG PVS volume, and could be a complementary method to existing visual rating scales. The method also showed promises for counting PVS number automatically rather than manually, decreasing the amount of counting time and reducing counting errors. We also provided ways of dealing with difficult and complicated cases, by increasing the number of threshold or by manual editing.

This method has limitations. The final optimized method only focused on the PVS in the BG region. It was harder to choose the CS standard slice at the first stage. Moreover, the shapes of the PVS in the CS region were not consistent, either linear or round shape, influenced by the vessels running in various directions. Finally, it was more frequent to have a high background signal caused by the diffuse hyperintensive lesions in the CS region than in the BG region which influenced the PVS detection. CS volume and count were deemed to be too variable to develop further at this point. This method requires manual editing and the efficiency in picking up the PVS largely depends on the skills of observers and the quality of the images. There is the potential for developing fully automated software based on the object-approach mechanism described by (Descombes et al., 2004).

A further comparison is needed to prove the efficiency of this method, by comparing results from this method with validated PVS visual rating scores (in Chapter 7). A study of the associations between PVS and WMH, cerebral atrophy, blood markers, and the BBB permeability would be useful to provide critical evidence in the study of small vessel disease mechanisms (in Chapter 8).

6.5 Figure

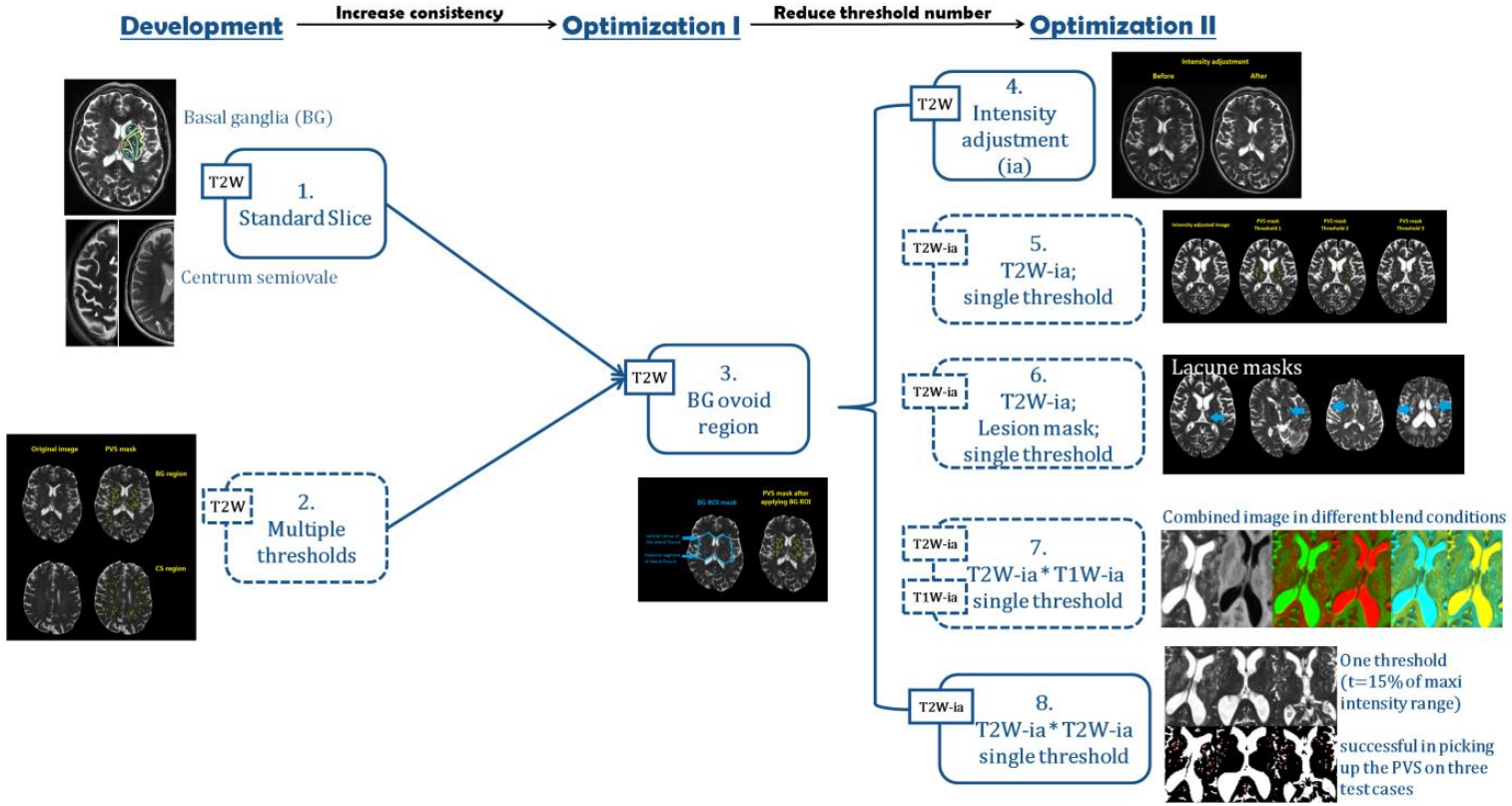

Figure 6.1 Steps in a multi-stage PVS segmentation approach.

Abbreviations: BG, basal ganglia; T2W, T2-weighted image; T1W, T1-weighted image; ia, image after intensity adjustment. The solid lines are the steps included in the final procedure for PVS segmentation method and dotted lines are steps tested in the development stage but not included in the final procedure.

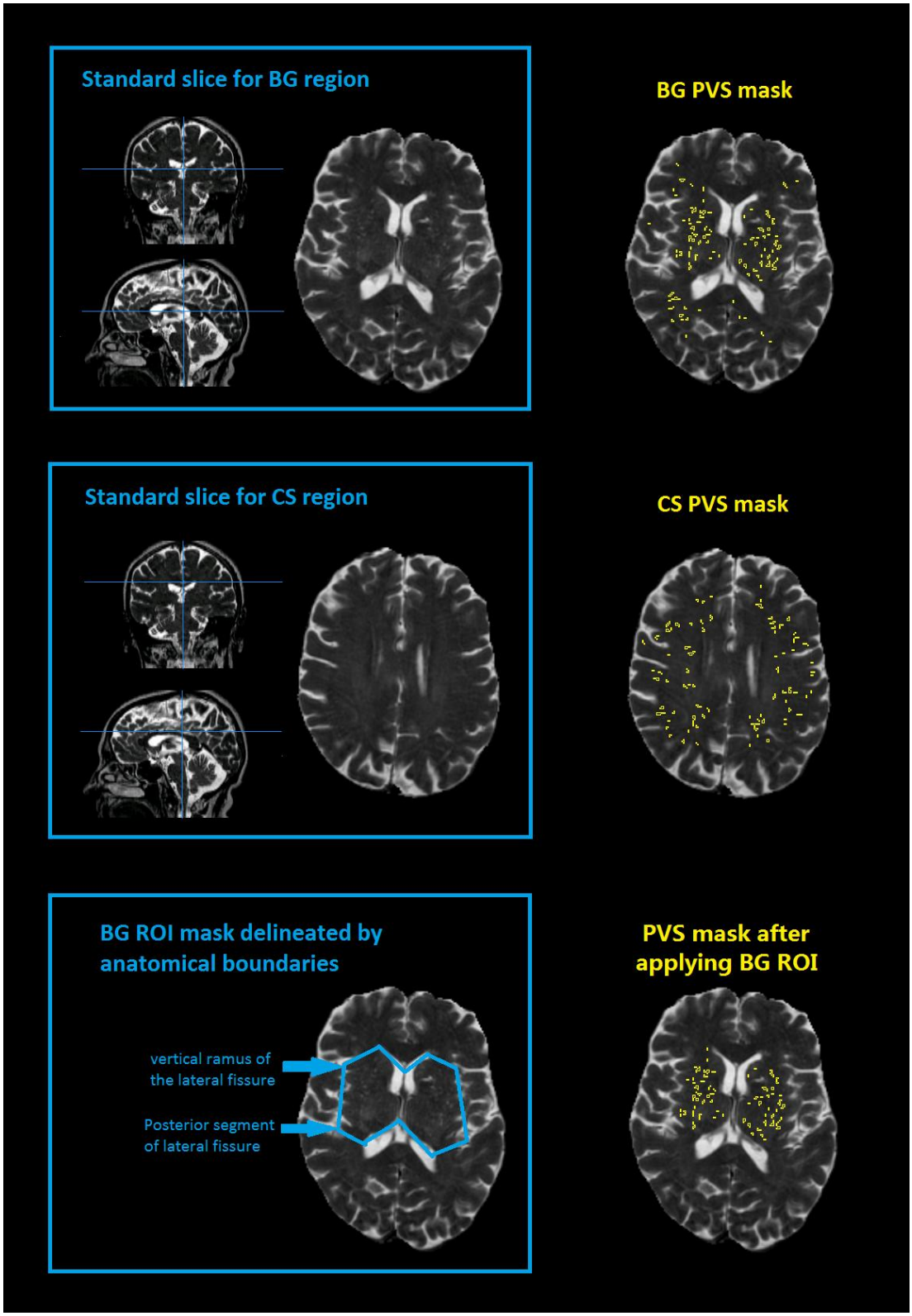

Figure 6.2 Standard slices for the BG and CS regions, and regions of interest (ROI) specifically to the BG regions delineated by anatomical boundaries.

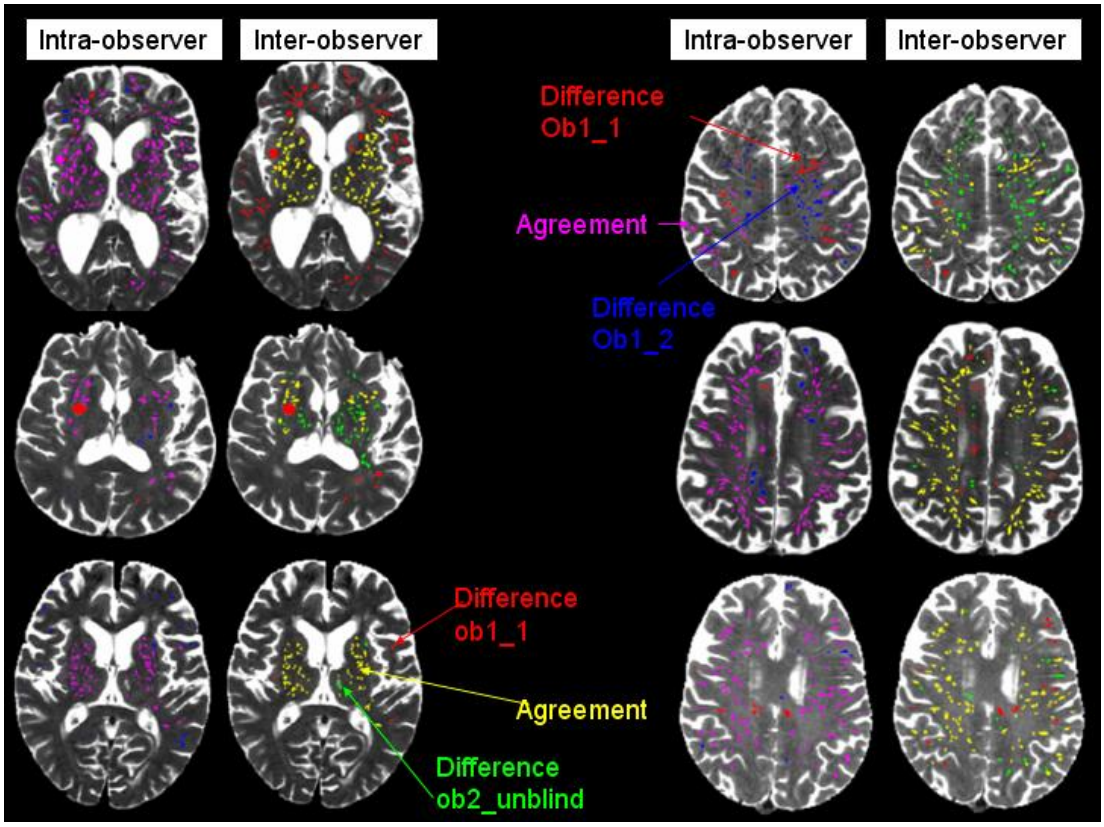

Figure 6.3 Location of intra- and inter-observer variability in the BG (Left) and CS (Right) regions.

On the left side, the first row demonstrates the intra-observer variability; the second row demonstrates the inter-observer variability of the PVS in the BG region. The images on the right show the intra- and inter-observer variability in the CS region. Dots in red indicate the PVS selected by Ob1 only for the first time but not for the second time. Dots in blue indicate the PVS selected by Ob 1 for the second time only. Dots in violet (the merged colour of red and blue) show the PVS selected by Ob1 for both time points, which represent the consistency of measurements within Ob1. Therefore the red and blue dots indicate the locations of intra-observer variability. The dots in green indicate the PVS selected only by Ob2 when unblinded to the standard slice number chosen by Ob1. The dots in yellow are the overlapping PVS selected by both observers, showing the consistency between observers. The red and green dots indicate the locations of inter-observer variability.

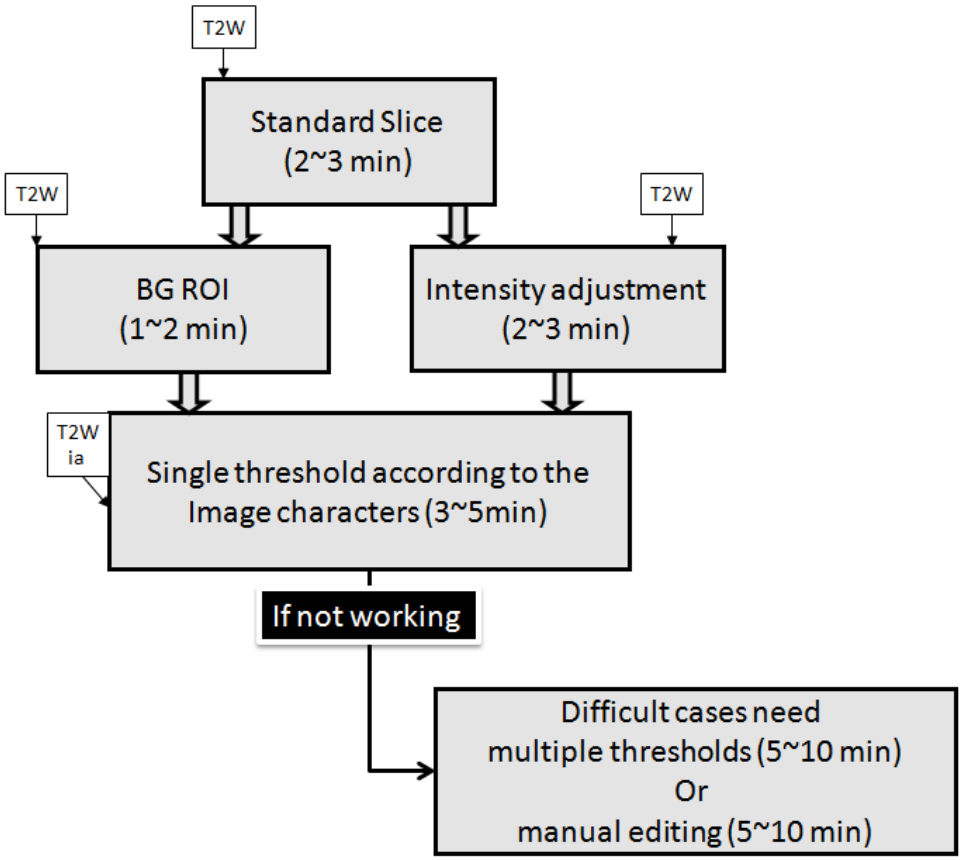

Figure 6.4 Illustration of final optimized PVS segmentation method.

Abbreviations: BG, basal ganglia; T2W, T2-weighted image; T2W ia, T2-weighted image after intensity adjustment.

6.6 Tables

Table 6.1 Anatomical location and range of PVS in commonly used rating scales.

The table was extracted from Potter's work of developing and validating a comprehensive visual rating scale (Potter, 2011).

Author-Year	Anatomical location	Scale and Range of PVS
Heier et al. , 1989	Lenticulostriate;	1-3 Mild; Moderate; Marked
	High convexity	<2mm 1 Mild
		2-3mm 2 Moderate
		>3mm 3 Marked
		>4mm upgrade to next level
Elster and Richardson, 1991	MB	Absent
		Present (1)Unilateral; (2)Bilateral
Adachi et al. , 2000	BG	0-3
		0=none lesions
		1=1-5
		2=6-10
		3>10
Di Costanzo et al. , 2001	Lenticulostriate;	1-3
	High convexity	<2mm 1
		2-3mm 2
		>3mm 3
Maclullich et al. , 2004	CS;	0-4
	BG;	0=none lesions
	Hippocampus	1=<10
		2=11-20
		3=21-40
		4=>40
Patankar et al. , 2005	CS;	0-5
	MB;	
	Subinsular;	
	BG scheme 1;2	
Groeschel et al. , 2006	Supratentorial white matter;	Dilated
	BG	Not dilated
Rouhl et al. , 2008	BG;	Low; Moderate; High
	CS round/oval;	Low <20
	CS linear	Moderate 20-50
		High >50

MB: midbrain; BG: basal ganglia; CS: centrum semiovale.

Table 6.2 Characteristics of the MRI sequences used in this study.

Study	LBC1936 Study (Wardlaw et al., 2011)
TR/TE/TI (ms)	9.7/3.984/500 (T1W)
TR/TE (ms)	940/15 (T2W)
TR/TE/ TI (ms)	9000/140/2200 (FLAIR)
Pixel bandwidth (KHz)	15.63 (T1W)
	12.5 (GRE)
	15.63 (FLAIR)
Matrix	192 x 192 (T1W)
	256 x 192(T2W)
	256 x 256(FLAIR)
Number of slices	160 (T1W)
	80 (T2W)
	40 (FLAIR)
Slice thickness (mm)	1.3 (T1W)
	2 (T2W)
	4 (FLAIR)
Inter-slice gap (mm)	0
Voxel size (mm^3)	1.3 x 1.3 x 1(T1W)
	1 x 1 x 2 (T2W)
	1 x 1 x 4 (FLAIR)

ms: millisecond; KHz: kilohertz; mm: millimetre; mm3: cubic millimetre.

Table 6.3 The effect of BG ROI mask in increasing PVS measurement consistency.

PVS count	Without BG ROI mask		With BG ROI mask	
	Mean	SD	Mean	SD
Intra (Ob1)	72.50	28.65	49.88	15.88
Intra (Ob2)	56.69	10.55	51.06	10.27
Inter (blinded)	-15.88	24.47	1.12	13.12
	-18.12	25.89	-0.50	13.36
Inter (unblinded)	-13.50	24.58	2.87	12.55
	-15.75	25.26	1.25	12.15

SD: standard deviation; BG: basal ganglia; BG ROI: basal ganglia regions of interests; Ob: observer.

Chapter 7 Validation of Perivascular spaces measurement method

7.1 Introduction

In chapter 6, we developed a computational perivascular spaces (PVS) method based on a validated PVS visual rating scale (Potter, 2011) and tested intra- and inter-observer variability. We included two regions for method development: basal ganglia (BG) and centrum semiovale (CS), and we found CS PVS were harder to quantify and had higher observer variability than in the PVS in the BG ovoid regions. Therefore, our final computational PVS method only included the BG ovoid regions which take about 10 minutes on average per case, and more time for further manual editing or multiple thresholds application for complicated cases. In this chapter, we will test the accuracy of this method in a larger sample by comparing its results (PVS count and volume) with the PVS visual rating scores (Maclullich et al., 2004; Potter, 2011).

7.2 Method

7.2.1 Patient information

We used the imaging data from 100 patients who participated in the BBB permeability study, the information about patients' recruitment and brain imaging procedure is given in Chapter 3. We applied the PVS final segmentation method (Figure 6.4 in Chapter 6) to measure PVS count and volume in the baseline scans of these 100 patients and in 46 of whom had follow-up scanning about three years later. The PVS count is the number of PVS dots appeared in the BG regions, and the PVS volume is the total volume of all these PVS dots, not the averaged volume for each dot which we will use the description 'PVS averaged volume of each dot' to specify .

7.2.2 PVS visual rating

A neuroradiologist rated the PVS in the BG regions as follows: 0=no PVS, 1=<10 PVS, 2=10–20 PVS, 3=21–40 PVS, and 4>=40 PVS, separately in the left and right hemispheres, and an 'overall' score using a scale previously developed by our group (Maclullich et al., 2004; Potter, 2011). PVS visual rating scales were available for all of these cases.

7.2.3 Statistical Analysis

In these 100 patients, we used linear regression to investigate the associations between BG PVS count/volume and BG PVS rating scales. All linear regression analyses were performed in R program version 2.15.2 (http://www.r-project.org/).

We also investigated the agreement of PVS computational results and visual rating results using marginal homogeneity (MH) analysis (MH program, v. 1.2, http://www.john-uebersax.com/stat/margin.htm). PVS computational count was condensed into a 'score' using the same standard as the PVS visual rating scores rating based on (no PVS was 0, less than 10 PVS was 1, 11 to 20 PVS was 2; 21 to 40 PVS was 3, and more than 40 PVS was 4).

7.3 Results

7.3.1 Association between BG PVS volume and BG count

In the 100 cases, BG PVS count increased significantly with BG PVS volume (coefficient of linear regression: 67.266; 95% confident intervals (95%CI): 57.927 to 76.604, Figure 7.1, all figures in this chapter are in section 7.5 Figures).

An increase of one millilitre (ml) in PVS volume leaded to an increase of 67 dots in PVS count. For baseline study, we restricted the analysis to the 46

patients who had follow-up scans, the results are similar and positive relationship still exists (93, 95% confident interval is 74 to 112). Follow-up linear regression results also indicated a high regression trend of PVS count and PVS volume (77, 95% confident interval is 61 to 92).

There was no association between the average size of PVS (here expressed as average PVS volume per count) and the PVS count (Figure 7.1), which is consistent with the visual observation that most PVS on MRI have similar sizes, no matter how few or many there are.

7.3.2 BG PVS count and BG PVS visual rating scores

For baseline 100 patients, BG PVS count increased with overall BG PVS visual score (2.114, 95%CI 1.364 to 2.864). The positive associations remained for comparing BG PVS computational count and left/right BG PVS visual rating scores. The subgroup of 46 patients who had both baseline and follow-up scans showed similar associations at both time points (Figure 7.2 Table 7.1, all tables in this chapter are in section 7.6 Tables).

7.3.3 BG PVS count and BG PVS visual rating scores (MH)

We then investigated the agreement of PVS computational measures and visual rating scores by comparing the BG PVS count and BG PVS visual score using MH analysis, and displayed the frequencies of the condensed PVS score from PVS computational method and PVS visual rating score in histograms. We condensed the raw PVS computational count to match the same scale range as for the PVS visual rating scale: from 0 to 4 (score 0=none PVS dots; 1=1~10 PVS dots; 2=11-20 PVS dots; 3=21-40 PVS dots; 4=>40 PVS dots or with high background intensity).

We found a similar spread of values for PVS computational and visual count scores. Histograms from both scoring systems showed two high frequency peaks. The highest peak at baseline was score 1, and it changed from 1 to 2 during follow-ups suggested the patients had worse PVS rating for follow-up (Figure 7.3).

The visual rating score tended to measure less than the PVS count rating when the number of PVS dots was low and more when the number was high. For example, for baseline BG PVS measurement, the smallest difference between both rating systems was in score 1, and the difference increased as the score increased (score 2 and 3), showed that it was hard to quantify PVS when the numbers of PVS dots increased.

The interval range of visual rating scores was from 0 to 4 but the PVS count scores was from 1 to 3, which suggested the visual rating scores spread better than the condensed scores from the PVS count. The PVS visual rating score showed a wider range implying that the visual rating detects smaller or more subtle PVS change than the PVS computational count score. Alternatively, the visual rating score was an estimate of PVS number not a precise count.

In sum, the histograms (Figure 7.3) show several points: a) for baseline, the computational and visual counts had a very similar distribution with the median score being 1 and second commonest score being 2; b) the difference between the rating systems increased as the score increased indicating that it was harder to quantify larger numbers of PVS; c) the visual rating score tended to measure less than the PVS computational count when there were few PVS and more when there were large numbers of PVS; d) there were

more PVS on the follow-up scans (median score 2 Indicating that agreement continued as the PVS count worsened with progressive SVD.

7.3.4 BG PVS volume and BG PVS visual rating scores

Similar as comparison between BG PVS count and BG PVS visual rating scores in the BG region, there were positive associations between PVS computational volume and visual rating scores (overall BG region, left and right part in the BG regions), for both time points scans (Figure 7.4, Table 7.2).

7.4 Discussion

The present study validated the PVS method we described in Chapter 6 in 100 patients with mild stroke, 46 of whom had follow up scans. We evaluated the associations between PVS count and volume, and PVS visual rating scores. There was significant associations between PVS volume and PVS count in the BG region. However, the average PVS size (PVS volume per count) was not associated with the PVS count, consistent with visual observations that PVS size in general does not vary with number. The PVS computational results (PVS count and volume) also agreed well with a widely used PVS visual rating score.

When the PVS count was converted into the same categories as used in the visual rating score and compared with the PVS visual rating scores, the results showed a similar pattern with a similar spread of curves, interval range and peaks but visual rating scores showed wider dynamic range than computational count converted to scores. The BG PVS count 'scores' (condensed from PVS count) and PVS visual rating scores have very good agreement when PVS are few (<20) but agreement decreases with increasing

number of PVS, a similar problem found with inter-observer agreement for PVS visual rating. Therefore the cases with high background signal or many diffuse WMH being assigned the highest score (score 4) when visually rating PVS to overcome this problem.

Though the current study quantified the PVS in the patients with lacunar or cortical strokes, PVS also appear in MRI scans from young and healthy volunteers who participate as controls for studying the mechanisms of ageing and brain diseases, and so this method should also be tested in normal subjects in further studies.

In the following chapter, I will use the BG PVS results obtained from this chapter to assess the associations between BG PVS count/volume and white matter hyperintensities, cerebral atrophy, CS PVS, blood markers and blood brain barrier permeability.

7.5 Figures

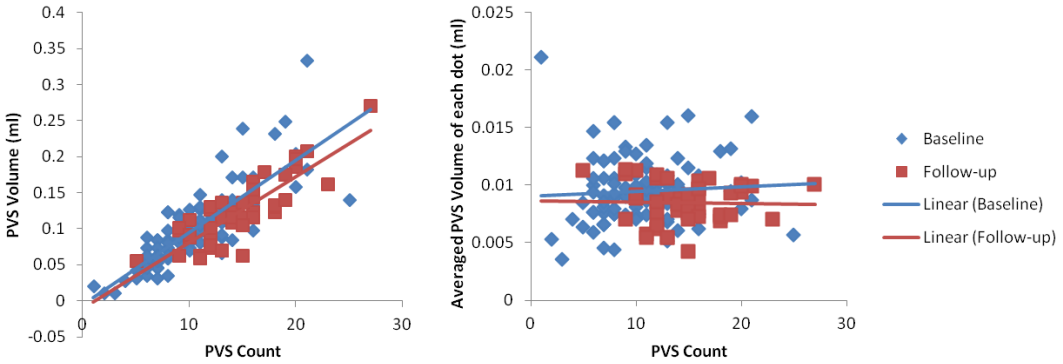

Figure 7.1 Associations between PVS volume (ml) and count in baseline 100 patients.

Left: Positive association between total PVS volume (ml) and count. The x axis represents the PVS count, which means the number of PVS dots obtained from the PVS computational method. The y axis is the total PVS volume expressed in millilitres which also obtained from the PVS computational method. The blue squares are results from baseline 100 patients. The red dots results from 46 of the 100 patients who had follow-up scans. Right: No association between averaged PVS volume and count in both baseline and follow-up. The y axis is the averaged PVS volume expressed in millilitres which is the PVS volume divided by PVS count.

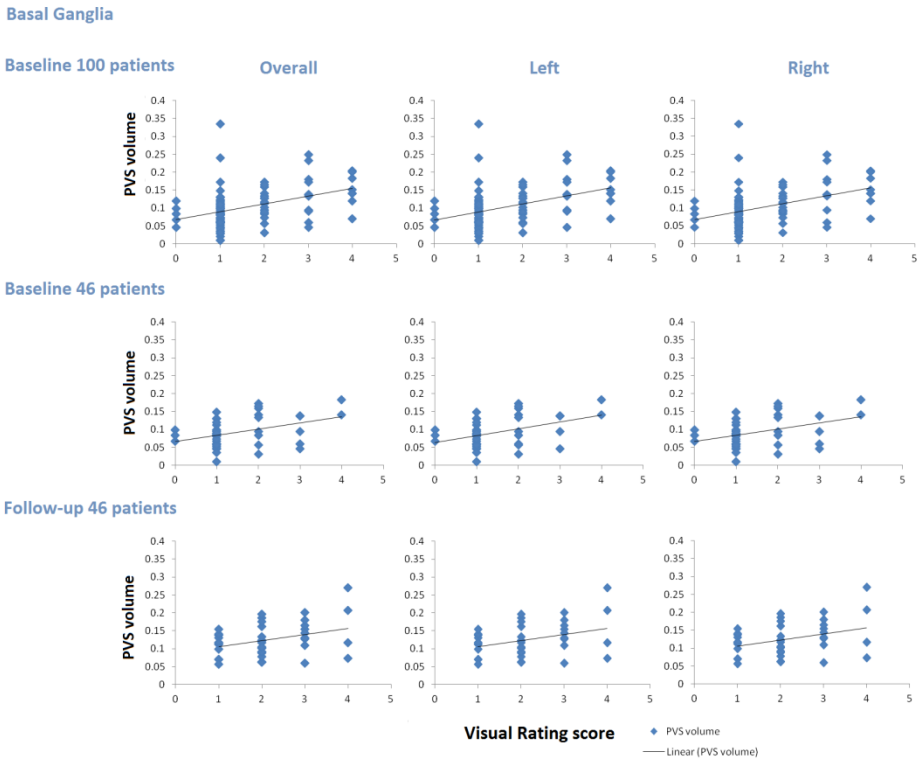

Figure 7.2 Associations between PVS count and PVS visual rating scores in BG region at baseline and follow-up.

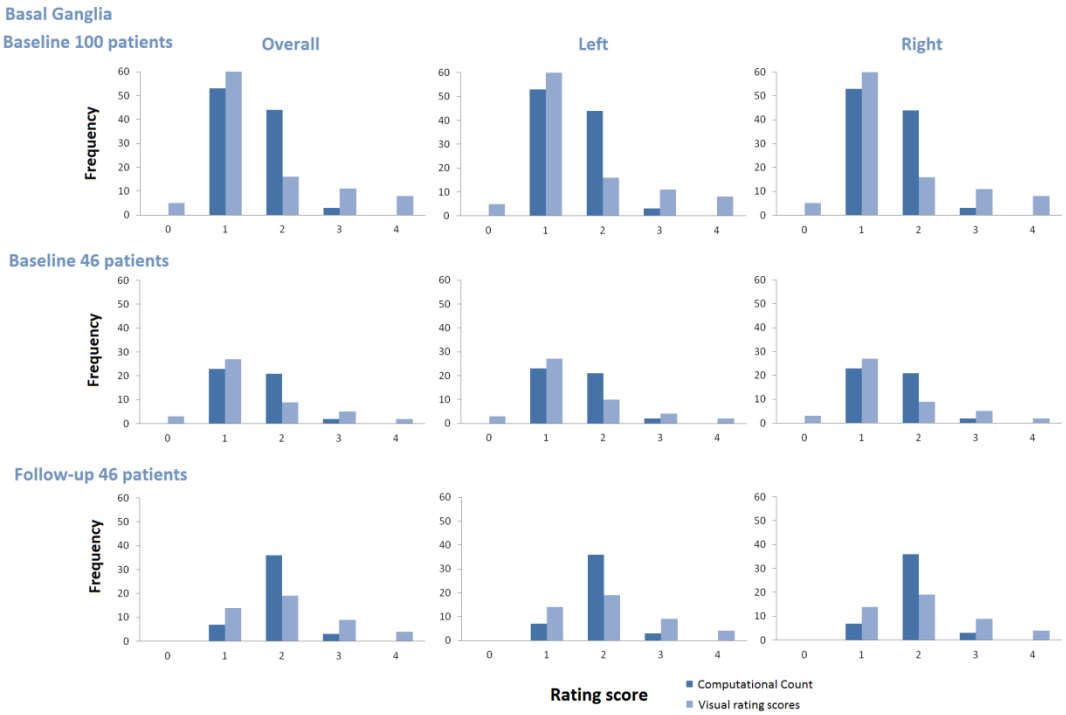

Figure 7.3 Comparison of PVS computational count condensed into a 'score' of similar range to the visual rating categories and PVS visual rating score at baseline and follow-up.

The x-axis in the histograms represents the values of the score intervals. The y-axis represents the frequency of two variables' occurrence. The results of the condensed score from PVS computational count are labelled in dark blue and the results from the PVS visual rating scores are labelled in light blue.

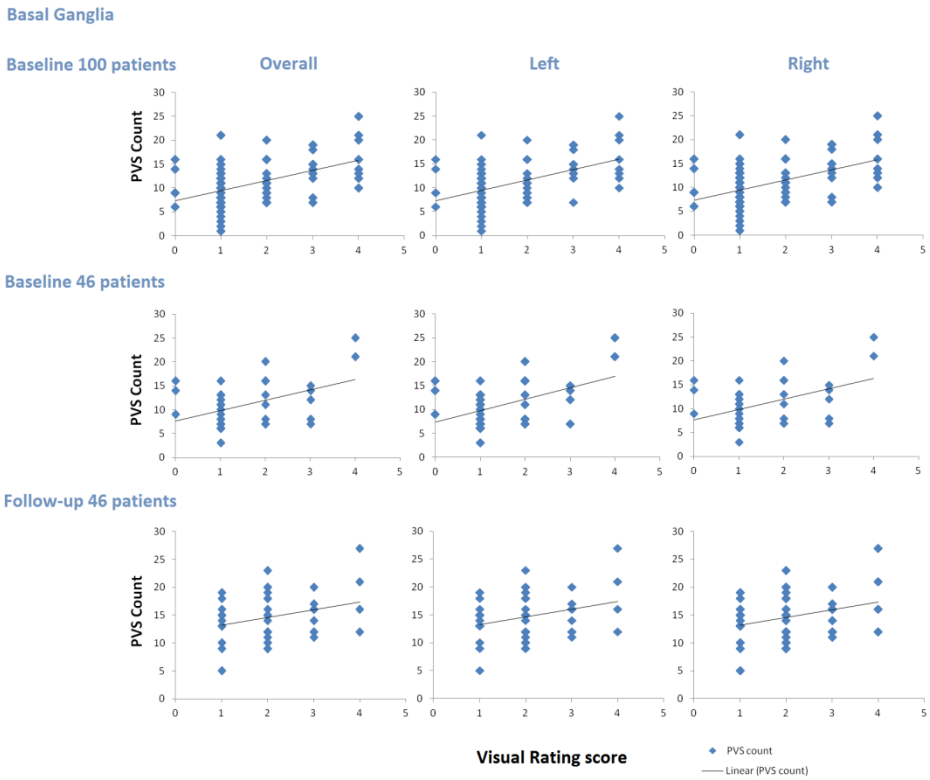

Figure 7.4 Associations between PVS count and PVS visual rating scores in BG region at baseline and follow-up.

7.6 Tables

Table 7.1 Associations between PVS count and PVS visual rating scores for baseline and follow-ups.

Associations	Coefficient	95% Confident Intervals	Coefficient of Variance
Baseline 100 patients			
BG Overall	2.114	1.364 to 2.864	36.291
BG Left	2.179	1.427 to 2.930	36.038
BG Right	2.130	1.372 to 2.887	36.310
Baseline 46 patients			
BG Overall	2.175	0.849 to 3.502	38.042
BG Left	2.372	1.031 to 3.713	37.444
BG Right	2.175	0.849 to 3.502	38.042
Follow-up 46 patients			
BG Overall	1.389	0.102 to 2.677	27.083
BG Left	1.389	0.102 to 2.677	27.083
BG Right	1.389	0.102 to 2.677	27.083

BG: basal ganglia; CI: confident interval; CV: coefficient of variances.

Table 7.2 Associations between PVS volume and PVS visual rating scores for baseline and follow-ups.

Associations	Coefficient	95% Confident Intervals	Coefficient of Variance
Baseline 100 patients			
BG Overall	0.022	0.012 to 0.031	48.638
BG Left	0.023	0.013 to 0.032	48.352
BG Right	0.022	0.013 to 0.032	48.500
Baseline 46 patients			
BG Overall	0.017	0.005 to 0.030	41.092
BG Left	0.019	0.007 to 0.031	40.472
BG Right	0.017	0.005 to 0.030	41.092
Follow-up 46 patients			
BG Overall	0.017	0.003 to 0.031	34.566
BG Left	0.017	0.003 to 0.031	34.566
BG Right	0.017	0.003 to 0.031	34.566

BG: basal ganglia; CI: confident interval; CV: coefficient of variances.

Chapter 8 Associations between PVS and WMH, atrophy, blood markers and BBB permeability

8.1 Introduction

Perivascular spaces (PVS) on magnetic resonance imaging (MRI) is an imaging marker for cerebral small vessel disease (SVD) (Zhu et al., 2010). PVS and other SVD features such as white matter hyperintensities (WMH), atrophy, microbleeds, lacunes and recent infarcts are inter-related (described in Chapter 1 and 2). Increasing numbers of PVS were also associated with blood brain barrier (BBB) permeability and cognitive dysfunction (Wardlaw, 2010).

Dynamic contrast enhancing MRI and contrast agent gadodiamide are used to detect BBB permeability. Gadodiamide (590 daltons) is a small molecule which crossed the abnormal BBB noninvasively (Tofts and Kermode, 1991). The dynamic contrast enhancing MRI was based on the assumption that greater signal enhancement over time links to higher concentration of contrast agent inferring a more severe breakdown of BBB (Armitage et al., 2011).

Apart from brain imaging techniques, blood marker levels in the peripheral circulatory system could be measured and used as markers to reflect endothelial function, inflammation and thrombosis status changes in the central nervous system. Blood markers relating to endothelial function, inflammation and thrombosis were found to be associated with SVD features such as WMH, and lacunar stroke (in Chapter 1). However, there were not many studies exploring the associations between blood markers and PVS.

There were four studies found associations between blood markers and PVS levels. Higher levels of PVS in the basal ganglia (BG) regions were significantly associated with higher levels of Immunoglobulin G against hypochlorite oxidized low-density lipoprotein in the blood after adjustment for age, sex, hypertension, large artery disease and patient types (lacunar stroke, hypertensive and controls). The results suggested that oxidized low-density lipoprotein may play a role in the PVS progression through endothelial dysfunction and antibody formation (Rouhl et al., 2010). Higher levels BG PVS were also significantly associated with higher neopterin after correction for age, sex, large vessel disease and patient group. Because neopterin is produced by activated monocytes or macrophages, the results may suggest a relation between monocyte/macrophage activation and PVS (Rouhl et al., 2011). In the 3C-Dijon study, researchers found that after adjusted for age, gender, hypertension and intracranial volume PVS severity in the basal ganglia regions is associated with increased Interleukin-6 (IL-6) level, which suggested role of inflammation in SVD (Satizabal et al., 2013). In the Lothian Birth Cohort 1936 study, increased centrium semiovale PVS numbers were significantly associated with raised plasma C-reactive protein levels after accounting for age, sex, stroke, and vascular risk factors (Aribisala et al., 2014).

In this study we aimed to investigate the associations between BG PVS count/volume and other SVD features such as WMH, atrophy and PVS in the centrum semiovale regions (CS). We also want to explore the associations between BG PVS count/volume and plasma markers of endothelial function, inflammation, and thrombosis and BBB permeability in the chronic phase of lacunar stroke and cortical stroke, after adjusting for risk factors such as age,

hypertension, smoking, diabetes and stroke types. This would help to identify more specific therapeutic targets to reduce the stroke and dementia burden caused by SVD.

8.2 Method

8.2.1 Patients information and risk factors

We used the same 100 patients with mild stroke who participated in the BBB permeability study (descriptions in Chapter 3). We had measured BG PVS count and volume (Chapter 7) in all 100 patients at baseline and in 46 of them who also had follow-up scans. We will use both the baseline and follow-up results to do the comparisons between BG PVS and SVD features (WMH, atrophy and CS PVS), and we will only use the results from baseline 100 patients to explore the associations between BG PVS count/volume and risk factors, blood markers and BBB permeability.

For risk factors, unlike binary risk factors such as hypertension and diabetes, there were originally four smoking categories which were N: non-smoker; R: recent smoker, less than a year; S: smoker; H: heavy smoker. In order to avoid small numbers in some of the smoking categories, we condensed recent smoker, smoker and heavy smoker into one category of current or ever smoker versus never smoker. We used this dichotomised smoking variable in most of our analysis. We will specify when we use four smoking categories in our comparisons.

8.2.2 WMH, atrophy and CS PVS visual rating scale

WMH were coded using Fazekas score, for periventricular WMH (PWMH) and deep WMH (DWMH) separately in the left and right hemispheres, and the overall score is the averaged score from both hemispheres (Wardlaw et

al., 2011). Brain atrophy were coded using a validated template (Farrell et al., 2009), with superficial and deep atrophy coded separately, and the whole atrophy is the sum of deep and superficial atrophy score. PVS in the CS regions were rated as follows: 0=no PVS, 1=<10 PVS, 2=10–20 PVS, 3=21–40 PVS, and 4>=40 PVS, separately in the left and right hemispheres, and an 'overall' score is the averaged score from both hemispheres using a scale previously developed by our group (Maclullich et al., 2004; Potter, 2011).

8.2.3 Blood marker measurement

We collected venous blood from each patient approximately two months post stroke onset to avoid the influence from the acute stroke phase. For each patient, we put the blood samples into two 2.5-mL ethylenediaminetetraacetic acid tubes and an 8-mL tube containing clot activator and gel. Then samples were all transferred on water ice and centrifuged at 3000 revolutions per minute for 10 minutes and stored them at -80°C.

Researchers in the clinical laboratories from the University of Glasgow blinded to the patients' clinical information helped us measure the following 10 blood markers using high sensitive assays (details for assays related to each blood marker were summarized in Table 8.1, all tables in this chapter are in section 8.6 Tables). We measured von-Willebrand factor (vWF), intracellular adhesion molecule 1 (ICAM-1), interleukin-6 (IL6), tumor necrosis factor alpha (TNFα), C-reactive protein (CRP), fibrinogen (Fib), prothrombin fragments 1 and 2 (F 1+2), thrombin-antithrombin complex (TAT), tissue plasminogen activator (tPA), and D dimer as markers of endothelial function, inflammation and thrombosis. We categorized them into relevant pathways as follows:

(1) Endothelial function: vWF, ICAM-1

(2) Inflammation: IL-6, TNF-α, CRP

(3) Thrombosis: Fib, F 1+2, TAT, tPA, D-dimer

8.2.4 BBB permeability measurement

The aim of this study was to assess the background status of the BBB, so it was done at least one month after the stroke and measurements were taken remotely from the recent stroke lesion to avoid any possible alterations caused by the acute effects of the stroke (Wardlaw et al., 2009; Wardlaw et al., 2008).We used a 1.5-Tesla MRI scanner (Signa LX; GE, Milwaukee, WI) and a fast spoiled gradient echo (FSPGR) sequence was run before and after intravenous contrast agent injection to assess BBB permeability in the 100 stroke patients who participated in the permeability study (details of patient recruitment in Chapter 3). The FSPGR sequence was run before contrast agent injection with flip angles of 2 degrees and 12 degrees. The sequence was repeated sequentially and consecutively after intravenous injection of 40 ml gadodiamide (Omniscan; GE Healthcare AS, Oslo, Norway) with flip angle of 12 degrees repeated 26 times with acquisition time of 69s after injection (Armitage et al., 2011; Wardlaw et al., 2009).

For each patient all permeability images were registered to the structural MRI. Small regions of interest (ROI: 9 voxels) were placed on the precontrast scan widely in white matter (84 ROIs), cortical gray matter (44 ROIs), deep gray matter (12 ROIs), cerebrospinal fluid (10 ROIs) and internal carotid/basilar arteries (3 ROIs), and sagittal sinus (2 ROIs) using a standard template sample (Armitage et al., 2011; Wardlaw et al., 2009). The signal enhancement from all ROIs was sampled from baseline to 30 minutes after

contrast agent injection (example of ROIs in WM, deep GM and SS were in Figure 8.5). The overall mean signal was calculated for each tissue type at each time point for each patient.

8.2.5 Statistical analysis

(1) Associations with SVD features

In these 100 patients, we used linear regression to investigate the associations between BG PVS count/volume, WMH visual rating scores (periventricular: PWMH; deep: DWMH) and volume, atrophy visual rating scores and brain volume, and CS visual rating scores. All linear regression analyses were performed in R program version 2.15.2 (http://www.r-project.org/).

(2) Associations with blood markers and risk factors

In the 100 patients, though all of them had blood drawn, blood marker data were missing for seven patients. Smoking status was missing for one patient.

We calculated:

(2-1) Mean and standard deviations (SD) for each blood marker.

(2-2) The influence of age, gender, hypertension, smoking, and diabetes on PVS count/volume.

(2-3) The influence of age, gender, hypertension, smoking, and diabetes on each blood marker.

(2-4) Associations between PVS count/volume and each blood marker (univariable linear regression) and associations between PVS count/volume and all blood markers (multivariable linear regression).

(2-5) Associations between PVS count/volume and each blood marker, with adjustment for age, gender, hypertension, smoking, and diabetes.

(2-6) Sensitivity analysis for associations between risk factors and PVS levels:

We investigated the associations between PVS count/volume and risk factors (smoking both two categories and four categories, diabetes, hypertension). We also used the dichotomised results for these three vascular risk factors and rated the appearance of each risk factor as score 1. We then added scores together to make a total risk factor score from 0 to 3 for each patient, and investigated the associations between PVS count/volume and total risk factor scores.

(2-7) Sensitivity analysis for associations between blood markers in each category and PVS levels:

We explored the associations between PVS count/volume and total blood markers values in three different categories mentioned above (endothelial function, inflammation and thrombosis).

We put the blood markers vWF and ICAM-1 into the endothelial function category, but probably they may belong to more than one category, for example, researchers considered them as markers of inflammation (Whiteley et al., 2011). In addition, we generated a total inflammatory category to include blood markers from both endothelium and inflammation categories (vWF, ICAM-1, IL-6, TNF-α and CRP). We investigated the associations between total values in total inflammatory category and PVS levels. We also assessed the association between PVS levels and the total values of 10 blood markers.

Initially, we tried to investigate the associations using blood marker concentration in each category. Due to differences of scale and units of measurement, we standardized the blood marker data. For each blood marker we calculated the mean and standard deviation (SD). Each measurement was then standardized by subtracting the mean and then dividing by the SD. The result of this is:

- The standardized blood marker data is unitless;
- The new mean of each blood marker is 0, and the new SD is 1;
- In a linear regression analysis, the coefficients for each blood marker will be directly comparable as they have no units and are on the same scale;
- The different blood marker variables can be added together with equal weighting for each blood marker.

Seven patients have missing values for some of these blood markers. We restricted the analysis to the 93 patients who have complete blood marker data.

(2-8) Influence of age and hypertension on smoking status.

In these 99 patients who had smoking status, we used two sample T test to compare the age difference and used chi-square to compare the hypertension difference in smoker and non-smoker groups.

All analyses were performed within Minitab (Minitab Inc, version 16). Alpha level for significance was $p<0.05$.

(3) Associations with BBB permeability

The data comprised signal enhancement values in each brain tissue measured at 26 time points. The first three time points were dropped from

the analysis because the low temporal resolution did not allow the accurate measurement of the first pass kinetics.

A linear mixed model was used in the signal enhancement analysis in the ROIs of white matter (WM), cortical grey matter (cortical GM), deep grey matter (deep GM), cerebrospinal fluid (CSF), internal carotid/basilar arteries (blood vessels), and sagittal sinus (SS). This mixed model could account for repeated measurements taken from the same patient, in this case by modelling the initial signal enhancement value (time point 4) of each patient as a random intercept to account for differences between patients and scanner drift (Armitage et al., 2011). Also each patient was modelled as a random effect to allow for repeated measurements over time being correlated within patients. The model also included fixed effects: age, sex, weight, stroke type and risk factors (hypertension, smoking and diabetes). Ignoring the lack of independence of multiple tissue measurements taken from an individual patient would result in a flawed analysis. Signal enhancement was the dependent variable, and all other variables were independent.

The residuals (the difference between the measured value and the model predicted value of signal enhancement) from the linear mixed model were assumed to be normally distributed with a mean of zero. The fit of the linear mixed model was assessed by examining Q-Q plots and histograms of the residuals. Analyses were performed separately for each brain tissue type (WM, cortical GM, deep GM, CSF, blood vessels and SS) as it was not possible to get acceptable residuals otherwise.

Using linear mixed modelling of the signal-time curves, we assessed the associations between PVS and signal change with time in different tissue types: WM, cortical GM, deep GM, CSF, blood vessels and SS.

From previous multivariable linear regression analysis, we found that there were strong correlations between PVS count/volume and age, and hypertension. We assessed the effect of possible collinearity on the results by repeating the analysis excluding PVS as an independent variable. The presence of collinearity often causes estimates of coefficients to change with the inclusion or exclusion of a variable.

We further explored the associations between signal enhancement and each different factor (age, sex, weight, stroke type and risk factors), adjusted for time only. All linear mixed modelling of the data was done by Dr Francesca Chappell in SAS 9.3 (www.sas.com) using PROC MIXED.

8.3 Results

The following results refer to the 100 patients with mild stroke, 51 with lacunar stroke and 49 with cortical stroke. The mean age is 69 years old, and ages ranged from 37 to 92 years old. The median score of stroke severity with the National Institute for Health Stroke Scale (NIHSS) was 2, and 62% had hypertension, 53% had smoking history and 15% had diabetes (see Table 5.1 in chapter 5)

8.3.1 Associations between BG PVS and SVD features

(1) WMH visual rating score/volume

For the baseline 100 patients, BG PVS computational count was positively associated with WMH visual rating (overall PWMH: 2.199, 95%CI 1.215 to 3.182; overall DWMH: 1.919, 95%CI 0.990 to 2.848). The associations of using WMH scores on the left or right hemispheres were similar as (Appendix H, Table H1 and H2, Figure H1 and H2). BG PVS count was also weakly although positively associated with WMH volume (0.065, 95% CI 0.034 to 0.096) (Figure 8.1, Table 8.2, all figures and tables in this chapter are in section 8.5 Figures and section 8.6 Tables).

The subgroup of 46 patients with long term follow-up, we found similar association as for 100 patients at baseline, both at baseline and follow-up (Table 8.2, Figure H1, H2 and H3 in Appendix H).

Similarly there were positive relationships between PVS computational volume and visual rating for both baseline and follow-up scans (Table 8.3) and for using WMH scores on the left or right hemispheres (Appendix H: Table H1 and H2, Figure H4, H5 and H6).

(2) Cerebral atrophy visual rating score/brain volume

In the baseline 100 patients, BG PVS count was positively associated with whole brain atrophy visual rating (1.012, 95%CI 0.489 to 1.535). BG PVS count increased as brain volume (as % of ICV) decreased (-0.326, 95%CI -0.526 to -0.127). BG PVS volume showed similar associations (Figure 8.2, Table 8.3).

Similarly, the associations still existed in the subgroup of 46 patients with long term follow-up at baseline and follow-up, and using scores from deep atrophy or superficial atrophy instead of the whole atrophy (Table H1, H2, Figure H6 to H10 in Appendix H).

(3) CS PVS visual rating score

In the baseline 100 patients, we did not find significant associations between BG PVS count/volume and CS visual rating scores (overall, left and right hemispheres). The associations remained insignificant in baseline and follow-up results in the subgroup of 46 patients with long term follow-up (Table 8.2, 8.3, H1, H2, Figure H11 and H12).

8.3.2 Associations between PVS and blood markers and risk factors

(1) Mean and SD for blood markers

We calculated the mean and standard deviations (SD) from patients for each blood marker using their original data (Table 8.4). After data standardization, the new mean of each blood marker is 0, and SD is 1.

(2) Influence of patient demographic features on BG PVS levels

Age is an important influencing factor for BG PVS levels, showing significant positive associations with both BG PVS count (p=0.003) and volume

(p=0.020). Hypertension is another crucial factor for BG PVS levels, showing a significant positive association with BG PVS count (p=0.013), although the association between hypertension and BG PVS volume did not reach significance. The association between BG PVS volume and male gender did not reach significance, which might be explained by the small number of patients (Table 8.5). No associations were seen between BG PVS count/volume and smoking or diabetes, which might relate to the small sample size.

(3) Influence of patient demographic features on blood markers

Both vWF and F 1+2 were associated with age, and the association between vWF and age is significant. The inflammatory marker IL-6 and the thrombosis markers Fib and tPA showed positive associations with smoking, particularly for tPA. No significant associations were seen between any blood markers and sex, hypertension and diabetes (Table 8.6).

(4) Associations between blood markers and BG PVS levels (unadjusted)

On univariable linear regression, the blood thrombosis marker F 1+2 was significantly associated with BG PVS count (p=0.050), and the blood thrombosis marker TAT was significantly associated with both BG PVS count (p=0.013) and BG PVS volume (p=0.037). There were no associations between other blood markers and BG PVS count/volume (Table 8.7). On multivariable linear regression of BG PVS count/volume with blood markers only, no association was found.

(5) Associations between blood markers and BG PVS levels (adjusted)

After adjusting the effect of age, sex, hypertension, smoking and diabetes, the association between blood marker TAT, F 1+2 and BG PVS became non-significant. The blood endothelial function marker vWF had become

negatively associated with BG PVS count (p=0.032). However, after adjustment, age and hypertension still remained significantly associated with BG PVS count/volume with almost all markers (Table 8.8: BG PVS count and Table 8.9: BG PVS volume). Male gender shows associations with BG PVS volume in the appearance of some blood markers, but none of them reached significance level.

(6) Sensitivity analysis: associations between risk factors and BG PVS levels

Apart from the association between hypertension and PVS levels, there was no significant association with diabetes and smoking (both two and four categories), though this analysis is probably limited by a small number of patients with diabetes and smoking (Table 8.10). Both PVS count and volume showed slight positive associations to total summed risk factor scores though this was not significant (Figure 8.3, Table 8.10).

Our result (Table 8.6) showed that IL-6, Fib and tPA are significantly associated with smoking. We further investigated whether smoking status is a confounding factor for the association between PVS and these blood markers. We used both the original four smoking categories and condensed them into two smoking categories to investigate the association between smoking and PVS and IL-6, Fib and tPA. The relationship between PVS and IL-6, Fib and tPA did not change when adjusted for smoking (Table 8.11).

(7) Sensitivity analysis: associations between blood marker categories and BG PVS levels

In the analysis of 93 patients, no significant associations were found between PVS count/volume and total summed blood marker category (Table 8.12), though individual blood markers in the endothelial function, inflammatory

and total inflammatory categories showed negative associations with PVS and thrombosis factors showed a positive association.

(8) Influence of age and hypertension on smoking

Because our result showed age and hypertension were two important factors for BG PVS (Table 8.8 and 8.9), so we wanted to know any associations with smoking were confounded by age and hypertension. We found that there was a difference between smoker and non-smoker, smoker were nearly four years younger than non-smoker though not significant (mean age of non-smoker: 68.7 years old, smoker: 64.9 years old, p=0.094) (Figure 8.4). There was no significant difference of hypertension status between smoker and non-smoker (Chi-Square=1.212, df=1, p=0.271). The associations between smoking and PVS or blood markers were not confounded by age.

8.3.3 Associations with BBB permeability

When analysed separately for each brain tissue type, the residuals for a model of signal enhancement in the blood vessels of internal carotid/basilar arteries showed that the model fit for blood vessel was poor (Figure 8.6), so we restricted further analysis to the remaining five tissue types of WM, cortical GM, deep GM, CSF, and SS.

(1) Univariable analysis: associations between PVS and signal enhancement (without adjusting)

PVS count was significantly associated with signal enhancement in WM, cortical GM, and CSF (Table 8.13). PVS volume was significantly associated with signal enhancement in cortical GM and borderline-significantly associated with WM (p=0.051, Table 8.14).

(2) Multivariable analysis: associations between different factors and signal enhancement (effect adjustment)

In all tissue types, signal enhancement was related to the PVS count and remained negatively associated, though no longer significant, after adjusting for time point, age, sex, weight, stroke type and risk factors (Table 8.15). Therefore the association between PVS count and signal enhancement in the WM might be significant if the sample size was larger ($p=0.07$).

Tissue signal enhancement was related to time significantly in all tissue types ($p<0.001$). In WM, GM and SS, signal enhancement decreased with time, but in the CSF, signal enhancement increased with time, which might be related to the contrast agent entering the CSF slowly. The hypothesis was contrast agent crossed the BBB soon after injection and then drained into CSF via PVS and direct diffusion from the brain to the ventricles over time (Abbott, 2004) (Table 8.15).

Increasing age was not always associated with increasing brain tissue signal enhancement. In contrast, increasing age was significantly associated with signal enhancement decreased with time in cortical GM ($p=0.025$) and CSF ($p=0.013$), and was also associated with signal enhancement decreased with time in WM though not significantly. Increasing age was associated with increasing signal in deep GM and SS, but these associations were not significant.

Male gender was associated with increasing signal enhancement in WM, CSF and SS, and female gender was associated with increasing signal enhancement in GM, but none of these associations were significant. The association between female gender and signal enhancement in the cortical GM might be significant if have a larger sample size ($p=0.076$).

Weight was negatively associated with signal enhancement in all tissue types, and associations were significant in WM (p=0.005), deep GM (p=0.002) and SS (p=0.005). Negative associations might be influenced by the contrast agent concentration: contrast dose was not adjusted for weight, and therefore patients of smaller weight had a higher contrast agent concentration.

Hypertension was related to increasing signal enhancement in WM and SS, smoking was related to higher signal enhancement in deep GM, CSF and SS, and diabetes related to worse BBB function in deep GM, but these associations were not significant. Fifteen patients with diabetes showed significant lower signal enhancement in CSF (p=0.032), which might indicate drainage dysfunction in the diabetes patients though need to confirm in larger sample.

We changed PVS count into PVS volume, and did the multivariable analysis again; the associations between different factors and permeability remained similar (Table 8.16).

Because in previous association analysis between PVS and risk factors, we found both age and hypertension were important influencing factors for PVS, so we did the collinearity check between PVS and all other factors by excluding PVS count/volume in the multivariable linear mixed model. The results from this analysis (Table 8.17) were similar as including PVS (Table 8.15 and 8.16), so we concluded that the possible effect of collinearity, because of the association between PVS and age and hypertension, was not an important consideration here.

8.4 Discussion

The significant associations seen for the BG PVS count/volume and WMH and cerebral atrophy were consistent with results seen in previous work (Doubal et al., 2010b; Potter et al., 2013; Rouhl et al., 2008; Zhu et al., 2010). Previous studies showed a positive association between visually rated BG and CS PVS scores (Doubal et al., 2010b; Potter, 2011; Potter et al., 2013). However, we did not find significant associations between the BG PVS count/volume and CS rating scores.

Apart from being as a SVD feature, PVS were seen in MS patients (Wuerfel et al., 2008) and were considered as a marker of inflammation. PVS were also associated with cognitive dysfunction such as in studies of lacunar infarcts and WMH (Rouhl et al., 2008), vascular dementia, Alzheimer's disease and mild cognitive impairment (Chen et al., 2011). PVS also appear in MRI scans from young and healthy volunteers who participate as controls for studying the mechanisms of ageing and brain diseases.

We drew the blood and performed the contrast enhancement MRI approximately two months post stroke onset, and our results may suggest the blood marker associations and BBB status in condition of chronic phase of stroke instead of acute phase.

Our results found that most of the blood markers we studied were not significantly associated with PVS count/volume. This is an exploratory hypothesis generating study, there is a possible relationship between PVS count/volume and thrombosis blood marker TAT on univariable analysis, and negative associations with endothelial function factor vWF after adjustment for age, gender, hypertension, smoking and diabetes. High vWF

level was considered a sign of endothelial cell dysfunction: studies showed that vWF protein is upregulated in the plasma of patients a variety of neurological diseases such as with stroke (Folsom et al., 1999), cerebral malaria (Hollestelle et al., 2006) and severe head injury (Yokota, 2007). However, a recent study demonstrated potential protective effect of vWF on BBB permeability using vWF knockout mice model. They showed that vWF inhibited the expression of claudin-5 which leaded to increased BBB permeability, but in the vWF knockout mice, increased claudin-5 expression did not provide protection to the BBB but actually be detrimental (Suidan et al., 2013).

For the associations, we could not be over optimistic about them; all of these associations still need to be confirmed by larger sample size, and considering the differences between lacunar and cortical stroke types.

We used standardized results in our comparisons between PVS and categorized blood markers. A disadvantage of standardization is a loss of ease of interpretation: the concept of a unit change no longer applies. However, we added blood marker data together to create new grouped variables of "endothelial function", "inflammation" and "thrombosis", which were not necessarily measured in any one particular unit. Blood markers in the endothelial function, inflammatory and total inflammatory categories showed negative associations with PVS and thrombosis factors showed a positive association. They might have opposite effects on PVS, and adding them together into a total blood marker category could cause the effects to cancel each other out. For further blood marker studies, it would be reasonable to explore the associations using blood markers in the same category which were measures of the same underlying function.

We found age and hypertension are important influencing factors for BG PVS count and volume, which is consistent with previous studies that PVS severity is associated with age and hypertension (Martinez-Ramirez et al., 2013; Potter et al., 2013; Rouhl et al., 2008; Wuerfel et al., 2008; Zhu et al., 2011; Zhu et al., 2010). Thus it is crucial to adjust for age and hypertension in further PVS analysis.

Smoking is a risk factor for some markers, but it is unclear whether this reflects the "poisoning" components in the cigarettes or the life habits related to smoking that influence these markers. In the multivariable analysis, we found inflammatory blood marker IL-6 and thrombosis blood makers Fib and tPA were significantly associated with smoking, however, we did not find significant associations between PVS and smoking status neither did Zhu in the 3C-Dijon study of 1818 patients, 108 of whom were current smoker (Zhu et al., 2010). In our study, we found that there was an age difference of four years between smoker and non-smoker which might confound the associations between smoking and PVS and blood markers, a larger sample is needed to explore the associations between PVS and smoking.

PVS count/volume were significantly associated with increasing permeability in cortical GM, and PVS count was also significantly correlated to higher permeability in WM and CSF in the univariable analysis before adjustment of other factors. After adjustment, PVS remained negatively associated permeability, however, the significance disappeared.

Body weight was negatively associated with permeability in nearly all multivariable analysis. The negative associations might be driven by

different contrast agent concentration; because in this study the contrast dose was not adjusted by body weight for each individual patient, all patients were given the same 40 ml contrast agent injection leading to smaller patients had higher contrast agent concentration. For further studies, it would be very helpful to adjust contrast agent does by body weight for each patients.

Further studies with a larger sample size would be useful to investigate the associations between PVS count and permeability in the WM, and between lacunar stroke and higher permeability in WM.

The permeability in CSF would be helpful to study the drainage function in patients' brain. The significant decreasing permeability in CSF might be an indicator drainage dysfunction in the diabetes patients, it needs further confirmation by larger sample size.

8.5 Figures

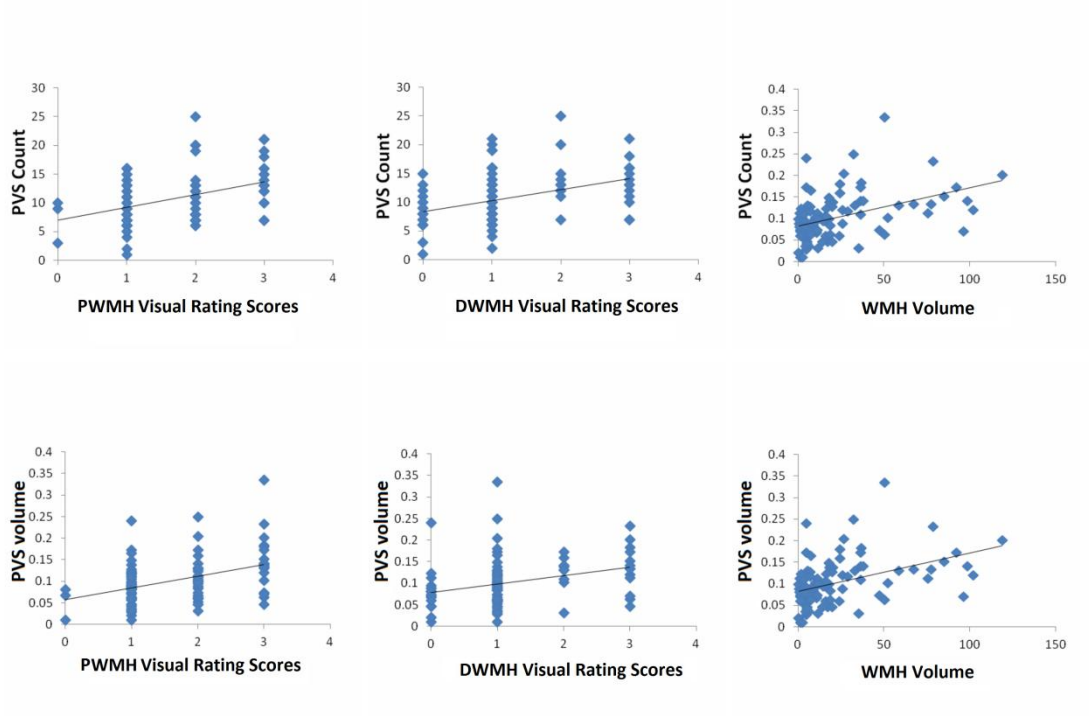

Figure 8.1 Associations between baseline 100 BG PVS count/volume and WMH (PWMH, DWMH visual rating scores, and WMH volume).

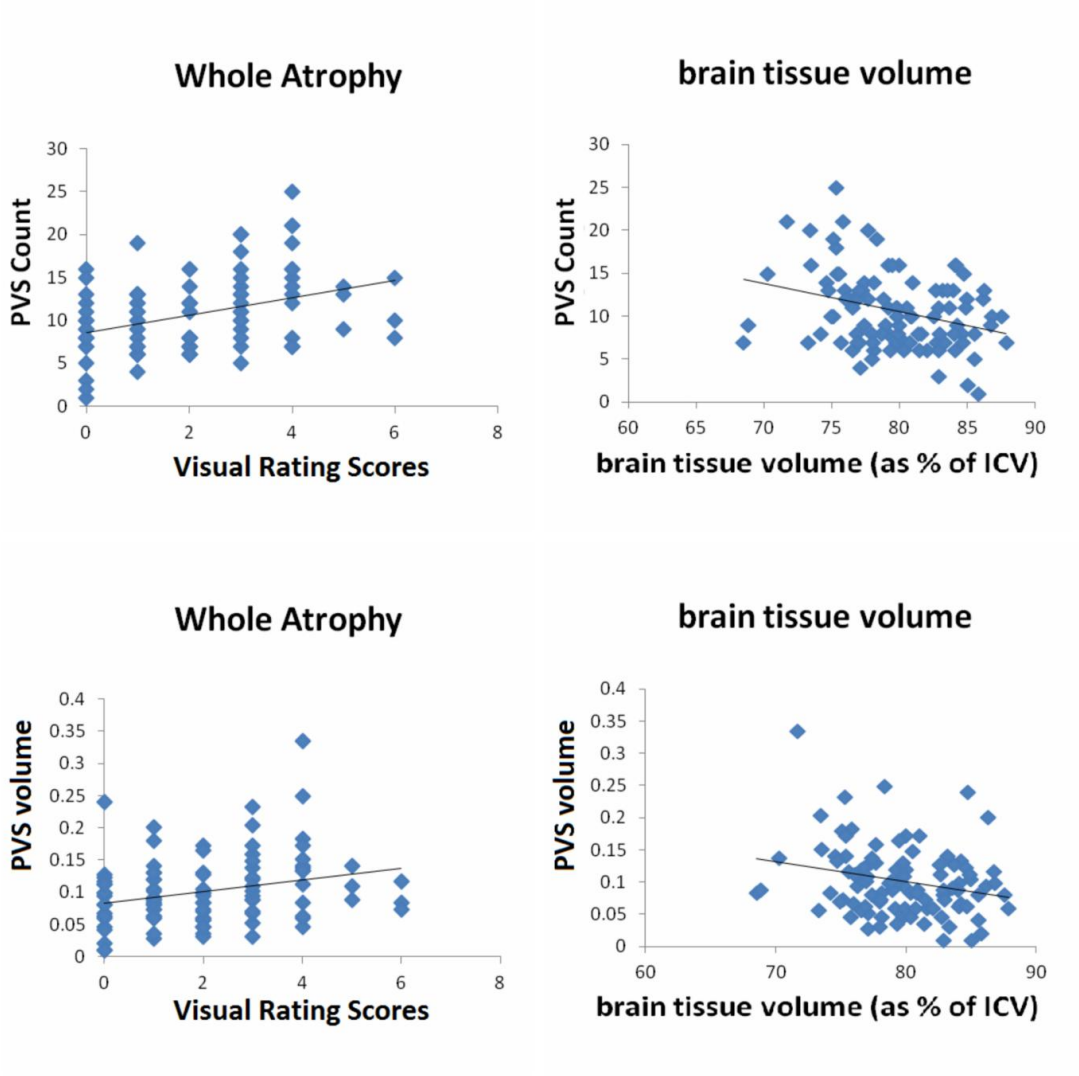

Figure 8.2 Associations between baseline 100 BG PVS count/volume and atrophy (brain atrophy visual rating scores, and brain tissue volume expressed as a percentage of ICV).

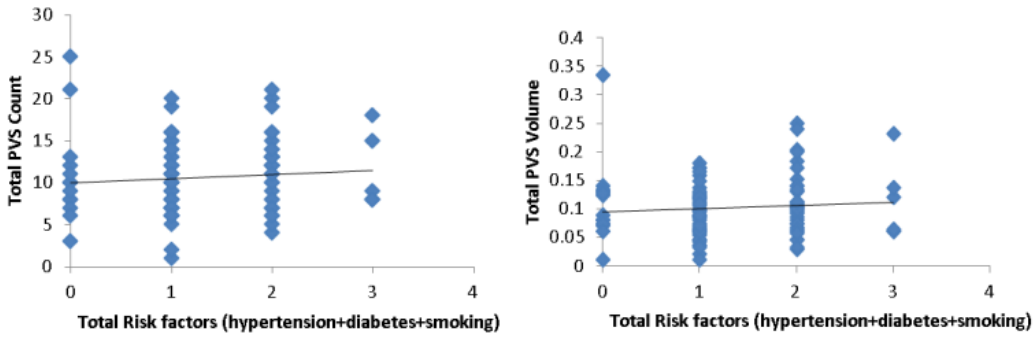

Figure 8.3 Association between BG PVS and total summed risk factor scores.

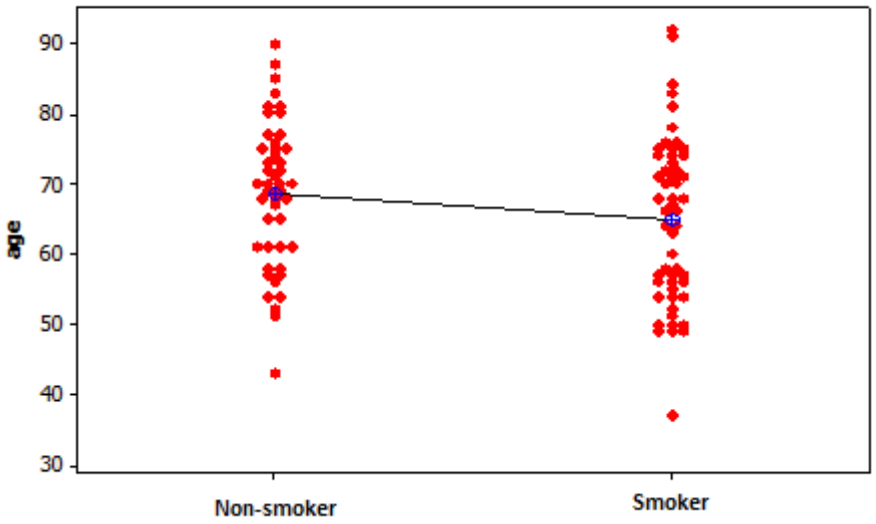

Figure 8.4 Individual value plot of age versus smoking status.

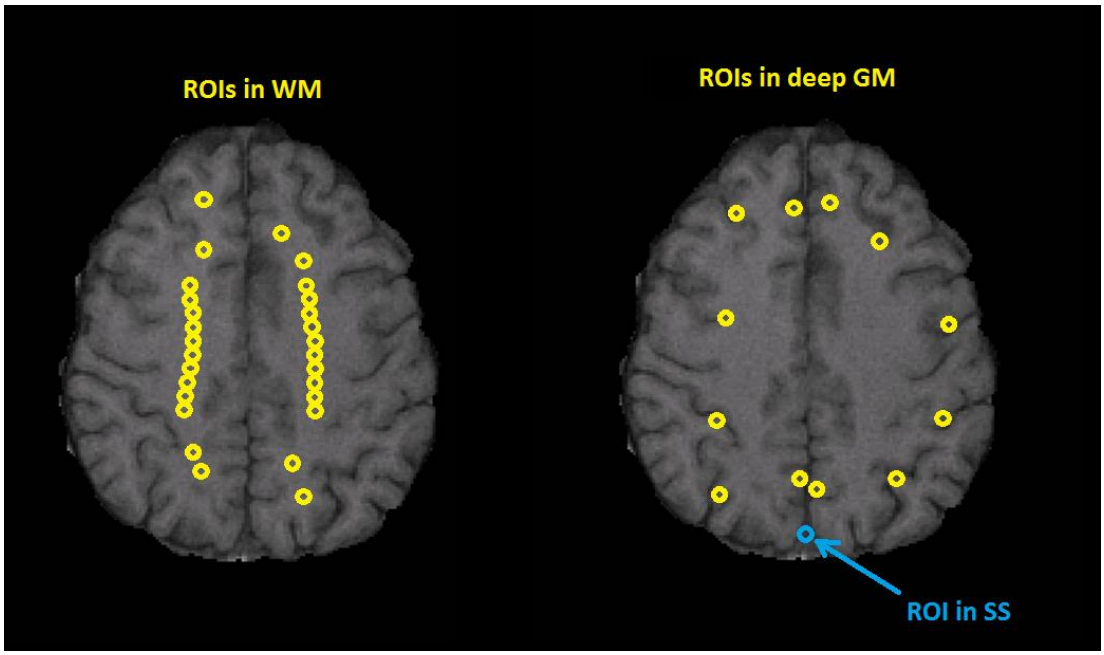

Figure 8.5 Example of the standard template for sampling regions of interest (ROIs: yellow circles) in white matter (WM) and deep gray matter (deep GM). One ROI in posterior sagittal sinus (SS) is highlighted by blue circle.

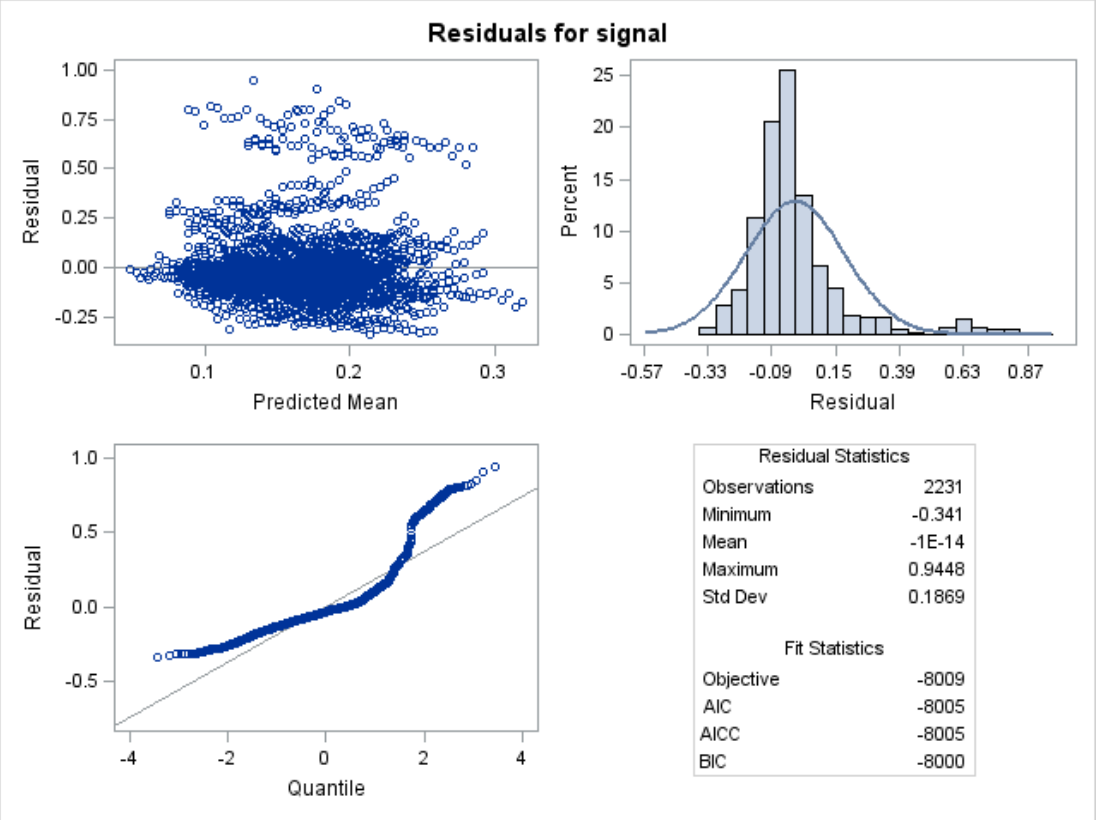

Figure 8.6 Residuals for a model of signal enhancement in blood vessels of internal carotid/basilar arteries (Q-Q plot and histogram).

8.6 Tables

Table 8.1 Assay details for blood markers.

Blood markers	Measurement method	Unit	Intra-assay CV	Inter-assay CV
Endothelial function				
vWF	ELISA (DAKO, High Wycombe, UK)	IU/dL	3.3%	4.2%
ICAM-1	ELISA (R&D Systems, Abingdon, UK)	ng/ml	3.6%	7.4%
Inflammation				
IL-6	ELISA (R&D Systems, Abingdon, UK)	pg/ml	7.5%	8.9%
TNF-α	ELISA (R&D Systems, Abingdon, UK)	pg/ml	8.4%	12.5%
CRP	Immunonephelometry (Prospec, Dade Behring Milton Keynes, UK)	mg/l	4.7%	8.3%
Thrombosis				
Fib	Immunonephelometry (Prospec, Dade Behring Milton Keynes, UK)	g/l	7.5%	8.9%
F 1+2	Immunonephelometry (Prospec, Dade Behring Milton Keynes, UK)	pg/ml	6.0%	9.0%
TAT	Immunonephelometry (Prospec, Dade Behring Milton Keynes, UK)	ng/ml	3.6%	4.3%
tPA	ELISA (Biopool AB, Umea Sweden)	ng/mL	6.6%	6.5%
D dimer	ELISA (Biopool AB, Umea Sweden)	ng/ml	4.7%	5.2%

ELISA: enzyme-linked immunosorbent assay, CV: coefficients of variation, vWF: von-Willebrand factor, ICAM-1 intracellular adhesion molecule 1; IL-6interleukin-6, TNF-α: tumor necrosis factor alpha, CRP: C-reactive protein; Fib: Fibrinogen, F 1+2: prothrombin fragments 1 and 2, TAT: thrombin-antithrombin complex, tPA: tissue plasminogen activator.

Table 8.2 Associations between BG PVS count and SVD features (WMH, atrophy and CS PVS) for baseline and follow-ups.

Associations	Coefficient of linear regression	95% CI	CV
Baseline 100 patients			
PWMH Overall	2.199	1.215 to 3.182	38.038
DWMH Overall	1.919	0.990 to 2.848	38.507
WMH volume	0.065	0.034 to 0.096	38.366
Whole Atrophy	1.012	0.489 to 1.535	38.855
Brain Volume in ICV	-0.326	-0.526 to -0.127	39.606
CS Overall	0.677	-0.279 to 1.633	41.268
Baseline 46 patients			
PWMH Overall	1.642	-0.062 to 3.347	40.793
DWMH Overall	2.626	1.014 to 4.238	38.097
WMH volume	0.115	0.029 to 0.202	39.404
Whole Atrophy	1.002	0.010 to 1.995	40.636
Brain Volume in ICV	-0.278	-0.691 to 0.136	41.648
CS Overall	-0.355	-2.002 to 1.292	42.412
Follow-up 46 patients			
PWMH Overall	0.841	-0.661 to 2.342	28.097
DWMH Overall	0.936	-0.419 to 2.291	27.893
WMH volume	0.07	0.011 to 0.129	26.818
Whole Atrophy	0.522	-0.179 to 1.223	27.797
Brain Volume in ICV	-0.124	-0.430 to 0.182	28.281
CS Overall	0.533	-0.893 to 1.958	28.315

CI: confident interval; CV: coefficient of variances; PWMH: periventricular white matter hyperintensities; DWMH: deep white matter hyperintensities; ICV: intracranial volume; CS: centrum semiovale.

Table 8.3 Associations between BG PVS volume and SVD features (WMH, atrophy and CS PVS) for baseline and follow-ups.

Associations	Coefficient of linear regression	95% CI	CV
Baseline 100 patients			
PWMH Overall	0.027	0.015 to 0.039	48.677
DWMH Overall	0.019	0.008 to 0.031	50.746
WMH volume	0.001	0.001 to 0.001	48.047
Whole Atrophy	0.009	0.002 to 0.016	51.603
Brain Volume in ICV	-0.003	-0.006 to -0.001	51.79
CS Overall	0.010	-0.001 to 0.022	52.618
Baseline 46 patients			
PWMH Overall	0.014	-0.001 to 0.029	43.158
DWMH Overall	0.020	0.005 to 0.035	41.592
WMH volume	0.001	0.000 to 0.002	41.788
Whole Atrophy	0.008	-0.001 to 0.017	43.31
Brain Volume in ICV	-0.002	-0.006 to 0.001	44.028
CS Overall	-0.006	-0.020 to 0.009	44.507
Follow-up 46 patients			
PWMH Overall	0.017	0.001 to 0.033	35.059
DWMH Overall	0.014	-0.001 to 0.028	35.552
WMH volume	0.001	0.001 to 0.002	32.117
Whole Atrophy	0.006	-0.002 to 0.013	36.101
Brain Volume in ICV	-2E-4	-0.004 to 0.003	36.926
CS Overall	0.008	-0.008 to 0.023	36.489

CI: confident interval; CV: coefficient of variances; PWMH: periventricular white matter hyperintensities; DWMH: deep white matter hyperintensities; ICV: intracranial volume; CS: centrum semiovale.

Table 8.4 Mean of original concentrations for each blood marker.

Blood markers	Original concentration mean (SD), unit
Endothelial function	
vWF (n=99)	127.1 (39.2), IU/dL
ICAM-1 (n=96)	166.9 (52.3), ng/ml
Inflammation	
IL-6 (n=98)	3.3 (2.1), pg/ml
TNF-α (n=99)	1.0 (0.8), pg/ml
CRP (n=99)	3.8 (9.0), mg/L
Thrombosis	
Fib (n=97)	3.9 (0.6), g/l
F 1+2 (n=99)	298.1 (213.9), pg/ml
TAT (n=99)	6.0 (5.9), ng/ml
tPA (n=99)	7.8 (3.2), ng/ml
D dimer (n=99)	160.7 (188.8), ng/ml

Table 8.5 Associations between BG PVS count/volume and age, gender, hypertension, smoking, and diabetes.

Coefficient (95%CI,p)	BG PVS count	BG PVS volume
Age	0.117 (0.040 to 0.194, p=0.003*)	0.001 (0.000 to 0.002, p=0.020*)
Male Sex	1.433 (-0.518 to 3.383, p=0.148)	0.023 (-0.002 to 0.047, p=0.072)
Hypertension	2.225 (0.476 to 3.973, p=0.013*)	0.022 (-0.001 to 0.044, p=0.056)
Smoking	-0.648 (-2.315 to 1.019, p=0.442)	-0.009 (-0.030 to 0.012, p=0.383)
Diabetes	-0.756 (-3.086 to 1.574, p=0.521)	-0.001 (-0.031 to 0.028, p=0.920)

***p<0.05; BG PVS count: total number of PVS dots in each patient in the selected BG regions; PVS volume: total volume of all the PVS dots; Age: age increase per year; Smoking: current or ever smoked versus never smoked.**

Table 8.6 Associations between blood markers and age, gender, hypertension, smoking, and diabetes.

Blood markers	Age	Male Sex	Hypertension	Smoking	Diabetes
Endothelial function					
vWF (n=98)	1.565 (0.870 to 2.260, p<0.001*)	-1.815 (-19.897 to 16.266, p=0.842)	-5.428 (-21.275 to 10.419, p=0.498)	5.499 (-9.764 to 20.762, p=0.476)	5.966 (-15.794 to 27.727, p=0.587)
ICAM-1 (n=95)	-0.487 (-1.510 to 0.537, p=0.347)	-0.758 (-27.848 to 26.331, p=0.956)	-13.698 (-37.106 to 9.710, p=0.248)	-7.535 (-30.061 to 14.991, p=0.508)	-5.699 (-38.728 to 27.330, p=0.733)
Inflammation					
IL-6 (n=97)	0.021 (-0.020 to 0.062, p=0.306)	0.044 (-1.022 to 1.110, p=0.935)	-0.015 (-0.955 to 0.925, p=0.974)	0.910 (0.010 to 1.811, p=0.048*)	-0.179 (-1.463 to 1.105, p=0.782)
TNF-α (n=98)	-0.004 (-0.019 to 0.012, p=0.621)	-0.193 (-0.593 to 0.207, p=0.339)	0.049 (-0.301 to 0.400, p=0.781)	-0.034 (-0.371 to 0.304, p=0.844)	0.022 (-0.460 to 0.503, p=0.929)
CRP (n=98)	0.036 (-0.135 to 0.208, p=0.675)	1.900 (-2.567 to 6.366, p=0.400)	2.240 (-1.674 to 6.154, p=0.259)	3.228 (-0.542 to 6.998, p=0.092)	-2.317 (-7.692 to 3.058, p=0.394)
Thrombosis					
Fib (n=96)	0.008 (-0.003 to 0.018, p=0.161)	0.178 (-0.097 to 0.454, p=0.202)	0.013 (-0.230 to 0.256, p=0.913)	0.287 (0.054 to 0.520, p=0.016*)	-0.126 (-0.457 to 0.205, p=0.452)
F 1+2 (n=98)	3.635 (-0.307 to 7.577, p=0.070)	-2.884 (-105.447 to 99.679, p=0.956)	38.677 (-51.211 to 128.565, p=0.395)	-77.362 (-163.940 to 9.216, p=0.079)	-94.426 (-217.858 to 29.006, p=0.132)
TAT (n=98)	0.064 (-0.048 to 0.176, p=0.258)	0.245 (-2.658 to 3.149, p=0.867)	1.309 (-1.236 to 3.854, p=0.310)	-1.705 (-4.156 to 0.746, p=0.170)	-0.507 (-4.002 to 2.988, p=0.774)
tPA (n=98)	-0.005 (-0.063 to 0.052, p=0.852)	1.170 (-0.332 to 2.673, p=0.125)	0.527 (-0.790 to 1.843, p=0.429)	2.165 (0.897 to 3.433, p=0.001*)	-0.036 (-1.844 to 1.772, p=0.969)
D dimer (n=98)	0.855 (-2.821 to 4.531, p=0.645)	27.421 (-68.217 to 123.059, p=0.570)	20.053 (-63.765 to 103.871, p=0.636)	0.546 (-80.186 to 81.278, p=0.989)	-62.350 (-177.447 to 52.747, p=0.285)

***p<0.05; Age: age increase per year; Smoking: current or ever versus never smoked.**

Table 8.7 Association between individual blood marker and BG PVS count/volume (univariable).

Blood markers	BG PVS count	BG PVS volume
Endothelial function		
vWF (n=99)	-0.005 (-0.028 to 0.018, p=0.660)	3.95E-05 (-23.81E-05 to 31.70E-05, p=0.778)
ICAM-1 (n=96)	-0.009 (-0.026 to 0.008, p=0.311)	-1.40E-05 (-22.67E-05 to 19.80E-05, p=0.893)
Inflammation		
IL-6 (n=98)	-0.108 (-0.529 to 0.313, p=0.612)	-1.10E-05 (-0.005 to 0.005, p=0.997)
TNF-α (n=99)	-0.702 (-1.825 to 0.422, p=0.218)	-0.003 (-0.017 to 0.011, p=0.640)
CRP (n=99)	-0.009 (-0.108 to 0.090, p=0.852)	-4.00E-05 (-124.94E-05 to 117.00E-05, p=0.948)
Thrombosis		
Fib (n=97)	-0.160 (-1.732 to 1.411, p=0.840)	0.003 (-0.016 to 0.022, p=0.753)
F 1+2 (n=99)	0.004 (0.000 to 0.008, p=0.050*)	3.92E-05 (-1.12E-05 to 9.00E-05, p=0.126)
TAT (n=99)	0.189 (0.041 to 0.336, p=0.013*)	0.002 (0.000 to 0.004, p=0.037*)
tPA (n=99)	-0.065 (-0.343 to 0.214, p=0.647)	-0.001 (-0.004 to 0.002, p=0.540)
D dimer (n=99)	0.002 (-0.003 to 0.007, p=0.386)	2.60E-05 (3.20E-05 to 8.30E-05, p=0.372)

***p<0.05; vWF: von-Willebrand factor, ICAM-1 intracellular adhesion molecule 1; IL-6interleukin-6, TNF-α: tumor necrosis factor alpha, CRP: C-reactive protein; Fib: Fibrinogen, F 1+2: prothrombin fragments 1 and 2, TAT: thrombin-antithrombin complex, tPA: tissue plasminogen activator.**

Table 8.8 Associations between BG PVS count and blood markers after adjusting for age, sex, hypertension, smoking, and diabetes.

Blood marker	Blood marker association	Age	Male Sex	Hypertension	Smoking	Diabetes
Endothelial function						
vWF (n=98)	-0.025 (-0.047 to -0.002, p=0.032*)	0.155 (0.072 to 0.239, p>0.001*)	1.364 (-0.605 to 3.333, p=0.172)	2.095 (0.365 to 3.824, p=0.018*)	-0.498 (-2.164 to 1.168, p=0.554)	-0.576 (-2.949 to 1.797, p=0.631)
ICAM-1 (n=95)	-0.003 (-0.019 to 0.013, p=0.747)	0.109 (0.031 to 0.187, p=0.007*)	1.259 (-0.798 to 3.316, p=0.227)	2.408 (0.617 to 4.199, p=0.009*)	-0.849 (-2.563 to 0.866, p=0.328)	-0.440 (-2.950 to 2.070, p=0.728)
Inflammation						
IL-6 (n=97)	-0.153 (-0.549 to 0.242, p=0.443)	0.123 (0.044 to 0.201, p=0.003*)	1.377 (-0.646 to 3.401, p=0.180)	2.158 (0.374 to 3.942, p=0.018*)	-0.532 (-2.279 to 1.215, p=0.547)	-0.697 (-3.135 to 1.742, p=0.572)
TNF-α (n=98)	-0.613 (-1.650 to 0.424, p=0.243)	0.114 (0.037 to 0.192, p=0.004*)	1.290 (-0.724 to 3.304, p=0.206)	2.259 (0.502 to 4.016, p=0.012*)	-0.654 (-2.346 to 1.037, p=0.444)	-0.710 (-3.121 to 1.701, p=0.560)
CRP (n=98)	-0.034 (-0.127 to 0.060, p=0.474)	0.118 (0.041 to 0.196, p=0.003*)	1.473 (-0.548 to 3.494, p=0.151)	2.304 (0.528 to 4.081, p=0.012*)	-0.525 (-2.251 to 1.201, p=0.547)	-0.801 (-3.234 to 1.631, p=0.514)
Thrombosis						
Fib (n=96)	-0.639 (-2.175 to 0.896, p=0.410)	0.123 (0.044 to 0.201, p=0.003*)	1.371 (-0.668 to 3.409, p=0.185)	2.091 (0.309 to 3.872, p=0.022*)	-0.335 (-2.102 to 1.431, p=0.707)	-0.649 (-3.087 to 1.788, p=0.598)
F 1+2 (n=98)	0.002 (-0.002 to 0.006, p=0.424)	0.111 (0.032 to 0.190, p=0.006*)	1.413 (-0.598 to 3.425, p=0.166)	2.165 (0.395 to 3.935, p=0.017*)	-0.507 (-2.234 to 1.220, p=0.561)	-0.568 (-3.019 to 1.883, p=0.646)
TAT (n=98)	0.122 (-0.020 to 0.264, p=0.091)	0.109 (0.032 to 0.186, p=0.006*)	1.379 (-0.609 to 3.366, p=0.172)	2.069 (0.318 to 3.820, p=0.021*)	-0.426 (-2.120 to 1.269, p=0.619)	-0.661 (-3.054 to 1.731, p=0.584)
tPA (n=98)	-0.074 (-0.351 to 0.204, p=0.600)	0.116 (0.039 to 0.194, p=0.004*)	1.495 (-0.547 to 3.536, p=0.149)	2.267 (0.495 to 4.040, p=0.013*)	-0.475 (-2.279 to 1.330, p=0.603)	-0.726 (-3.152 to 1.700, p=0.554)
D dimer (n=98)	0.001 (-0.003 to 0.005, p=0.661)	0.116 (0.038 to 0.194, p=0.004*)	1.382 (-0.638 to 3.402, p=0.178)	2.209 (0.440 to 3.979, p=0.015*)	-0.634 (-2.337 to 1.068, p=0.461)	-0.663 (-3.105 to 1.779, p=0.591)

***p<0.05; PVS count: total number of PVS dots in each patient; Age: age increase per year; Smoking: current or ever smoked.**

Table 8.9 Associations between BG PVS volume and blood markers after adjusting for age, sex, hypertension, smoking, and diabetes.

Blood marker	Blood marker association	Age	Male Sex	Hypertension	Smoking	Diabetes
Endothelial function						
vWF (n=98)	1.28E-04 (4.19E-04 to 1.62E-04, p=0.383)	0.001 (0.000 to 0.002, p=0.014*)	0.022 (-0.004 to 0.047, p=0.095)	0.021 (-0.001 to 0.043, p=0.065)	-0.008 (-0.030 to 0.013, p=0.453)	3.03E-04 (-0.030 to 0.031, p=0.984)
ICAM-1 (n=95)	0.53E-04 (-1.51E-04 to 2.57E-04, p=0.606)	0.001 (0.000 to 0.002, p=0.026*)	0.019 (-0.007 to 0.046, p=0.145)	0.024 (0.001 to 0.047, p=0.038*)	-0.009 (-0.031 to 0.013, p=0.400)	0.004 (-0.028 to 0.036, p=0.804)
Inflammation						
IL-6 (n=97)	-2.27E-04 (-0.005 to 0.005, p=0.927)	0.001 (0.000 to 0.002, p=0.011*)	0.020 (-0.005 to 0.045, p=0.113)	0.019 (-0.003 to 0.041, p=0.096)	-0.010 (-0.032 to 0.011, p=0.351)	0.002 (-0.029 to 0.032, p=0.908)
TNF-α (n=98)	-0.002 (-0.015 to 0.011, p=0.757)	0.001 (0.000 to 0.002, p=0.022*)	0.021 (-0.004 to 0.047, p=0.100)	0.022 (-0.001 to 0.044, p=0.056)	-0.009 (-0.030 to 0.013, p=0.412)	-4.18E-04 (-0.031 to 0.030, p=0.978)
CRP (n=98)	-2.59E-04 (-0.001 to 0.001, p=0.664)	0.001 (0.000 to 0.002, p=0.020*)	0.022 (-0.003 to 0.048, p=0.087)	0.022 (0.000 to 0.045, p=0.053)	-0.008 (-0.030 to 0.014, p=0.467)	-0.001 (-0.032 to 0.030, p=0.945)
Thrombosis						
Fib (n=96)	-0.001 (-0.021 to 0.018, p=0.906)	0.001 (0.000 to 0.002, p=0.024*)	0.021 (-0.005 to 0.047, p=0.116)	0.021 (-0.002 to 0.043, p=0.075)	-0.007 (-0.030 to 0.015, p=0.515)	0.001 (-0.031 to 0.032, p=0.971)
F 1+2 (n=98)	0.16E-04 (-0.35E-04 to 0.67E-04, p=0.535)	0.001 (0.000 to 0.002, p=0.031*)	0.022 (-0.004 to 0.047, p=0.091)	0.021 (-0.001 to 0.043, p=0.065)	-0.008 (-0.029 to 0.014, p=0.490)	0.001 (-0.030 to 0.032, p=0.946)
TAT (n=98)	0.001 (-0.001 to 0.003, p=0.163)	0.001 (0.000 to 0.002, p=0.031*)	0.021 (-0.004 to 0.047, p=0.094)	0.020 (-0.002 to 0.042, p=0.078)	-0.007 (-0.028 to 0.015, p=0.538)	1.84E-04 (-0.030 to 0.031, p=0.990)
tPA (n=98)	-0.001 (-0.005 to 0.002, p=0.451)	0.001 (0.000 to 0.002, p=0.022*)	0.023 (-0.002 to 0.049, p=0.075)	0.022 (0.000 to 0.045, p=0.050*)	-0.006 (-0.029 to 0.017, p=0.604)	-0.001 (-0.031 to 0.030, p=0.974)
D dimer (n=98)	0.16E-04 (-0.39E-04 to 0.71E-04, p=0.571)	0.001 (0.000 to 0.002, p=0.023*)	0.021 (-0.004 to 0.047, p=0.099)	0.021 (-0.001 to 0.044, p=0.061)	-0.009 (-0.030 to 0.013, p=0.414)	0.001 (-0.030 to 0.031, p=0.973)

***p<0.05; PVS count: total number of PVS dots in each patient; Age: age increase per year; Smoking: current or ever smoked.**

Table 8.10 Associations between BG PVS count/volume and risk factors (smoking, diabetes, hypertension and total summed risk factors).

	Smoking: 4 categories (N, R, S, H)	Smoking: 2 categories (N, Y)	Diabetes (N, Y)	Hypertension (N, Y)	Total summed risk factors (0-3)
BG PVS count	R: -4.884 (-10.058 to 0.290, p=0.064) S: -1.508 (-3.525 to 0.510, p=0.141) H: 0.151 (-2.217 to 2.519, p=0.900)	Y: -1.104 (-2.872 to 0.664, p=0.218)	Y: -0.738 (-3.212 to 1.736, p=0.555)	Y: 2.725 (0.982 to 4.468, p=0.003*)	1:-1.082 (-3.832 to 1.669, p=0.437) 2: 0.516 (-2.397 to 3.429, p=0.726) 3: 0.000 (-4.351 to 4.351, p>0.999)
BG PVS volume	R: -0.046 (-0.109 to 0.018, p=0.155) S: -0.019 (-0.043 to 0.006, p=0.139) H: 0.002 (-0.027 to 0.031, p=0.907)	Y: -0.013 (-0.034 to 0.009, p=0.239)	Y: -0.001 (-0.031 to 0.029, p=0.954)	Y: 0.027 (0.005 to 0.048, p=0.016*)	1: -0.021 (-0.054 to 0.012, p=0.215) 2: -0.001 (-0.036 to 0.035, p=0.971) 3: 0.000 (-0.053 to 0.053, p=0.994)

***p<0.05; N: not present; Y: present. R: recent smoker; S: smoker; H: heavy smoker.**

Table 8.11 Association between smoking, BG PVS and blood markers IL-6, Fib, tPA.

	BG PVS count	BG PVS volume
IL-6 (n=97)		
smoking (4 categories)	R:-4.949 (-10.168 to 0.269, p=0.063)	R: -0.046 (-0.109 to 0.017, p=0.150)
	S:-1.528 (-3.600 to 0.545, p=0.147)	S: -0.022 (-0.047 to 0.003, p=0.080)
	H:0.536 (-1.973 to 3.045, p=0.672)	H: 0.005 (-0.026 to 0.035, p=0.766)
	IL-6:-0.139 (-0.570 to 0.292, p=0.523)	**IL-6: -1.7E-04 (-0.005 to 0.005, p=0.948)**
smoking (2 categories)	Y: -1.070 (-2.914 to 0.773, p=0.252)	Y: -0.015 (-0.037 to 0.007, p=0.183)
	IL-6: -0.057 (-0.488 to 0.374, p=0.792)	**IL-60.001 (-0.004 to 0.006, p=0.790)**
Fib (n=96)		
smoking (4 categories)	R: -4.709 (-9.885 to 0.467, p=0.074)	R: -0.044 (-0.108 to 0.020, p=0.172)
	S: -1.381 (-3.485 to 0.722, p=0.195)	S: -0.019 (-0.045 to 0.007, p=0.152)
	H: 0.544 (-1.936 to 3.024, p=0.664)	H: 0.004 (-0.026 to 0.035, p=0.777)
	Fib: -0.099 (-1.719 to 1.521, p=0.904)	**Fib: 0.004 (-0.016 to 0.025, p=0.659)**
smoking (2 categories)	Y: -0.938 (-2.801 to 0.925, p=0.320)	Y: -0.013 (-0.035 to 0.010, p=0.278)
	Fib: 0.038 (-1.596 to 1.673, p=0.963)	**Fib: 0.006 (-0.014 to 0.026, p=0.574)**
tPA (n=98)		
smoking (4 categories)	R: -4.837 (-10.074 to 0.400, p=0.070)	R: -0.045 (-0.109 to 0.020, p=0.170)
	S: -1.446 (-3.583 to 0.692, p=0.183)	S: -0.017 (-0.043 to 0.009, p=0.199)
	H: 0.409 (-2.137 to 2.955, p=0.751)	H: 0.006 (-0.025 to 0.037, p=0.701)
	tPA:-0.028 (-0.325 to 0.269, p=0.853)	**tPA: -0.001 (-0.004 to 0.003, p=0.706)**
smoking (2 categories)	Y: -1.036 (-2.957 to 0.885, p=0.287)	Y: -0.011 (-0.035 to 0.012, p=0.351)
	tPA: -0.012 (-0.312 to 0.288, p=0.938)	**tPA: -0.001 (-0.004 to 0.003, p=0.777)**

N: not present; Y: present. R: recent smoker; S: smoker; H: heavy smoker.

Table 8.12 Associations results between BG PVS count/volume and categorized blood markers (standardized).

Coefficient (95% CI, p value)	(1) Endothelial function	(2) Inflammation	(3) Thrombosis	(4) Total inflammation	(5) Total markers
BG PVS count	-0.243	-0.145	0.163	-0.138	1.34 E-04
	(-0.850 to 0.364, p=0.428)	(-0.540 to 0.251, p=0.469)	(-0.157 to 0.483, p=0.315)	(-0.432 to 0.157, p=0.355)	(-0.184 to 0.183, p=0.998)
BG PVS volume	0.001	-0.001	0.002	-2.00 E-04	0.001
	(-0.007 to 0.008, p=0.864)	(-0.005 to 0.004, p=0.833)	(-0.002 to 0.006, p=0.329)	(-0.004 to 0.003, p=0.941)	(-0.002 to 0.003, p=0.611)

Table 8.13 Estimates of the change in signal enhancement per unit change in PVS count adjusted for time.

Tissue	Signal enhancement	P value
White matter	-0.0005 (-0.001,-0.00006)	0.026*
Cortical grey matter	-0.0016 (-0.0028,-0.0003)	0.016*
Deep grey matter	-0.0004 (-0.0018,0.00098)	0.57
Cerebrospinal fluid	-0.005 (-0.0098,-0.0002)	0.043*
Sagittal sinus	-0.0016 (-0.021,0.01785)	0.89

Table 8.14 Estimates of the change in signal enhancement per unit change in PVS volume adjusted for time.

Tissue	Signal enhancement	P value
White matter	-0.040 (-0.081,0.0002)	0.051
Cortical grey matter	-0.131 (-0.238,-0.024)	0.017*
Deep grey matter	-0.038 (-0.153,0.078)	0.52
Cerebrospinal fluid	-0.302 (-0.710,0.105)	0.15
Sagittal sinus	-0.024 (-1.653,1.606)	0.98

Table 8.15 Estimates of the effect of PVS count, time, age, sex (male versus female), weight, stroke type (lacunar versus cortical) and risk factors (hypertension, smoking and diabetes: present versus absent) on signal enhancement in WM, cortical GM, deep GM, CSF and SS.

Coefficient (95%CI,p)	WM	cortical GM	deep GM	CSF	SS
PVS count	-4.9E-4 (-10.1E-4 to 0.4E-4, p=0.070)	-7.0E-4 (-20.7E-4 to 6.7E-4, p=0.317)	-1.0E-4 (-15.9E-4 to 13.9E-4, p=0.898)	-0.001 (-0.007 to 0.004, p=0.608)	-0.005 (-0.027 to 0.016, p=0.631)
Time	-4.6E-4 (-5.1E-4 to -4.1E-4, p<0.001*)	-7.9E-4 (-8.5E-4 to -7.4E-4, p<0.001*)	-8.2E-4 (-9.0E-4 to -7.4E-4, p<0.001*)	4.1E-3 (3.7E-3 to 4.4E-3, p<0.001*)	-0.016 (-0.016 to -0.015, p<0.001*)
Age	-1.0E-4 (-3.2E-4 to 1.2E-4, p=0.370)	-6.6E-4 (-12.4E-4 to -0.8E-4, p=0.025*)	0.2E-4 (-6.1E-4 to 6.5E-4, p=0.957)	-0.003 (-0.005 to -0.001, p=0.013*)	0.003 (-0.006 to 0.012, p=0.485)
Sex	0.003 (-0.002 to 0.009, p=0.259)	-0.014 (-0.029 to 0.001, p=0.076)	-0.002 (-0.019 to 0.014, p=0.786)	0.006 (-0.051 to 0.064, p=0.826)	0.069 (-0.168 to 0.306, p=0.570)
Weight	-2.4E-4 (-4.0E-4 to -0.7E-4, p=0.005*)	-3.3E-4 (-7.6E-4 to 1.0E-4, p=0.128)	-7.3E-4 (-12.0E-4 to -2.6E-4, p=0.002*)	-2.5E-4 (18.8E-4 to 13.9E-4, p=0.765)	-0.010 (-0.017 to -0.003, p=0.004*)
Stroke type	0.004 (-0.001 to 0.009, p=0.082)	0.004 (-0.008 to 0.016, p=0.496)	-0.005 (-0.017 to 0.008, p=0.479)	-0.005 (-0.049 to 0.040, p=0.838)	0.086 (-0.097 to 0.269, p=0.356)
Hypertension	0.003 (-0.002 to 0.007, p=0.279)	-0.002 (-0.014 to 0.010, p=0.770)	-0.001 (-0.014 to 0.012, p=0.932)	-0.024 (-0.069 to 0.022, p=0.308)	0.094 (-0.093 to 0.281, p=0.325)
Smoking	-0.002 (-0.006 to 0.002, p=0.416)	-0.005 (-0.016 to 0.006, p=0.335)	0.008 (-0.004 to 0.020, p=0.181)	0.029 (-0.013 to 0.071, p=0.175)	0.057 (-0.114 to 0.229, p=0.512)
Diabetes	-0.004 (-0.010 to 0.002, p=0.206)	-0.003 (-0.019 to 0.012, p=0.694)	0.011 (-0.006 to 0.028, p=0.197)	-0.065 (-0.124 to -0.006, p=0.032*)	-0.015 (-0.258 to 0.228, p=0.904)

Table 8.16 Estimates of the effect of PVS volume, time, age, sex (male versus female), weight, stroke type (lacunar versus cortical) and risk factors (hypertension, smoking and diabetes: present versus absent) on signal enhancement WM, cortical GM, deep GM, CSF and SS.

Coefficient (95%CI,p)	WM	cortical GM	deep GM	CSF	SS
PVS volume	-0.040 (-0.083 to 0.003, p=0.068)	-0.069 (-0.181 to 0.043, p=0.229)	-0.015 (-0.137 to 0.107, p=0.810)	-0.024 (-0.451 to 0.403, p=0.911)	-0.453 (-2.207 to 1.301, p=0.612)
Time	-4.6E-4 (-5.1E-4 to -4.1E-4, p<0.001*)	-7.9E-4 (-8.5E-4 to -7.4E-4, p<0.001*)	-8.2E-4 (-9.0E-4 to -7.4E-4, p<0.001*)	4.1E-3 (3.7E-3 to 4.4E-3, p<0.001*)	-0.016 (-0.016 to -0.015, p<0.001*)
Age	-1.1E-4 (-3.3E-4 to 1.1E-4, p=0.331)	-6.5E-4 (-12.2E-4 to -0.9E-4, p=0.024*)	0.3E-4 (-6.0E-4 to 6.5E-4, p=0.935)	-0.003 (-0.005 to -0.001, p=0.008*)	0.003 (-0.006 to 0.012, p=0.486)
Sex	0.004 (-0.002 to 0.010, p=0.195)	-0.013 (-0.028 to 0.003, p=0.104)	-0.002 (-0.019 to 0.015, p=0.812)	0.006 (-0.052 to 0.064, p=0.840)	0.075 (-0.165 to 0.315, p=0.540)
Weight	-2.5E-4 (-4.1E-4 to -0.8E-4, p=0.004*)	-3.5E-4 (-7.7E-4 to 0.8E-4, p=0.112)	-7.3E-4 (-12.0E-4 to -2.6E-4, p=0.002*)	-2.9E-4 (-19.2E-4 to 13.4E-4, p=0.730)	-0.010 (-0.017 to -0.003, p=0.004*)
Stroke type	0.005 (0.000 to 0.009, p=0.050*)	0.005 (-0.007 to 0.017, p=0.406)	-0.004 (-0.017 to 0.008, p=0.501)	-0.004 (-0.049 to 0.041, p=0.853)	0.092 (-0.092 to 0.277, p=0.326)
Hypertension	0.002 (-0.002 to 0.007, p=0.306)	-0.002 (-0.014 to 0.010, p=0.766)	-4.7E-4 (-0.013 to 0.012, p=0.943)	-0.026 (-0.071 to 0.020, p=0.267)	0.093 (-0.093 to 0.278, p=0.328)
Smoking	-0.002 (-0.006 to 0.002, p=0.414)	-0.005 (-0.016 to 0.005, p=0.325)	0.008 (-0.004 to 0.020, p=0.184)	0.030 (-0.012 to 0.071, p=0.166)	0.057 (-0.114 to 0.229, p=0.513)
Diabetes	-0.004 (-0.010 to 0.002, p=0.207)	-0.003 (-0.019 to 0.012, p=0.682)	0.011 (-0.006 to 0.028, p=0.200)	-0.064 (-0.123 to -0.005, p=0.035*)	-0.015 (-0.258 to 0.228, p=0.903)

Table 8.17 Estimates of the effect time, age, sex (male versus female), weight, stroke type (lacunar versus cortical) and risk factors (hypertension, smoking and diabetes: present versus absent) on signal enhancement in WM, cortical GM, deep GM, CSF and SS.

Coefficient (95%CI,p)	WM	cortical GM	deep GM	CSF	SS
Time	-4.6E-4 (-5.1E-4 to -4.0E-4, p<0.001*)	-7.9E-4 (-8.5E-4 to -7.4E-4, p<0.001*)	-8.2E-4 (-9.0E-4 to -7.4E-4, p<0.001*)	4.1E-3 (3.7E-3 to 4.4E-3, p<0.001*)	-0.016 (-0.016 to -0.015, p<0.001*)
Age	-1.7E-4 (-3.8E-4 to -0.4E-4, p=0.121)	-7.6E-4 (-13.0E-4 to -2.1E-4, p=0.007*)	0.4E-5 (-59.0E-5 to 59.5E-5, p=0.990)	-0.003 (-0.005 to -0.001, p=0.005*)	0.002 (-0.006 to 0.011, p=0.564)
Sex	0.003 (-0.003 to 0.009, p=0.319)	-0.014 (-0.029 to 0.001, p=0.065)	-0.002 (-0.019 to 0.014, p=0.778)	0.005 (-0.052 to 0.063, p=0.851)	0.065 (-0.171 to 0.300, p=0.590)
Weight	-2.5E-4 (-4.2E-4 to -0.8E-4, p=0.003*)	-3.5E-4 (-7.8E-4 to 0.7E-4, p=0.104)	-7.3E-4 (-11.9E-4 to -2.0E-4, p=0.002*)	-2.5E-4 (-18.8E-4 to 13.9E-4, p=0.726)	-0.010 (-0.017 to -0.003, p=0.003*)
Stroke type	0.004 (-0.001 to 0.009, p=0.085)	0.004 (-0.008 to 0.016, p=0.494)	-0.005 (-0.017 to 0.000, p=0.476)	-0.005 (-0.049 to 0.040, p=0.839)	0.086 (-0.096 to 0.269, p=0.353)
Hypertension	0.002 (-0.003 to 0.006, p=0.474)	-0.003 (-0.015 to 0.009, p=0.611)	-0.001 (-0.013 to 0.012, p=0.909)	-0.026 (-0.070 to 0.018, p=0.249)	0.084 (-0.098 to 0.266, p=0.363)
Smoking	-0.001 (-0.006 to 0.003, p=0.505)	-0.005 (-0.016 to 0.006, p=0.374)	0.008 (-0.004 to 0.020, p=0.174)	0.030 (-0.012 to 0.071, p=0.159)	0.061 (-0.110 to 0.231, p=0.485)
Diabetes	-0.003 (-0.009 to 0.003, p=0.276)	-0.002 (-0.018 to 0.013, p=0.762)	0.011 (-0.006 to 0.028, p=0.188)	-0.063 (-0.122 to -0.005, p=0.034*)	-0.009 (-0.251 to 0.232, p=0.939)

Chapter 9 Discussion

9.1 Main results

9.1.1 Blood brain barrier (BBB) literature review

We summarized the blood brain barrier (BBB) normal structures from the level of neurovascular unit (NVU), perivascular spaces (PVS, one of the components NVU), and junctional proteins located in the endothelium. PVS function importantly in cereral fluid drainage and inflammation, which are also associated with various cerebral diseases, and enlarged PVS are important imaging markers for cerebral small vessel disease. The PVS abnormalities link the microscopic changes of BBB with hyperintensities on T2-weighted magnetic resonance imaging, which are a more macroscopic view and more visualized way to observe (Figure 9.1).

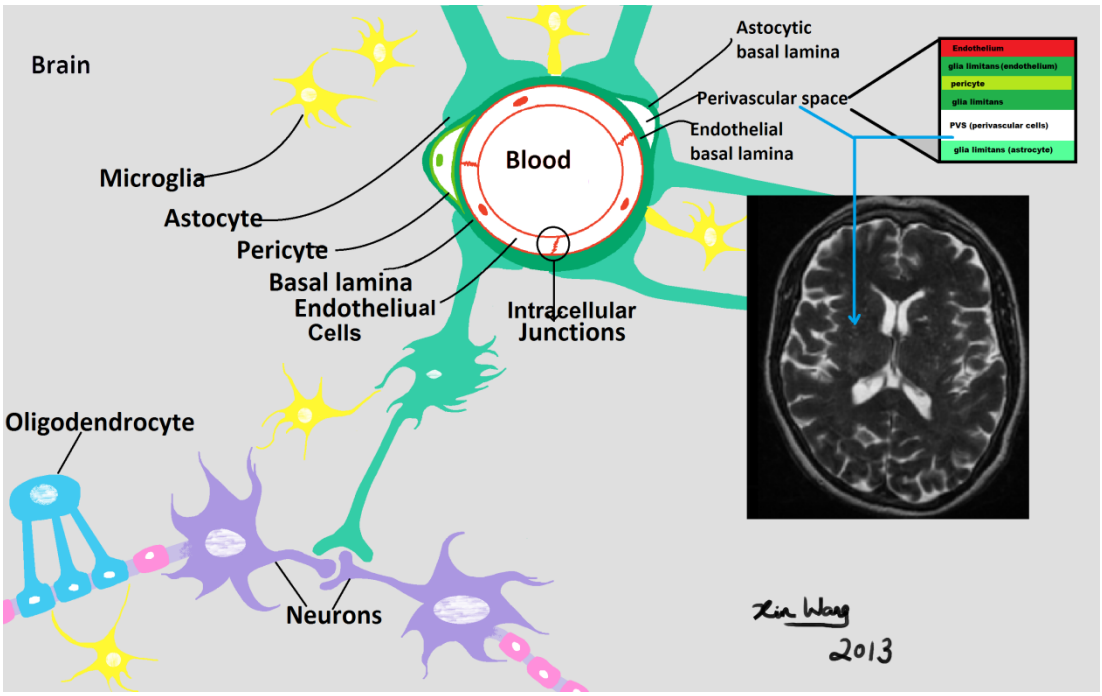

Figure 9.1 The abnormalities of PVS link the BBB microscopic structures with macroscopic view which shown in the brain imaging (blue lines).

Under ischemic stimulus, cytokines such as matrix metalloproteinases, vascular endothelial growth factor and tissue plasminogen activator exacerbate the disruption of BBB.

9.1.2 Accurate white matter hyperintensities (WMH) measurement

We used the colour fusion MCMxxxVI method (Hernandez et al., 2010) in the white matter hyperintensities (WMH) measurement. This colour fusion method enabled a wider colour range, offering more threshold levels (65536 levels) than a single sequence grey scale image such as fluid attenuated inversion recovery (FLAIR) sequence (256 levels) for tissue identification.

We also excluded WMH artefacts and stroke lesions. In order to know the frequent WMH artefacts on FLAIR image (which is commonly used for WMH identification), I reviewed existing articles relating to WMH artefacts on FLAIR, and used the information to make a WMH artefacts frequency training guide and applied this information in our WMH segmentation training. I also summarized the WMH frequencies in 46 patients, and our WMH artefact results were consistent with the published literatures: cerebrospinal fluid (CSF) flow artefacts and patient movements were two of the most frequent artefacts influencing large areas in the brain image. In both cross-sectional and longitudinal studies of WMH, we found that failed to exclude stroke lesions from WMH could lead to misleading estimates of WMH volumes and progression, and would double the sample size needed for clinical trials which use WMH as a measure.

These aspects give valuable information for large clinical trials and observational studies relating to WMH mechanism and cognition, and in genetic or drug trials which use WMH as an outcome measure. For example,

in a large randomized clinical trial of anti-hyperintensive drug perindopril PROGRESS (Perindopril Protection Against Recurrent Stroke Study) (Dufouil et al., 2005), the WMH progression was used as an outcome measure in 192 hypertensive patients who had both baseline and follow-up magnetic resonance imaging (MRI) scans. They carefully controlled the image registration, image signal histogram equalization and display to ensure comparable image characteristics in terms of anatomical feature and signal intensity. They used a semi-automatic method to measure the WMH volume on T2W image and carefully excluded the hypointense lesions on T1-weighted (T1W) sequence which they considered as stroke lesions.

However, T1W image is not sensitive for acute or old stroke lesion detection, and T2W is not the best sequence for WMH, so their conclusion about the effect of the drug treatment on WMH could be distorted by its effect on stroke.

9.1.3 Basal ganglia (BG) PVS measurement and associations

PVS visual rating scores are widely used in previous studies, this is the first time analysis were taken to assess the associations between volumetric PVS (BG PVS computational count/volume) and SVD markers, blood markers and BBB permeability.

In order to develop a computational PVS method, we reviewed current studies that described any computational methods suitable for PVS quantification. Our final optimized method was suitable for PVS count and volume measurement in the basal ganglia (BG) regions. We also suggested ways of dealing with difficult and complicated cases. The BG PVS results

from this computational method showed good agreement within and between observers and with a validated visual rating scale.

In the BG PVS associations investigations, we found that there were significant associations between the BG PVS count/volume and WMH and cerebral atrophy, which were consistent with previous studies (Doubal et al., 2010b; Potter et al., 2013; Rouhl et al., 2008; Zhu et al., 2010). We also found that age and hypertension were two important influencing factors for BG PVS. On univariable linear regression analysis we found that the blood thrombosis marker thrombin-antithrombin complex (TAT) and fragments 1 and 2 of prothrombin (F 1+2) were significantly associated with BG PVS. After adjusting for age, sex, hypertension, smoking and diabetes, the association between thrombosis blood markers F 1+2, TAT and BG PVS became non-significant, but the blood endothelial function marker von-Willebrand factor (vWF) had become negatively associated with increasing BG PVS count, which suggested more vWF release may provide desired BBB flexibility during certain disease states and could be potentially (Suidan et al., 2013).

On the BBB permeability imaging univariable analysis, BG PVS count was significantly associated with signal enhancement in white matter (WM), cortical gray matter (GM), and CSF. BG PVS volume was significantly associated with signal enhancement in cortical GM and borderline-significantly associated with WM. After adjusting for time point, age, sex, weight, stroke type and risk factors, the associations became insignificant. The results may be influenced by sample size, scanner drift, subtle signal changes in BBB and encourage further studies in the associations between PVS and BBB permeability.

9.2 Strengths

9.2.1 BBB literature

We summarized the literature relating to PVS systematically, including the aspects of PVS ultrastructure, functions such as immune cell accumulation, transmigration, and drainage, associations with inflammatory disease and cerebral small vessel disease (SVD). We systematically summarized ischemic triggers for BBB change.

I generated figures illustrating the combined information from most updated literature. The visulasation work enlightens my thoughts and makes it easrier for me to see what are lacking in a broad view.

9.2.2 Good study design in primary data source- the Mild Stroke Study

I used data from 100 patients which was previously recruited in the Mild Stroke Study.

(1) Control and Careful blinding

In this study of lacunar stroke and SVD mechanism, we recruited age-matched mild cortical ischemic stroke as controls to adjust for risk factors. Normal ageing subjects without stroke lesions would not be appropriate to be used as controls as any associations found between lacunar strokes could just be with any other types of stroke, not with lacunar stroke specifically.

We analysed imaging features blindly to all patients' clinical characteristics and follow-up scans were analysed separately and blindly to the results from the baseline.

(2) Prospective study

The recruitment for this study was prospective and as consecutive as possible. The patients with clinical features of acute lacunar stroke and mild cortical stroke (as controls) who were seen at a large academic teaching hospital between January 2005 and July 2007 were included in this study (Wardlaw et al., 2009).

All patients underwent investigations for stroke causes such as carotid Doppler ultrasound, electrocardiogram, blood tests and brain imaging. All patients underwent standard structural MRI brain imaging on the same scanner using the same protocol, which included sagittal T1W, axial T2-weighted, diffusion-weighted imaging, FLAIR, and gradient-recalled echo sequences (GRE).

A trained stroke physician assessed all patients and defined the clinical stroke subtypes according to the Oxfordshire Community Stroke Project classification (Bamford et al., 1991). Lacunar stroke was defined as pure motor disorder and/or sensory loss, or ataxic hemiparesis; mild cortical stroke was defined as being equivalent to a partial anterior circulation stroke, the definition did not take account of risk factors. Following initial clinical classification, a standardized radiological classification system was used for recoding the presence, site, and size of the recent infarct using diagnostic MRI (high signal on diffusion imaging, low signal on apparent diffusion coefficient map) by an experienced neuroradiologist (Wardlaw et al., 2009). The radiological stroke subtype was based on the acute lesion, and the presence and characteristics of any old stroke lesions were recorded (Wardlaw et al., 2009). When the clinical and radiological classifications differed, the radiological classification was used because 20% of cortical

stroke were clinically misdiagnosed as lacunar stroke and vice versa (Potter et al., 2010a). Because about one third of the patients with mild stroke have negative MRI of recent infarct, if no visible stroke lesions on the scan, the clinical classification was used (Doubal et al., 2010a). Both the clinical and radiological classifications were used to decide a final stroke subtype classification after systematically reviewed and discussed by stroke expert panel on a weekly basis.

A variety of patients' characteristics were recorded, such as patients' demography (age, gender, weight, and race), vascular risk factors of stroke and SVD (history of hypertension, smoking, diabetes, alcohol use and so forth), severity of stroke (National Institutes of Health Stroke Scale), cardiovascular diseases (ischemic heart disease, peripheral vascular disease, or transient ischemic attack) and drug treatment before the stroke.

Because the patients' information was collected and recoded prospectively and systematically, so we had a fairly large and complete dataset of both MR imaging and patients' characteristics which can be used to explore potential associations and confounders of SVD features and BBB permeability.

(3) Longitudinal and cross-sectional studies

Using the imaging and clinical data from 100 patients and 46 of whom had long term follow-ups; we were able to assess cross-sectional comparisons between SVD features and risk factors, blood markers and BBB permeability. We could also investigate the longitudinal progression of WMH, atrophy and PVS over time, and the factors relating to the progression.

(4) Data management and expert support

In this study, all the clinical and imaging relating data had been put into a master database, which had been verified, and was handy to find and do comparisons. The stroke subtype definition had been classified using standardised classification systems and discussed by a stroke expert panel. Image segmentation of radiological features such as WMH, atrophy, PVS, and stroke lesions had been guided and checked by an experienced neuroradiologist. Statistical analysis and modelling were supported from a medical statistician.

9.2.3 Accurate WMH measurement

In the WMH measurement, we used MCMxxxVI method (Hernandez et al., 2010), which used fused pairs of FLAIR and GRE sequences. Each image pixel of the fused pairs was projected into the Red and Green (RG) colour space, and the WMH volumes were calculated using minimum variance quantisation (Hernandez et al., 2010). This colour fusion method enabled a wider colour range, offering more threshold levels (65536 levels) than a single FLAIR sequence (256 levels) for tissue identification. Comparison results with other multispectral methods showed that the MCMxxxVI method can provide fast and accurate WMH measurement (Hernandez et al., 2012). WMH segmentation was done blindly to patients' clinical characteristics and follow-up image segmentation was done blind to the results at baseline. We also carefully excluded WMH artefacts and stroke lesions which mimic the WMH and influence its accurate measurement at both time points and progression.

9.3 Limitations

9.3.1 Literature review

We tried to do a review of the cellular and other components of the BBB as systematically as possible; however, it is an enormous topic and it was not possible to assess all aspects within PhD time limit, so we focused on the BBB structure of endothelial junction proteins and PVS, and ischemic and inflammatory triggers as they are pathologically and anatomically relevant to imaging findings and SVD mechnism. We searched PVS, ischemic trigger for BBB and WMH artefact systematically and also checked reference lists from review papers. We tried to make it as complete as possible, however limited by searching tools, we were unable to include all relating papers exclusively and may have missed some papers which mentioned these topics in their introduction or discussion part, but not as their main topic.

9.3.2 More refinements needed in further WMH method

We used eight patients in the pilot study to test refinements of the WMH segmentation method, as the segmentation which should be accurate and not laborious and suitable for later WMH cross-sectional and longitudinal analysis. We were able to find that the colour fusion method (MCMxxxVI) method was more superior to single sequence thresholding methods in terms of tissue identification and less time consuming as adjusted by an visual inspection of the different methods.

The number of patients in the pilot study was not enough to do a formal statistical analysis to find out which method was the most efficient. In order to do such comparisons, we need a larger dataset and should include all available methods (far more than the seven experiments), which was not the main aim of the pilot study and was beyond the time limit of this PhD.

Moreover, any current semi-automatic and automatic WMH segmentation method cannot avoid visual inspection and manual editing especially when condensing the distorting effect of WMH artefacts and stroke lesions frequently shown on the images.

9.3.3 Patient recruitment and data collection

The data I used from 100 patients who were prospectively and consecutively recruited in the Mild Stroke Study BBB permeability study and 46 of them returned for follow-up scans. The sample size, though reasonable for the cross-sectional and longitudinal comparisons of SVD features such as white matter hyperintensities, atrophy, perivascular spaces and BBB permeability, was too small for analysing lacunes (only seven patients had lacunes) and not large enough to do comparisons. Though diabetes was one of the risk factors for SVD and related to BBB permeability in other studies, we were unable to find potential associations between diabetes possibly due to its small number of patients who had diabetes (15 patients). We tried to have a complete dataset for all the patients, however, due to radiographer error and unsuccessful contrast agent injections, there were permeability data unavailable in three patients; smoking status was missing in one patient, and some of the blood marker were missing in seven patients. Some of the insignificant results might be confirmed by larger sample sizes.

There were more male than female, and patients who had lacunar stroke were slightly younger than patients with cortical stroke in our study which has probably not influenced the generalizability of our results although further studies are required. We managed to recruit every consecutive patient where possible accounted for ineligible patients, scanner

unavailability, staff absences, and patient refusals and our sample was not biased by exclusions (Wardlaw et al., 2009).

9.3.4 PVS measurements limited to BG regions

In the beginning, we chose both BG and centrum semiovale (CS) as regions of interest to develop the semi-automatic PVS quantification method. However, we found that PVS in the CS were harder to quantify than the BG PVS because CS PVS were frequently running through the scan slice and sometimes obscured by confluent WMH. This was the same as the problem found in the development of a validated PVS rating scale where BG PVS showed higher observer agreement than in the BG regions (Potter, 2011). Therefore in later method optimization steps we limited PVS in the BG ovoid regions to increase measurement consistency.

Similar to the findings in this study, in a study of the associations between visual PVS scores and SVD features, Doubal et.al (Doubal et al., 2010b) using the same dataset found the same associations between BG PVS scores and WMH scores, Potter et.al (Potter et al., 2013) using a different dataset found that BG PVS were significantly associated with advancing age, CS PVS, atrophy and lacunar stroke, and CS PVS were mainly associated with BG PVS. Because BG PVS and CS PVS are inter-related, the associations we found between BG PVS and WMH, atrophy, blood markers and BBB permeability are likely to be generalized but require testing in larger dataset.

9.3.5 MRI technique development

Recent development of MRI scanner and new algorithms [1] produce high contrast resolution images, which is helpful for subtle lesions detection. In our study, a 1.5 T MRI scanner was used, and the imaging quality was

compromised by various limitations, including total scanning time, large slice thickness and uncontrolled patient movement. Fast slice acquisition techniques reduce image acquisition time to a fraction of a second, which minimise artefact caused by patients' movements (Gholipour et al., 2010). The increased signal at higher field strength (3.0 T) in recent MRI scanners also produces better overall image quality than these captured by 1.5 T (Bachmann et al., 2006). The new development in MRI devices and algorithms enables 3D reconstruction from volumetric images, which helps to assess anatomical structures and disease progression (Gholipour et al., 2010; Yang et al., 2011) and this trend will facilitate further researches in SVD and BBB.

9.4 Implications for further studies

9.4.1 BBB studies

In our human BBB structure literature search, in both the junctional proteins and PVS (Figure 9.2), we found that there was a lack of human anatomical and pathological studies and systematic description in regard to the different parts of the vascular tree in the brain. Our general concept of BBB structures and functions were mostly based on experimental evidence fragments from various animal and disease models under different triggers or microenvironment, which made it hard to compare studies, account for differences between animal models or even summarize them systematically. For example, we hypothesized that human general structure of PVS in the brain using combined information limited human untrastructural studies. There is a need for systematic reviews of BBB structure along the vascular tree in the same animal and more human studies of BBB structure.

Apart from junction proteins and PVS (Figure 9.2), researchers have increased interest in the interactions between endothelium and pericyte or glial cells. Besides their structural support for endothelium, pericytes have bidirectional contractile function in controlling capillary size and so play a major role in controlling cerebral blood flows (Peppiatt et al., 2006). Glial cells are involved in signal transport through a various factors they produced and removal of metabolic by-products (Alvarez et al., 2013; Xie et al., 2013). Systematic literature reviews of these two components in NVU are essential for further BBB studies.

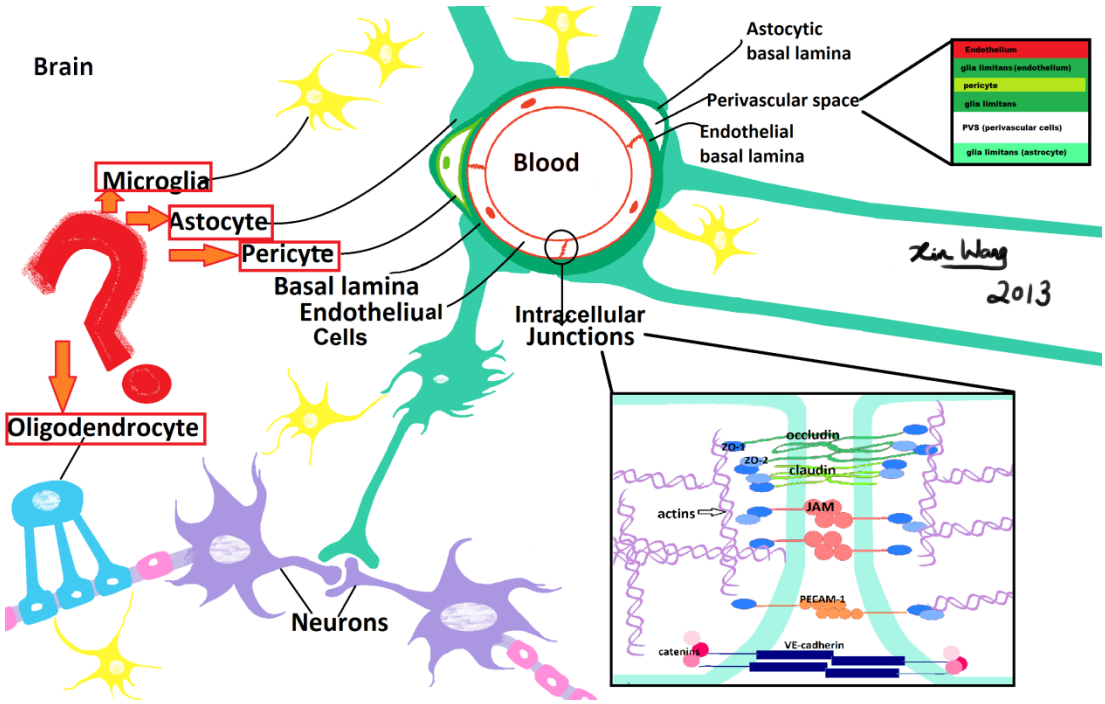

Figure 9.2 Increasing interests of pericyte and glias cells.

9.4.2 Unsolved questions for WMH artefacts

In the WMH artefacts chapter, there were three types of 'artefacts' we considered but we did not find relevant experiment and standards to deal with them in the previous literature: the "bright skull circle", "dirty WM" and "bright dots above the lateral ventricles" (Figure 9.3, the same as Figure

4.3). “Dirty WM” may not be an artefact; better ways of dealing with them consistently would be beneficial for further studies.

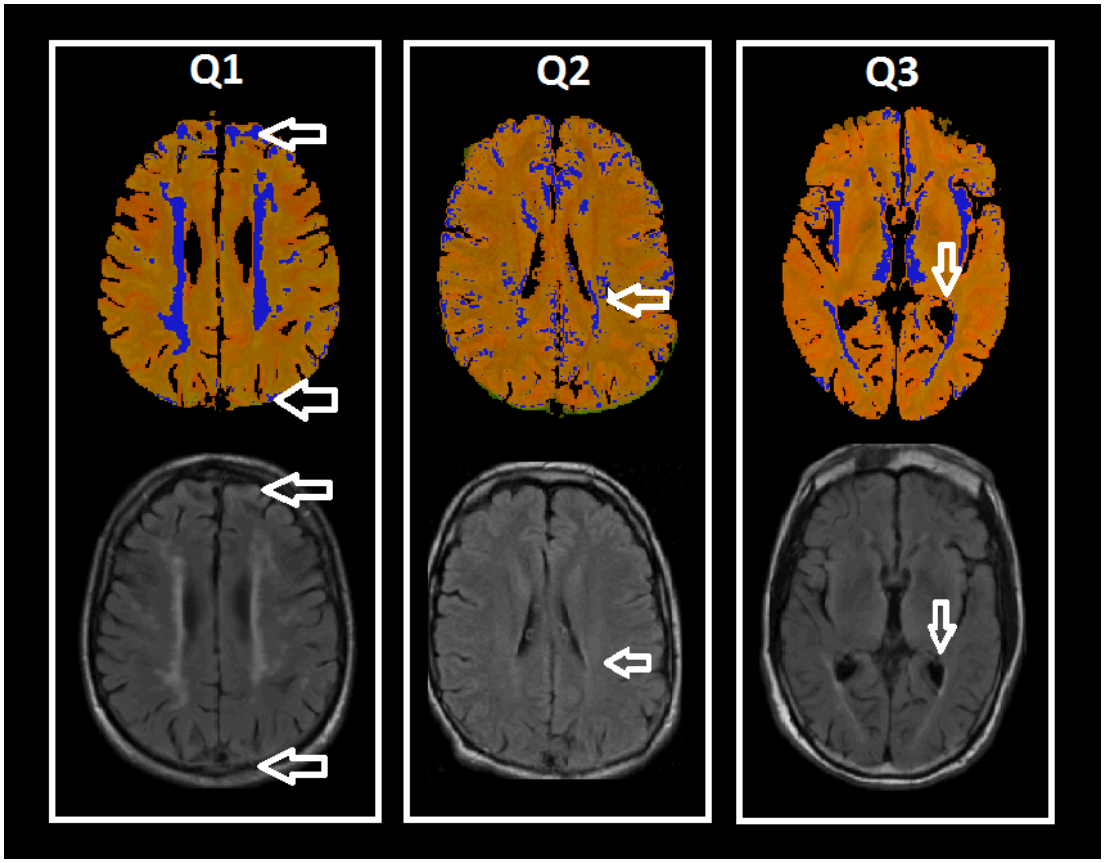

Figure 9.3 Three unsolved questions for WMH artefacts: “bright skull circle”, “dirty WM” and “bright dots above the lateral ventricles”

9.4.3 Stimuli for BBB dysfunctions

Besides the triggers relating to the ischemic and inflammatory stimuli of the BBB permeability mentioned in Chapter 2, other factors such as salt intake, smoking, sleeping problem (Xie et al., 2013), alcohol intake and hyperglycemia could potentially affect BBB function.

Increasing evidence showed that a high salt diet from food and drinks (more than 6 grams per day: (He et al., 2010)) have increasing risk of hypertension, cardiovascular disease, renal disease, osteoporosis, stomach cancer and obesity (He and MacGregor, 2009). Both animal experiments and human

epidemiological studies showed that a high salt diet had an effect on stroke, independent of and in addition to hypertension (He and MacGregor, 2009). High-salt intake also influenced nitric oxide (NO) metabolism. NO is a small molecule produced by endothelial nitric oxide synthases in response to shear from increased blood flow in arteries and has very important function as a vasodilator of the blood vessels. Levels of NO metabolites in plasma and urine, and endothelial-dependent vasodilation have been used to assess NO bioactivity in humans and showed that decreased NO-metabolite excretion and increased blood pressure were observed after high-salt intake (Hoffmann et al., 2007; Knottnerus et al., 2009). Inhibition of NO production may play a role in mediating endothelial dysfunction in high salt microenvironment.

Cigarette smoking was a risk factor for SVD (Khan et al., 2007) and was significantly related to stroke after adjusting age and hypertension (Wolf et al., 1988). Blood marker results from both smokers and non-smokers showed that smokers contained higher levels of vWF and more cytotoxic to endothelial cells in vitro (Blann and McCollum, 1993). Smoking was significantly associated with systemic inflammation in men because smokers had higher values for white blood cell count, fibrinogen, plasma viscosity, and C-reactive protein when compared to non-smokers (Frohlich et al., 2003). Smoking influenced proliferation, maturity state, activity and immune responses of immune cells in cultured cells and experimental animals. One molecular mechanism behind the association between smoking and inflammation involved the nuclear factor kappa B which is a gene transcription factor mediates gene transcription and cytokine expression. There was an increase in nuclear factor kappa B DNA binding in current

smokers smoking patients when compared with non-smokers (Goncalves et al., 2011). Smoking may possibly trigger BBB permeability through its effect on endothelium and inflammation through tissue plasminogen activator, Interleukin-6 or fibrinogen.

Worsening or disturbance of sleep was progressively associated with many neurological disorders such as dementia, stroke and death in humans (Montagna et al., 2003; Underwood, 2013). The brain is fragile to neurotoxic waste but it lacks a conventional lymphatic system which removes high metabolic products through lymphatic vessels. The PVS plays a crucial role in removing waste and fluid from the brain. The convective changes between cerebrospinal fluid (CSF) influx along the arteries and interstitial fluid (ISF) around the veins functioned homologous to peripheral lymphatic system and were named as the "glymphatic" system based on their dependence on aquaporin-4 water channels on astrocytic endfeet (Xie et al., 2013). Recently researchers found that cortical interstitial space increases by more than two thirds during sleep compared with awake state, and sleeping facilitated the efficient clear out of amyloid-β (Xie et al., 2013). Sleeping also assisted the removal of other neurotoxic compounds (e.g. adenosine) or supressed their production (e.g. noradrenaline) (Herculano-Houzel, 2013; Underwood, 2013; Xie et al., 2013). Therefore, sleeping is probably even more important than presumably thought for balanced cerebral metabolism and its disturbance could be a trigger for neurotoxic waste accumulation, exacerbate BBB malfunction and further lead to neurological disorders.

Alcohol abuse is related to cerebral atrophy and WMH (den Heijer et al., 2004; Mann et al., 2001). Alcohol abuse maybe another trigger for BBB dysfunction. In cultured bovine brain microvascular endothelial cells,

oxidative stress induced by ethanol metabolism lead to myosin light chain kinase activation and tight junction phosphorylation. The cytoskeletal alterations resulted in BBB impairment which was assessed by transendothelial electrical resistance (Haorah et al., 2005a; Haorah et al., 2005b; Haorah et al., 2007).

Diabetic patients had increased BBB permeability suggested on contrast enhancement MRI (Starr et al., 2003). Expression and activity of MMPs is increased in diabetic patients and MMPs also enhance blood coagulability, and they contribute to acute thrombotic occlusion of vessels (Kadoglou et al., 2005). MMP was associated with junction protein degradation and was a known mediator of BBB impairment. In the diabetic rat models, both hyperglycaemia and increased plasma MMP activity contributed to increased BBB permeability through decreased tight junction proteins (occludin and ZO-1) production and disruption (Hawkins et al., 2007). Targeting to decrease plasma MMP activity may benefit BBB protection in diabetic patients.

9.4.4 Further risk factors studies

In our studies of risk factor association and BBB stimuli, we found the risk factors smoking, hypertension and alcohol could be refined in the analysis and salt intake and sleeping difficulties should be considered as risk factors.

For smoking, dichotomous categories (never versus ever smoked) was better than four smoking categories which separated ever smoked into recent smoker, smoker and heavy smoker; could the fewer categories increased statistical power by having larger numbers of patients in the same category. Apart from having a potentially bad life style behind the smoking habit, one

study reported that relative risk of stroke in heavy smokers (greater than 40 cigarettes per day) was doubled than that of light smokers (fewer than ten cigarettes per day) (Wolf et al., 1988), that results probably influenced by the age difference which they did not adjust for. Our results between blood markers and smoking still need to be confirmed by a larger sample size.

In recent cancer studies, researchers suggested that there was no safe threshold for alcohol and high consumption increased cancer risk (Nelson et al., 2013). Should the behaviour of alcohol drinking as a risk factor such as smoking, hypertension and diabetes, instead of just measuring the alcohol excess intake in the future? However, if we need to use the amount of alcohol intake as a risk factor, there is need to set a standard of converting different types of alcohol intake into ethanol intake, which is very hard to apply in reality (Vasdev et al., 2006).

For the current study, we measured patients' blood pressures at the time of scanning; however, this was probably not very representative of the patient's usual blood pressure. For future studies, we suggest a more detailed blood pressure measurement, for example, by monitoring patients' 24-hour blood pressure to identify patients' usual blood pressure and other parameters such as blood pressure variability.

Apart from refinements of traditional risk factors listed above, we suggest adding salt intake and sleeping problems as risk factors in further studies.

9.4.5 Optimization in PVS rating scale

The PVS visual rating score categories needs further modifications. The PVS category intervals are equal in size from score 0 to 2 (0=no PVS, 1=<10 PVS, 2=11–20 PVS), but not for higher scores, for example for score 3 it is 21-40

PVS. Score 3 could possibly be narrowed down and possible separated into two scores, for example 3=21-30 PVS and 4=31-40, to make the spread of scores better. There is a need for more standardized ways to deal with high background signal instead of giving it score 4.

9.4.6 Further optimization in PVS method

The volumetric PVS measurement method (Descombes et al., 2004) could be considered in further use if one could remove intense programming and be modified as user friendly. The multiple thresholds step in our method could be applied in further PVS studies and the time-consuming problem of finding thresholds could be solved by making the multiple threshold selection and combination part automatic, probably through a program that one only needs to input values of the first and last threshold. Both optimizations would possibly be complementary methods in CS PVS measurement.

9.4.7 More ways to improve pathological brain segmentation and analysis

Future studies of SVD should avoid using bias field corrected images in stroke and WMH segmentation with better methods of removing bias field artefacts without distorting the true lesions. It is essential to adjust statistical analysis for age and hypertension, especially for PVS studies, because they are two important influencing factors for PVS.

9.4.8 Peripheral blood marker studies

Apart from blood markers of endothelial function, inflammation and thrombosis measured in the current study, further studies investing associations between blood markers and PVS could consider measuring oxidized low-density lipoprotein and neopterin.

9.5 Recent publications relating to novel imaging markers

Besides the contrast agent gadodiamide we used in the dynamic contrast enhancing MRI to detect BBB permeability, other imaging marker such as 11C-[R]-PK11195 used in positron emission tomography (PET) (Radlinska et al., 2009) and targeted MRI contrast agent (Hoyte et al., 2010) enabled sensitive detection of inflammatory processes in human and mice. 11C-[R]-PK11195 used in human PET imaging is a radioligand which binds to the mitochondrial membrane of cerebral activated microglia cells (Radlinska et al., 2009). Targeted MRI contrast agent based on iron oxide microparticles enabled visualization of vascular cell adhesion molecule 1 (VCAM-1) through their specific binding at the acute stage of ischemia (Hoyte et al., 2010). Based on the same mechanism, other junctional proteins located in the cerebral endothelium could be potentially selected as targets and be visualized in vivo. These two types of imaging markers showed promising potentials for imaging studies, however, more metabolic and drainage kinetic experiments are needed to prove their safeties before use in clinical studies.

9.6 Conclusions

In conclusion, neuroimaging is essential for cerebral SVD and BBB dysfunction investigation, and PVS is an important imaging feature of SVD which related to BBB permeability. In this work, we highlighted the importance of BBB and PVS pathophysiology, and highlighted the importance of WMH accurate measurement by excluding artefacts and stroke lesions. We developed a BG PVS computational method and this is the first time analysis examined the associations between BG PVS computational

count/volume and SVD markers, blood markers and BBB permeability, which will hopefully be helpful in future investigations of SVD diagnostic and prognostic significance.

Reference List

Abbott, N.J., 2004. Evidence for bulk flow of brain interstitial fluid: significance for physiology and pathology. Neurochem Int 45, 545-552.

Abbott, N.J., Ronnback, L., Hansson, E., 2006. Astrocyte-endothelial interactions at the blood-brain barrier. Nat Rev Neurosci 7, 41-53.

Abraham, C.S., Harada, N., Deli, M.A., Niwa, M., 2002. Transient forebrain ischemia increases the blood-brain barrier permeability for albumin in stroke-prone spontaneously hypertensive rats. Cell Mol Neurobiol 22, 455-462.

Abu Fanne, R., Nassar, T., Yarovoi, S., Rayan, A., Lamensdorf, I., Karakoveski, M., Vadim, P., Jammal, M., Cines, D.B., Higazi, A.A., 2010. Blood-brain barrier permeability and tPA-mediated neurotoxicity. Neuropharmacology 58, 972-980.

Adibhatla, R.M., Hatcher, J.F., 2008. Tissue plasminogen activator (tPA) and matrix metalloproteinases in the pathogenesis of stroke: therapeutic strategies. CNS Neurol Disord Drug Targets 7, 243-253.

Aggarwal, S., Yurlova, L., Simons, M., 2011. Central nervous system myelin: structure, synthesis and assembly. Trends Cell Biol 21, 585-593.

Agrawal, S., Anderson, P., Durbeej, M., van Rooijen, N., Ivars, F., Opdenakker, G., Sorokin, L.M., 2006. Dystroglycan is selectively cleaved at the parenchymal basement membrane at sites of leukocyte extravasation in experimental autoimmune encephalomyelitis. J Exp Med 203, 1007-1019.

Ahn, B.J., Lee, H.J., Shin, M.W., Choi, J.H., Jeong, J.W., Kim, K.W., 2009. Ninjurin1 is expressed in myeloid cells and mediates endothelium adhesion in the brains of EAE rats. Biochem Biophys Res Commun 387, 321-325.

Al-Saeed, O., Athyal, R., Ismail, M., Sheikh, M., 2012. Significance of Virchow-Robin spaces in patients newly diagnosed with multiple sclerosis: a case-control study in an Arab population. Med Princ Pract 21, 447-451.

Alkan, O., Kizilkilic, O., Yildirim, T., Alibek, S., 2009. Comparison of contrast-enhanced T1-weighted FLAIR with BLADE, and spin-echo T1-weighted sequences in intracranial MRI. Diagn Interv Radiol 15, 75-80.

Alvarez, J.I., Katayama, T., Prat, A., 2013. Glial influence on the blood brain barrier. Glia 61, 1939-1958.

Ampawong, S., Combes, V., Hunt, N.H., Radford, J., Chan-Ling, T., Pongponratn, E., Grau, G.E., 2011. Quantitation of brain edema and localisation of aquaporin 4

expression in relation to susceptibility to experimental cerebral malaria. Int J Clin Exp Pathol 4, 566-574.

Andrews, A.L., Bucchieri, F., Arima, K., Izuhara, K., Holgate, S.T., Davies, D.E., Holloway, J.W., 2007. Effect of IL-13 receptor alpha2 levels on the biological activity of IL-13 variant R110Q. J Allergy Clin Immunol 120, 91-97.

Anthony, I.C., Crawford, D.H., Bell, J.E., 2003. B lymphocytes in the normal brain: contrasts with HIV-associated lymphoid infiltrates and lymphomas. Brain 126, 1058-1067.

Anthoons, J.A., Van Marck, E.A., Gigase, P.L., Stevens, W.J., 1989. Immunohistochemical characterization of the mononuclear cells in the brain of the rat with an experimental chronic Trypanosoma brucei gambiense infection. Parasitol Res 75, 251-256.

Appelman, A.P., Exalto, L.G., van der Graaf, Y., Biessels, G.J., Mali, W.P., Geerlings, M.I., 2009. White matter lesions and brain atrophy: more than shared risk factors? A systematic review. Cerebrovasc Dis 28, 227-242.

Aprile, I., Scapeccia, M., Principi, M., Ottaviano, P., 2003. The effect of magnetisation transfer contrast on cerebrospinal fluid on motion artefacts on fluid-attenuated inversion-recovery images. Neuroradiology 45, 893-895.

Aribisala, B.S., Valdes Hernandez, M.C., Royle, N.A., Morris, Z., Munoz Maniega, S., Bastin, M.E., Deary, I.J., Wardlaw, J.M., 2012. Brain atrophy associations with white matter lesions in the ageing brain: the Lothian Birth Cohort 1936. Eur Radiol 23, 1084-1092.

Aribisala, B.S., Wiseman, S., Morris, Z., Valdes-Hernandez, M.C., Royle, N.A., Maniega, S.M., Gow, A.J., Corley, J., Bastin, M.E., Starr, J., Deary, I.J., Wardlaw, J.M., 2014. Circulating inflammatory markers are associated with magnetic resonance imaging-visible perivascular spaces but not directly with white matter hyperintensities. Stroke 45, 605-607.

Armitage, P.A., Farrall, A.J., Carpenter, T.K., Doubal, F.N., Wardlaw, J.M., 2011. Use of dynamic contrast-enhanced MRI to measure subtle blood-brain barrier abnormalities. Magn Reson Imaging 29, 305-314.

Armulik, A., Abramsson, A., Betsholtz, C., 2005. Endothelial/pericyte interactions. Circ Res 97, 512-523.

Armulik, A., Genove, G., Mae, M., Nisancioglu, M.H., Wallgard, E., Niaudet, C., He, L., Norlin, J., Lindblom, P., Strittmatter, K., Johansson, B.R., Betsholtz, C., 2010. Pericytes regulate the blood-brain barrier. Nature 468, 557-561.

Attwell, D., Buchan, A.M., Charpak, S., Lauritzen, M., Macvicar, B.A., Newman, E.A., 2010. Glial and neuronal control of brain blood flow. Nature 468, 232-243.

Atwood, L.D., Wolf, P.A., Heard-Costa, N.L., Massaro, J.M., Beiser, A., D'Agostino, R.B., DeCarli, C., 2004. Genetic variation in white matter hyperintensity volume in the Framingham Study. Stroke 35, 1609-1613.

Azevedo, F.A., Carvalho, L.R., Grinberg, L.T., Farfel, J.M., Ferretti, R.E., Leite, R.E., Jacob Filho, W., Lent, R., Herculano-Houzel, S., 2009. Equal numbers of neuronal and nonneuronal cells make the human brain an isometrically scaled-up primate brain. J Comp Neurol 513, 532-541.

Bachmann, R., Reilmann, R., Schwindt, W., Kugel, H., Heindel, W., Kramer, S., 2006. FLAIR imaging for multiple sclerosis: a comparative MR study at 1.5 and 3.0 Tesla. Eur Radiol 16, 915-921.

Bailey, W.M., 2007. Fast fluid attenuated inversion recovery (FLAIR) imaging and associated artefacts in magnetic resonance imaging (MRI). Radiography 13, 283-290.

Bakshi, R., Caruthers, S.D., Janardhan, V., Wasay, M., 2000. Intraventricular CSF pulsation artifact on fast fluid-attenuated inversion-recovery MR images: analysis of 100 consecutive normal studies. AJNR Am J Neuroradiol 21, 503-508.

Balabanov, R., Beaumont, T., Dore-Duffy, P., 1999. Role of central nervous system microvascular pericytes in activation of antigen-primed splenic T-lymphocytes. J Neurosci Res 55, 578-587.

Balabanov, R., Washington, R., Wagnerova, J., Dore-Duffy, P., 1996. CNS microvascular pericytes express macrophage-like function, cell surface integrin alpha M, and macrophage marker ED-2. Microvasc Res 52, 127-142.

Balda, M.S., Matter, K., 2000. The tight junction protein ZO-1 and an interacting transcription factor regulate ErbB-2 expression. EMBO J 19, 2024-2033.

Bamford, J., Sandercock, P., Dennis, M., Burn, J., Warlow, C., 1991. Classification and natural history of clinically identifiable subtypes of cerebral infarction. Lancet 337, 1521-1526.

Barrow, A.D., Burgess, S.C., Howes, K., Nair, V.K., 2003. Monocytosis is associated with the onset of leukocyte and viral infiltration of the brain in chickens infected with the very virulent Marek's disease virus strain C12/130. Avian Pathol 32, 183-191.

Bartels, A.L., Kortekaas, R., Bart, J., Willemsen, A.T., de Klerk, O.L., de Vries, J.J., van Oostrom, J.C., Leenders, K.L., 2009. Blood-brain barrier P-glycoprotein

function decreases in specific brain regions with aging: a possible role in progressive neurodegeneration. Neurobiol Aging 30, 1818-1824.

Bartels, A.L., Willemsen, A.T., Kortekaas, R., de Jong, B.M., de Vries, R., de Klerk, O., van Oostrom, J.C., Portman, A., Leenders, K.L., 2008. Decreased blood-brain barrier P-glycoprotein function in the progression of Parkinson's disease, PSP and MSA. J Neural Transm 115, 1001-1009.

Bauer, A.T., Burgers, H.F., Rabie, T., Marti, H.H., 2010. Matrix metalloproteinase-9 mediates hypoxia-induced vascular leakage in the brain via tight junction rearrangement. J Cereb Blood Flow Metab 30, 837-848.

Bazzoni, G., Dejana, E., 2004. Endothelial cell-to-cell junctions: molecular organization and role in vascular homeostasis. Physiol Rev 84, 869-901.

Bazzoni, G., Martinez-Estrada, O.M., Orsenigo, F., Cordenonsi, M., Citi, S., Dejana, E., 2000. Interaction of junctional adhesion molecule with the tight junction components ZO-1, cingulin, and occludin. J Biol Chem 275, 20520-20526.

Bechmann, I., Galea, I., Perry, V.H., 2007. What is the blood-brain barrier (not)? Trends Immunol 28, 5-11.

Bechmann, I., Kwidzinski, E., Kovac, A.D., Simburger, E., Horvath, T., Gimsa, U., Dirnagl, U., Priller, J., Nitsch, R., 2001. Turnover of rat brain perivascular cells. Exp Neurol 168, 242-249.

Bell, R.D., Winkler, E.A., Sagare, A.P., Singh, I., LaRue, B., Deane, R., Zlokovic, B.V., 2010. Pericytes control key neurovascular functions and neuronal phenotype in the adult brain and during brain aging. Neuron 68, 409-427.

Beschorner, R., Schluesener, H.J., Gozalan, F., Meyermann, R., Schwab, J.M., 2002. Infiltrating CD14+ monocytes and expression of CD14 by activated parenchymal microglia/macrophages contribute to the pool of CD14+ cells in ischemic brain lesions. J Neuroimmunol 126, 107-115.

Bitar, R., Leung, G., Perng, R., Tadros, S., Moody, A.R., Sarrazin, J., McGregor, C., Christakis, M., Symons, S., Nelson, A., Roberts, T.P., 2006. MR pulse sequences: what every radiologist wants to know but is afraid to ask. Radiographics 26, 513-537.

Bjarnegard, M., Enge, M., Norlin, J., Gustafsdottir, S., Fredriksson, S., Abramsson, A., Takemoto, M., Gustafsson, E., Fassler, R., Betsholtz, C., 2004. Endothelium-specific ablation of PDGFB leads to pericyte loss and glomerular, cardiac and placental abnormalities. Development 131, 1847-1857.

Bland, J.M., Altman, D.G., 1986. Statistical methods for assessing agreement between two methods of clinical measurement. Lancet 1, 307-310.

Blann, A.D., McCollum, C.N., 1993. Adverse influence of cigarette smoking on the endothelium. Thromb Haemost 70, 707-711.
Bloch, O., Manley, G.T., 2007. The role of aquaporin-4 in cerebral water transport and edema. Neurosurg Focus 22, E3.

Boado, R.J., Pardridge, W.M., 2002. Glucose deprivation and hypoxia increase the expression of the GLUT1 glucose transporter via a specific mRNA cis-acting regulatory element. J Neurochem 80, 552-554.

Bogie, J.F., Stinissen, P., Hellings, N., Hendriks, J.J., 2011. Myelin-phagocytosing macrophages modulate autoreactive T cell proliferation. J Neuroinflammation 8, 85.

Boven, L.A., Middel, J., Verhoef, J., De Groot, C.J., Nottet, H.S., 2000. Monocyte infiltration is highly associated with loss of the tight junction protein zonula occludens in HIV-1-associated dementia. Neuropathol Appl Neurobiol 26, 356-360.

Bradbury, M.W., Cserr, H.F., Westrop, R.J., 1981. Drainage of cerebral interstitial fluid into deep cervical lymph of the rabbit. Am J Physiol 240, F329-336.

Bradl, M., Lassmann, H., 2009. Oligodendrocytes: biology and pathology. Acta Neuropathol 119, 37-53.

Bradley, W.G., Jr., Whittemore, A.R., Watanabe, A.S., Davis, S.J., Teresi, L.M., Homyak, M., 1991. Association of deep white matter infarction with chronic communicating hydrocephalus: implications regarding the possible origin of normal-pressure hydrocephalus. AJNR Am J Neuroradiol 12, 31-39.

Breviario, F., Caveda, L., Corada, M., Martin-Padura, I., Navarro, P., Golay, J., Introna, M., Gulino, D., Lampugnani, M.G., Dejana, E., 1995. Functional properties of human vascular endothelial cadherin (7B4/cadherin-5), an endothelium-specific cadherin. Arterioscler Thromb Vasc Biol 15, 1229-1239.

Bronstein, J.M., Tiwari-Woodruff, S., Buznikov, A.G., Stevens, D.B., 2000. Involvement of OSP/claudin-11 in oligodendrocyte membrane interactions: role in biology and disease. J Neurosci Res 59, 706-711.

Brooks, T.A., Hawkins, B.T., Huber, J.D., Egleton, R.D., Davis, T.P., 2005. Chronic inflammatory pain leads to increased blood-brain barrier permeability and tight junction protein alterations. Am J Physiol Heart Circ Physiol 289, H738-743.

Brown, R.C., Davis, T.P., 2005. Hypoxia/aglycemia alters expression of occludin and actin in brain endothelial cells. Biochem Biophys Res Commun 327, 1114-1123.

Brown, W.R., Moody, D.M., Challa, V.R., Thore, C.R., Anstrom, J.A., 2002. Venous collagenosis and arteriolar tortuosity in leukoaraiosis. J Neurol Sci 203-204, 159-163.

Cahoy, J.D., Emery, B., Kaushal, A., Foo, L.C., Zamanian, J.L., Christopherson, K.S., Xing, Y., Lubischer, J.L., Krieg, P.A., Krupenko, S.A., Thompson, W.J., Barres, B.A., 2008. A transcriptome database for astrocytes, neurons, and oligodendrocytes: a new resource for understanding brain development and function. J Neurosci 28, 264-278.

Carare, R.O., Bernardes-Silva, M., Newman, T.A., Page, A.M., Nicoll, J.A., Perry, V.H., Weller, R.O., 2008. Solutes, but not cells, drain from the brain parenchyma along basement membranes of capillaries and arteries: significance for cerebral amyloid angiopathy and neuroimmunology. Neuropathol Appl Neurobiol 34, 131-144.

Cardoso, F.L., Brites, D., Brito, M.A., 2010. Looking at the blood-brain barrier: molecular anatomy and possible investigation approaches. Brain Res Rev 64, 328-363.

Carvey, P.M., Hendey, B., Monahan, A.J., 2009. The blood-brain barrier in neurodegenerative disease: a rhetorical perspective. J Neurochem 111, 291-314.

Chang, H.W., Wu, V.C., Huang, C.Y., Huang, H.Y., Chen, Y.M., Chu, T.S., Wu, K.D., Hsieh, B.S., 2008. D4 dopamine receptor enhances angiotensin II-stimulated aldosterone secretion through PKC-epsilon and calcium signaling. Am J Physiol Endocrinol Metab 294, E622-629.

Chen, W., Song, X., Zhang, Y., 2011. Assessment of the Virchow-Robin Spaces in Alzheimer disease, mild cognitive impairment, and normal aging, using high-field MR imaging. AJNR Am J Neuroradiol 32, 1490-1495.

Choi, P., Ren, M., Phan, T.G., Callisaya, M., Ly, J.V., Beare, R., Chong, W., Srikanth, V., 2012. Silent infarcts and cerebral microbleeds modify the associations of white matter lesions with gait and postural stability: population-based study. Stroke 43, 1505-1510.

Cianfoni, A., Martin, M.G., Du, J., Hesselink, J.R., Imbesi, S.G., Bradley, W.G., Bydder, G.M., 2006. Artifact simulating subarachnoid and intraventricular hemorrhage on single-shot, fast spin-echo fluid-attenuated inversion recovery images caused by head movement: A trap for the unwary. AJNR Am J Neuroradiol 27, 843-849.

Cirrito, J.R., Deane, R., Fagan, A.M., Spinner, M.L., Parsadanian, M., Finn, M.B., Jiang, H., Prior, J.L., Sagare, A., Bales, K.R., Paul, S.M., Zlokovic, B.V., Piwnica-Worms, D., Holtzman, D.M., 2005. P-glycoprotein deficiency at the blood-brain barrier increases amyloid-beta deposition in an Alzheimer disease mouse model. J Clin Invest 115, 3285-3290.

Clay, C.C., Rodrigues, D.S., Ho, Y.S., Fallert, B.A., Janatpour, K., Reinhart, T.A., Esser, U., 2007. Neuroinvasion of fluorescein-positive monocytes in acute simian immunodeficiency virus infection. J Virol 81, 12040-12048.

Cohen-Kashi Malina, K., Cooper, I., Teichberg, V.I., 2009. Closing the gap between the in-vivo and in-vitro blood-brain barrier tightness. Brain Res 1284, 12-21.

Cordonnier, C., Al-Shahi Salman, R., Wardlaw, J., 2007. Spontaneous brain microbleeds: systematic review, subgroup analyses and standards for study design and reporting. Brain 130, 1988-2003.

Corkill, R.G., Garnett, M.R., Blamire, A.M., Rajagopalan, B., Cadoux-Hudson, T.A., Styles, P., 2003. Multi-modal MRI in normal pressure hydrocephalus identifies pre-operative haemodynamic and diffusion coefficient changes in normal appearing white matter correlating with surgical outcome. Clin Neurol Neurosurg 105, 193-202.

Cuevas, P., Gutierrez-Diaz, J.A., Reimers, D., Dujovny, M., Diaz, F.G., Ausman, J.I., 1984. Pericyte endothelial gap junctions in human cerebral capillaries. Anat Embryol (Berl) 170, 155-159.

Cui, L., Zhang, X., Yang, R., Wang, L., Liu, L., Li, M., Du, W., 2010. Neuroprotection of early and short-time applying atorvastatin in the acute phase of cerebral ischemia: down-regulated 12/15-LOX, p38MAPK and cPLA2 expression, ameliorated BBB permeability. Brain Res 1325, 164-173.

Cumurciuc, R., Guichard, J.P., Reizine, D., Gray, F., Bousser, M.G., Chabriat, H., 2006. Dilation of Virchow-Robin spaces in CADASIL. Eur J Neurol 13, 187-190.

Curati, W.L., Oatridge, A., Herlihy, A.H., Hajnal, J.V., Puri, B.K., Bydder, G.M., 2001. Contributions of an adiabatic initial inversion pulse and K-space re-ordered by inversion-time at each slice position (KRISP) to control of CSF artifacts and visualization of the brain in FLAIR magnetic resonance imaging. Clin Radiol 56, 375-384.

Dbouk, H.A., Mroue, R.M., El-Sabban, M.E., Talhouk, R.S., 2009. Connexins: a myriad of functions extending beyond assembly of gap junction channels. Cell Commun Signal 7, 4.

de la Monte, S., Castro, F., Bonilla, N.J., Gaskin de Urdaneta, A., Hutchins, G.M., 1985. The systemic pathology of Venezuelan equine encephalitis virus infection in humans. Am J Trop Med Hyg 34, 194-202.

de Leeuw, F.E., Korf, E., Barkhof, F., Scheltens, P., 2006. White matter lesions are associated with progression of medial temporal lobe atrophy in Alzheimer disease. Stroke 37, 2248-2252.

Deane, R., Wu, Z., Zlokovic, B.V., 2004. RAGE (yin) versus LRP (yang) balance regulates alzheimer amyloid beta-peptide clearance through transport across the blood-brain barrier. Stroke 35, 2628-2631.

Deary, I.J., Gow, A.J., Taylor, M.D., Corley, J., Brett, C., Wilson, V., Campbell, H., Whalley, L.J., Visscher, P.M., Porteous, D.J., Starr, J.M., 2007. The Lothian Birth Cohort 1936: a study to examine influences on cognitive ageing from age 11 to age 70 and beyond. BMC Geriatr 7, 28.

Debette, S., Markus, H.S., 2010. The clinical importance of white matter hyperintensities on brain magnetic resonance imaging: systematic review and meta-analysis. BMJ 341, c3666.

Dejana, E., 1996. Endothelial adherens junctions: implications in the control of vascular permeability and angiogenesis. J Clin Invest 98, 1949-1953.

Dejana, E., Lampugnani, M.G., Martinez-Estrada, O., Bazzoni, G., 2000. The molecular organization of endothelial junctions and their functional role in vascular morphogenesis and permeability. Int J Dev Biol 44, 743-748.

Del Maschio, A., De Luigi, A., Martin-Padura, I., Brockhaus, M., Bartfai, T., Fruscella, P., Adorini, L., Martino, G., Furlan, R., De Simoni, M.G., Dejana, E., 1999. Leukocyte recruitment in the cerebrospinal fluid of mice with experimental meningitis is inhibited by an antibody to junctional adhesion molecule (JAM). J Exp Med 190, 1351-1356.

del RÃ-o Hortega, P.o., Penfield, W., 1927. Cerebral cicatrix: the reaction of neuroglia and microglia to brain wounds.

del Zoppo, G.J., 2010a. The neurovascular unit in the setting of stroke. J Intern Med 267, 156-171.

del Zoppo, G.J., 2010b. The neurovascular unit, matrix proteases, and innate inflammation. Ann N Y Acad Sci 1207, 46-49.

del Zoppo, G.J., Milner, R., 2006. Integrin-matrix interactions in the cerebral microvasculature. Arterioscler Thromb Vasc Biol 26, 1966-1975.

DeLisser, H.M., Newman, P.J., Albelda, S.M., 1994. Molecular and functional aspects of PECAM-1/CD31. Immunol Today 15, 490-495.

den Heijer, T., Vermeer, S.E., van Dijk, E.J., Prins, N.D., Koudstaal, P.J., van Duijn, C.M., Hofman, A., Breteler, M.M., 2004. Alcohol intake in relation to brain magnetic resonance imaging findings in older persons without dementia. Am J Clin Nutr 80, 992-997.

Descombes, X., Kruggel, F., Wollny, G., Gertz, H.J., 2004. An object-based approach for detecting small brain lesions: application to Virchow-Robin spaces. IEEE Trans Med Imaging 23, 246-255.

Di Costanzo, A., Di Salle, F., Santoro, L., Bonavita, V., Tedeschi, G., 2001. Dilated Virchow-Robin spaces in myotonic dystrophy: frequency, extent and significance. Eur Neurol 46, 131-139.

Dienel, G.A., 2012. Brain lactate metabolism: the discoveries and the controversies. J Cereb Blood Flow Metab 32, 1107-1138.

Dore-Duffy, P., 2008. Pericytes: pluripotent cells of the blood brain barrier. Curr Pharm Des 14, 1581-1593.

Dore-Duffy, P., Cleary, K., 2010. Morphology and properties of pericytes. Methods Mol Biol 686, 49-68.

Doubal, F.N., Dennis, M.S., Wardlaw, J.M., 2010a. Characteristics of patients with minor ischaemic strokes and negative MRI: a cross-sectional study. J Neurol Neurosurg Psychiatry 82, 540-542.

Doubal, F.N., MacLullich, A.M., Ferguson, K.J., Dennis, M.S., Wardlaw, J.M., 2010b. Enlarged perivascular spaces on MRI are a feature of cerebral small vessel disease. Stroke 41, 450-454.

Du, Y., Dreyfus, C.F., 2002. Oligodendrocytes as providers of growth factors. J Neurosci Res 68, 647-654.

Dufouil, C., Chalmers, J., Coskun, O., Besancon, V., Bousser, M.G., Guillon, P., MacMahon, S., Mazoyer, B., Neal, B., Woodward, M., Tzourio-Mazoyer, N., Tzourio, C., 2005. Effects of blood pressure lowering on cerebral white matter hyperintensities in patients with stroke: the PROGRESS (Perindopril Protection Against Recurrent Stroke Study) Magnetic Resonance Imaging Substudy. Circulation 112, 1644-1650.

Dufouil, C., de Kersaint-Gilly, A., Besancon, V., Levy, C., Auffray, E., Brunnereau, L., Alperovitch, A., Tzourio, C., 2001. Longitudinal study of blood pressure and white matter hyperintensities: the EVA MRI Cohort. Neurology 56, 921-926.

Duz, B., Oztas, E., Erginay, T., Erdogan, E., Gonul, E., 2007. The effect of moderate hypothermia in acute ischemic stroke on pericyte migration: an ultrastructural study. Cryobiology 55, 279-284.

Ekre, O., Borjesson, M., Edvardsson, N., Eliasson, T., Mannheimer, C., 2003. Feasibility of spinal cord stimulation in angina pectoris in patients with chronic pacemaker treatment for cardiac arrhythmias. Pacing Clin Electrophysiol 26, 2134-2141.

ElAli, A., Hermann, D.M., 2011. ATP-binding cassette transporters and their roles in protecting the brain. Neuroscientist 17, 423-436.

Erasmus, L., Hurter, D., NaudÃ©, M., Kritzinger, H., Acho, S., 2009. A short overview of MRI artefacts. South African Journal of Radiology 8.

Erdfelder, E., Faul, F., Buchner, A., 1996. GPOWER: A general power analysis program. Behavior research methods, instruments, & computers 28, 1-11.

Esiri, M.M., Gay, D., 1990. Immunological and neuropathological significance of the Virchow-Robin space. J Neurol Sci 100, 3-8.

Etemadifar, M., Hekmatnia, A., Tayari, N., Kazemi, M., Ghazavi, A., Akbari, M., Maghzi, A.H., 2010. Features of Virchow-Robin spaces in newly diagnosed multiple sclerosis patients. Eur J Radiol 80, e104-108.

Eugenin, E.A., Clements, J.E., Zink, M.C., Berman, J.W., 2011. Human immunodeficiency virus infection of human astrocytes disrupts blood-brain barrier integrity by a gap junction-dependent mechanism. J Neurosci 31, 9456-9465.

Farkas, E., Luiten, P.G., 2001. Cerebral microvascular pathology in aging and Alzheimer's disease. Prog Neurobiol 64, 575-611.

Farrall, A.J., Wardlaw, J.M., 2007. Blood-brain barrier: ageing and microvascular disease--systematic review and meta-analysis. Neurobiol Aging 30, 337-352.

Farrell, C., Chappell, F., Armitage, P.A., Keston, P., Maclullich, A., Shenkin, S., Wardlaw, J.M., 2009. Development and initial testing of normal reference MR images for the brain at ages 65-70 and 75-80 years. Eur Radiol 19, 177-183.

Feigin, V.L., Lawes, C.M., Bennett, D.A., Anderson, C.S., 2003. Stroke epidemiology: a review of population-based studies of incidence, prevalence, and case-fatality in the late 20th century. Lancet Neurol 2, 43-53.

Ferguson, K.J., Wardlaw, J.M., Edmond, C.L., Deary, I.J., Maclullich, A.M., 2005. Intracranial area: a validated method for estimating intracranial volume. J Neuroimaging 15, 76-78.

Fiala, M., Liu, Q.N., Sayre, J., Pop, V., Brahmandam, V., Graves, M.C., Vinters, H.V., 2002. Cyclooxygenase-2-positive macrophages infiltrate the Alzheimer's disease brain and damage the blood-brain barrier. Eur J Clin Invest 32, 360-371.

Fisher, C.M., 1968. The arterial lesions underlying lacunes. Acta Neuropathol 12, 1-15.

Fisher, C.M., 1979. Capsular infarcts: the underlying vascular lesions. Arch Neurol 36, 65-73.

Fisher, C.M., 1982. Lacunar strokes and infarcts: a review. Neurology 32, 871-876.

Fisher, C.M., 1998. Lacunes: small, deep cerebral infarcts. 1965. Neurology 50, 841 and 811 pages following.

Flossmann, E., 2006. Genetics of ischaemic stroke; single gene disorders. Int J Stroke 1, 131-139.

Folsom, A.R., Rosamond, W.D., Shahar, E., Cooper, L.S., Aleksic, N., Nieto, F.J., Rasmussen, M.L., Wu, K.K., 1999. Prospective study of markers of hemostatic function with risk of ischemic stroke. The Atherosclerosis Risk in Communities (ARIC) Study Investigators. Circulation 100, 736-742.

Fox, N.C., Schott, J.M., 2004. Imaging cerebral atrophy: normal ageing to Alzheimer's disease. Lancet 363, 392-394.

Franke, C.L., van Swieten, J.C., van Gijn, J., 1991. Residual lesions on computed tomography after intracerebral hemorrhage. Stroke 22, 1530-1533.

Franklin, R.J., Bussey, T.J., 2013. Do your glial cells make you clever? Cell Stem Cell 12, 265-266.

Frohlich, M., Sund, M., Lowel, H., Imhof, A., Hoffmeister, A., Koenig, W., 2003. Independent association of various smoking characteristics with markers of systemic inflammation in men. Results from a representative sample of the general population (MONICA Augsburg Survey 1994/95). Eur Heart J 24, 1365-1372.

Furuse, M., Fujita, K., Hiiragi, T., Fujimoto, K., Tsukita, S., 1998. Claudin-1 and -2: novel integral membrane proteins localizing at tight junctions with no sequence similarity to occludin. J Cell Biol 141, 1539-1550.

Furuse, M., Furuse, K., Sasaki, H., Tsukita, S., 2001. Conversion of zonulae occludentes from tight to leaky strand type by introducing claudin-2 into Madin-Darby canine kidney I cells. J Cell Biol 153, 263-272.

Furuse, M., Hirase, T., Itoh, M., Nagafuchi, A., Yonemura, S., Tsukita, S., 1993. Occludin: a novel integral membrane protein localizing at tight junctions. J Cell Biol 123, 1777-1788.

Furuse, M., Itoh, M., Hirase, T., Nagafuchi, A., Yonemura, S., Tsukita, S., 1994. Direct association of occludin with ZO-1 and its possible involvement in the localization of occludin at tight junctions. J Cell Biol 127, 1617-1626.

Galea, I., Palin, K., Newman, T.A., Van Rooijen, N., Perry, V.H., Boche, D., 2005. Mannose receptor expression specifically reveals perivascular macrophages in normal, injured, and diseased mouse brain. Glia 49, 375-384.

Garde, E., Lykke Mortensen, E., Rostrup, E., Paulson, O.B., 2005. Decline in intelligence is associated with progression in white matter hyperintensity volume. J Neurol Neurosurg Psychiatry 76, 1289-1291.

Garden, G.A., Moller, T., 2006. Microglia biology in health and disease. J Neuroimmune Pharmacol 1, 127-137.

Gauden, V., Hu, D.E., Kurokawa, T., Sarker, M.H., Fraser, P.A., 2007. Novel technique for estimating cerebrovascular permeability demonstrates capsazepine protection following ischemia-reperfusion. Microcirculation 14, 767-778.

Gawne-Cain, M.L., Silver, N.C., Moseley, I.F., Miller, D.H., 1997. Fast FLAIR of the brain: the range of appearances in normal subjects and its application to quantification of white-matter disease. Neuroradiology 39, 243-249.

Gay, F.W., 2006. Early cellular events in multiple sclerosis. Intimations of an extrinsic myelinolytic antigen. Clin Neurol Neurosurg 108, 234-240.

Gholipour, A., Estroff, J.A., Warfield, S.K., 2010. Robust super-resolution volume reconstruction from slice acquisitions: application to fetal brain MRI. IEEE Trans Med Imaging 29, 1739-1758.

Giri, R., Shen, Y., Stins, M., Du Yan, S., Schmidt, A.M., Stern, D., Kim, K.S., Zlokovic, B., Kalra, V.K., 2000. beta-amyloid-induced migration of monocytes across human brain endothelial cells involves RAGE and PECAM-1. Am J Physiol Cell Physiol 279, C1772-1781.

Goncalves, R.B., Coletta, R.D., Silverio, K.G., Benevides, L., Casati, M.Z., da Silva, J.S., Nociti, F.H., Jr., 2011. Impact of smoking on inflammation: overview of molecular mechanisms. Inflamm Res 60, 409-424.

Gorantla, S., Makarov, E., Finke-Dwyer, J., Castanedo, A., Holguin, A., Gebhart, C.L., Gendelman, H.E., Poluektova, L., 2010. Links between progressive HIV-1 infection of humanized mice and viral neuropathogenesis. Am J Pathol 177, 2938-2949.

Gorelick, P.B., Scuteri, A., Black, S.E., Decarli, C., Greenberg, S.M., Iadecola, C., Launer, L.J., Laurent, S., Lopez, O.L., Nyenhuis, D., Petersen, R.C., Schneider, J.A., Tzourio, C., Arnett, D.K., Bennett, D.A., Chui, H.C., Higashida, R.T., Lindquist, R., Nilsson, P.M., Roman, G.C., Sellke, F.W., Seshadri, S., 2011. Vascular contributions to cognitive impairment and dementia: a statement for healthcare professionals from the american heart association/american stroke association. Stroke 42, 2672-2713.

Gouw, A.A., van der Flier, W.M., Fazekas, F., van Straaten, E.C., Pantoni, L., Poggesi, A., Inzitari, D., Erkinjuntti, T., Wahlund, L.O., Waldemar, G., Schmidt, R., Scheltens, P., Barkhof, F., 2008a. Progression of white matter hyperintensities and incidence of new lacunes over a 3-year period: the Leukoaraiosis and Disability study. Stroke 39, 1414-1420.

Gouw, A.A., van der Flier, W.M., van Straaten, E.C., Pantoni, L., Bastos-Leite, A.J., Inzitari, D., Erkinjuntti, T., Wahlund, L.O., Ryberg, C., Schmidt, R., Fazekas, F., Scheltens, P., Barkhof, F., 2008b. Reliability and sensitivity of visual scales versus volumetry for evaluating white matter hyperintensity progression. Cerebrovasc Dis 25, 247-253.

Greenberg, S.M., Vernooij, M.W., Cordonnier, C., Viswanathan, A., Al-Shahi Salman, R., Warach, S., Launer, L.J., Van Buchem, M.A., Breteler, M.M., 2009. Cerebral microbleeds: a guide to detection and interpretation. Lancet Neurol 8, 165-174.

Gregory, T.F., Rennels, M.L., Blaumanis, O.R., Fujimoto, K., 1985. A method for microscopic studies of cerebral angioarchitecture and vascular-parenchymal relationships, based on the demonstration of 'paravascular' fluid pathways in the mammalian central nervous system. J Neurosci Methods 14, 5-14.

Groeschel, S., Chong, W.K., Surtees, R., Hanefeld, F., 2006. Virchow-Robin spaces on magnetic resonance images: normative data, their dilatation, and a review of the literature. Neuroradiology 48, 745-754.

Guillemaud, R., Brady, M., 1997. Estimating the bias field of MR images. IEEE Trans Med Imaging 16, 238-251.

Guillemin, G.J., Brew, B.J., 2004. Microglia, macrophages, perivascular macrophages, and pericytes: a review of function and identification. J Leukoc Biol 75, 388-397.

Hajnal, J.V., Oatridge, A., Herlihy, A.H., Bydder, G.M., 2001. Reduction of CSF artifacts on FLAIR images by using adiabatic inversion pulses. AJNR Am J Neuroradiol 22, 317-322.

Haller, S., Kovari, E., Herrmann, F.R., Cuvinciuc, V., Tomm, A.M., Zulian, G.B., Lovblad, K.O., Giannakopoulos, P., Bouras, C., 2013. Do brain T2/FLAIR white matter hyperintensities correspond to myelin loss in normal aging? A radiologic-neuropathologic correlation study. Acta Neuropathol Commun 1, 14.

Hanisch, U.K., Kettenmann, H., 2007. Microglia: active sensor and versatile effector cells in the normal and pathologic brain. Nat Neurosci 10, 1387-1394.

Hansson, E., Ronnback, L., 2003. Glial neuronal signaling in the central nervous system. FASEB J 17, 341-348.

Haorah, J., Heilman, D., Knipe, B., Chrastil, J., Leibhart, J., Ghorpade, A., Miller, D.W., Persidsky, Y., 2005a. Ethanol-induced activation of myosin light chain kinase leads to dysfunction of tight junctions and blood-brain barrier compromise. Alcohol Clin Exp Res 29, 999-1009.

Haorah, J., Knipe, B., Leibhart, J., Ghorpade, A., Persidsky, Y., 2005b. Alcohol-induced oxidative stress in brain endothelial cells causes blood-brain barrier dysfunction. J Leukoc Biol 78, 1223-1232.

Haorah, J., Ramirez, S.H., Schall, K., Smith, D., Pandya, R., Persidsky, Y., 2007. Oxidative stress activates protein tyrosine kinase and matrix metalloproteinases leading to blood-brain barrier dysfunction. J Neurochem 101, 566-576.

Hawkins, B.T., Lundeen, T.F., Norwood, K.M., Brooks, H.L., Egleton, R.D., 2007. Increased blood-brain barrier permeability and altered tight junctions in experimental diabetes in the rat: contribution of hyperglycaemia and matrix metalloproteinases. Diabetologia 50, 202-211.

Hawkins, C.P., McLaughlin, J.E., Kendall, B.E., McDonald, W.I., 1993. Pathological findings correlated with MRI in HIV infection. Neuroradiology 35, 264-268.
Hawkins, R.A., O'Kane, R.L., Simpson, I.A., Vina, J.R., 2006. Structure of the blood-brain barrier and its role in the transport of amino acids. J Nutr 136, 218S-226S.

He, F.J., Jenner, K.H., Macgregor, G.A., 2010. WASH-world action on salt and health. Kidney Int 78, 745-753.

He, F.J., MacGregor, G.A., 2009. A comprehensive review on salt and health and current experience of worldwide salt reduction programmes. J Hum Hypertens 23, 363-384.

He, G., Lu, T., Lu, B., Xiao, D., Yin, J., Liu, X., Qiu, G., Fang, M., Wang, Y., 2012. Perivascular and perineural extension of formed and soluble blood elements in an intracerebral hemorrhage rat model. Brain Res 1451, 10-18.

Herculano-Houzel, S., 2013. Neuroscience. Sleep it out. Science 342, 316-317.

Herlihy, A.H., Hajnal, J.V., Curati, W.L., Virji, N., Oatridge, A., Puri, B.K., Bydder, G.M., 2001a. Reduction of CSF and blood flow artifacts on FLAIR images of the brain with k-space reordered by inversion time at each slice position (KRISP). AJNR Am J Neuroradiol 22, 896-904.

Herlihy, A.H., Oatridge, A., Curati, W.L., Puri, B.K., Bydder, G.M., Hajnal, J.V., 2001b. FLAIR imaging using nonselective inversion pulses combined with slice excitation order cycling and k-space reordering to reduce flow artifacts. Magn Reson Med 46, 354-364.

Hermann, D.M., Bassetti, C.L., 2007. Implications of ATP-binding cassette transporters for brain pharmacotherapies. Trends Pharmacol Sci 28, 128-134.

Hernandez, M.D., Ferguson, K.J., Chappell, F.M., Wardlaw, J.M., 2010. New multispectral MRI data fusion technique for white matter lesion segmentation: method and comparison with thresholding in FLAIR images. Eur Radiol 20, 1684-1691.

Hernandez, M.D., Gallacher, P.J., Bastin, M.E., Royle, N.A., Maniega, S.M., Deary, I.J., Wardlaw, J.M., 2012. Automatic segmentation of brain white matter and white matter lesions in normal aging: comparison of five multispectral techniques. Magn Reson Imaging 30, 222-229.

Hernandez, M.D., Piper, R.J., Wang, X., Deary, I.J., Wardlaw, J.M., 2013. Towards the automatic computational assessment of enlarged perivascular spaces on brain magnetic resonance images: A systematic review. J Magn Reson Imaging.

Hernandez Mdel, C., Ferguson, K.J., Chappell, F.M., Wardlaw, J.M., 2010. New multispectral MRI data fusion technique for white matter lesion segmentation: method and comparison with thresholding in FLAIR images. Eur Radiol 20, 1684-1691.

Hess, D.C., Abe, T., Hill, W.D., Studdard, A.M., Carothers, J., Masuya, M., Fleming, P.A., Drake, C.J., Ogawa, M., 2004. Hematopoietic origin of microglial and perivascular cells in brain. Exp Neurol 186, 134-144.

Hickey, W.F., 2001. Basic principles of immunological surveillance of the normal central nervous system. Glia 36, 118-124.

Hirase, T., Kawashima, S., Wong, E.Y., Ueyama, T., Rikitake, Y., Tsukita, S., Yokoyama, M., Staddon, J.M., 2001. Regulation of tight junction permeability and occludin phosphorylation by Rhoa-p160ROCK-dependent and -independent mechanisms. J Biol Chem 276, 10423-10431.

Hochwald, G.M., Nakamura, S., Chase, R., Gorelick, J., 1984. Cerebrospinal fluid glucose and leukocyte responses in experimental meningitis. J Neurol Sci 63, 381-391.

Hoffmann, I.S., Alfieri, A.B., Cubeddu, L.X., 2007. Effects of lifestyle changes and metformin on salt sensitivity and nitric oxide metabolism in obese salt-sensitive Hispanics. J Hum Hypertens 21, 571-578.

Hollestelle, M.J., Donkor, C., Mantey, E.A., Chakravorty, S.J., Craig, A., Akoto, A.O., O'Donnell, J., van Mourik, J.A., Bunn, J., 2006. von Willebrand factor propeptide in malaria: evidence of acute endothelial cell activation. Br J Haematol 133, 562-569.

Hoyte, L.C., Brooks, K.J., Nagel, S., Akhtar, A., Chen, R., Mardiguian, S., McAteer, M.A., Anthony, D.C., Choudhury, R.P., Buchan, A.M., Sibson, N.R., 2010. Molecular magnetic resonance imaging of acute vascular cell adhesion molecule-1 expression in a mouse model of cerebral ischemia. J Cereb Blood Flow Metab 30, 1178-1187.

Huber, J.D., Hau, V.S., Borg, L., Campos, C.R., Egleton, R.D., Davis, T.P., 2002. Blood-brain barrier tight junctions are altered during a 72-h exposure to lambda-carrageenan-induced inflammatory pain. Am J Physiol Heart Circ Physiol 283, H1531-1537.

Huber, J.D., Witt, K.A., Hom, S., Egleton, R.D., Mark, K.S., Davis, T.P., 2001. Inflammatory pain alters blood-brain barrier permeability and tight junctional protein expression. Am J Physiol Heart Circ Physiol 280, H1241-1248.

Hughes, V., 2012. Microglia: The constant gardeners. Nature 485, 570-572.

Hutchings, M., Weller, R.O., 1986. Anatomical relationships of the pia mater to cerebral blood vessels in man. J Neurosurg 65, 316-325.

Itoh, M., Nagafuchi, A., Yonemura, S., Kitani-Yasuda, T., Tsukita, S., 1993. The 220-kD protein colocalizing with cadherins in non-epithelial cells is identical to ZO-1, a tight junction-associated protein in epithelial cells: cDNA cloning and immunoelectron microscopy. J Cell Biol 121, 491-502.

Jain, R.K., 2003. Molecular regulation of vessel maturation. Nat Med 9, 685-693.

Jeerakathil, T., Wolf, P.A., Beiser, A., Massaro, J., Seshadri, S., D'Agostino, R.B., DeCarli, C., 2004. Stroke risk profile predicts white matter hyperintensity volume: the Framingham Study. Stroke 35, 1857-1861.

Jenkinson, M., Bannister, P., Brady, M., Smith, S., 2002. Improved optimization for the robust and accurate linear registration and motion correction of brain images. Neuroimage 17, 825-841.

Jin, A.Y., Tuor, U.I., Rushforth, D., Kaur, J., Muller, R.N., Petterson, J.L., Boutry, S., Barber, P.A., 2010. Reduced blood brain barrier breakdown in P-selectin deficient mice following transient ischemic stroke: a future therapeutic target for treatment of stroke. BMC Neurosci 11.

Jokinen, H., Kalska, H., Ylikoski, R., Madureira, S., Verdelho, A., Gouw, A., Scheltens, P., Barkhof, F., Visser, M.C., Fazekas, F., Schmidt, R., O'Brien, J., Hennerici, M., Baezner, H., Waldemar, G., Wallin, A., Chabriat, H., Pantoni, L., Inzitari, D., Erkinjuntti, T., 2009. MRI-defined subcortical ischemic vascular disease: baseline clinical and neuropsychological findings. The LADIS Study. Cerebrovasc Dis 27, 336-344.

Kadoglou, N.P., Daskalopoulou, S.S., Perrea, D., Liapis, C.D., 2005. Matrix metalloproteinases and diabetic vascular complications. Angiology 56, 173-189.

Kallmes, D.F., Hui, F.K., Mugler, J.P., 3rd, 2001. Suppression of cerebrospinal fluid and blood flow artifacts in FLAIR MR imaging with a single-slab three-dimensional pulse sequence: initial experience. Radiology 221, 251-255.

Kapeller, P., Barber, R., Vermeulen, R.J., Ader, H., Scheltens, P., Freidl, W., Almkvist, O., Moretti, M., del Ser, T., Vaghfeldt, P., Enzinger, C., Barkhof, F., Inzitari, D., Erkinjunti, T., Schmidt, R., Fazekas, F., 2003. Visual rating of age-related white matter changes on magnetic resonance imaging: scale comparison, interrater agreement, and correlations with quantitative measurements. Stroke 34, 441-445.

Kaur, J., Tuor, U.I., Zhao, Z., Barber, P.A., 2011. Quantitative MRI reveals the elderly ischemic brain is susceptible to increased early blood-brain barrier permeability following tissue plasminogen activator related to claudin 5 and occludin disassembly. J Cereb Blood Flow Metab 31, 1874-1885.

Kelly, K.A., Li, X., Tan, Z., VanGilder, R.L., Rosen, C.L., Huber, J.D., 2009. NOX2 inhibition with apocynin worsens stroke outcome in aged rats. Brain Res 1292, 165-172.

Khan, U., Porteous, L., Hassan, A., Markus, H.S., 2007. Risk factor profile of cerebral small vessel disease and its subtypes. J Neurol Neurosurg Psychiatry 78, 702-706.

Kibayashi, K., Mastri, A.R., Hirsch, C.S., 1996. Neuropathology of human immunodeficiency virus infection at different disease stages. Hum Pathol 27, 637-642.

Kida, S., Ellison, D.W., Steart, P.V., Iannotti, F., Weller, R.O., 1994. Perivascular edema fluid pathway in astrocytic tumors. Acta Neurochir Suppl (Wien) 60, 384-386.

Kida, S., Steart, P.V., Zhang, E.T., Weller, R.O., 1993. Perivascular cells act as scavengers in the cerebral perivascular spaces and remain distinct from pericytes, microglia and macrophages. Acta Neuropathol 85, 646-652.

Kim, S.U., de Vellis, J., 2005. Microglia in health and disease. J Neurosci Res 81, 302-313.

Kirk, J., Plumb, J., Mirakhur, M., McQuaid, S., 2003. Tight junctional abnormality in multiple sclerosis white matter affects all calibres of vessel and is associated with blood-brain barrier leakage and active demyelination. J Pathol 201, 319-327.

Klock, C., Cerski, M., Goldani, L.Z., 2009. Histopathological aspects of neurocryptococcosis in HIV-infected patients: autopsy report of 45 patients. Int J Surg Pathol 17, 444-448.

Knottnerus, I.L., Ten Cate, H., Lodder, J., Kessels, F., van Oostenbrugge, R.J., 2009. Endothelial dysfunction in lacunar stroke: a systematic review. Cerebrovasc Dis 27, 519-526.

Koehler, R.C., Roman, R.J., Harder, D.R., 2009. Astrocytes and the regulation of cerebral blood flow. Trends Neurosci 32, 160-169.

Kooi, E.J., van Horssen, J., Witte, M.E., Amor, S., Bo, L., Dijkstra, C.D., van der Valk, P., Geurts, J.J., 2009. Abundant extracellular myelin in the meninges of patients with multiple sclerosis. Neuropathol Appl Neurobiol 35, 283-295.

Koustova, E., Sei, Y., McCarty, T., Espey, M.G., Ming, R., Morse, H.C., 3rd, Basile, A.S., 2000. Accelerated development of neurochemical and behavioral deficits in LP-BM5 infected mice with targeted deletions of the IFN-gamma gene. J Neuroimmunol 108, 112-121.

Krauss, J.K., Droste, D.W., Vach, W., Regel, J.P., Orszagh, M., Borremans, J.J., Tietz, A., Seeger, W., 1996. Cerebrospinal fluid shunting in idiopathic normal-pressure hydrocephalus of the elderly: effect of periventricular and deep white matter lesions. Neurosurgery 39, 292-299; discussion 299-300.

Krauss, J.K., Regel, J.P., Vach, W., Orszagh, M., Jungling, F.D., Bohus, M., Droste, D.W., 1997. White matter lesions in patients with idiopathic normal pressure hydrocephalus and in an age-matched control group: a comparative study. Neurosurgery 40, 491-495; discussion 495-496.

Kreutzberg, G.W., 1996. Microglia: a sensor for pathological events in the CNS. Trends Neurosci 19, 312-318.

Krueger, M., Bechmann, I., 2009. CNS pericytes: concepts, misconceptions, and a way out. Glia 58, 1-10.

Kubota, K., Furuse, M., Sasaki, H., Sonoda, N., Fujita, K., Nagafuchi, A., Tsukita, S., 1999. Ca(2+)-independent cell-adhesion activity of claudins, a family of integral membrane proteins localized at tight junctions. Curr Biol 9, 1035-1038.

Kwee, R.M., Kwee, T.C., 2007. Virchow-Robin spaces at MR imaging. Radiographics 27, 1071-1086.

Lackner, P., Beer, R., Helbok, R., Broessner, G., Engelhardt, K., Brenneis, C., Schmutzhard, E., Pfaller, K., 2006. Scanning electron microscopy of the neuropathology of murine cerebral malaria. Malar J 5, 116.

Lampugnani, M.G., Dejana, E., 2007. Adherens junctions in endothelial cells regulate vessel maintenance and angiogenesis. Thromb Res 120 Suppl 2, S1-6.

Lavdas, E., Mavroidis, P., Kostopoulos, S., Glotsos, D., Roka, V., Topalzikis, T., Bakas, A., Oikonomou, G., Papanikolaou, N., Batsikas, G., Kaffes, I., Kechagias, D., 2012. Improvement of image quality using BLADE sequences in brain MR imaging. Magn Reson Imaging 31, 189-200.

Leech, S., Kirk, J., Plumb, J., McQuaid, S., 2007. Persistent endothelial abnormalities and blood-brain barrier leak in primary and secondary progressive multiple sclerosis. Neuropathol Appl Neurobiol 33, 86-98.

Liebner, S., Fischmann, A., Rascher, G., Duffner, F., Grote, E.H., Kalbacher, H., Wolburg, H., 2000. Claudin-1 and claudin-5 expression and tight junction morphology are altered in blood vessels of human glioblastoma multiforme. Acta Neuropathol 100, 323-331.

Liou, L.M., Chen, C.F., Guo, Y.C., Cheng, H.L., Lee, H.L., Hsu, J.S., Lin, R.T., Lin, H.F., 2010. Cerebral white matter hyperintensities predict functional stroke outcome. Cerebrovasc Dis 29, 22-27.

Lisanti, C., Carlin, C., Banks, K.P., Wang, D., 2007. Normal MRI appearance and motion-related phenomena of CSF. AJR Am J Roentgenol 188, 716-725.

Longstreth, W.T., Jr., Arnold, A.M., Beauchamp, N.J., Jr., Manolio, T.A., Lefkowitz, D., Jungreis, C., Hirsch, C.H., O'Leary, D.H., Furberg, C.D., 2005. Incidence, manifestations, and predictors of worsening white matter on serial cranial magnetic resonance imaging in the elderly: the Cardiovascular Health Study. Stroke 36, 56-61.

Loos, C.M., Staals, J., Wardlaw, J.M., van Oostenbrugge, R.J., 2012. Cavitation of deep lacunar infarcts in patients with first-ever lacunar stroke: a 2-year follow-up study with MR. Stroke 43, 2245-2247.

Lopez, A.D., Mathers, C.D., Ezzati, M., Jamison, D.T., Murray, C.J., 2006. Global and regional burden of disease and risk factors, 2001: systematic analysis of population health data. Lancet 367, 1747-1757.

Lummel, N., Schoepf, V., Burke, M., Brueckmann, H., Linn, J., 2011. 3D fluid-attenuated inversion recovery imaging: reduced CSF artifacts and enhanced sensitivity and specificity for subarachnoid hemorrhage. AJNR Am J Neuroradiol 32, 2054-2060.

Maclullich, A.M., Wardlaw, J.M., Ferguson, K.J., Starr, J.M., Seckl, J.R., Deary, I.J., 2004. Enlarged perivascular spaces are associated with cognitive function in healthy elderly men. J Neurol Neurosurg Psychiatry 75, 1519-1523.

Mann, K., Agartz, I., Harper, C., Shoaf, S., Rawlings, R.R., Momenan, R., Hommer, D.W., Pfefferbaum, A., Sullivan, E.V., Anton, R.F., Drobes, D.J., George, M.S., Bares, R., Machulla, H.J., Mundle, G., Reimold, M., Heinz, A., 2001. Neuroimaging in alcoholism: ethanol and brain damage. Alcohol Clin Exp Res 25, 104S-109S.

Mantyla, R., Aronen, H.J., Salonen, O., Korpelainen, M., Peltonen, T., Standertskjold-Nordenstam, C., Erkinjuntti, T., 1999a. The prevalence and distribution of white-matter changes on different MRI pulse sequences in a post-stroke cohort. Neuroradiology 41, 657-665.

Mantyla, R., Aronen, H.J., Salonen, O., Pohjasvaara, T., Korpelainen, M., Peltonen, T., Standertskjold-Nordenstam, C.G., Kaste, M., Erkinjuntti, T., 1999b. Magnetic resonance imaging white matter hyperintensities and mechanism of ischemic stroke. Stroke 30, 2053-2058.

Mark, K.S., Davis, T.P., 2002. Cerebral microvascular changes in permeability and tight junctions induced by hypoxia-reoxygenation. Am J Physiol Heart Circ Physiol 282, H1485-1494.

Marquine, M.J., Attix, D.K., Goldstein, L.B., Samsa, G.P., Payne, M.E., Chelune, G.J., Steffens, D.C., 2010. Differential patterns of cognitive decline in anterior and posterior white matter hyperintensity progression. Stroke 41, 1946-1950.

Martinez-Ramirez, S., Pontes-Neto, O.M., Dumas, A.P., Auriel, E., Halpin, A., Quimby, M., Gurol, M.E., Greenberg, S.M., Viswanathan, A., 2013. Topography of dilated perivascular spaces in subjects from a memory clinic cohort. Neurology 80, 1551-1556.

Mathers, C.D., Boerma, T., Ma Fat, D., 2009. Global and regional causes of death. Br Med Bull 92, 7-32.

Mathis, C., Collin, L., Borrelli, E., 2003. Oligodendrocyte ablation impairs cerebellum development. Development 130, 4709-4718.

McCaffrey, G., Staatz, W.D., Quigley, C.A., Nametz, N., Seelbach, M.J., Campos, C.R., Brooks, T.A., Egleton, R.D., Davis, T.P., 2007. Tight junctions contain oligomeric protein assembly critical for maintaining blood-brain barrier integrity in vivo. J Neurochem 103, 2540-2555.

McCandless, E.E., Piccio, L., Woerner, B.M., Schmidt, R.E., Rubin, J.B., Cross, A.H., Klein, R.S., 2008a. Pathological expression of CXCL12 at the blood-brain barrier correlates with severity of multiple sclerosis. Am J Pathol 172, 799-808.

McCandless, E.E., Zhang, B., Diamond, M.S., Klein, R.S., 2008b. CXCR4 antagonism increases T cell trafficking in the central nervous system and improves survival from West Nile virus encephalitis. Proc Natl Acad Sci U S A 105, 11270-11275.

McCarthy, K.M., Skare, I.B., Stankewich, M.C., Furuse, M., Tsukita, S., Rogers, R.A., Lynch, R.D., Schneeberger, E.E., 1996. Occludin is a functional component of the tight junction. J Cell Sci 109 (Pt 9), 2287-2298.

Mercier, F., Mambie, S., Hatton, G.I., 2006. Brain macrophages: enigmas and conundrums. Blood-Brain Barriers: From Ontogeny to Artificial Interfaces, Volume 1, 129-165.

Meyer, T.N., Schwesinger, C., Denker, B.M., 2002. Zonula occludens-1 is a scaffolding protein for signaling molecules. Galpha(12) directly binds to the Src homology 3 domain and regulates paracellular permeability in epithelial cells. J Biol Chem 277, 24855-24858.

Mitic, L.L., Anderson, J.M., 1998. Molecular architecture of tight junctions. Annu Rev Physiol 60, 121-142.

Mitic, L.L., Van Itallie, C.M., Anderson, J.M., 2000. Molecular physiology and pathophysiology of tight junctions I. Tight junction structure and function: lessons from mutant animals and proteins. Am J Physiol Gastrointest Liver Physiol 279, G250-254.

Montagna, P., Gambetti, P., Cortelli, P., Lugaresi, E., 2003. Familial and sporadic fatal insomnia. Lancet Neurol 2, 167-176.

Moreau, F., Patel, S., Lauzon, M.L., McCreary, C.R., Goyal, M., Frayne, R., Demchuk, A.M., Coutts, S.B., Smith, E.E., 2012. Cavitation after acute symptomatic lacunar stroke depends on time, location, and MRI sequence. Stroke 43, 1837-1842.
Morris, Z., Whiteley, W.N., Longstreth, W.T., Jr., Weber, F., Lee, Y.C., Tsushima, Y., Alphs, H., Ladd, S.C., Warlow, C., Wardlaw, J.M., Al-Shahi Salman, R., 2009. Incidental findings on brain magnetic resonance imaging: systematic review and meta-analysis. BMJ 339, b3016.

Mrak, R.E., Griffin, W.S., 2005. Glia and their cytokines in progression of neurodegeneration. Neurobiol Aging 26, 349-354.

Muller, W.A., 2003. Leukocyte-endothelial-cell interactions in leukocyte transmigration and the inflammatory response. Trends Immunol 24, 327-334.

Musa-Aziz, R., Chen, L.M., Pelletier, M.F., Boron, W.F., 2009. Relative CO2/NH3 selectivities of AQP1, AQP4, AQP5, AmtB, and RhAG. Proc Natl Acad Sci U S A 106, 5406-5411.

Naganawa, S., Kawai, H., Fukatsu, H., Ishigaki, T., Komada, T., Maruyama, K., Takizawa, O., 2004a. High-speed imaging at 3 Tesla: a technical and clinical review with an emphasis on whole-brain 3D imaging. Magn Reson Med Sci 3, 177-187.

Naganawa, S., Koshikawa, T., Nakamura, T., Kawai, H., Fukatsu, H., Ishigaki, T., Komada, T., Maruyama, K., Takizawa, O., 2004b. Comparison of flow artifacts between 2D-FLAIR and 3D-FLAIR sequences at 3 T. Eur Radiol 14, 1901-1908.

Nakagawa, S., Deli, M.A., Nakao, S., Honda, M., Hayashi, K., Nakaoke, R., Kataoka, Y., Niwa, M., 2007. Pericytes from brain microvessels strengthen the barrier integrity in primary cultures of rat brain endothelial cells. Cell Mol Neurobiol 27, 687-694.

Neema, M., Guss, Z.D., Stankiewicz, J.M., Arora, A., Healy, B.C., Bakshi, R., 2009. Normal findings on brain fluid-attenuated inversion recovery MR images at 3T. AJNR Am J Neuroradiol 30, 911-916.

Nelson, D.E., Jarman, D.W., Rehm, J., Greenfield, T.K., Rey, G., Kerr, W.C., Miller, P., Shield, K.D., Ye, Y., Naimi, T.S., 2013. Alcohol-attributable cancer deaths and years of potential life lost in the United States. Am J Public Health 103, 641-648.

Neuwelt, E.A., Bauer, B., Fahlke, C., Fricker, G., Iadecola, C., Janigro, D., Leybaert, L., Molnar, Z., O'Donnell, M.E., Povlishock, J.T., Saunders, N.R., Sharp, F., Stanimirovic, D., Watts, R.J., Drewes, L.R., 2011. Engaging neuroscience to advance translational research in brain barrier biology. Nat Rev Neurosci 12, 169-182.

Newman, P.J., 1997. The biology of PECAM-1. J Clin Invest 100, S25-29.

Nishioku, T., Matsumoto, J., Dohgu, S., Sumi, N., Miyao, K., Takata, F., Shuto, H., Yamauchi, A., Kataoka, Y., 2010. Tumor necrosis factor-alpha mediates the blood-brain barrier dysfunction induced by activated microglia in mouse brain microvascular endothelial cells. J Pharmacol Sci 112, 251-254.

Nishitsuji, K., Hosono, T., Nakamura, T., Bu, G., Michikawa, M., 2011. Apolipoprotein E regulates the integrity of tight junctions in an isoform-dependent manner in an in vitro blood-brain barrier model. J Biol Chem 286, 17536-17542.

Nitta, T., Hata, M., Gotoh, S., Seo, Y., Sasaki, H., Hashimoto, N., Furuse, M., Tsukita, S., 2003. Size-selective loosening of the blood-brain barrier in claudin-5-deficient mice. J Cell Biol 161, 653-660.

Norrving, B., 2008. Lacunar infarcts: no black holes in the brain are benign. Pract Neurol 8, 222-228.

Nyberg, E., Sandhu, G.S., Jesberger, J., Blackham, K.A., Hsu, D.P., Griswold, M.A., Sunshine, J.L., 2012. Comparison of brain MR images at 1.5T using BLADE and rectilinear techniques for patients who move during data acquisition. AJNR Am J Neuroradiol 33, 77-82.

Oatridge, A., Curati, W.L., Herlihy, A.H., Hajnal, J.V., Virji, N., Puri, B.K., Bydder, G.M., 2001. Evaluation of a FLAIR sequence designed to reduce CSF and blood

flow artifacts by use of k-space reordered by inversion time at each slice position (KRISP) in high grade gliomas of the brain. J Comput Assist Tomogr 25, 251-256.

Omidi, Y., Barar, J., Ahmadian, S., Heidari, H.R., Gumbleton, M., 2008. Characterization and astrocytic modulation of system L transporters in brain microvasculature endothelial cells. Cell Biochem Funct 26, 381-391.

Ostermann, G., Weber, K.S., Zernecke, A., Schroder, A., Weber, C., 2002. JAM-1 is a ligand of the beta(2) integrin LFA-1 involved in transendothelial migration of leukocytes. Nat Immunol 3, 151-158.

Owen, J.B., Sultana, R., Aluise, C.D., Erickson, M.A., Price, T.O., Bu, G., Banks, W.A., Butterfield, D.A., 2010. Oxidative modification to LDL receptor-related protein 1 in hippocampus from subjects with Alzheimer disease: implications for Abeta accumulation in AD brain. Free Radic Biol Med 49, 1798-1803.

Owens, T., Bechmann, I., Engelhardt, B., 2008. Perivascular spaces and the two steps to neuroinflammation. J Neuropathol Exp Neurol 67, 1113-1121.

Padden, M., Leech, S., Craig, B., Kirk, J., Brankin, B., McQuaid, S., 2007. Differences in expression of junctional adhesion molecule-A and beta-catenin in multiple sclerosis brain tissue: increasing evidence for the role of tight junction pathology. Acta Neuropathol 113, 177-186.

Pantoni, L., 2010. Cerebral small vessel disease: from pathogenesis and clinical characteristics to therapeutic challenges. Lancet Neurol 9, 689-701.

Pantoni, L., Garcia, J.H., 1997. Pathogenesis of leukoaraiosis: a review. Stroke 28, 652-659.

Pantoni, L., Garcia, J.H., Gutierrez, J.A., 1996. Cerebral white matter is highly vulnerable to ischemia. Stroke 27, 1641-1646; discussion 1647.

Pardridge, W.M., 2007. Blood-brain barrier delivery. Drug Discov Today 12, 54-61.

Patankar, T.F., Mitra, D., Varma, A., Snowden, J., Neary, D., Jackson, A., 2005. Dilatation of the Virchow-Robin space is a sensitive indicator of cerebral microvascular disease: study in elderly patients with dementia. AJNR Am J Neuroradiol 26, 1512-1520.

Paul, R., Zhang, Z.G., Eliceiri, B.P., Jiang, Q., Boccia, A.D., Zhang, R.L., Chopp, M., Cheresh, D.A., 2001. Src deficiency or blockade of Src activity in mice provides cerebral protection following stroke. Nat Med 7, 222-227.

Pelvig, D.P., Pakkenberg, H., Stark, A.K., Pakkenberg, B., 2008. Neocortical glial cell numbers in human brains. Neurobiol Aging 29, 1754-1762.

Peppiatt, C.M., Howarth, C., Mobbs, P., Attwell, D., 2006. Bidirectional control of CNS capillary diameter by pericytes. Nature 443, 700-704.

Perry, V.H., Nicoll, J.A., Holmes, C., 2010. Microglia in neurodegenerative disease. Nat Rev Neurol 6, 193-201.

Petito, C.K., Olarte, J.P., Roberts, B., Nowak, T.S., Jr., Pulsinelli, W.A., 1998. Selective glial vulnerability following transient global ischemia in rat brain. J Neuropathol Exp Neurol 57, 231-238.

Petito, C.K., Torres-Munoz, J.E., Zielger, F., McCarthy, M., 2006. Brain CD8+ and cytotoxic T lymphocytes are associated with, and may be specific for, human immunodeficiency virus type 1 encephalitis in patients with acquired immunodeficiency syndrome. J Neurovirol 12, 272-283.

Phal, P.M., Usmanov, A., Nesbit, G.M., Anderson, J.C., Spencer, D., Wang, P., Helwig, J.A., Roberts, C., Hamilton, B.E., 2008. Qualitative comparison of 3-T and 1.5-T MRI in the evaluation of epilepsy. AJR Am J Roentgenol 191, 890-895.

Piontek, J., Winkler, L., Wolburg, H., Muller, S.L., Zuleger, N., Piehl, C., Wiesner, B., Krause, G., Blasig, I.E., 2008. Formation of tight junction: determinants of homophilic interaction between classic claudins. FASEB J 22, 146-158.

Polledo, L., Gonzalez, J., Benavides, J., Martinez-Fernandez, B., Ferreras, M.C., Marin, J.F., 2012. Perivascular inflammatory cells in ovine Visna/maedi encephalitis and their possible role in virus infection and lesion progression. J Neurovirol 18, 532-537.

Pollock, H., Hutchings, M., Weller, R.O., Zhang, E.T., 1997. Perivascular spaces in the basal ganglia of the human brain: their relationship to lacunes. J Anat 191 (Pt 3), 337-346.

Potter, G., Doubal, F., Jackson, C., Sudlow, C., Dennis, M., Wardlaw, J., 2010a. Associations of clinical stroke misclassification ('clinical-imaging dissociation') in acute ischemic stroke. Cerebrovasc Dis 29, 395-402.

Potter, G.M., 2011. Neuroimaging of cerebral small vessel disease. The University of Edinburgh, Molecular and Clinical Medicine thesis and dissertation collection.

Potter, G.M., Doubal, F.N., Jackson, C.A., Chappell, F.M., Sudlow, C.L., Dennis, M.S., Wardlaw, J.M., 2010b. Counting cavitating lacunes underestimates the burden of lacunar infarction. Stroke 41, 267-272.

Potter, G.M., Doubal, F.N., Jackson, C.A., Chappell, F.M., Sudlow, C.L., Dennis, M.S., Wardlaw, J.M., 2013. Enlarged perivascular spaces and cerebral small vessel disease. Int J Stroke.

Potter, G.M., Marlborough, F.J., Wardlaw, J.M., 2011. Wide variation in definition, detection, and description of lacunar lesions on imaging. Stroke 42, 359-366.

Prins, N.D., van Straaten, E.C., van Dijk, E.J., Simoni, M., van Schijndel, R.A., Vrooman, H.A., Koudstaal, P.J., Scheltens, P., Breteler, M.M., Barkhof, F., 2004. Measuring progression of cerebral white matter lesions on MRI: visual rating and volumetrics. Neurology 62, 1533-1539.

Quaegebeur, A., Segura, I., Carmeliet, P., 2010. Pericytes: blood-brain barrier safeguards against neurodegeneration? Neuron 68, 321-323.

Radlinska, B.A., Ghinani, S.A., Lyon, P., Jolly, D., Soucy, J.P., Minuk, J., Schirrmacher, R., Thiel, A., 2009. Multimodal microglia imaging of fiber tracts in acute subcortical stroke. Ann Neurol 66, 825-832.

Rajasekaran, A.K., Hojo, M., Huima, T., Rodriguez-Boulan, E., 1996. Catenins and zonula occludens-1 form a complex during early stages in the assembly of tight junctions. J Cell Biol 132, 451-463.

Reinke, E.K., Lee, J., Zozulya, A., Karman, J., Muller, W.A., Sandor, M., Fabry, Z., 2007. Short-term sPECAM-Fc treatment ameliorates EAE while chronic use hastens onset of symptoms. J Neuroimmunol 186, 86-93.

Rennels, M.L., Gregory, T.F., Blaumanis, O.R., Fujimoto, K., Grady, P.A., 1985. Evidence for a 'paravascular' fluid circulation in the mammalian central nervous system, provided by the rapid distribution of tracer protein throughout the brain from the subarachnoid space. Brain Res 326, 47-63.

Robb, R.A., Hanson, D.P., 1995. 10 The ANALYZE Software System for Visualization and Analysis in Surgery Simulation. Computer-Integrated Surgery: Technology and Clinical Applications, 175.

Roher, A.E., Kuo, Y.M., Esh, C., Knebel, C., Weiss, N., Kalback, W., Luehrs, D.C., Childress, J.L., Beach, T.G., Weller, R.O., Kokjohn, T.A., 2003. Cortical and leptomeningeal cerebrovascular amyloid and white matter pathology in Alzheimer's disease. Mol Med 9, 112-122.

Romanitan, M.O., Popescu, B.O., Spulber, S., Bajenaru, O., Popescu, L.M., Winblad, B., Bogdanovic, N., 2010. Altered expression of claudin family proteins in Alzheimer's disease and vascular dementia brains. J Cell Mol Med 14, 1088-1100.

Romanitan, M.O., Popescu, B.O., Winblad, B., Bajenaru, O.A., Bogdanovic, N., 2007. Occludin is overexpressed in Alzheimer's disease and vascular dementia. J Cell Mol Med 11, 569-579.

Rosell, A., Cuadrado, E., Ortega-Aznar, A., Hernandez-Guillamon, M., Lo, E.H., Montaner, J., 2008. MMP-9-positive neutrophil infiltration is associated to blood-

brain barrier breakdown and basal lamina type IV collagen degradation during hemorrhagic transformation after human ischemic stroke. Stroke 39, 1121-1126.

Rosenberg, G.A., 2009. Inflammation and white matter damage in vascular cognitive impairment. Stroke 40, S20-23.

Rosenberg, G.A., Yang, Y., 2007. Vasogenic edema due to tight junction disruption by matrix metalloproteinases in cerebral ischemia. Neurosurg Focus 22, E4.

Rost, N.S., Rahman, R.M., Biffi, A., Smith, E.E., Kanakis, A., Fitzpatrick, K., Lima, F., Worrall, B.B., Meschia, J.F., Brown, R.D., Jr., Brott, T.G., Sorensen, A.G., Greenberg, S.M., Furie, K.L., Rosand, J., 2010. White matter hyperintensity volume is increased in small vessel stroke subtypes. Neurology 75, 1670-1677.

Rouget, C., 1874. Note sur le developpement de la tunique contractile des vaisseaux. Compt Rend Acad Sci 59, 559-562.

Rouhl, R.P., Damoiseaux, J.G., Lodder, J., Theunissen, R.O., Knottnerus, I.L., Staals, J., Henskens, L.H., Kroon, A.A., de Leeuw, P.W., Tervaert, J.W., van Oostenbrugge, R.J., 2011. Vascular inflammation in cerebral small vessel disease. Neurobiol Aging 33, 1800-1806.

Rouhl, R.P., van Oostenbrugge, R.J., Knottnerus, I.L., Staals, J.E., Lodder, J., 2008. Virchow-Robin spaces relate to cerebral small vessel disease severity. J Neurol 255, 692-696.

Rouhl, R.P., van Oostenbrugge, R.J., Theunissen, R.O., Knottnerus, I.L., Staals, J., Henskens, L.H., Kroon, A.A., de Leeuw, P.W., Lodder, J., Tervaert, J.W., Damoiseaux, J.G., 2010. Autoantibodies against oxidized low-density lipoprotein in cerebral small vessel disease. Stroke 41, 2687-2689.

Rubin, L.L., Staddon, J.M., 1999. The cell biology of the blood-brain barrier. Annu Rev Neurosci 22, 11-28.

Rudin, W., Pongponratn, E., Jenni, L., 1984. Electron-microscopic localization of Trypanosoma brucei gambiense transmitted by Glossina morsitans centralis in Microtus montanus. Acta Trop 41, 325-334.

Sa-Pereira, I., Brites, D., Brito, M.A., 2012. Neurovascular unit: a focus on pericytes. Mol Neurobiol 45, 327-347.

Sachdev, P., Cathcart, S., Shnier, R., Wen, W., Brodaty, H., 1999. Reliability and validity of ratings of signal hyperintensities on MRI by visual inspection and computerised measurement. Psychiatry Res 92, 103-115.

Sagar, D., Lamontagne, A., Foss, C.A., Khan, Z.K., Pomper, M.G., Jain, P., 2012. Dendritic cell CNS recruitment correlates with disease severity in EAE via CCL2

chemotaxis at the blood-brain barrier through paracellular transmigration and ERK activation. J Neuroinflammation 9, 245.

Sakakibara, A., Furuse, M., Saitou, M., Ando-Akatsuka, Y., Tsukita, S., 1997. Possible involvement of phosphorylation of occludin in tight junction formation. J Cell Biol 137, 1393-1401.

Salmina, A.B., 2009. Neuron-glia interactions as therapeutic targets in neurodegeneration. J Alzheimers Dis 16, 485-502.

Santos, M., Gold, G., Kovari, E., Herrmann, F.R., Bozikas, V.P., Bouras, C., Giannakopoulos, P., 2009. Differential impact of lacunes and microvascular lesions on poststroke depression. Stroke 40, 3557-3562.

Satizabal, C.L., Zhu, Y.C., Dufouil, C., Tzourio, C., 2013. Inflammatory proteins and the severity of dilated Virchow-Robin Spaces in the elderly. J Alzheimers Dis 33, 323-328.

Satoh, S., Hitomi, A., Ikegaki, I., Kawasaki, K., Nakazono, O., Iwasaki, M., Mohri, M., Asano, T., 2010. Amelioration of endothelial damage/dysfunction is a possible mechanism for the neuroprotective effects of Rho-kinase inhibitors against ischemic brain damage. Brain Res Bull 81, 191-195.

Schenkel, A.R., Mamdouh, Z., Chen, X., Liebman, R.M., Muller, W.A., 2002. CD99 plays a major role in the migration of monocytes through endothelial junctions. Nat Immunol 3, 143-150.

Schley, D., Carare-Nnadi, R., Please, C.P., Perry, V.H., Weller, R.O., 2006. Mechanisms to explain the reverse perivascular transport of solutes out of the brain. J Theor Biol 238, 962-974.

Schmidt, H., 1983. The pathogenesis of trypanosomiasis of the CNS. Studies on parasitological and neurohistological findings in trypanosoma rhodesiense infected vervet monkeys. Virchows Arch A Pathol Anat Histopathol 399, 333-343.

Selvarajah, J., Scott, M., Stivaros, S., Hulme, S., Georgiou, R., Rothwell, N., Tyrrell, P., Jackson, A., 2009. Potential surrogate markers of cerebral microvascular angiopathy in asymptomatic subjects at risk of stroke. Eur Radiol 19, 1011-1018.

Seul, M., O'Gorman, L., Sammon, M.J., 2000. Practical Algorithms for Image Analysis with CD-ROM: Description, Examples, and Code. Cambridge University Press.

Shibata, M., Yamada, S., Kumar, S.R., Calero, M., Bading, J., Frangione, B., Holtzman, D.M., Miller, C.A., Strickland, D.K., Ghiso, J., Zlokovic, B.V., 2000. Clearance of Alzheimer's amyloid-ss(1-40) peptide from brain by LDL receptor-related protein-1 at the blood-brain barrier. J Clin Invest 106, 1489-1499.

Shin, H., Hsueh, Y.P., Yang, F.C., Kim, E., Sheng, M., 2000. An intramolecular interaction between Src homology 3 domain and guanylate kinase-like domain required for channel clustering by postsynaptic density-95/SAP90. J Neurosci 20, 3580-3587.

Shoamanesh, A., Kwok, C.S., Benavente, O., 2011. Cerebral microbleeds: histopathological correlation of neuroimaging. Cerebrovasc Dis 32, 528-534.

Shprecher, D., Schwalb, J., Kurlan, R., 2008. Normal pressure hydrocephalus: diagnosis and treatment. Curr Neurol Neurosci Rep 8, 371-376.

Siegelman, J., Fleit, H.B., Peress, N.S., 1987. Characterization of immunoglobulin G-Fc receptor activity in the outflow system of the cerebrospinal fluid. Cell Tissue Res 248, 599-605.

Silbert, L.C., Nelson, C., Howieson, D.B., Moore, M.M., Kaye, J.A., 2008. Impact of white matter hyperintensity volume progression on rate of cognitive and motor decline. Neurology 71, 108-113.

Silverberg, G.D., Miller, M.C., Machan, J.T., Johanson, C.E., Caralopoulos, I.N., Pascale, C.L., Heile, A., Klinge, P.M., 2010. Amyloid and Tau accumulate in the brains of aged hydrocephalic rats. Brain Res 1317, 286-296.

Simard, J.M., Kent, T.A., Chen, M., Tarasov, K.V., Gerzanich, V., 2007. Brain oedema in focal ischaemia: molecular pathophysiology and theoretical implications. Lancet Neurol 6, 258-268.

Simpson, I.A., Carruthers, A., Vannucci, S.J., 2007a. Supply and demand in cerebral energy metabolism: the role of nutrient transporters. J Cereb Blood Flow Metab 27, 1766-1791.

Simpson, J.E., Ince, P.G., Higham, C.E., Gelsthorpe, C.H., Fernando, M.S., Matthews, F., Forster, G., O'Brien, J.T., Barber, R., Kalaria, R.N., Brayne, C., Shaw, P.J., Stoeber, K., Williams, G.H., Lewis, C.E., Wharton, S.B., 2007b. Microglial activation in white matter lesions and nonlesional white matter of ageing brains. Neuropathol Appl Neurobiol 33, 670-683.

Sims, D.E., 2000. Diversity within pericytes. Clin Exp Pharmacol Physiol 27, 842-846.

Sixt, M., Engelhardt, B., Pausch, F., Hallmann, R., Wendler, O., Sorokin, L.M., 2001. Endothelial cell laminin isoforms, laminins 8 and 10, play decisive roles in T cell recruitment across the blood-brain barrier in experimental autoimmune encephalomyelitis. J Cell Biol 153, 933-946.

Sled, J.G., Zijdenbos, A.P., Evans, A.C., 1998. A nonparametric method for automatic correction of intensity nonuniformity in MRI data. IEEE Trans Med Imaging 17, 87-97.

Snowdon, D.A., Greiner, L.H., Mortimer, J.A., Riley, K.P., Greiner, P.A., Markesbery, W.R., 1997. Brain infarction and the clinical expression of Alzheimer disease. The Nun Study. JAMA 277, 813-817.

Sobocka, M.B., Sobocki, T., Babinska, A., Hartwig, J.H., Li, M., Ehrlich, Y.H., Kornecki, E., 2004. Signaling pathways of the F11 receptor (F11R; a.k.a. JAM-1, JAM-A) in human platelets: F11R dimerization, phosphorylation and complex formation with the integrin GPIIIa. J Recept Signal Transduct Res 24, 85-105.

Soliven, B., 2001. Calcium signalling in cells of oligodendroglial lineage. Microsc Res Tech 52, 672-679.

Staines, D.R., Brenu, E.W., Marshall-Gradisnik, S., 2008. Postulated role of vasoactive neuropeptide-related immunopathology of the blood brain barrier and Virchow-Robin spaces in the aetiology of neurological-related conditions. Mediators Inflamm 2008, 792428.

Starr, J.M., Farrall, A.J., Armitage, P., McGurn, B., Wardlaw, J., 2009. Blood-brain barrier permeability in Alzheimer's disease: a case-control MRI study. Psychiatry Res 171, 232-241.

Starr, J.M., Wardlaw, J., Ferguson, K., MacLullich, A., Deary, I.J., Marshall, I., 2003. Increased blood-brain barrier permeability in type II diabetes demonstrated by gadolinium magnetic resonance imaging. J Neurol Neurosurg Psychiatry 74, 70-76.

Stoll, G., Jander, S., Schroeter, M., 1998. Inflammation and glial responses in ischemic brain lesions. Prog Neurobiol 56, 149-171.

Storey, P., 2006. Introduction to magnetic resonance imaging and spectroscopy. Methods Mol Med 124, 3-57.

Strong, K., Mathers, C., Bonita, R., 2007. Preventing stroke: saving lives around the world. Lancet Neurol 6, 182-187.

Stuckey, S.L., Goh, T.D., Heffernan, T., Rowan, D., 2007. Hyperintensity in the subarachnoid space on FLAIR MRI. AJR Am J Roentgenol 189, 913-921.

Suidan, G.L., Brill, A., De Meyer, S.F., Voorhees, J.R., Cifuni, S.M., Cabral, J.E., Wagner, D.D., 2013. Endothelial Von Willebrand factor promotes blood-brain barrier flexibility and provides protection from hypoxia and seizures in mice. Arterioscler Thromb Vasc Biol 33, 2112-2120.

Taheri, S., Gasparovic, C., Huisa, B.N., Adair, J.C., Edmonds, E., Prestopnik, J., Grossetete, M., Shah, N.J., Wills, J., Qualls, C., Rosenberg, G.A., 2011. Blood-brain barrier permeability abnormalities in vascular cognitive impairment. Stroke 42, 2158-2163.

Tanaka, N., Abe, T., Kojima, K., Nishimura, H., Hayabuchi, N., 2000. Applicability and advantages of flow artifact-insensitive fluid-attenuated inversion-recovery MR sequences for imaging the posterior fossa. AJNR Am J Neuroradiol 21, 1095-1098.

Tao-Cheng, J.H., Brightman, M.W., 1988. Development of membrane interactions between brain endothelial cells and astrocytes in vitro. Int J Dev Neurosci 6, 25-37.

Tarnaris, A., Tamangani, J., Fayeye, O., Kombogiorgas, D., Murphy, H., Gan, Y.C., Flint, G., 2011. Virchow-Robin spaces in idiopathic normal pressure hydrocephalus: a surrogate imaging marker for coexisting microvascular disease? Acta Neurochir Suppl 113, 33-37.

Thal, D.R., 2009. The pre-capillary segment of the blood-brain barrier and its relation to perivascular drainage in Alzheimer's disease and small vessel disease. ScientificWorldJournal 9, 557-563.

Tofts, P.S., Kermode, A.G., 1991. Measurement of the blood-brain barrier permeability and leakage space using dynamic MR imaging. 1. Fundamental concepts. Magn Reson Med 17, 357-367.

Tomas-Camardiel, M., Venero, J.L., Herrera, A.J., De Pablos, R.M., Pintor-Toro, J.A., Machado, A., Cano, J., 2005. Blood-brain barrier disruption highly induces aquaporin-4 mRNA and protein in perivascular and parenchymal astrocytes: protective effect by estradiol treatment in ovariectomized animals. J Neurosci Res 80, 235-246.

Tomimoto, H., Akiguchi, I., Suenaga, T., Nishimura, M., Wakita, H., Nakamura, S., Kimura, J., 1996. Alterations of the blood-brain barrier and glial cells in white-matter lesions in cerebrovascular and Alzheimer's disease patients. Stroke 27, 2069-2074.

Topakian, R., Barrick, T.R., Howe, F.A., Markus, H.S., 2009. Blood-brain barrier permeability is increased in normal-appearing white matter in patients with lacunar stroke and leucoaraiosis. J Neurol Neurosurg Psychiatry 81, 192-197.

Tsai, C.Y., Chow, N.H., Ho, T.S., Lei, H.Y., 1997. Intracerebral injection of myelin basic protein (MBP) induces inflammation in brain and causes paraplegia in MBP-sensitized B6 mice. Clin Exp Immunol 109, 127-133.

Turner, R.J., Vink, R., 2012. Combined tissue plasminogen activator and an NK1 tachykinin receptor antagonist: an effective treatment for reperfusion injury following acute ischemic stroke in rats. Neuroscience 220, 1-10.

Uchiyama, Y., Kunieda, T., Asano, T., Kato, H., Hara, T., Kanematsu, M., Iwama, T., Hoshi, H., Kinosada, Y., Fujita, H., 2008. Computer-aided diagnosis scheme for classification of lacunar infarcts and enlarged Virchow-Robin spaces in brain MR images. Conf Proc IEEE Eng Med Biol Soc 2008, 3908-3911.

Uh, J., Yezhuvath, U., Cheng, Y., Lu, H., 2010. In vivo vascular hallmarks of diffuse leukoaraiosis. J Magn Reson Imaging 32, 184-190.

Umeda, K., Matsui, T., Nakayama, M., Furuse, K., Sasaki, H., Furuse, M., Tsukita, S., 2004. Establishment and characterization of cultured epithelial cells lacking expression of ZO-1. J Biol Chem 279, 44785-44794.

Underwood, E., 2013. Neuroscience. Sleep: the brain's housekeeper? Science 342, 301.

Valdes Hernandez Mdel, C., Gallacher, P.J., Bastin, M.E., Royle, N.A., Maniega, S.M., Deary, I.J., Wardlaw, J.M., 2011. Automatic segmentation of brain white matter and white matter lesions in normal aging: comparison of five multispectral techniques. Magn Reson Imaging 30, 222-229.

van den Heuvel, D.M., ten Dam, V.H., de Craen, A.J., Admiraal-Behloul, F., Olofsen, H., Bollen, E.L., Jolles, J., Murray, H.M., Blauw, G.J., Westendorp, R.G., van Buchem, M.A., 2006a. Increase in periventricular white matter hyperintensities parallels decline in mental processing speed in a non-demented elderly population. J Neurol Neurosurg Psychiatry 77, 149-153.

van den Heuvel, D.M., ten Dam, V.H., de Craen, A.J., Admiraal-Behloul, F., van Es, A.C., Palm, W.M., Spilt, A., Bollen, E.L., Blauw, G.J., Launer, L., Westendorp, R.G., van Buchem, M.A., 2006b. Measuring longitudinal white matter changes: comparison of a visual rating scale with a volumetric measurement. AJNR Am J Neuroradiol 27, 875-878.

Vasdev, S., Gill, V., Singal, P.K., 2006. Beneficial effect of low ethanol intake on the cardiovascular system: possible biochemical mechanisms. Vasc Health Risk Manag 2, 263-276.

Veltkamp, R., Bieber, K., Wagner, S., Beynon, C., Siebing, D.A., Veltkamp, C., Schwaninger, M., Marti, H.H., 2006. Hyperbaric oxygen reduces basal lamina degradation after transient focal cerebral ischemia in rats. Brain Res 1076, 231-237.

Vermeer, S.E., Longstreth, W.T., Jr., Koudstaal, P.J., 2007. Silent brain infarcts: a systematic review. Lancet Neurol 6, 611-619.

Von Kalle, T., Blank, B., Fabig-Moritz, C., MÃ¼ller-Abt, P., Zieger, M., Wohlfarth, K., Winkler, P., 2010. Diagnostic Relevant Reduction of Motion Artifacts in the Posterior Fossa by syngo BLADE Imaging. Differentiation 53, 81.

von Tell, D., Armulik, A., Betsholtz, C., 2006. Pericytes and vascular stability. Exp Cell Res 312, 623-629.

Wachtel, M., Frei, K., Ehler, E., Fontana, A., Winterhalter, K., Gloor, S.M., 1999. Occludin proteolysis and increased permeability in endothelial cells through tyrosine phosphatase inhibition. J Cell Sci 112 (Pt 23), 4347-4356.

Wagner, H.J., Pilgrim, C., Brandl, J., 1974. Penetration and removal of horseradish peroxidase injected into the cerebrospinal fluid: role of cerebral perivascular spaces, endothelium and microglia. Acta Neuropathol 27, 299-315.

Walker, W.S., 1999. Separate precursor cells for macrophages and microglia in mouse brain: immunophenotypic and immunoregulatory properties of the progeny. J Neuroimmunol 94, 127-133.

Wang, G., Guo, Q., Hossain, M., Fazio, V., Zeynalov, E., Janigro, D., Mayberg, M.R., Namura, S., 2009. Bone marrow-derived cells are the major source of MMP-9 contributing to blood-brain barrier dysfunction and infarct formation after ischemic stroke in mice. Brain Res 1294, 183-192.

Wang, X., Valdes Hernandez, M.C., Doubal, F., Chappell, F.M., Wardlaw, J.M., 2012. How much do focal infarcts distort white matter lesions and global cerebral atrophy measures? Cerebrovasc Dis 34, 336-342.

Wang, Y., Kilic, E., Kilic, U., Weber, B., Bassetti, C.L., Marti, H.H., Hermann, D.M., 2005. VEGF overexpression induces post-ischaemic neuroprotection, but facilitates haemodynamic steal phenomena. Brain 128, 52-63.

Wardlaw, J.M., 2008. What is a lacune? Stroke 39, 2921-2922.

Wardlaw, J.M., 2010. Blood-brain barrier and cerebral small vessel disease. J Neurol Sci 299, 66-71.

Wardlaw, J.M., Bastin, M.E., Valdes Hernandez, M.C., Maniega, S.M., Royle, N.A., Morris, Z., Clayden, J.D., Sandeman, E.M., Eadie, E., Murray, C., Starr, J.M., Deary, I.J., 2011. Brain aging, cognition in youth and old age and vascular disease in the Lothian Birth Cohort 1936: rationale, design and methodology of the imaging protocol. Int J Stroke 6, 547-559.

Wardlaw, J.M., Brindle, W., Casado, A.M., Shuler, K., Henderson, M., Thomas, B., Macfarlane, J., Munoz Maniega, S., Lymer, K., Morris, Z., Pernet, C., Nailon, W., Ahearn, T., Mumuni, A.N., Mugruza, C., McLean, J., Chakirova, G., Tao, Y.T., Simpson, J., Stanfield, A.C., Johnston, H., Parikh, J., Royle, N.A., De Wilde, J., Bastin, M.E., Weir, N., Farrall, A., Valdes Hernandez, M.C., 2012. A systematic review of the utility of 1.5 versus 3 Tesla magnetic resonance brain imaging in clinical practice and research. Eur Radiol 22, 2295-2303.

Wardlaw, J.M., Doubal, F., Armitage, P., Chappell, F., Carpenter, T., Munoz Maniega, S., Farrall, A., Sudlow, C., Dennis, M., Dhillon, B., 2009. Lacunar stroke is associated with diffuse blood-brain barrier dysfunction. Ann Neurol 65, 194-202.

Wardlaw, J.M., Doubal, F.N., Valdes-Hernandez, M., Wang, X., Chappell, F.M., Shuler, K., Armitage, P.A., Carpenter, T.C., Dennis, M.S., 2013a. Blood-brain barrier permeability and long-term clinical and imaging outcomes in cerebral small vessel disease. Stroke 44, 525-527.

Wardlaw, J.M., Farrall, A., Armitage, P.A., Carpenter, T., Chappell, F., Doubal, F., Chowdhury, D., Cvoro, V., Dennis, M.S., 2008. Changes in background blood-brain barrier integrity between lacunar and cortical ischemic stroke subtypes. Stroke 39, 1327-1332.

Wardlaw, J.M., Ferguson, K.J., Graham, C., 2004. White matter hyperintensities and rating scales-observer reliability varies with lesion load. J Neurol 251, 584-590.

Wardlaw, J.M., Lewis, S.C., Keir, S.L., Dennis, M.S., Shenkin, S., 2006. Cerebral microbleeds are associated with lacunar stroke defined clinically and radiologically, independently of white matter lesions. Stroke 37, 2633-2636.

Wardlaw, J.M., Sandercock, P.A., Dennis, M.S., Starr, J., 2003. Is breakdown of the blood-brain barrier responsible for lacunar stroke, leukoaraiosis, and dementia? Stroke 34, 806-812.

Wardlaw, J.M., Smith, C., Dichgans, M., 2013b. Mechanisms of sporadic cerebral small vessel disease: insights from neuroimaging. Lancet Neurol 12, 483-497.

Wardlaw, J.M., Smith, E.E., Biessels, G.J., Cordonnier, C., Fazekas, F., Frayne, R., Lindley, R.I., O'Brien, J.T., Barkhof, F., Benavente, O.R., Black, S.E., Brayne, C., Breteler, M., Chabriat, H., Decarli, C., de Leeuw, F.E., Doubal, F., Duering, M., Fox, N.C., Greenberg, S., Hachinski, V., Kilimann, I., Mok, V., Oostenbrugge, R., Pantoni, L., Speck, O., Stephan, B.C., Teipel, S., Viswanathan, A., Werring, D., Chen, C., Smith, C., van Buchem, M., Norrving, B., Gorelick, P.B., Dichgans, M., 2013c. Neuroimaging standards for research into small vessel disease and its contribution to ageing and neurodegeneration. Lancet Neurol 12, 822-838.

Warlow, C., Sudlow, C., Dennis, M., Wardlaw, J., Sandercock, P., 2003. Stroke. Lancet 362, 1211-1224.

Watzlawik, J., Warrington, A.E., Rodriguez, M., 2010. Importance of oligodendrocyte protection, BBB breakdown and inflammation for remyelination. Expert Rev Neurother 10, 441-457.

Whiteley, W., Wardlaw, J., Dennis, M., Lowe, G., Rumley, A., Sattar, N., Welsh, P., Green, A., Andrews, M., Sandercock, P., 2011. The use of blood biomarkers to

predict poor outcome after acute transient ischemic attack or ischemic stroke. Stroke 43, 86-91.

Wiesmann, M., Mayer, T.E., Yousry, I., Medele, R., Hamann, G.F., Bruckmann, H., 2002. Detection of hyperacute subarachnoid hemorrhage of the brain by using magnetic resonance imaging. J Neurosurg 96, 684-689.

Willinek, W.A., Gieseke, J., von Falkenhausen, M., Neuen, B., Schild, H.H., Kuhl, C.K., 2003. Sensitivity encoding for fast MR imaging of the brain in patients with stroke. Radiology 228, 669-675.

Willis, C.L., 2010. Glia-induced reversible disruption of blood-brain barrier integrity and neuropathological response of the neurovascular unit. Toxicol Pathol 39, 172-185.

Willis, C.L., 2011. Imaging in vivo astrocyte/endothelial cell interactions at the blood-brain barrier. Methods Mol Biol 814, 515-529.

Witt, K.A., Mark, K.S., Hom, S., Davis, T.P., 2003. Effects of hypoxia-reoxygenation on rat blood-brain barrier permeability and tight junctional protein expression. Am J Physiol Heart Circ Physiol 285, H2820-2831.

Wolburg, H., Lippoldt, A., 2002. Tight junctions of the blood-brain barrier: development, composition and regulation. Vascul Pharmacol 38, 323-337.

Wolburg, H., Noell, S., Wolburg-Buchholz, K., Mack, A., Fallier-Becker, P., 2009. Agrin, aquaporin-4, and astrocyte polarity as an important feature of the blood-brain barrier. Neuroscientist 15, 180-193.

Wolf, P.A., D'Agostino, R.B., Kannel, W.B., Bonita, R., Belanger, A.J., 1988. Cigarette smoking as a risk factor for stroke. The Framingham Study. JAMA 259, 1025-1029.

Wolfle, W.T., Johnson, R.E., Minko, I.G., Lloyd, R.S., Prakash, S., Prakash, L., 2005. Human DNA polymerase iota promotes replication through a ring-closed minor-groove adduct that adopts a syn conformation in DNA. Mol Cell Biol 25, 8748-8754.

Wuerfel, J., Haertle, M., Waiczies, H., Tysiak, E., Bechmann, I., Wernecke, K.D., Zipp, F., Paul, F., 2008. Perivascular spaces--MRI marker of inflammatory activity in the brain? Brain 131, 2332-2340.

Wyss, M.T., Jolivet, R., Buck, A., Magistretti, P.J., Weber, B., 2011. In vivo evidence for lactate as a neuronal energy source. J Neurosci 31, 7477-7485.

Xie, L., Kang, H., Xu, Q., Chen, M.J., Liao, Y., Thiyagarajan, M., O'Donnell, J., Christensen, D.J., Nicholson, C., Iliff, J.J., Takano, T., Deane, R., Nedergaard, M., 2013. Sleep drives metabolite clearance from the adult brain. Science 342, 373-377.

Yamada, S., DePasquale, M., Patlak, C.S., Cserr, H.F., 1991. Albumin outflow into deep cervical lymph from different regions of rabbit brain. Am J Physiol 261, H1197-1204.

Yang, D., Xie, Z., Stephenson, D., Morton, D., Hicks, C.D., Brown, T.M., Sriram, R., O'Neill, S., Raunig, D., Bocan, T., 2011. Volumetric MRI and MRS provide sensitive measures of Alzheimer's disease neuropathology in inducible Tau transgenic mice (rTg4510). Neuroimage 54, 2652-2658.

Yokota, H., 2007. Cerebral endothelial damage after severe head injury. J Nippon Med Sch 74, 332-337.

Young, V.G., Halliday, G.M., Kril, J.J., 2008. Neuropathologic correlates of white matter hyperintensities. Neurology 71, 804-811.

Zhang, E.T., Inman, C.B., Weller, R.O., 1990. Interrelationships of the pia mater and the perivascular (Virchow-Robin) spaces in the human cerebrum. J Anat 170, 111-123.

Zhang, E.T., Richards, H.K., Kida, S., Weller, R.O., 1992. Directional and compartmentalised drainage of interstitial fluid and cerebrospinal fluid from the rat brain. Acta Neuropathol 83, 233-239.

Zhou, J., Kong, H., Hua, X., Xiao, M., Ding, J., Hu, G., 2008. Altered blood-brain barrier integrity in adult aquaporin-4 knockout mice. Neuroreport 19, 1-5.

Zhu, Y.C., Dufouil, C., Mazoyer, B., Soumare, A., Ricolfi, F., Tzourio, C., Chabriat, H., 2011. Frequency and location of dilated Virchow-Robin spaces in elderly people: a population-based 3D MR imaging study. AJNR Am J Neuroradiol 32, 709-713.

Zhu, Y.C., Tzourio, C., Soumare, A., Mazoyer, B., Dufouil, C., Chabriat, H., 2010. Severity of dilated Virchow-Robin spaces is associated with age, blood pressure, and MRI markers of small vessel disease: a population-based study. Stroke 41, 2483-2490.

Zipser, B.D., Johanson, C.E., Gonzalez, L., Berzin, T.M., Tavares, R., Hulette, C.M., Vitek, M.P., Hovanesian, V., Stopa, E.G., 2007. Microvascular injury and blood-brain barrier leakage in Alzheimer's disease. Neurobiol Aging 28, 977-986.

Zlokovic, B.V., 2008. The blood-brain barrier in health and chronic neurodegenerative disorders. Neuron 57, 178-201.

Zlokovic, B.V., 2011. Neurovascular pathways to neurodegeneration in Alzheimer's disease and other disorders. Nat Rev Neurosci 12, 723-738.

Zonta, M., Angulo, M.C., Gobbo, S., Rosengarten, B., Hossmann, K.A., Pozzan, T., Carmignoto, G., 2003. Neuron-to-astrocyte signaling is central to the dynamic control of brain microcirculation. Nat Neurosci 6, 43-50.

Appendices

Appendix (A) Appendix table for BBB literature

Table A1. Effects of cytokines, enzymes, drugs and other stimuli which increase or decrease BBB permeability after the ischemic stimulus.

Effectors	Type	Increase or decrease BBB permeability	Reference
VEGF	Cytokine	Increase	Paul, 2001
Src	Enzyme	Increase (VEGF)	
Src Inhibitor	Antibody	Decrease	
Src deficiency	Gene knockout	Decrease	
VEGF	Cytokine	Increase	Wang, 2005
Capsazepine	Drug	Decrease	Gauden, 2007
tPA	Cytokine	Increase	Kelly, 2009
NOX2	Enzyme	Increase (ROS)	
Apocynin (NOX2 inhibitor)	Drug	Increase (aged)	
Apocynin (NOX2 inhibitor)	Drug	Decrease (young)	
MMP-9	Cytokine	Increase	Wang, 2009
MMP-9 deficiency	Gene knockout	Decrease	
Rho-kinase inhibitors	Antibody	Decrease	Satoh, 2010
MMP-9	Cytokine	Increase (TJ: occludin, ZO-1)	Bauer, 2010
VEGF	Cytokine	Increase (TJ, MMP-9)	
MMP-9 inhibitor	Antibody	Decrease	
VEGF inhibitor	Antibody	Decrease	
tPA	Cytokine	Increase	Abu Fanne, 2010
P-selectin	Surface protein	Increase	Jin, 2010
P-selectin deficiency	Gene knockout	Decrease	
Atorvastatin	Drug	Decrease (TJ)	Cui, 2010
NK1 tachykinin receptor antagonist	Antagonist	Decrease	Turner, 2012
NK1 tachykinin receptor antagonist +tPA	Antagonist + Cytokine	Decrease	

Abbreviations:
VEGF: Vascular endothelial growth factor; MMP: Matrix metalloproteinase; tPA: Tissue plasminogen activator; NOX2: NADPH oxidase; ROS: reactive oxygen species; TJ: tight junctions; ZO-1: Zonula occlnden-1.

Appendix (B) Image segmentation manuals

Appendix (B1) Intracranial volume (ICV) segmentation Manual

Edit brain mask to create intracranial volume (ICV) mask

After extracting the brain mask using **Object Extractor** module, we use the region definition tools in the **Region of Interest** module to edit the brain mask into intracranial volume (ICV) mask within a 3-D volume image. The Sample Options in **Region of Interest** model allow measuring the volume of ICV.

The brain mask extraction process can be divided as follows:

- Load image and brain mask
- Change the name to ICV (and change colour to red)
- Edit and save the ICV mask
- Calculate the ICV
- Save and change ICV in the AnalyzeImage(7.5) format

1. Load the GRE image from directory. Click on **Load** to load the image, and click on image icon to highlight that image.

2. Open the **Region of Interest** module 

(**Measure > Region of Interest**). Choose **File > Load Object Map** and load the brain mask object map from the directory (in this example BM225.obj). Open the **Objects** window (**View > Objects**), change **Object** from Original to Object_2 (Figure 1 [A]). Change **Name** from Object_2 to **ICV** (Figure 1 [B]), and **Color** to red (default color for the second object). Click **Done** to dismiss the Objects.

3. The first slice of the volume is automatically displayed when the ROI module is opened. You can move to a different slice using the **Show Next** and **Show Previous** 

Slice Power Bar buttons above the image. You can use **Double current**

size and **Halve current size**  to adjust the displaying image size. The buttons below the image display allow you to modify the defined objects: **Edit** and **Delete** objects. If after defining the region it is unsatisfactory, click the **Undo** button (Figure 2). The fused FLAIR and GRE images are used as reference images through the editing.

When one slice contains no suitable objects, click **Clear Regions** 

on the left side of the window to clear all regions defined on this slice.

Figure 3 and 4 are examples of deleting and editing ICV mask by ROI.

4. When we need to separate one object into more than two objects in order to do further editing, we use the **Manual Trace tool** 

. We first need to change the **Object To Define** button below the image into **Original**, and then click and hold the mouse to begin drawing the trace, release the mouse button to end the trace. The one object will be divided into more than two objects (in the example of Figure 5, one object is separated into two objects).

5. After finishing editing the whole ICV mask, check the whole mask before further steps. Save the ICV object map though **File > Save Object Map**, name it as ICV.

6. In the Sample Options window set the following (Figure 6):

- Sample Type: Object(s), check the ICV
- Summing: On
- Sample: All Slices
- Log Stats: On

After setting as above, click **Sample Images**. The module will now sample the defined object ('ICV'). The ROI Stat Log will automatically be returned, displaying the object statistics. Click **Save** to save the ICV volume, then Exit.

7. AnalyzeImage(7.5) format is useful for cerebrospinal fluid (CSF) segmentation using MCMxxxVI method, so we also save the ICV mask in the AnalyzeImage(7.5) format. Open the **Objects** window (**View > Objects**), click the **Save Binary**, the save options will automatically be returned and change the **Name** into ICV, then click **Save** (Figure 7). The binary mask is saved and highlighted in the Analyze workspace, then click **File > Save** and navigate to the directory where you would like to save the data set and specify a name (ICV in this example). Use the Format drop-down menu to specify the **AnalyzeImage(7.5)** format to save, then click **Save** (Figure 8).

8. Because the default image direction are different between Matlab and Analyze software, the ICV mask generated in Analyze software need to be flipped direction for the further use. **File > Save as > Flip/Shift**, select X, Y and Z directions.

When finished, save the ICV_XYZ in both objectmap format and AnalyzeImage(7.5) format (Figure 9).

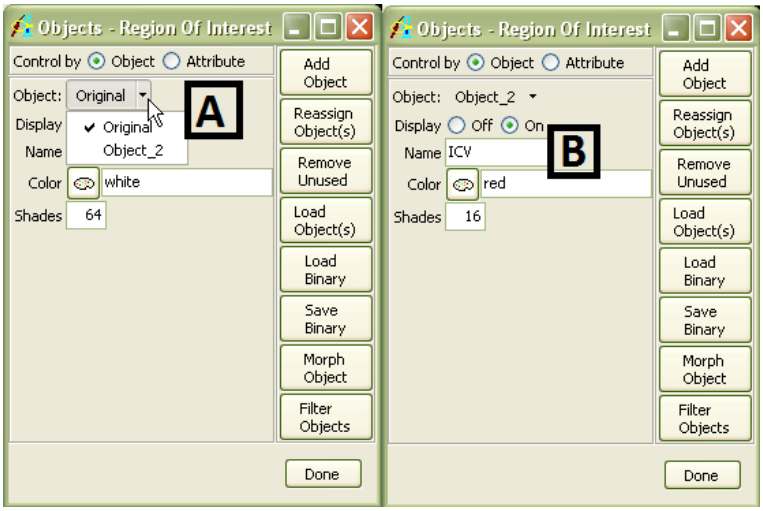

Figure 1. Set object and name for ICV mask.

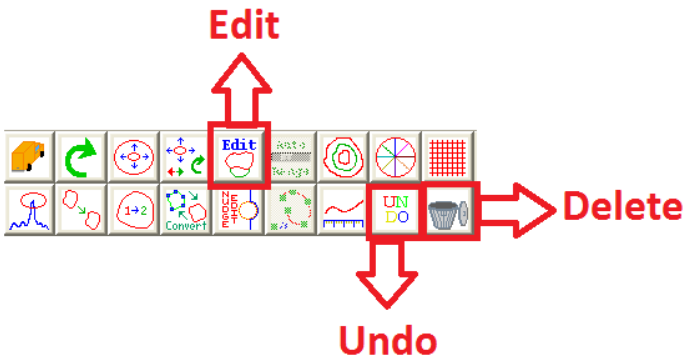

Figure 2. Edit, Delete and Undo image modifying buttons in Region of Interest model.

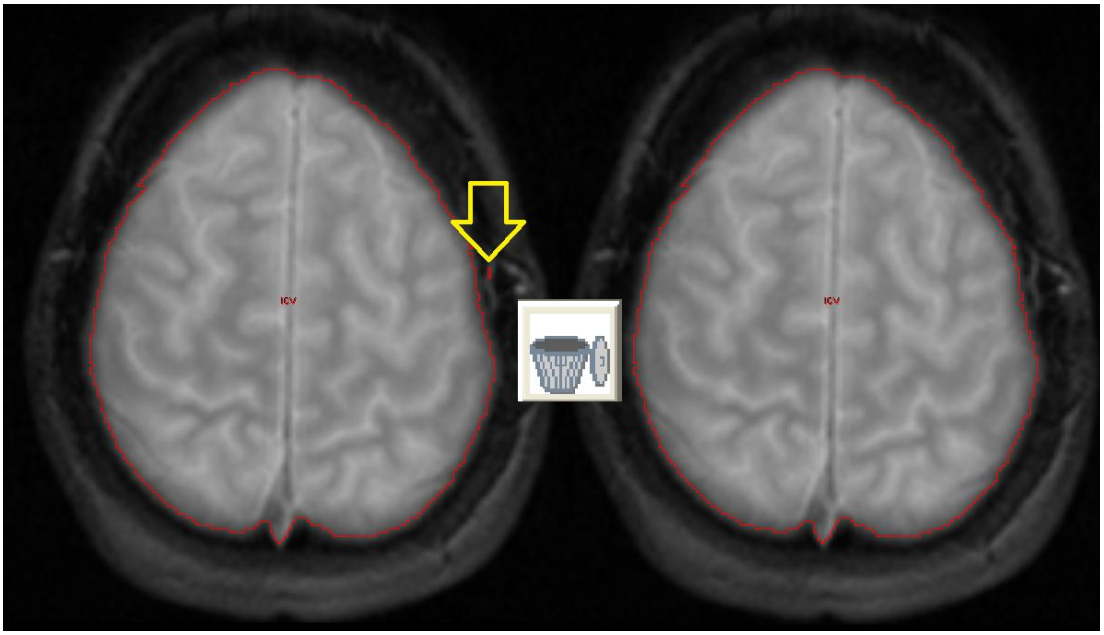

Figure 3. Object deleting using ROI. The yellow arrow points to the object needs deleting. The left image is before deleting, and the right image is after deleting.

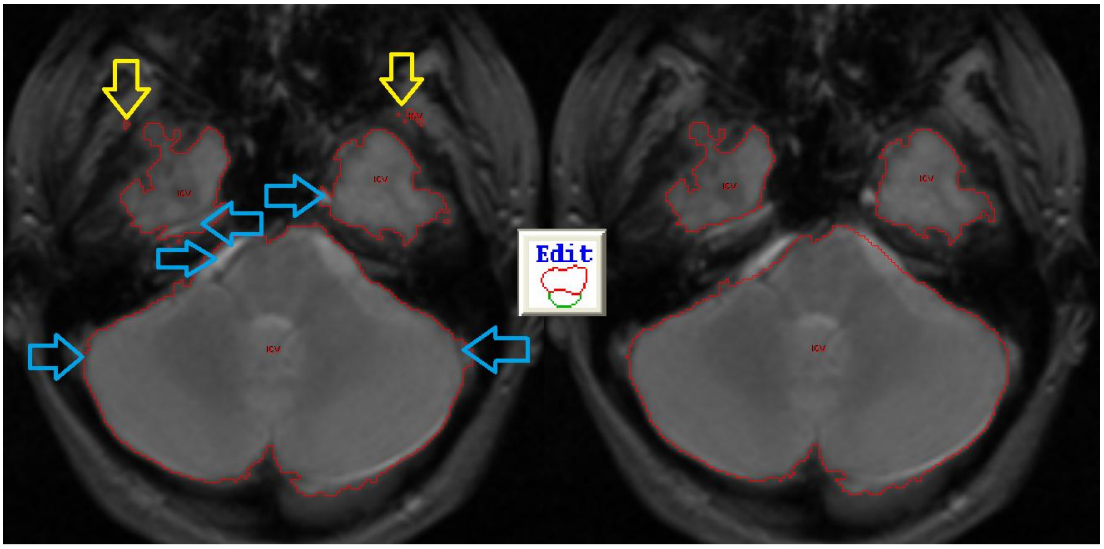

Figure 4. Object editing using ROI. The yellow arrows point to the objects need deleting and the blue arrows points to the places need editing. The left image is the ICV mask before editing, and the right image is after editing.

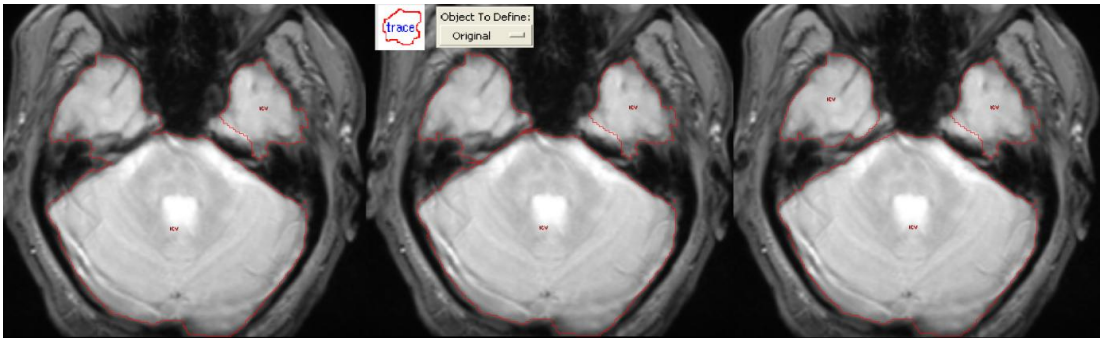

Figure 5. Manual trace tool. Before drawing the manual trace (Left), setting and drawing for manual trace (Middle), and after drawing the manual trace and editing (Right).

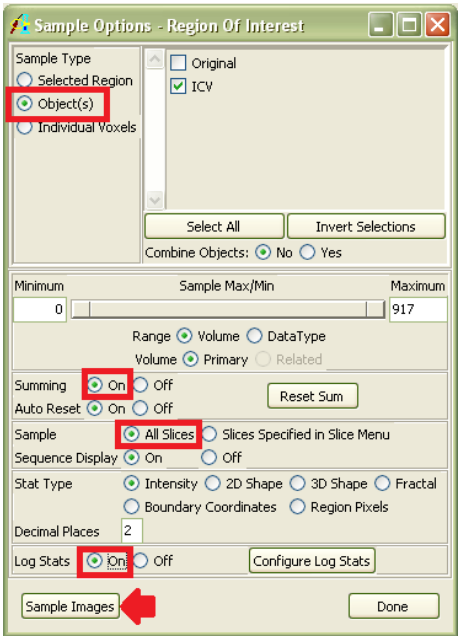

Figure 6. Sample Options for ICV. After changing the settings in rectangles, press Sample Images (an arrow pointing to the Sample Images button).

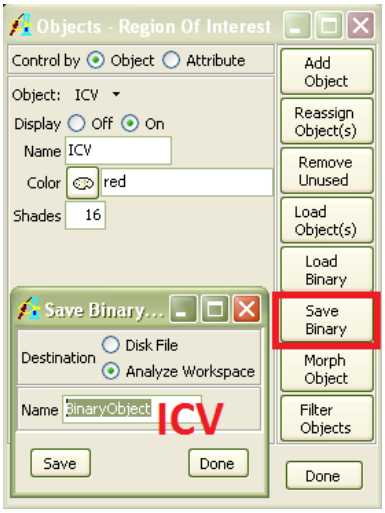

Figure 7. Save binary mask for ICV.

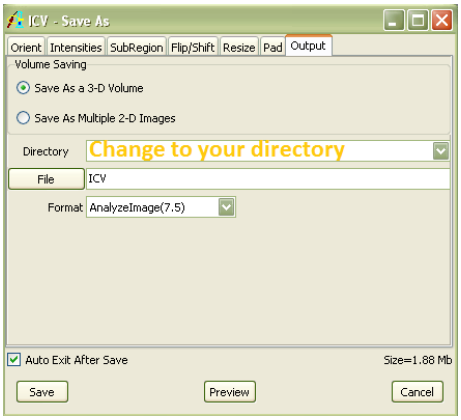

Figure 8. Save ICV mask in AnalyzeImage(7.5) format.

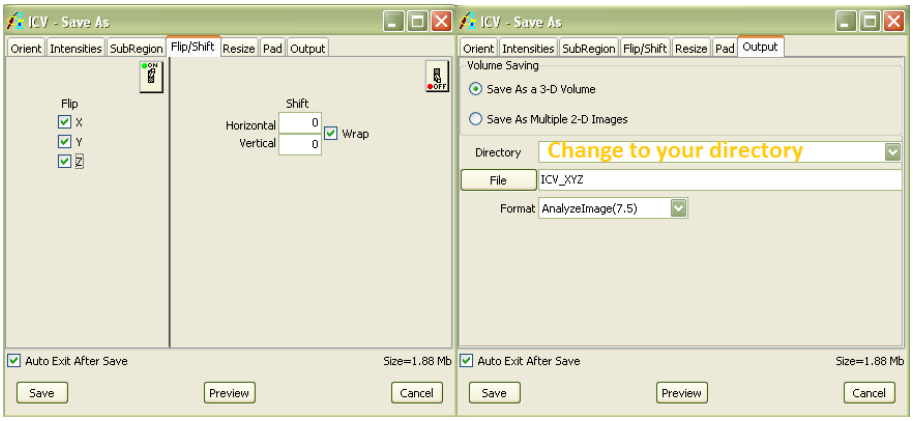

Figure 9. Save ICV_XYZ in AnalyzeImage(7.5) format.

Appendix (B2) Image Registration Manual

We registered Fluid attenuated inversion recovery (FLAIR), gradient-recalled echo (GRE) and T2-weighted (T2W) images to the permeability fspgr_12 image by using ANALYZE 10.0 **3-D Voxel Registration** module, which allows us to spatially register two volume images, based on the Normalized Mutual Information algorithm. The volume registration process can be divided as follows:

- Load images
- Intensity adjustment
- 3D-voxel registration
- Save transformed image
- Manual registry for unsuccessful automated registration

We took the registration of T2W image into permeability image to demonstrate the registration process:

1. Load both permeability and T2W images from directory. Click on **Load** to load the images. Select the permeability image first, and then while holding down the <Ctrl> key, select the T2W image (resulting in both being selected, Base image: permeability image; Match image: T2W image).

2. Open the **3-D Voxel Registration** module (**Register > 3-D Voxel**).

Open the **Blend** window  (**Generate > Blend**). Different colour combinations under the **Blend** window assist evaluate the registration visually. Different blend options are in Figure 1. In this case, we set the Blend Type to Green-Red, the 'Red-Green' blend option will help evaluate the registration. Click **Done** to dismiss the window.

3. Open the **Intensity** option (**View > Intensity**), use the slider bar to change the **Maximum** intensity level. Intensity display change also help evaluate the registration visually (Figure 2).

4. Press the Register PowerBar button  or choose **Generate > Register**.

5. Examine the center 'Fused' column. Save the transformed image when the registration is acceptable. Select **File > Save Transformed** and save the transformed T2W image in AnalyzeImage(7.5) format (Figure 3, red arrow). Change the name and save directory.

6. When the automatic registration done above is not acceptable, manually adjust the registration scale. Open the **Manual Registration** (**Tools > Manual menu**). Click **Reset Matrix** in the Manual tool (Figure 4, red arrow), this will reset the match volume to the original starting position. Choose the extent from 'coarse' to 'very fine', then click on the direction arrows to adjust the registration scale (Figure 4, red regtangles). When the registration is acceptable, save the transformed image into AnalyzeImage(7.5) format.

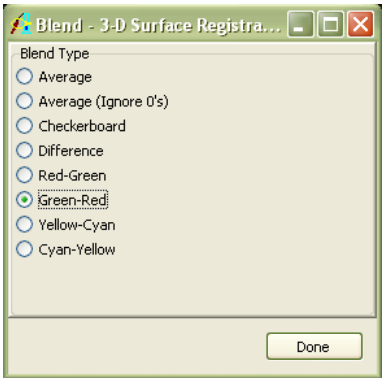

Figure 1. Different colour options in the Blend.

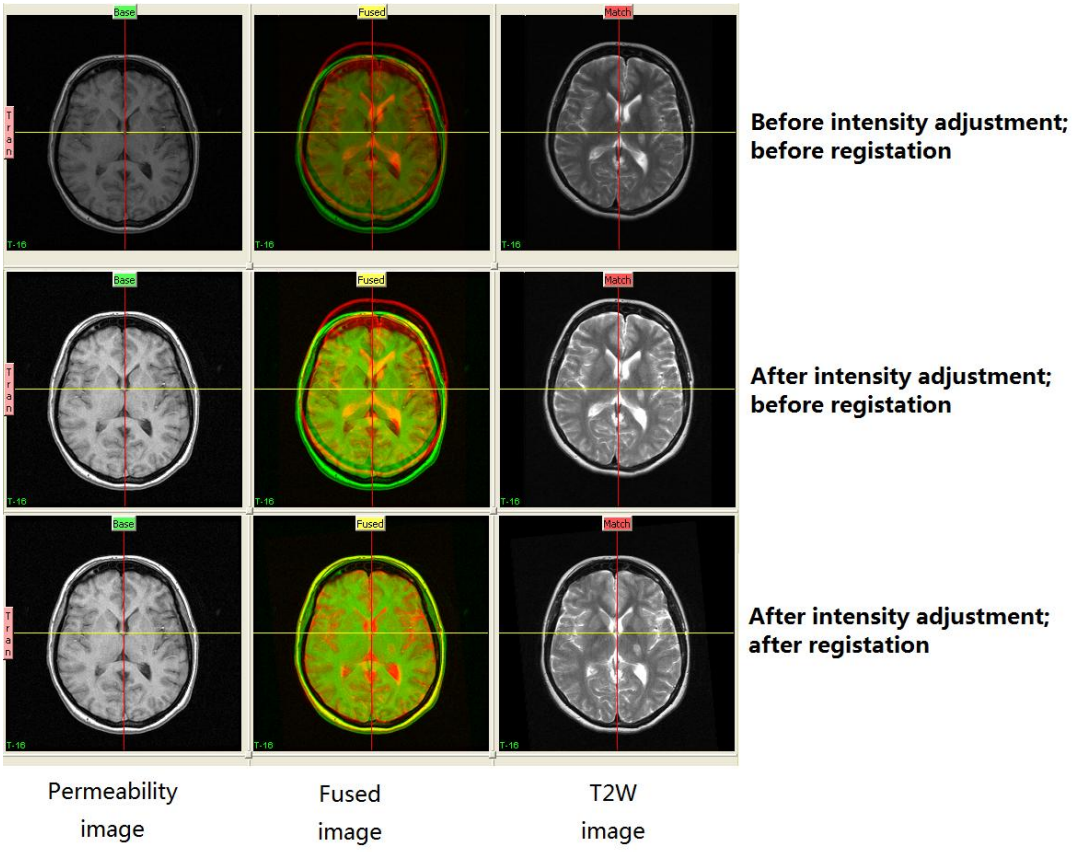

Figure 2. Intensity adjustment and registration in the 3D-Voxel registration (direction axial was selected as an example).

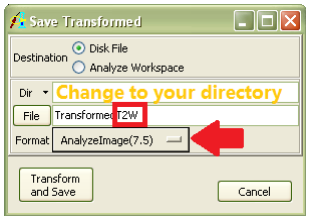

Figure 3. Save transformed image.

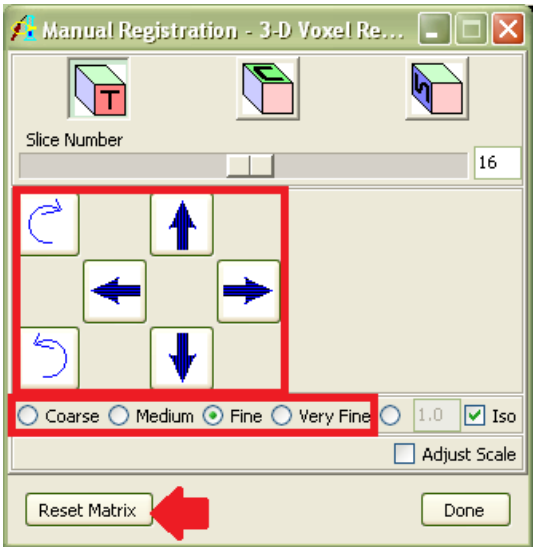

Figure 4. Manually registration.

Appendix (C) WMH artifacts training guide

(http://www.sbirc.ed.ac.uk/research/imageanalysis.html)

(1) Fourth ventricle; aqueduct; cisterns

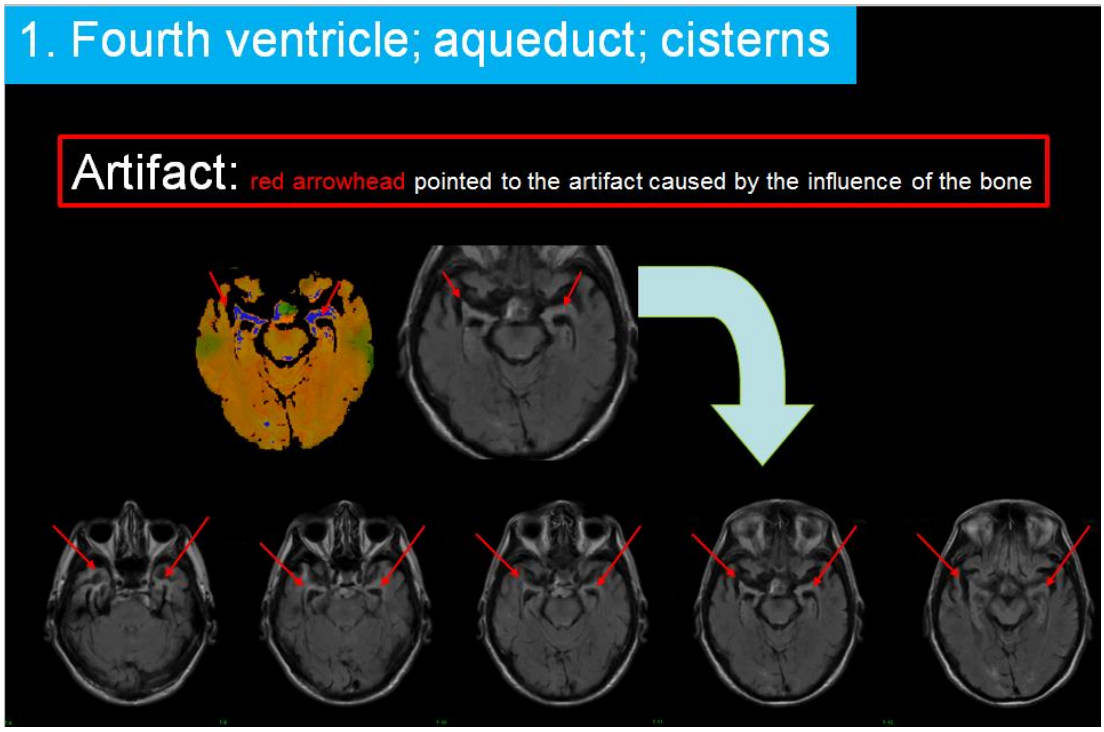

(2) Bilateral sylvian fissures and insular cortex

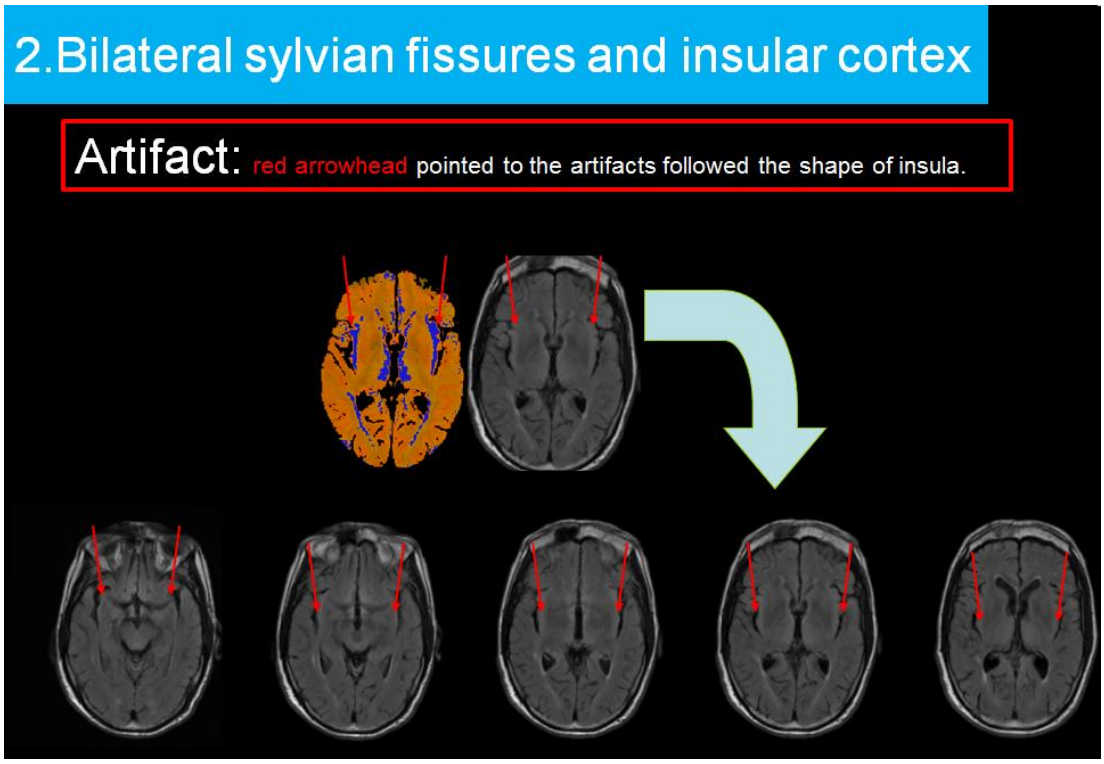

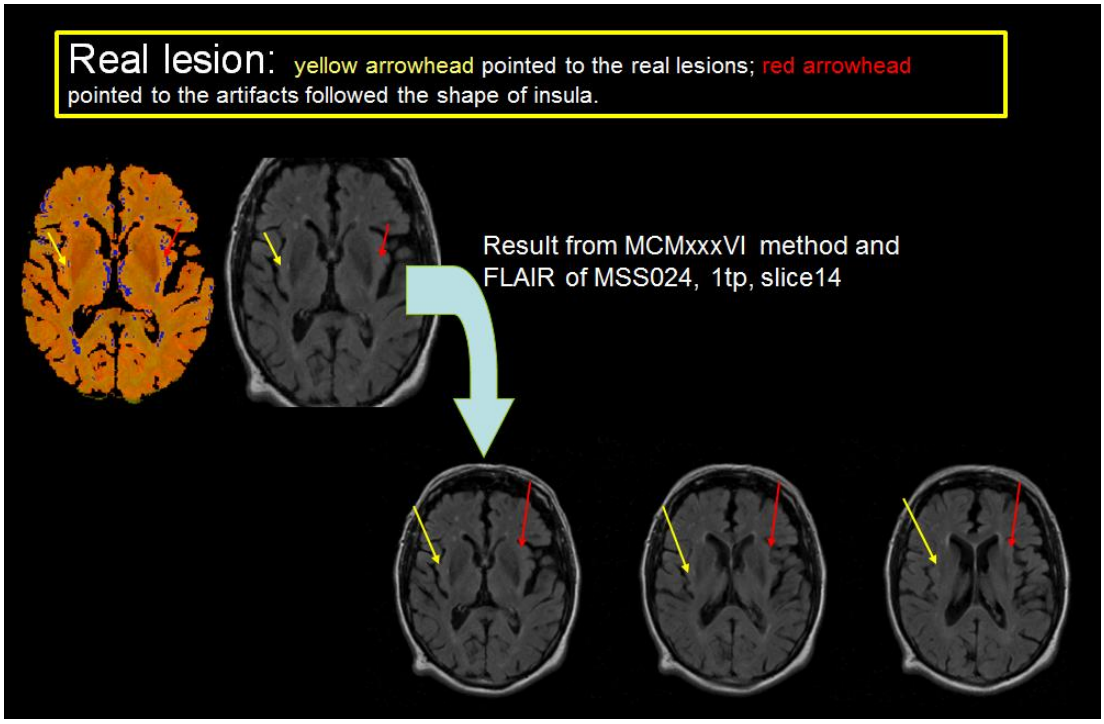

(3) White matter tracts

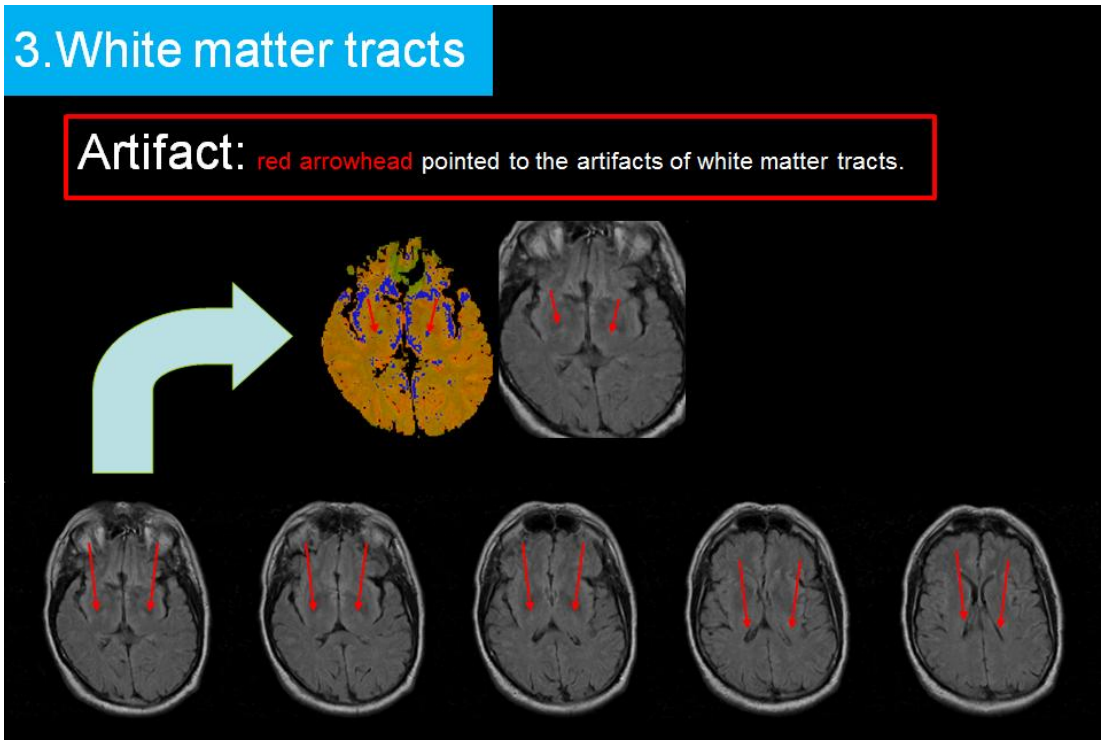

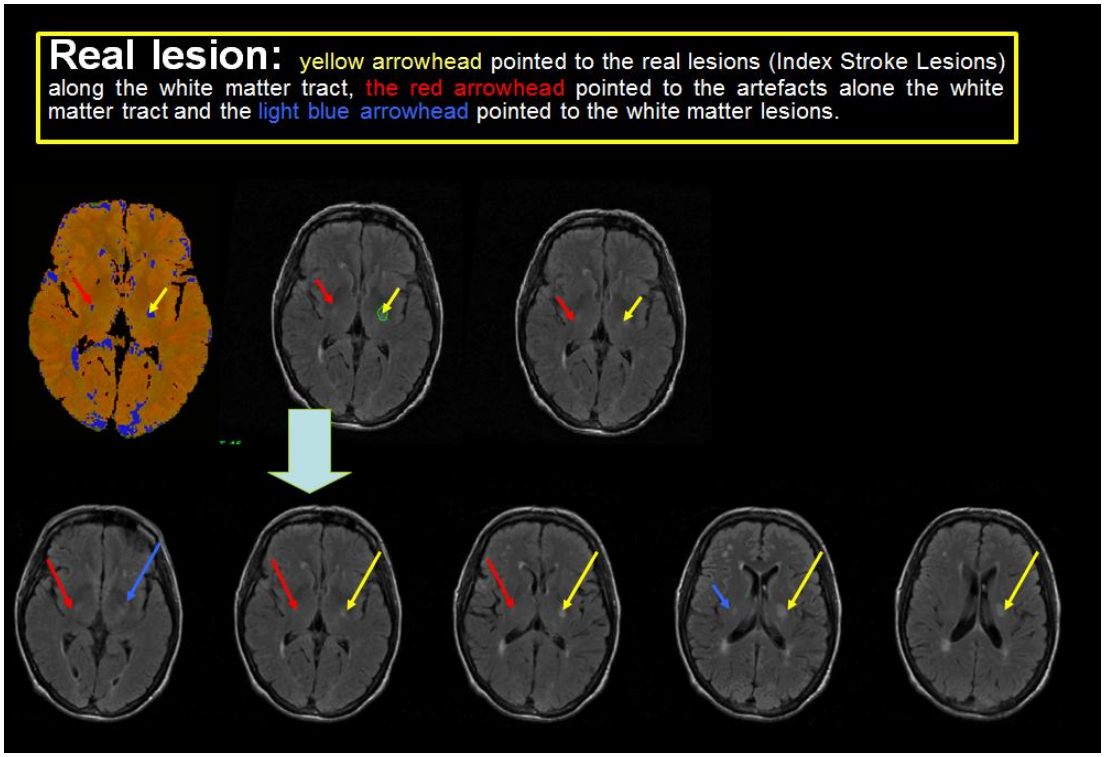

(4) Dirty white matters

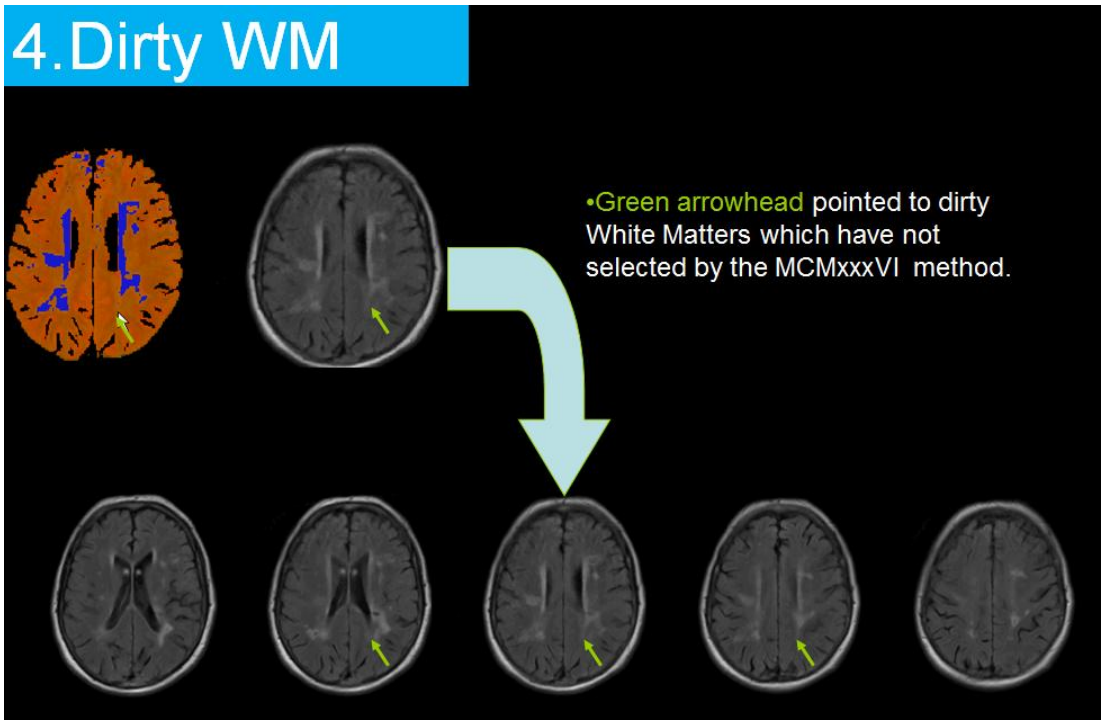

(5) Subtle Dots near ventricles

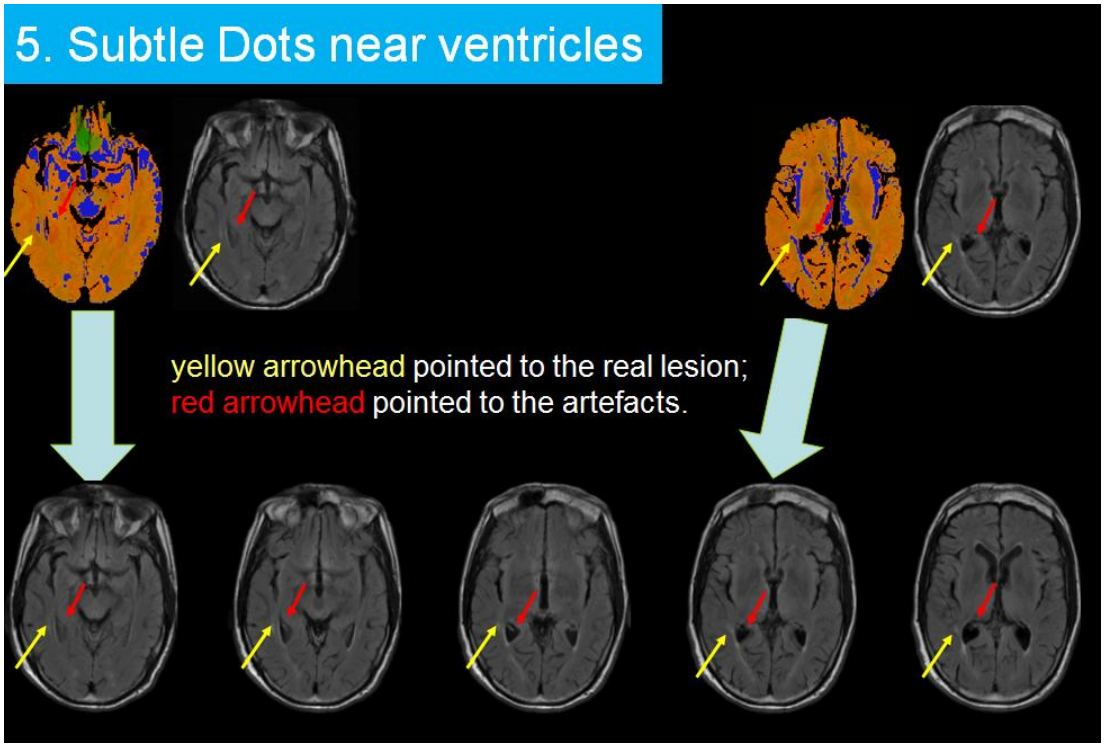


Artefacts: red arrowhead pointed to the artefact.

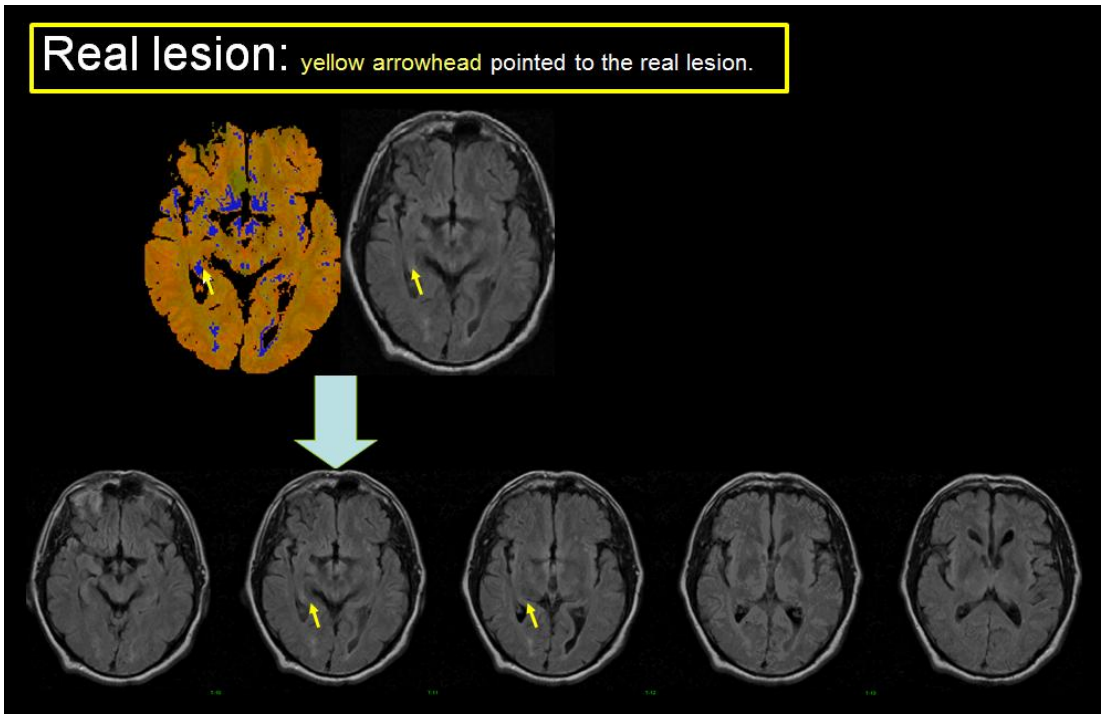
Real lesion: yellow arrowhead pointed to the real lesion.

(6) Bright skull circle

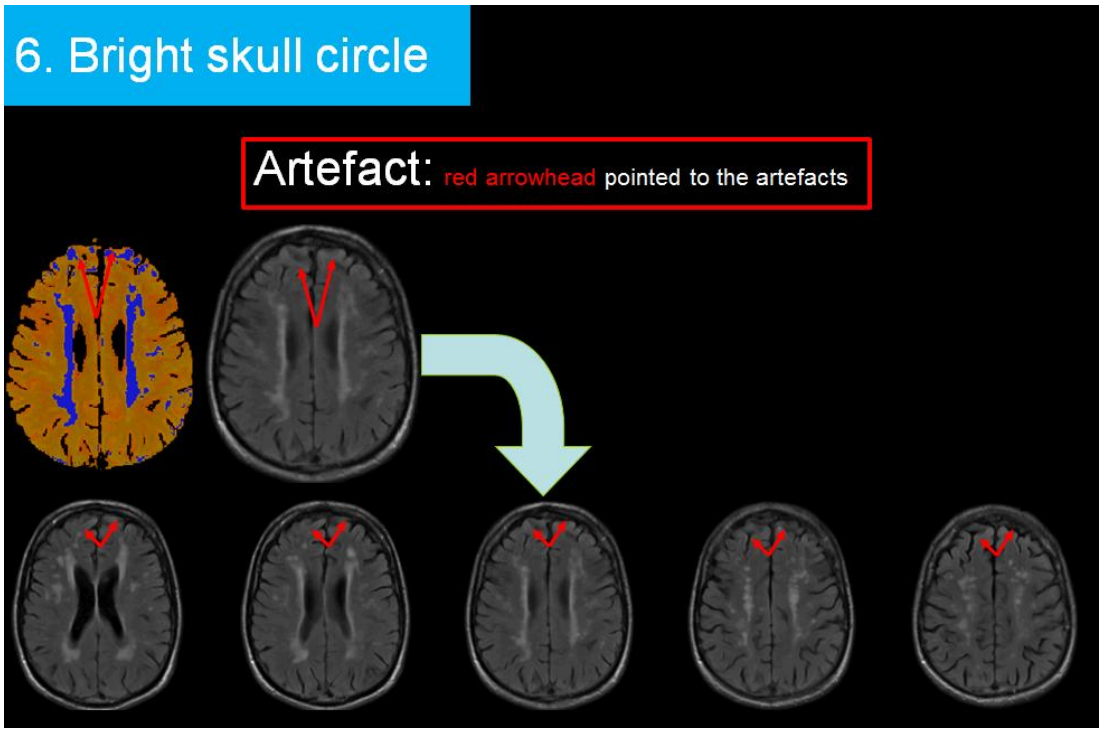

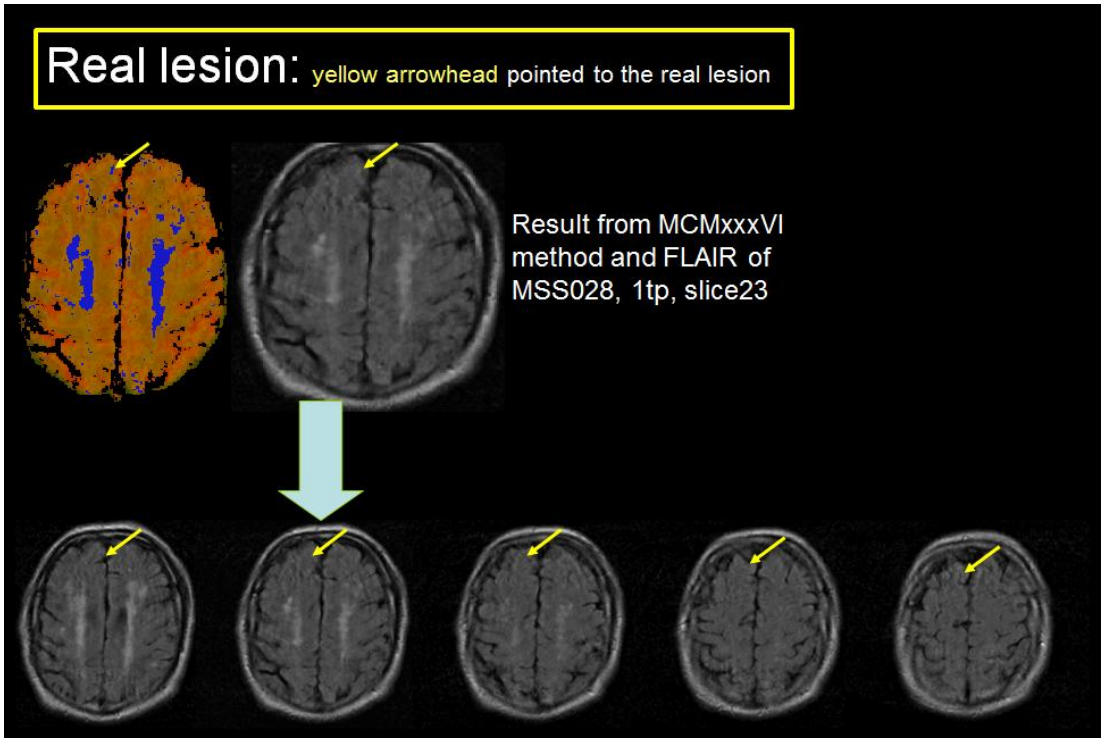

Appendix (D) Chapter 5 non-parametric results adjusted for head size.

Table D1. Results from non-parametric tests (Wilcoxon Signed Rank Test) for differences in white matter hyperintensities (WMH) according to inclusion/exclusion of lacunes or stroke lesions (SL), adjusted for inter-subject differences in head size using the intracranial volume (ICV).

Total 46 patients: median (IQR) as a percentage of ICV (%)	*Baseline*	*Follow-up*	*Difference (change from Baseline to Follow-up)*
WMH excluding lacunes and SL	0.61 % (IQR=0.42-1.02)	0.86 % (IQR=0.60-1.28)	0.23 % (IQR=0.08-0.57)
WMH including lacunes	0.61 % (IQR=0.42-1.03)	0.87 % (IQR=0.60-1.28)	0.23 % (IQR=0.08-0.58)
Wilcoxon Signed Ranks Test	**Z=-2.366 p=0.018**	**Z=-2.366 p=0.018**	**Z=-1.690 p=0.091**
WMH including SL	0.77 % (IQR=0.47-1.92)	1.08 % (IQR=0.69-2.56)	0.32 % (IQR=0.08-0.76)
Wilcoxon Signed Ranks Test	**Z=-5.012 p<0.001**	**Z=-4.937 p<0.001**	**Z=-1.849 p=0.064**
WMH including lacunes and SL	0.77 % (IQR=0.48-1.92)	1.09 % (IQR=0.69-2.56)	0.32 % (IQR=0.08-0.77)
Wilcoxon Signed Ranks Test	**Z=-5.012 p<0.001**	**Z=-4.937 p<0.001**	**Z=-1.921 p=0.055**
13 patients with only WMH: median (IQR) as a percentage of ICV (%)	*Baseline*	*Follow-up*	*Difference (change from Baseline to Follow-up)*
WMH	0.48 % (IQR=0.32-0.61)	0.60 % (IQR=0.46-1.01)	0.21 % (IQR=0.01-0.52)
26 patients with WMH and SL: median (IQR) as a percentage of ICV (%)	*Baseline*	*Follow-up*	*Difference (change from Baseline to Follow-up)*
WMH excluding SL	0.61 % (IQR=0.39-1.02)	0.87 % (IQR=0.63-1.28)	0.18 % (IQR=0.09-0.54)
WMH including SL	1.10 % (IQR=0.53-1.92)	1.48 % (IQR=0.83-2.56)	0.35 % (IQR=0.12-0.92)
Wilcoxon Signed Ranks Test	**Z=-4.457 p<0.001**	**Z=-4.372 p<0.001**	**Z=-1.892 p=0.058**
7 patients with lacunes: median (IQR) as a percentage of ICV (%)	*Baseline*	*Follow-up*	*Difference (change from Baseline to Follow-up)*
WMH excluding SL and lacunes	1.38 % (IQR=0.65-2.78)	1.95 % (IQR=0.86-3.66)	0.42 % (IQR=0.21-0.88)
WMH including lacunes	1.42 % (IQR=0.68-2.80)	2.00 % (IQR=0.90-3.69)	0.42 % (IQR=0.22-0.89)

Wilcoxon Signed Ranks Test	**Z=-2.366 p=0.018**	**Z=-2.366 p=0.018**	**Z=-1.690 p=0.091**
WMH including SL	2.04 % (IQR=1.01-4.60)	2.85 % (IQR=1.08-3.73)	0.64 % (IQR=0.08-0.87)
Wilcoxon Signed Ranks Test	**Z=-2.366 p=0.018**	**Z=-2.366 p=0.018**	**Z=-0.338 p=0.735**
WMH including lacunes and SL	2.08 % (IQR=1.02-4.63)	2.90 % (IQR=1.09-3.76)	0.64 % (IQR=0.08-0.87)
Wilcoxon Signed Ranks Test	**Z=-2.366 p=0.018**	**Z=-2.366 p=0.018**	**Z=-0.338 p=0.735**
33 patients with index stroke: median (IQR) as a percentage of ICV (%)	*Baseline*	*Follow-up*	*Difference(change from Baseline to Follow-up)*
WMH excluding SL and lacunes	0.65 % (IQR=0.45-1.27)	1.00 % (IQR=0.67-1.74)	0.24 % (IQR=0.10-0.58)
WMH including lacunes	0.68 % (IQR=0.45-1.27)	1.00 % (IQR=0.67-1.76)	0.24% (IQR=0.10-0.58)
Wilcoxon Signed Ranks Test	**Z=-2.366 p=0.018**	**Z=-2.366 p=0.018**	**Z=-1.690 p=0.091**
WMH including SL	1.18 % (IQR=0.58-2.21)	1.86 % (IQR=0.86-2.95)	0.35 % (IQR=0.12-0.84)
Wilcoxon Signed Ranks Test	**Z=-5.012 p<0.001**	**Z=-4.937 p<0.001**	**Z=-1.849 p=0.064**
WMH including lacunes and SL	1.18 % (IQR=0.58-2.22)	1.86 % (IQR=0.86-2.99)	0.35 % (IQR=0.12-0.85)
Wilcoxon Signed Ranks Test	**Z=-5.012 p<0.001**	**Z=-4.937 p<0.001**	**Z=-1.921 p=0.055**

Appendix (E) Detailed perivascular space (PVS) segmentation steps and manuals

E1-Detailed eight PVS segmentation steps in Figure 6.1

Step 1-Choice of standard slices in the basal ganglia (BG) and centrum semiovale (CS)

Based on the PVS visual rating scale user guide, all the slices through the BG and CS regions would be reviewed. In the BG region, one slice which shows the highest number or area of PVS, and also contains at least one characteristic structure in the BG as shown in Figure E1 was selected to be the standard slice in the BG region. In the CS region, one slice between the slice containing the vertex and the slice containing the lateral ventricles was chosen as standard slice (Figure E2).

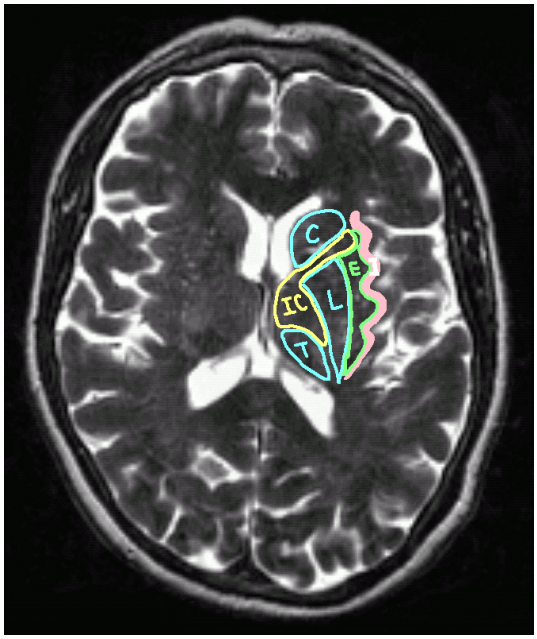

Figure E1 Typical anatomical structures in the basal ganglia region. C: Caudate nucleus ; IC: Internal Capsule; T: Thalamus; L: Lentiform nucleus; E: External Capsule; I: Insular cortex (Figure adapted from the PVS visual rating scale and user guide http://www.bric.ed.ac.uk/documents/epvs-rating-scale-user-guide.pdf).

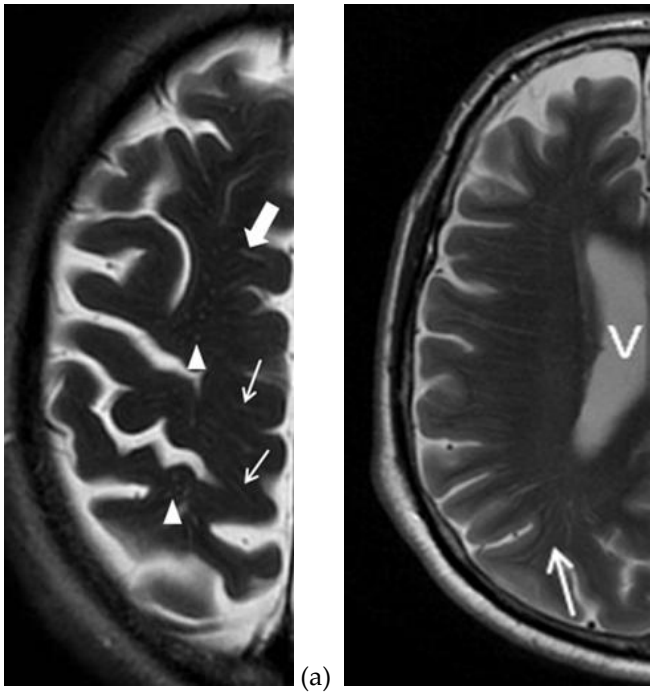

(a) (b)

Figure E2 An illustration of the structures which helps choice of the standard slice in the CS. (a) Slice containing the vertex; (b) Slice containing the lateral ventricles (Figure adopted from the Potter et al. PVS visual rating scale and user guide http://www.bric.ed.ac.uk/documents/epvs-rating-scale-user-guide.pdf).

Step 2-Multiple thresholds: in the BG and CS regions.

In order to reduce the intensity influence of the non-brain tissue on the T2-weighted (T2W) image, the T2W was combined with the intracranial (ICV) mask, which removed the extracranial tissues (Figure E3). Both the T2W image and the ICV mask were loaded into Analyze™ software Workspace, and were combined using a 'multiple' function, which is based on the dot product algorithm.

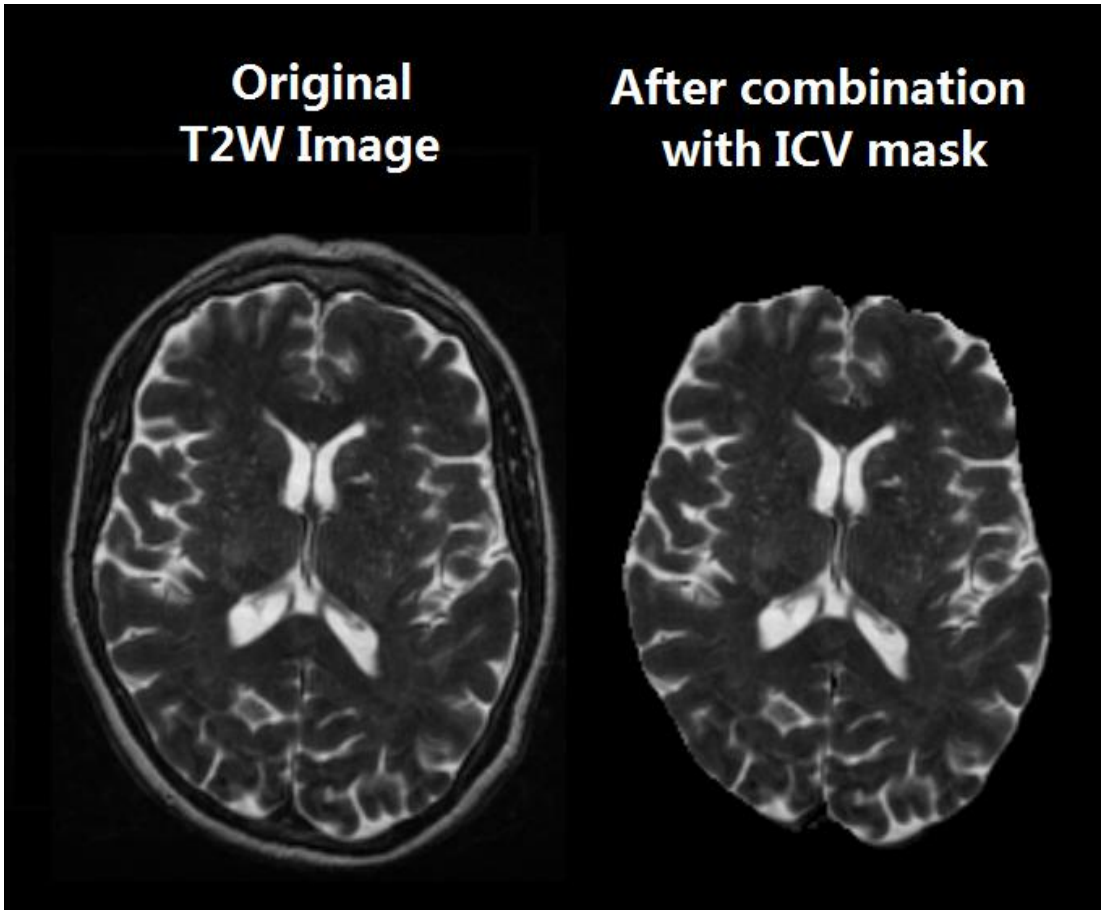

Figure E3 Combination of T2W image and ICV mask reduced the influence of extracranial tissues on the T2W image (in the BG region).

The combined image was then used as input image to segment the PVS by the 'Object Counter' function. In the 'Object Counter' module, we set the 'Max. Size' to '12' and 'Min. Size' to '2' (the maximum/minimum area size of each object). The minimum was set to 2 voxels instead of 1 to avoid image background noise. By definition, the PVS diameter is less than 3 mm (Kwee and Kwee, 2007), so the area of one PVS dot is less than 9 mm^2. The image information (Figure E4, parameters related to voxel size were highlighted by the yellow rectangle) showed that both the height and width of one voxel are 1mm, thus the 2-D area of 9 voxels are equal to 9 mm^2. And we increased 3 voxels in the maximum size setting to include linear structured PVS.

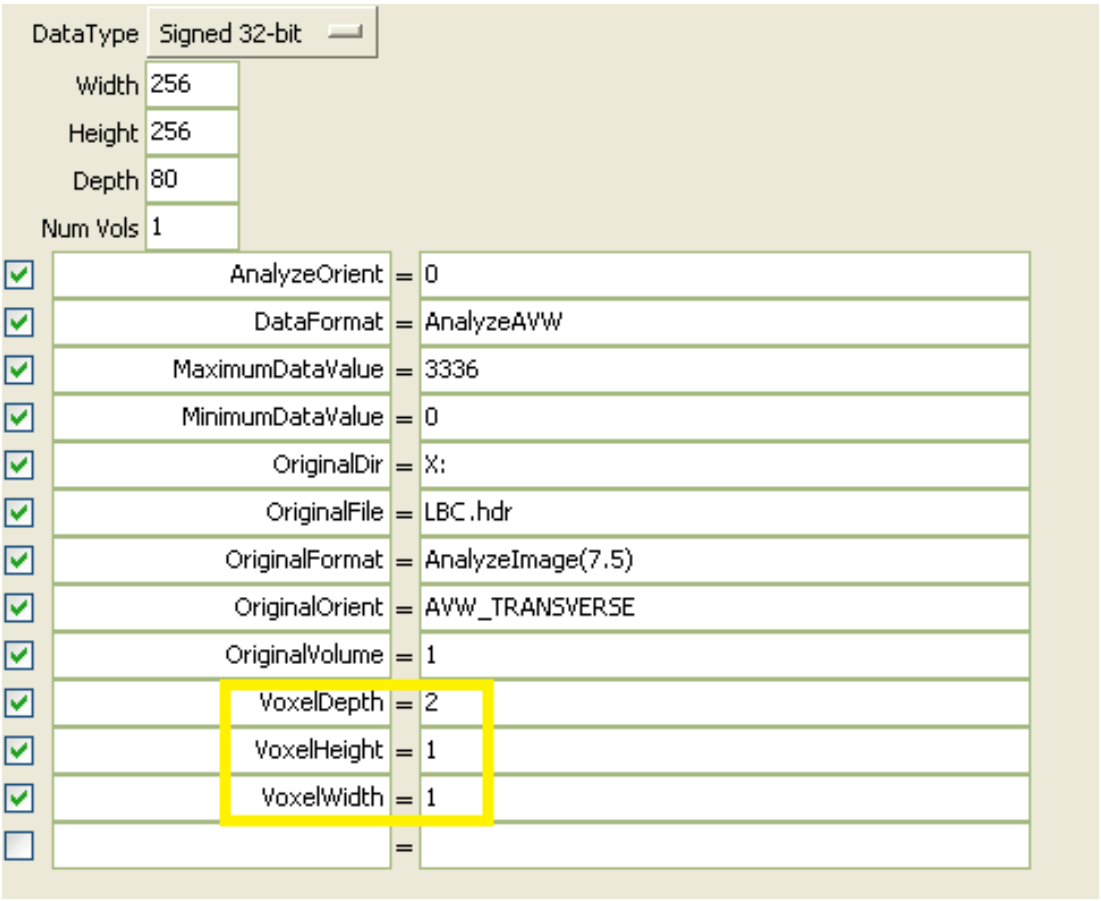

Figure E4 Image information from the combined image of T2W image and ICV mask.

The setting of threshold (t) began when the PVS dots appeared on the binary image. Then the threshold was increased in 3% increments until there were no obvious PVS dots appearing in the binary image. The segmented volumes from individual thresholds were saved in the Analyze™ software workspace, and all of these segmented volumes were combined as the final PVS mask. This was then used to count and calculate the number and volume of the PVS (Figure E5).

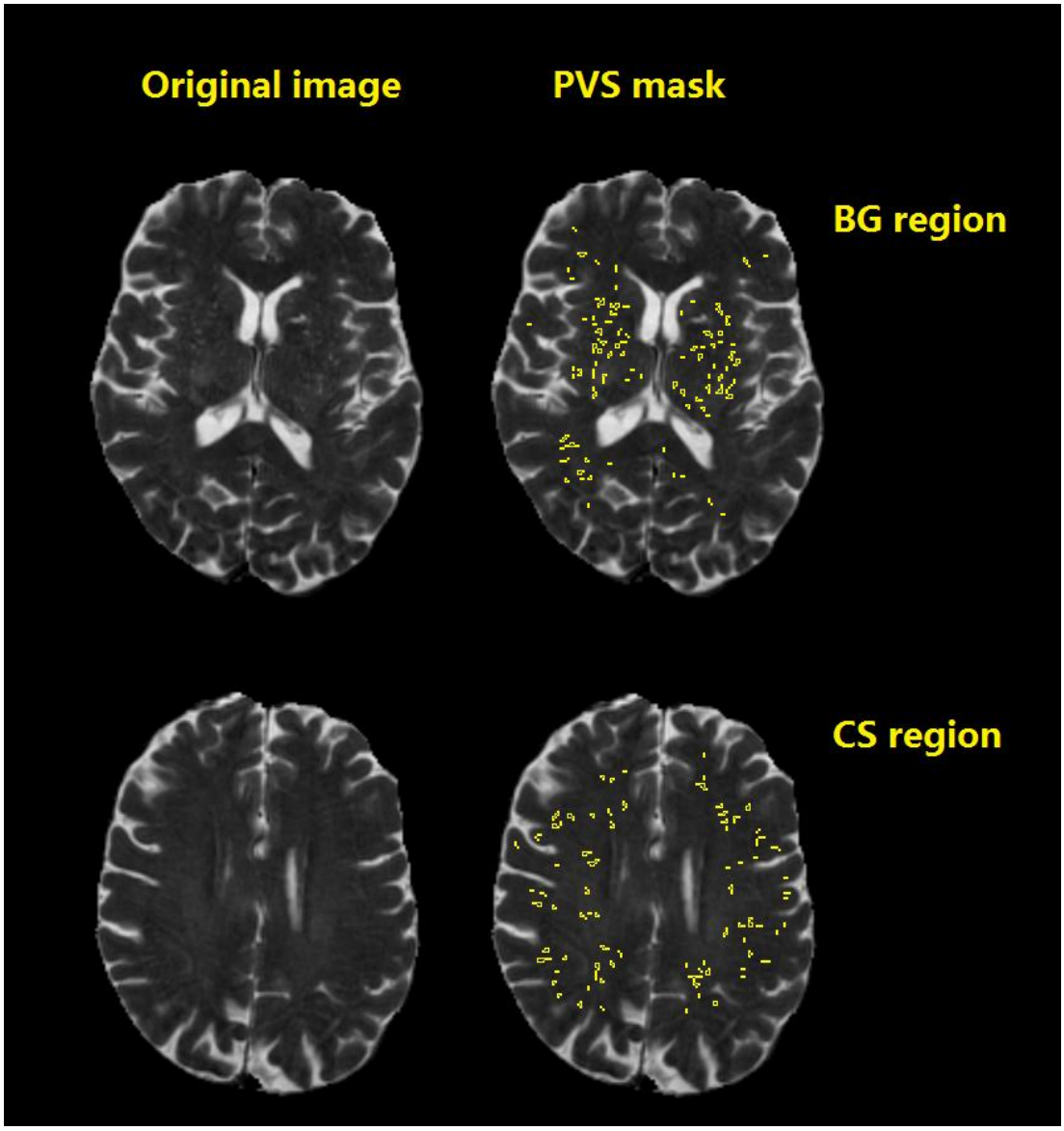

Figure E5 PVS mask generated from multiple thresholds (highlighted in yellow) in the BG and CS regions.

Both observers performed the above segmentation steps twice. For both times, Ob1 used the same slice. Ob2 performed one set of measurements blinded to the slice number used by Ob1, and for the second set of measurements Ob2 used the same slice as Ob1. The results were documented as: first measurement from Ob1 (Ob1_1); second measurement from Ob1 (Ob1_2); first measurement from Ob2 when blinded to the slice number (Ob2_1); and second measurement from Ob2 unblinded to the slice number used by Ob1 (Ob2_2).

Step 3-Multiple thresholds: specifically in the BG ovoid regions.

In this step, we aimed to increase the measurement consistency. The results from the previous step suggested that restricting the measurements within the two ovoid regions in the BG might give higher consistency and lower observer variability than other parts of the BG and CS regions. Thus, in this step, we set the regions of interest (ROI) specifically to the two ovoid regions in the BG instead of the whole brain (ICV).

We consistently used the anatomical structures: vertical ramus of the lateral fissure and posterior segment of lateral fissure to set the boundaries for the mask of ovoid regions in the BG (BG ROI). The BG ROI mask was generated for each case (Figure E6). The PVS segmentation steps were the same as described in Step 2 except changing the ICV mask into BG ROI mask.

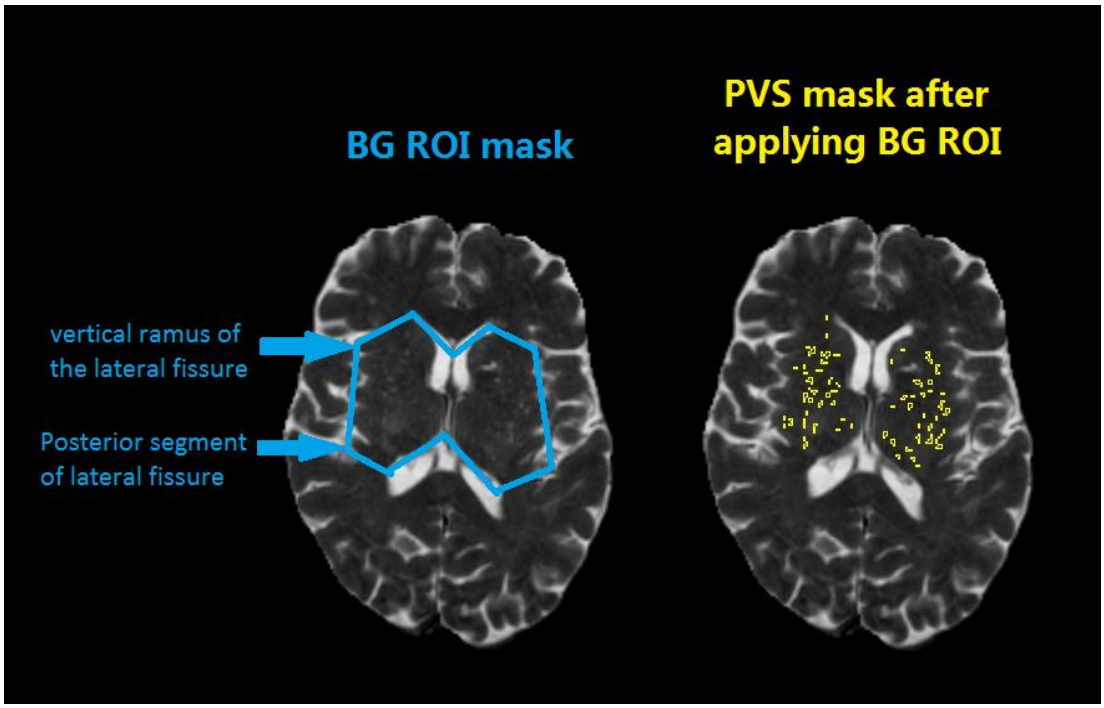

Figure E6 Anatomical boundaries for the mask of ovoid regions in the BG (BG ROI) and the PVS mask after applying BG ROI.

Step 4. Generation of the T2W intensity adjusted image.

The different amount of threshold applied was considered to be related to the image intensity. In this step, we adjusted the intensity of images adjustment used was based on the theory of 'histogram equalization' (Seul et al., 2000). It involved mapping the values of the input intensity image to new values when 1% of the highest intensities and 1% of the lowest intensities were saturated. The intensity adjustment changed the areas of lower local contrast to a higher contrast and allowed the most frequent intensity values to spread out effectively (Figure E7).

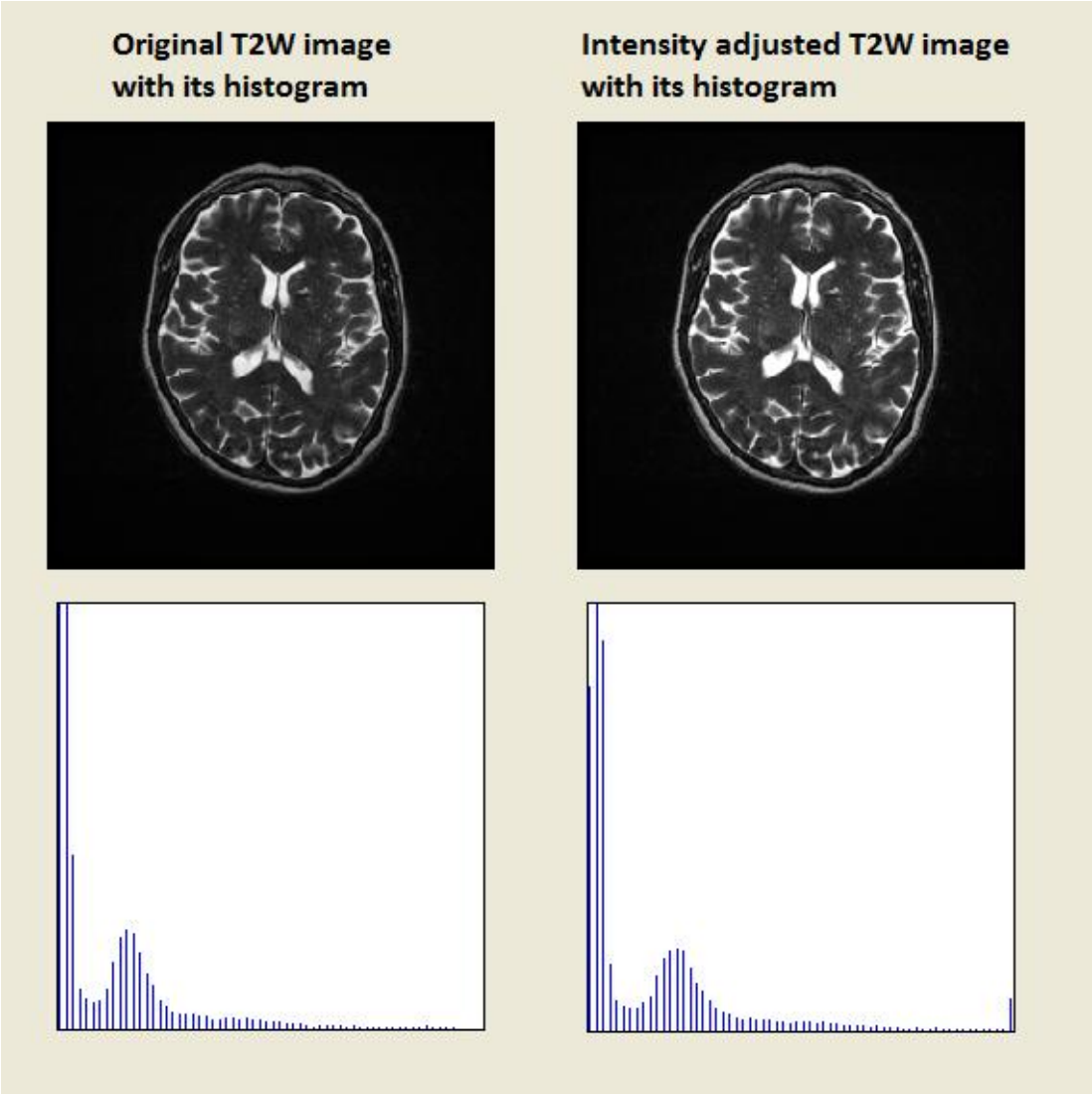

Figure E7 The effect of 'histogram equalization' on image intensity.

Step 5-Applying one threshold to the BG ROI of intensity adjusted T2W image.

In this step, we aimed to apply a single threshold on the intensity adjusted images for the PVS segmentation. We then tested whether using the same threshold for all cases would be effective in picking up most of the PVS dots in BG ROI using the T2W intensity adjusted image.

For the first aim, for each case, we applied three thresholds separately to the intensity adjusted T2W image combined with BG ROI mask. These three thresholds should include the most of the PVS dots, and we recorded the PVS volume and count for each threshold (Figure E8).

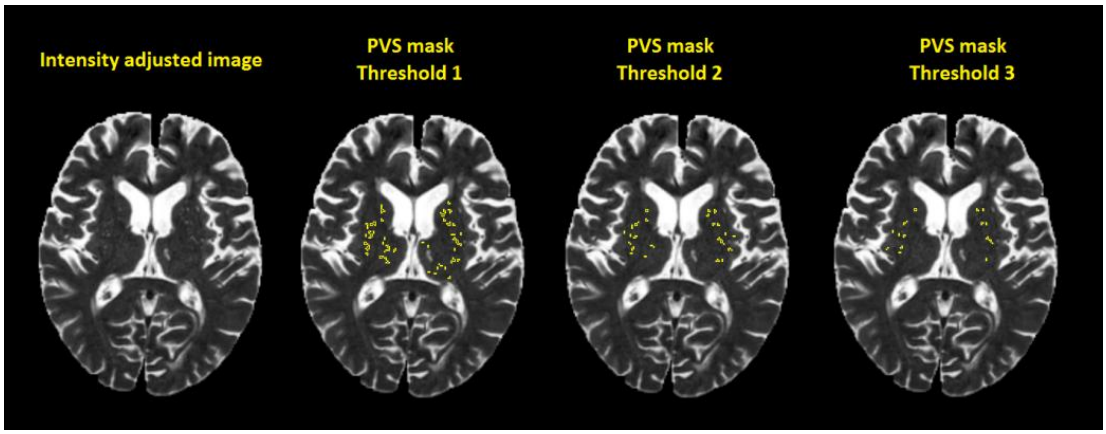

Figure E8 PVS masks generated from three different thresholds.

To solve the question of using the same threshold for all cases, an experienced neuroradiologist picked one PVS mask which included the most cavitied PVS and did not include artifacts from the three PVS masks generated from the previous step. This process was done when the neuroradiologist was blinded to the patients' information, the threshold values and the PVS results. We used the threshold values refer to the best fitting PVS masks been picked and calculated the average of these thresholds. We also tested the efficiency of this averaged threshold in assessing the PVS each case, which proved not successful for all cases.

Step 6-Applying the lacune mask to the BG ROI of the intensity adjusted T2W image.

Because the intensity of PVS is similar to the lacunes on MR images, and because there is an overlapping in size between PVS and lacunes (3-5mm) (Hernandez et al., 2013), we wanted to know whether the appearance of the lacunes would influence the PVS segmentation and whether applying the lacune mask before the PVS segmentation would improve the segmentation efficiency. Within the 16 cases, four of them had lacunes. We manually generated the lacune mask on the FLAIR image , based on a region-growing algorithm in Analyze 10.0 software (Robb and Hanson, 1995). Then we applied the lacune masks to the BG ROI in the intensity adjusted T2W images (Figure E9).

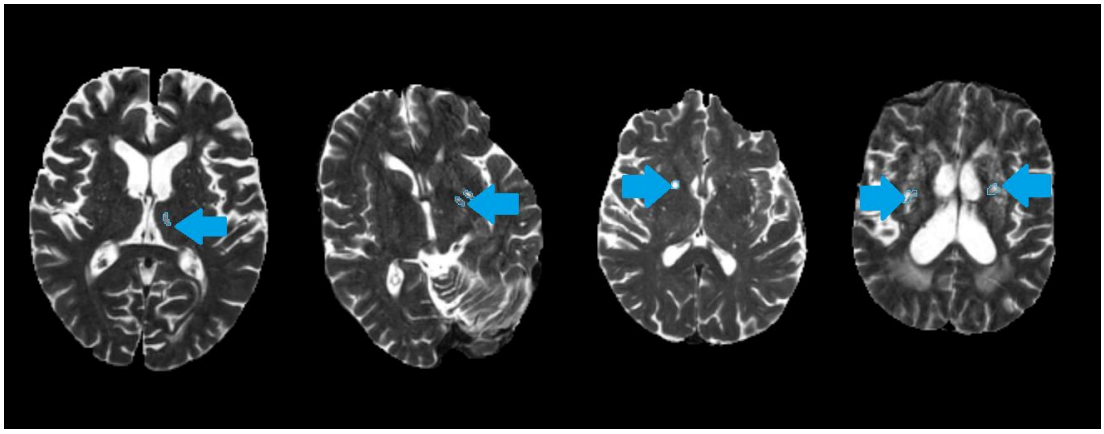

Figure E9 Lacune masks highlighted in blue (arrows pointing to) in four testing cases.

Step 7. Applying one threshold to the BG ROI of a combined image of intensity adjusted T1-weighted (T1W) and intensity adjusted T2W.

Previous optimization results in the Step 5 and 6 showed that the use of an intensity adjusted T2W image itself failed to find a common threshold for all cases. Applying a lacune mask was not successful either. Therefore, combining intensity adjusted T2W images with other MRI sequences was considered for further optimization.

T2W images were found to be the best images to identify PVS (Kwee and Kwee, 2007). T1-weighted images (T1W) had also been used in PVS visualization (Groeschel et al., 2006; Zhu et al., 2010). PVS were visualized as hyperintense regions on T2W image and as hypointense regions on T1W. Their combination use was applied to detect PVS visually in several computational methods (Sachdev et al., 1999; Uchiyama et al., 2008; Wuerfel et al., 2008). Thus in this step, three cases with severe and confluent lesions were selected for testing the efficiency of T2W intensity adjusted image and T1W intensity adjusted image.

In this step we wanted to know whether applying one threshold to the BG ROI of the combined image (T2W and T1W images after intensity adjustment) could be successful in identifying the PVS. The combination of images was achieved by the dot product function in the 'Image Calculator' in the Analyze™ software (same operations as described in the Step 2).

Step 8. Applying one threshold to the BG ROI of the combined image of two intensity adjusted T2W images.

In this step we used the same set cases and combination method described in Step 7 to test the PVS segmentation efficiency of applying one threshold to the BG ROI of the combined image (two T2W images after intensity adjustment).

E2-Manual of multiple thresholds using Object Counter in Analyze™ 10.0 software (Step 2)

(1) Loading files

(1.1) Open Analyze™ 10.0 by double clicking in the icon. The main window will appear.

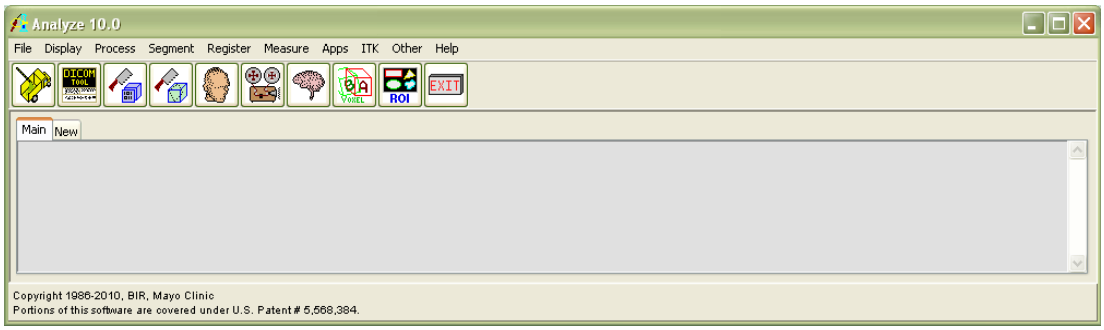

(1.2) Select **File** | **Load**

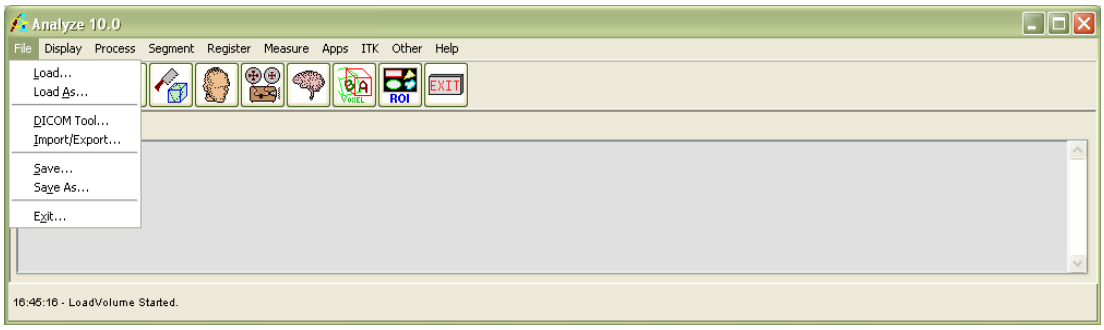

(1.3) Load the T2-weighted image (T2W) and intracranial volume (ICV) mask in Analyze format in the explorer's **Load** window that appear in the screen. The image volume selected will appear loaded and highlighted in the Analyze window.

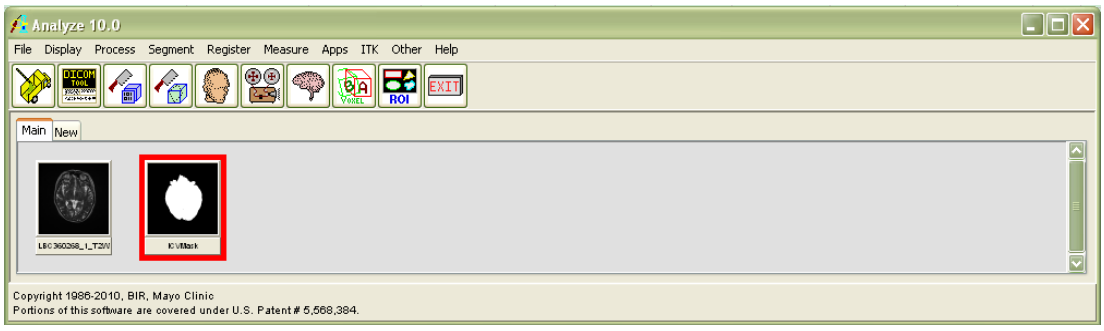

(2) Multiple ICV mask by T2W image

(2.1) Choose ICV mask, then select **Process**| **Image Calculator**

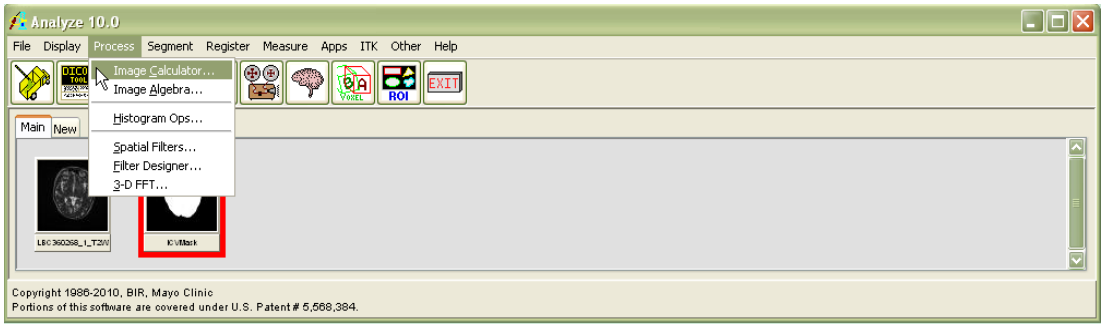

(2.2) Press  , and then drag the T2W image into the Image Calculator.

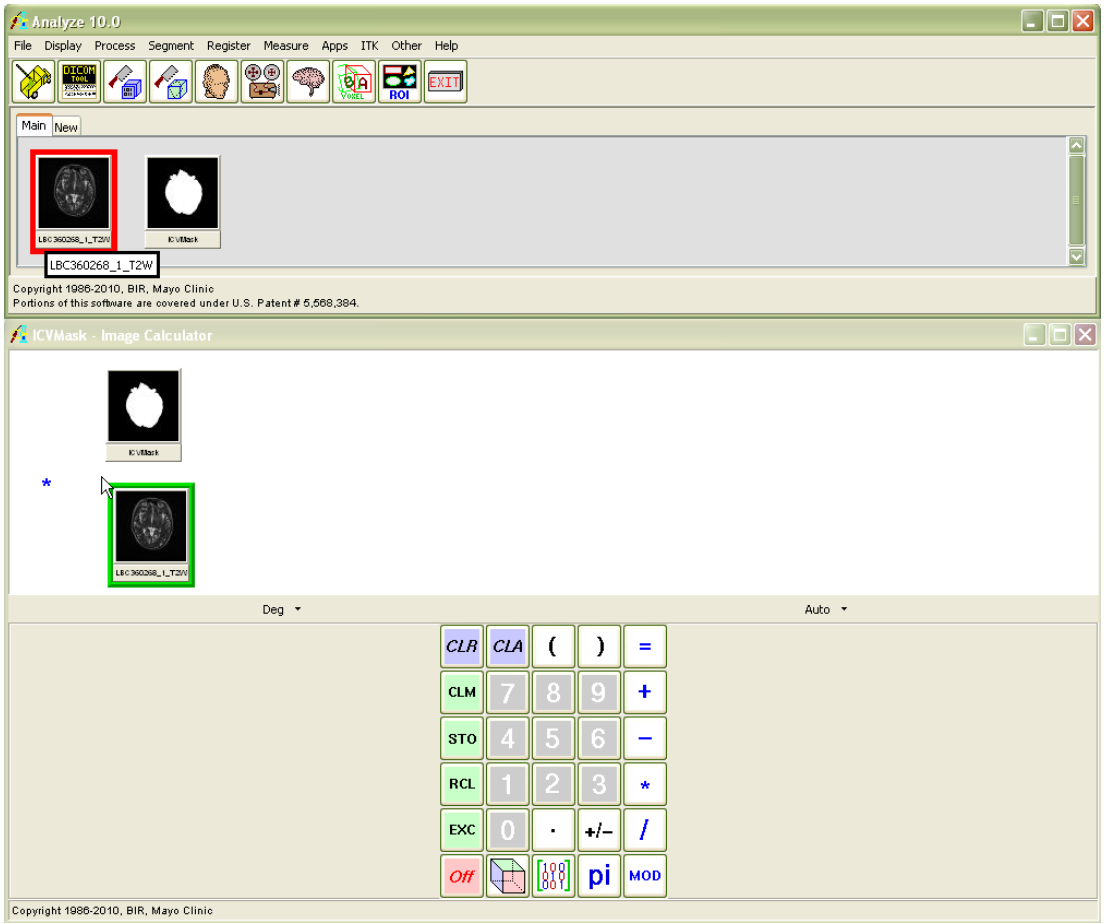

(2.3) Press [=], choose “Change a Copy of the Loaded Volume”.

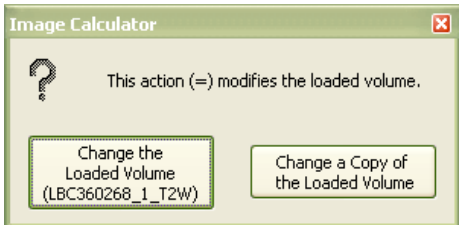

The combined image would appear in both Image Calculator Workspace and the main Analyze Workspace.

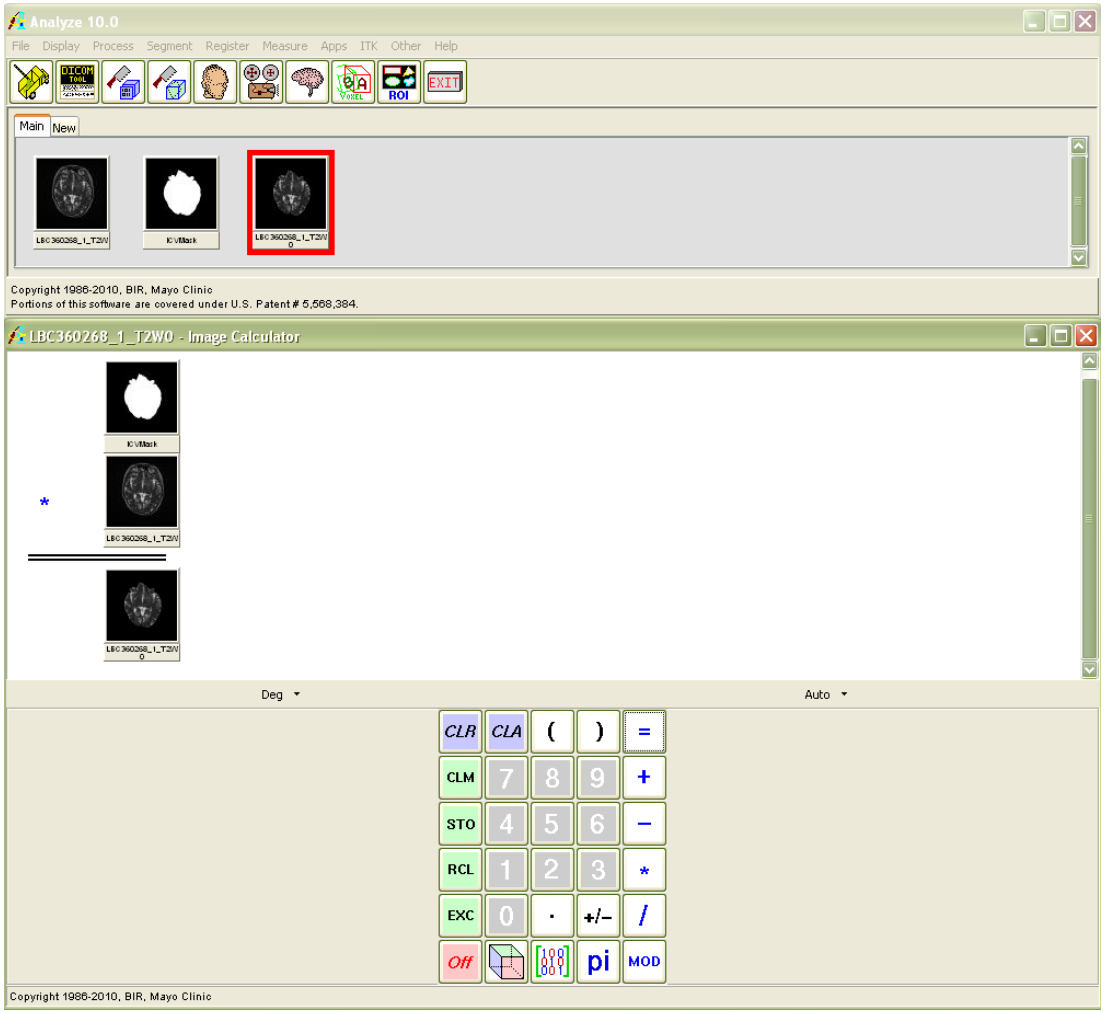

(2.4) Close Image Calculator; choose the combined image in the Analyze Workspace, select **File**| **Save As,** named as **LBC36xxxx_ICVT2,** in AnalyzeImage(7.5) format.

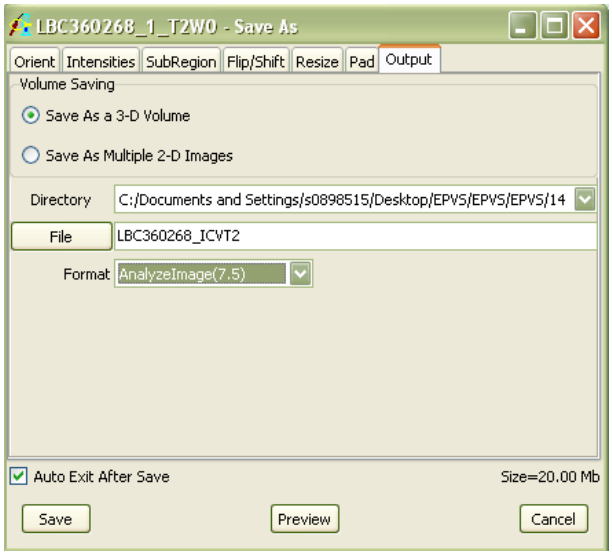

(3) Settings and Segmenting for PVS by Object Counter

Take the segmenting of PVS in the Basal Ganglia as an example, the segmenting of PVS in the Centrum Semiovale follows the same procedure.

(3.1) Load **LBC36xxxx_ICVT2** image, then select **Measure** | **Object Counter.**

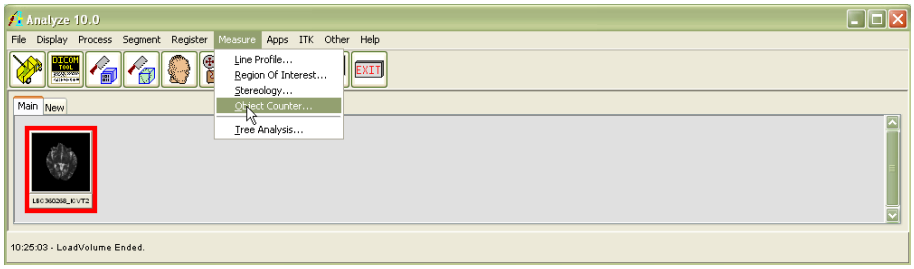

(3.2) Basic setting.

The image would appear in the "**Connect**" tab (**2D; Neighbors: 8**) as default. Click on  button for increasing the size of the image and select the slice you chose for

Basal Ganglia in "Standard slices Choosing" step (in this case, slice 48). Set **Max. Size 12** and **Min. Size** as **2**.

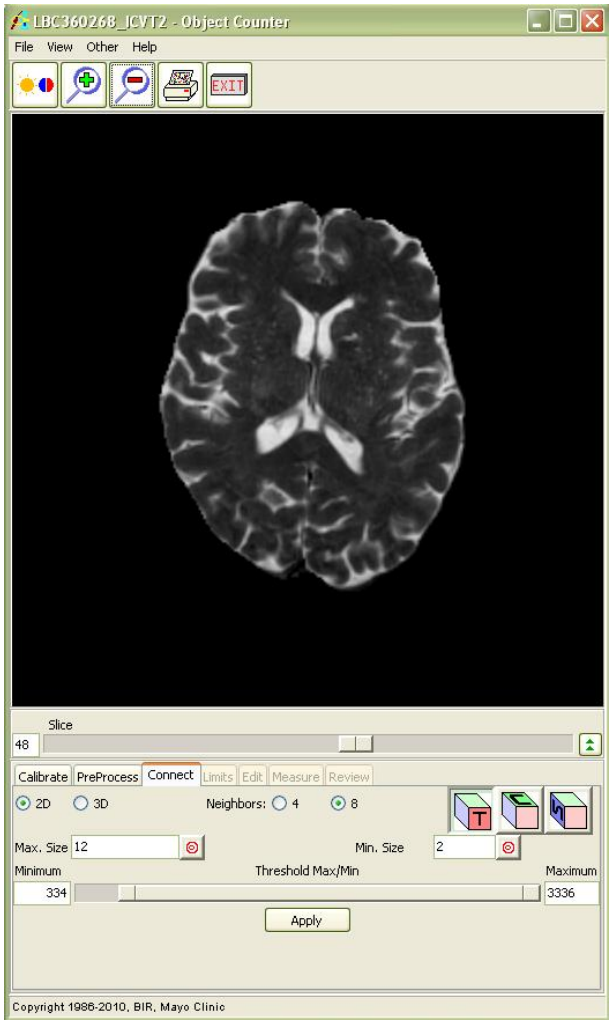

The Max. Size means the number of voxels, which depends on the voxel sizes, in the LBC study, the voxel sizes are

VoxelDepth	=	2
VoxelHeight	=	1
VoxelWidth	=	1

, the height is 1 mm, and the width is 1 mm. The area of one voxel in this 2D image is $1mm^2$.The maximum area of an PVS dot should be 9 mm^2 (less than 3 mm maximum diameter); however, it was set to 12 to include linear structured PVS.

For all the cases, the Min. Size was set to 2 to avoid the noise from the background of the images.

(3.3) Threshold setting and segmenting.

When the threshold is low, it is useful to include the PVS which are not so hyper intensive; but it cannot distinguish the hyperintensive PVS from CSF in the ventricles and white matter hyperintensities (WMH). When the threshold is high, all the objects are more separated, it is useful to include the hyper intensive PVS, but may fail to include the non-hyperintensive PVS.

- Always start from 600 (intensity displayed in the Analyze software): if for some cases, when set the threshold t=600, there is no obvious PVS dots, but all merged backgrounds, then try to start from higher threshold, e.g. 700 or 800.
- Then add 100 more to the previous threshold until there is no obvious PVS appear in the binary image. Save all the Segmented Volume in the Analyze Workspace.
- Use the same set of intervals of a hundred thresholds for all the cases (range from 600 to 1500) to include all potential PVS in the images.

In this example case, set the Minimun Threshold to 600, press "**Apply**".

Then press the "**Limit**" tab, set the Z Min and Z Max into the same Basal Ganglia slice (in this case, slice 48).

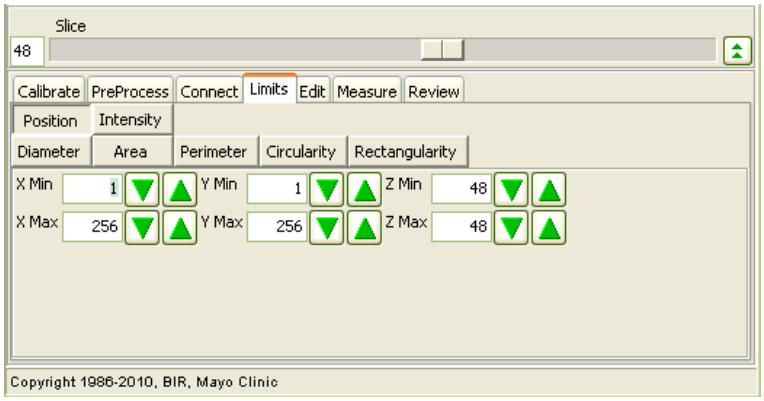

Then select **File | Save Segmented Volume,** named **"t600"** (t means threshold and 600 is the threshold chosen for this segment).

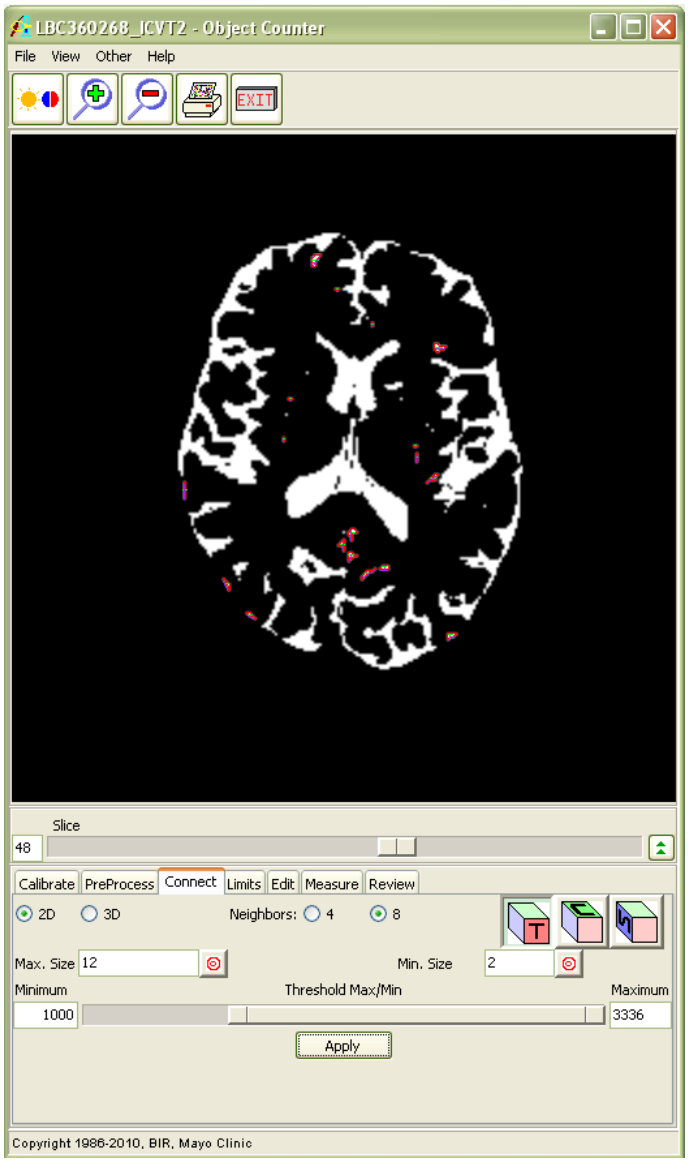

In this case, there is no obvious PVS appear in the binary image when threshold=1000. Save all the Segmented Volume in the Analyze Workspace.

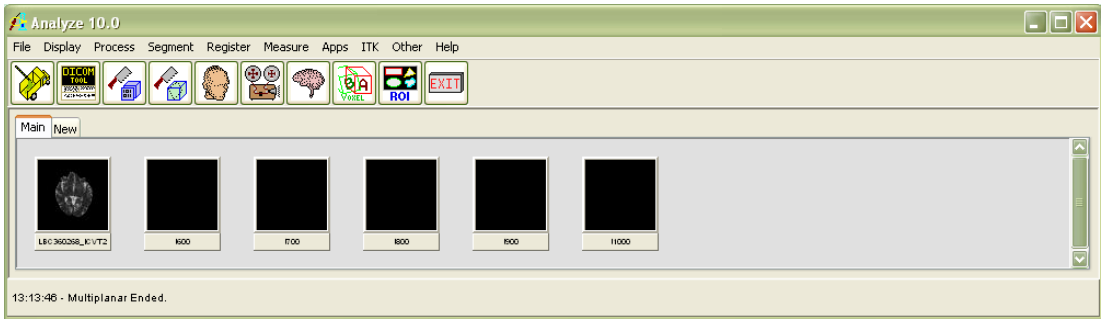

(4) Create PVS mask

(4.1) Combine all these segmented volumes in the Image Calculator.

Select **Process** | **Image Calculator**, press + to combine all the segmented volumes into one mask.

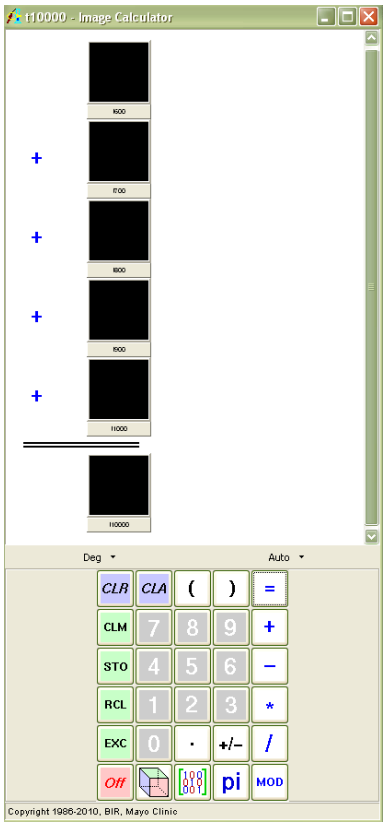

(4.2) Close Image Calculator and choose the combined image in the Analyze Workspace, select **File**| **Save As,** named as **LBC36xxxx_BG,** in **OBJMAP** format. Need to change the "**Intensity Scale- Output**" into "**Unsigned 8-bit**", and then press "**Save**".

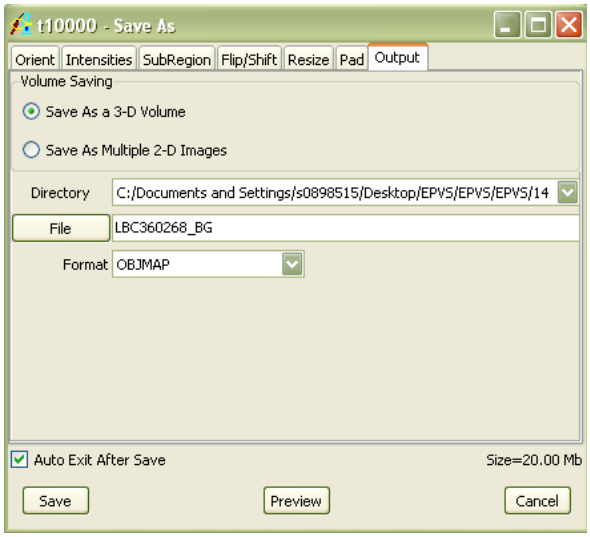

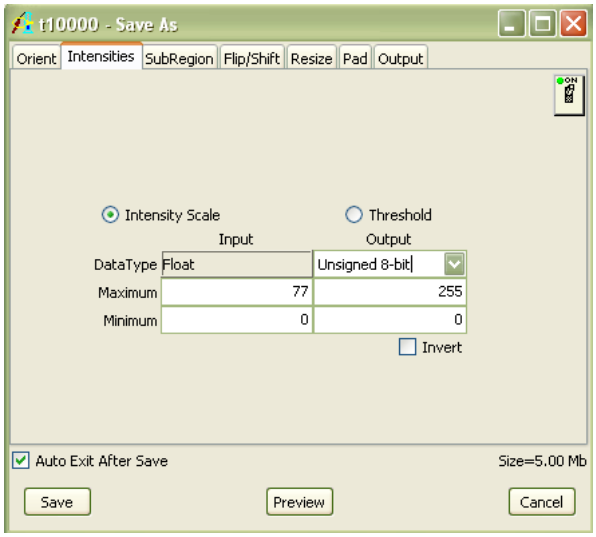

(4.3) Combine all the objects into the same object in the Region Of Interest.

Click on the **LBC36xxxx_ICVT2** image in Analyze Workspace, and then select **Measure | Region Of Interest (ROI)**.

In the ROI, select File | Load Object Map, load the **LBC36xxxx_BG** object map.

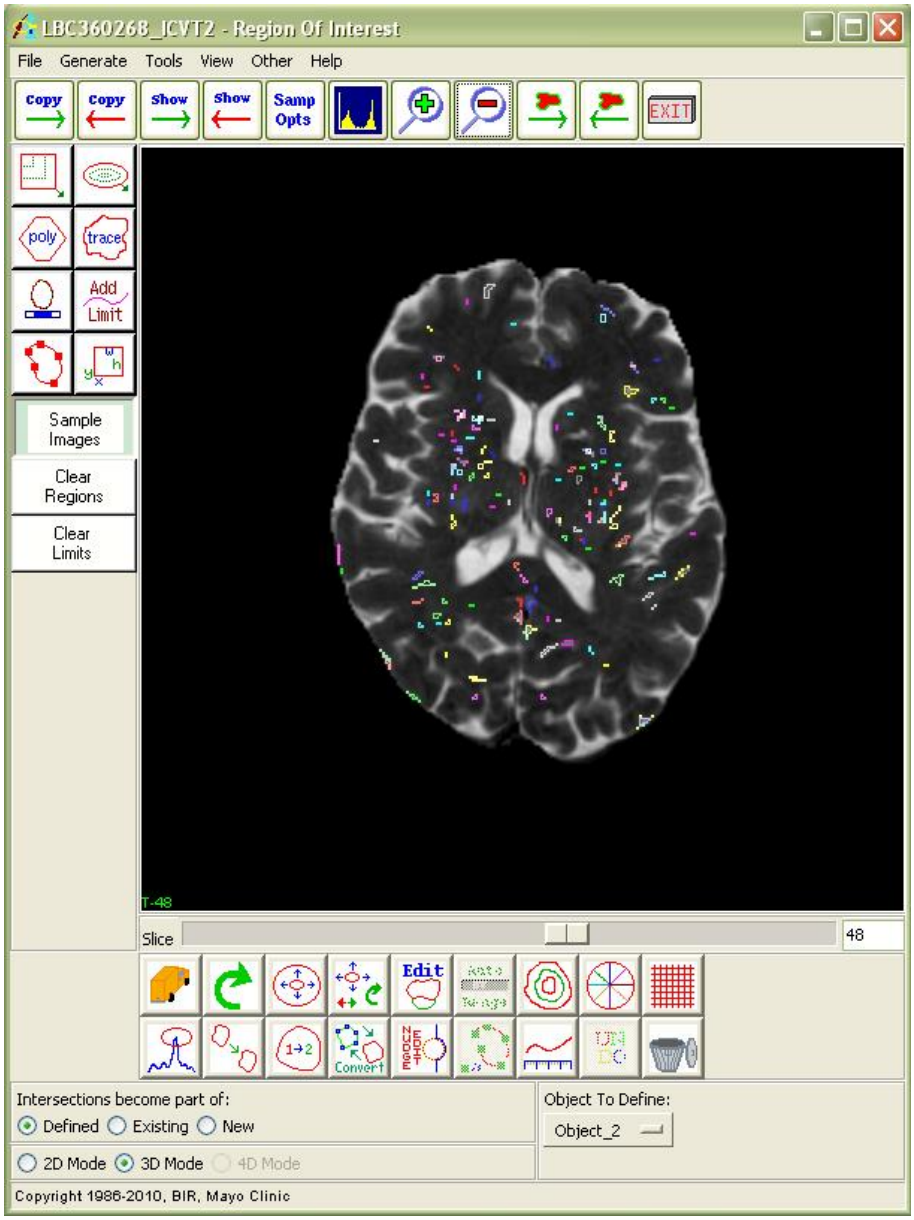

Open the **View | Objects window**. Once you're in the Objects window, select the "**Reassign Object(s)**" button. The Reassign Object(s) window will be returned and you can select all the objects except Object 1 (because Object 1 is the default object for background) and reassign them to a single object (always select Object_2, you could also reassign them to any other objects, the only difference would be the colour of the object map you generated). Once you have your objects selected, click **Apply**.

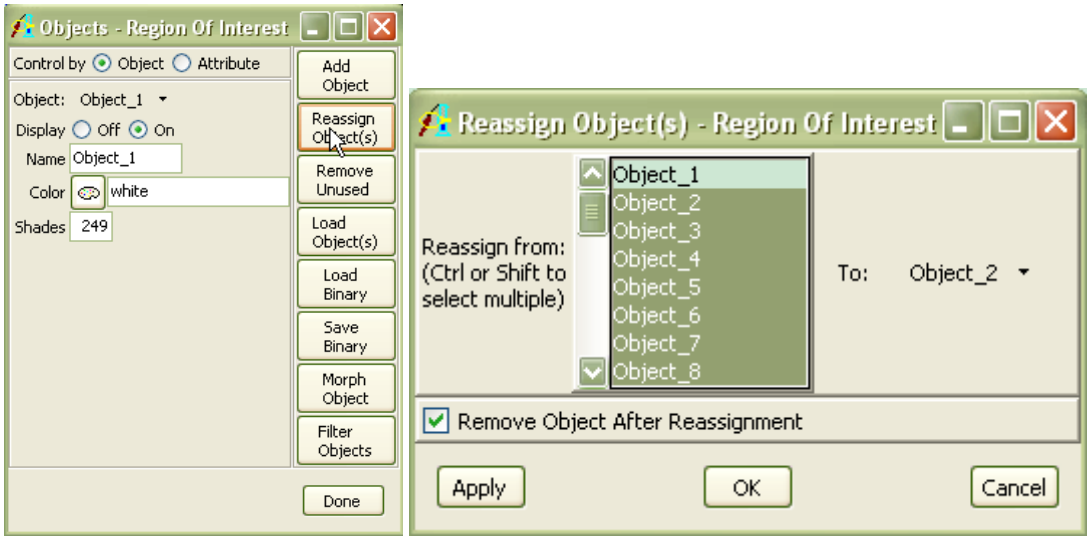

Then in the objects window, change the **Name (PVS)** and **Color (red)** of the object. If you have already choose Object_2 in the "**Reassign Object(s)**" step, then do not need to change the colour.

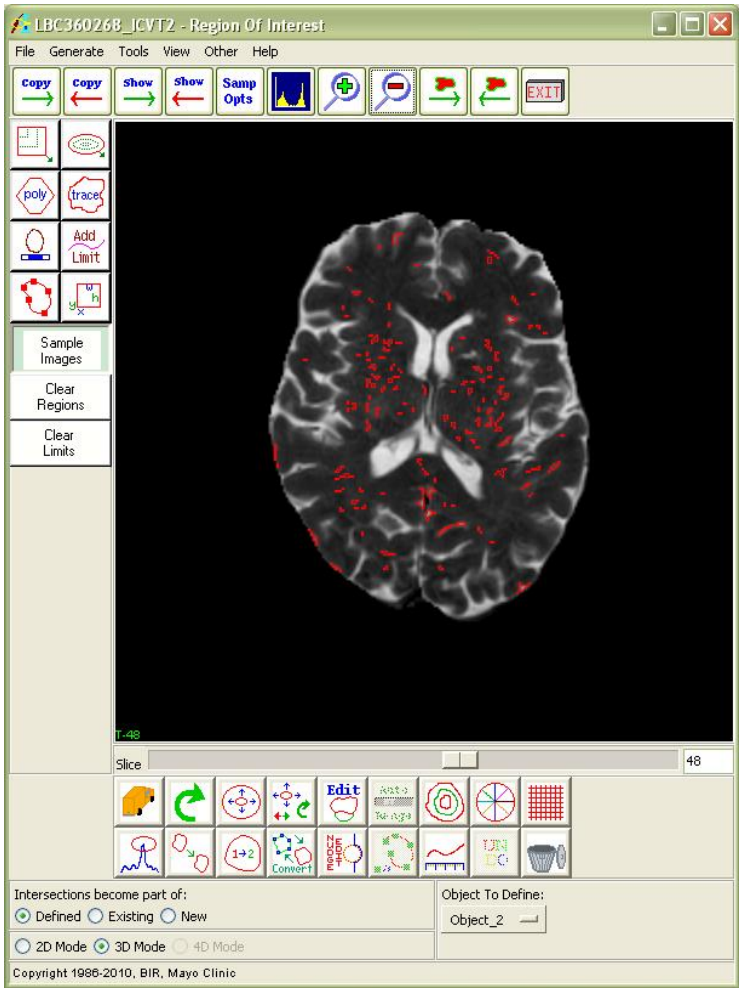

(4.4) Use  to remove false positive near surface of the brain, ventricles, sulci and WMH. Go through the slices before and after the slice we chose, and use another T2 image as a reference.

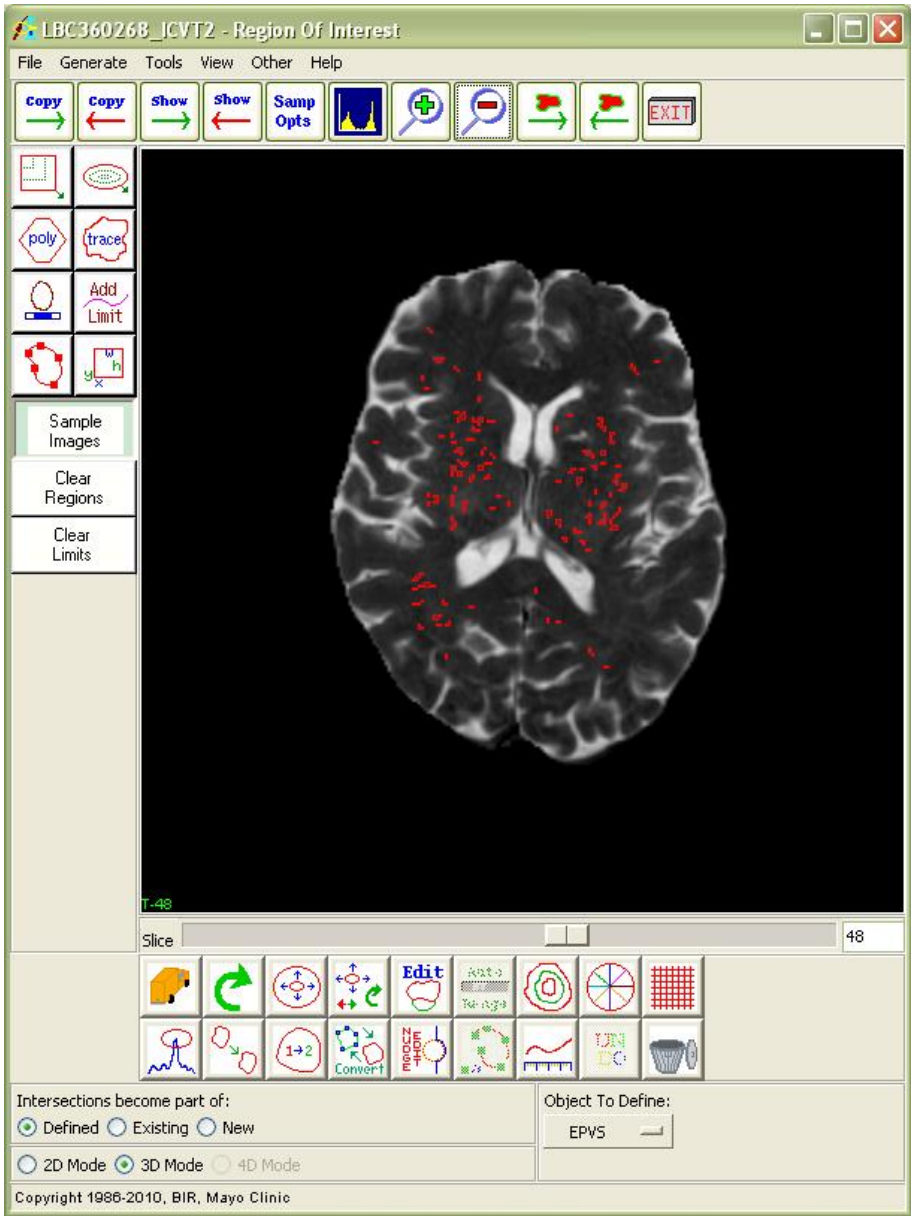

(4.5) Before close the Region of Interests module, save the object map, named as **LBC36xxxx_BG**. This object map also needs to be saved in the AnalyzeImage(7.5) format for further use.

In order to save this object map in AnalyzeImage(7.5) format, open **View | Objects window**, select the object as PVS, then click "**Save Binary**" button, named as **LBC36xxxx_BG**, saved in the "**Analyze Workspace**", then click "**Save**" and "**Save it**".

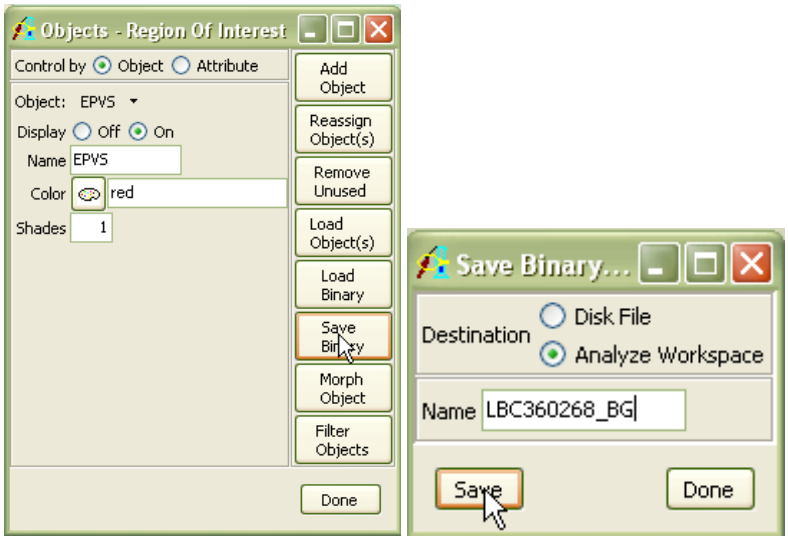

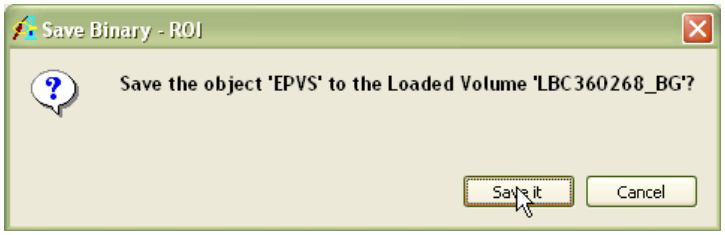

The saved binary object image would appear in the main Analyze Workspace and highlighted in the Analyze window. Then select **File**| **Save As,** named as **LBC36xxxx_BG,** in AnalyzeImage(7.5) format.

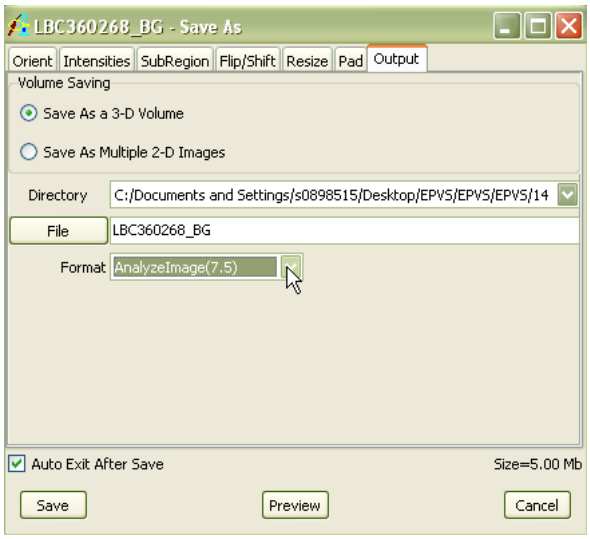

(5) Calculate the Counts and Areas of PVS

(5.1) Calculate the Counts and Areas in Object Counter.

Load the T2W image in Analyze Working space, and then open the Object Counter, then select **File** | **Load** Volume, load LBC36xxxx_BG which is in **AnalyzeImage(7.5)** format.

Then choose slice of BG, change the **Min.Size** as **2**, click **Apply**.

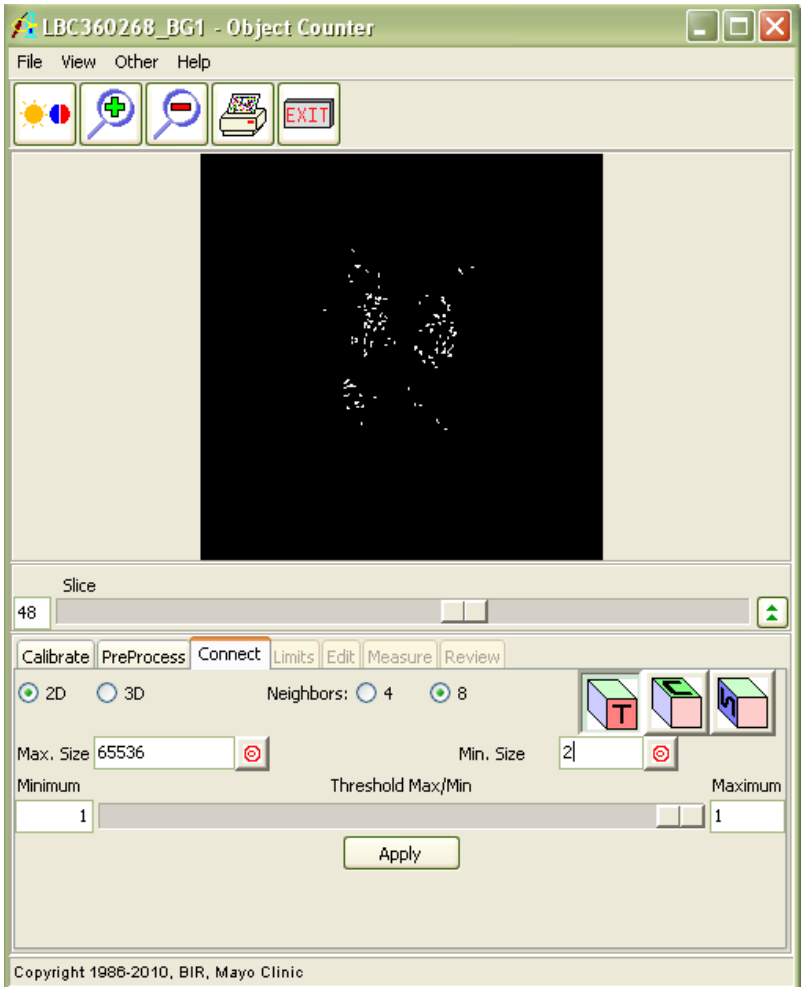

(5.2) Select the "**Measure**" tag, tick the "**Area**", press "**Log Measurements**" button.

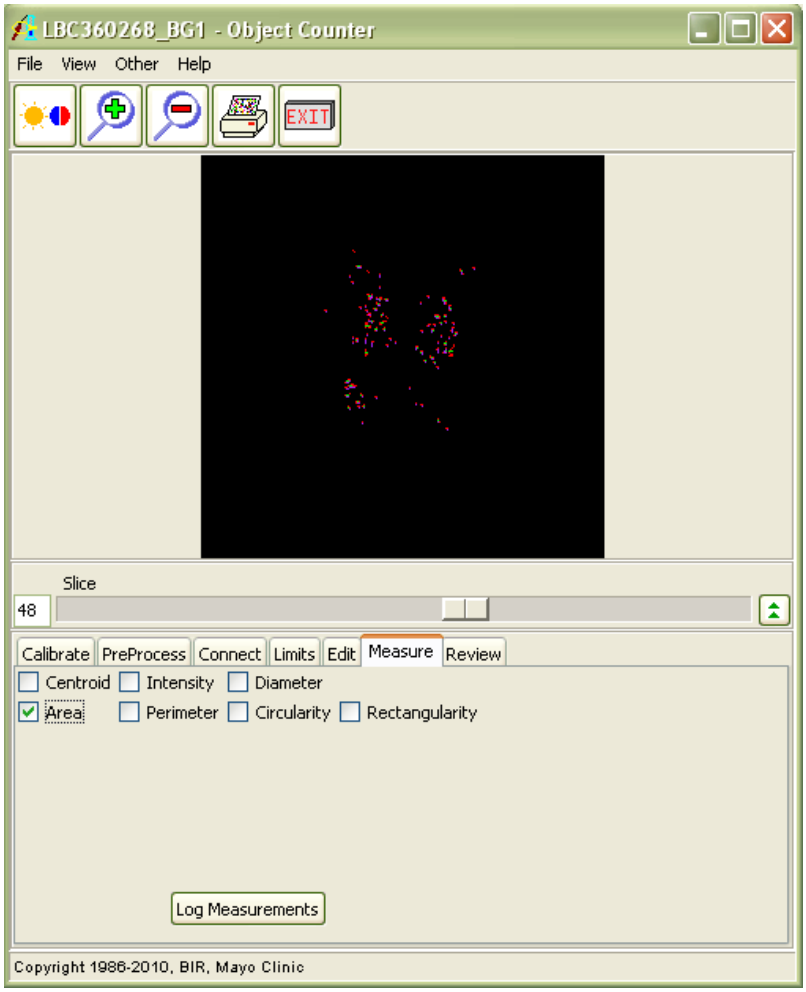

(5.3) A window with the final report (summarised and/or detailed). From the summarised report, you could get the average area of the PVS and total number; from the detailed report, you could get the area of each individual PVS. Right-click when the mouse is over this window to save the report. Write down the results (both count and area) in your spreadsheet.

E3-Manual of intensity adjustment (Step 4)

(1) Convert the T2-weighted images from nifti format to Analyze 7.5 format using Analyze software.

(1.1) Open Analyze 10.0 by double clicking in the icon. The main window will appear.

(1.2) Select File | Load

(1.3) Load the original T2-weighted image in nifti format to the explorer's Load window that appear in the screen. The image volume selected will appear loaded and highlighted in the Analyze window.

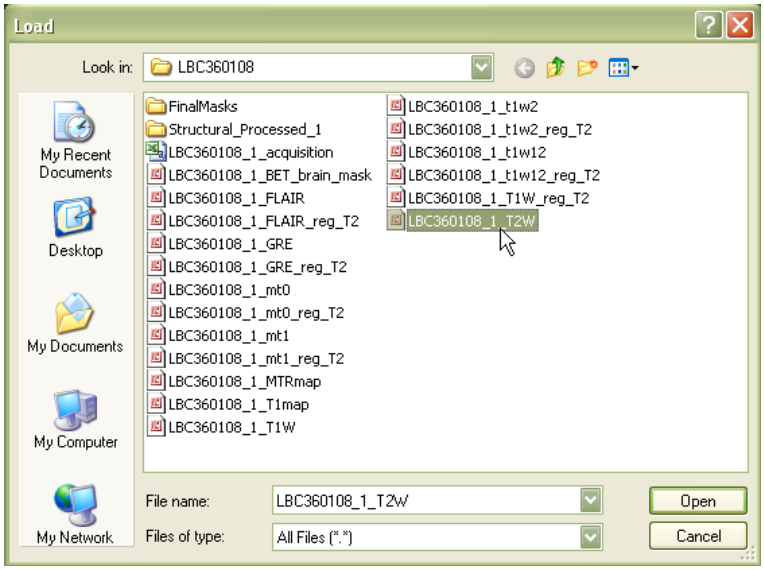

(1.4) Select File | Save, choose 'Save', in the AnalyzeImage(7.5) format.

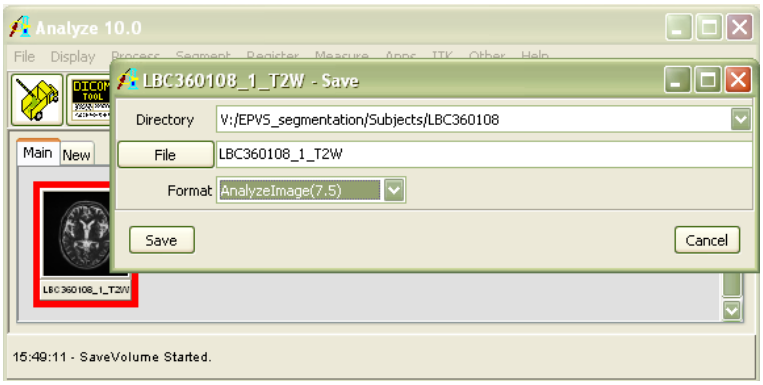

2. In the MATLAB, call the intensity adjustment function.

(2.1) Open the 'V:\EPVS_segmentation folder', double click the 'intensity_adjustment_EPVS. MATLAB M-file'.

```
% Function to do intensity adjustment

function intensity_adjustment_EPVS(input_file,out_file);

[data,dim,vox,type]=read_analyze_volume_BRIC(input_file);
data=imrotate(data,90);

I = double(zeros(dim(2),dim(1)));
d = uint8(zeros(dim(2),dim(1),dim(3)));

for i=1:dim(3)
    I=data(:,:,i)./max(max(data(:,:,i)));
    d(:,:,i)= im2uint8(I);
    mri1(:,:,i)=imadjust(d(:,:,i));
    mri2(:,:,i)= adapthisteq(d(:,:,i));
end

clear I d;

data1 = imrotate(mri1,-90);
data2 = imrotate(mri2,-90);

write_analyze_volume_BRIC(out_file,dim,vox,'testdata',data1,'uint8');
write_analyze_volume_BRIC(strcat(out_file,'_2'),dim,vox,'testdata',data2,'uint8');
```

(2.2) Press the green arrowhead  or F5 to run the program

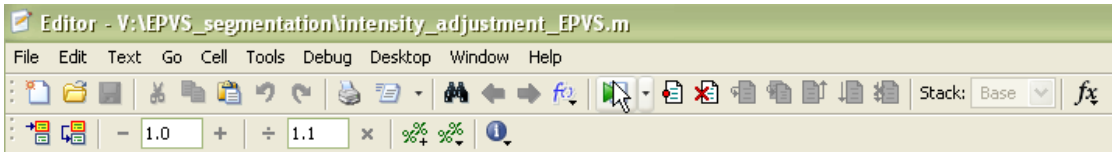

In the command window would appear an error

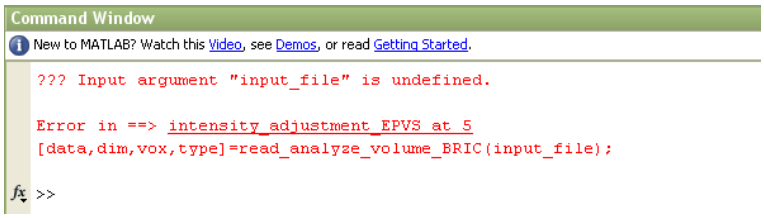

After the '>>', type in

'intensity_adjustment_EPVS('V:\EPVS_segmentation\Subjects\LBC360108\LBC360108_1_T2w',

'V:\EPVS_segmentation\Subjects\LBC360108\LBC360108_1_T2w_adj')'

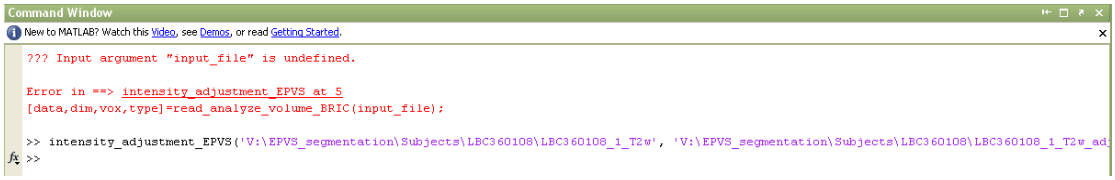

Appendix (F) Observer agreement in the PVS method development and validation

Two observers measured PVS twice in Step 2, 3 and 5 (refer to Figure 6.1 in Chapter 6 and Appendix E) on two separate occasions. Observer 1 used the same standard slices both times. Observer 2 was blinded to the standard slice number chosen by me for the first measurement, and was unblinded for the second measurement. We calculated the mean and standard deviation (SD) of the intra- and inter-observer variability of PVS volume and count summarized them in the **Table F1 and F2**.

Table F1 Summary of intra- and inter-observer variability for **PVS volume (voxels)** measurements from different steps.

Location	Image	Variability Type	Mean	SD
Step 2- Multiple thresholds in the CS region				
CS	T2W	Intra (Ob1)	307.81	146.37
		Intra (Ob2)	336.59	99.19
		Inter (b)	31.50	82.30
			29.00	84.83
		Inter(u)	28.56	84.33
			26.06	90.89
Step 2- Multiple thresholds in the BG region				
BG	T2W	Intra (Ob1)	321.66	136.47
		Intra (Ob2)	249.22	53.90
		Inter (b)	-74.69	114.04
			-83.63	124.03
		Inter(u)	-61.25	103.82
			-70.19	113.13
Step 3- Multiple thresholds specifically in the BG ovoid region (BG ROI)				
BG ovoid region	T2W	Intra (Ob1)	232.31	75.90
		Intra (Ob2)	226.75	53.57
		Inter (b)	-7.56	60.96
			-12.19	60.74
		Inter(u)	1.06	53.13
			-3.56	47.84
Step 5- Applying one threshold to the BG ROI of intensity adjusted T2W				
BG ovoid region	T2W-ia	Intra (Ob1)	321.66	136.47
		Intra (Ob2)	249.22	53.90
		Inter (b)	-74.69	114.04
			-83.63	124.03
		Inter(u)	-61.25	103.82
			-70.19	113.13

SD: standard deviation; T2W: T2-weighted; ia: image after intensity adjustment; BG: basal ganglia; CS: centrum semiovale; BG ROI: basal ganglia regions of interests; Ob: observer; b: blinded; u: unblinded.

Table F2 Summary of intra- and inter-observer variability for **PVS count (number of dots)** measurements from different steps.

Location	Image	Variability Type	Mean	SD
Step 2- Multiple thresholds in the CS region				
CS	T2W	Intra (Ob1)	73.66	32.92
		Intra (Ob2)	79.19	20.17
		Inter (b)	6.12	27.66
			4.81	23.40
		Inter(u)	6.25	25.14
			4.94	21.02
Step 2- Multiple thresholds in the BG region				
BG	T2W	Intra (Ob1)	72.50	28.65
		Intra (Ob2)	56.69	10.55
		Inter (b)	-15.88	24.47
			-18.12	25.89
		Inter(u)	-13.5	24.58
			-15.75	25.26
Step 3- Multiple thresholds specifically in the BG ovoid region (BG ROI)				
BG ovoid region	T2W	Intra (Ob1)	49.88	15.88
		Intra (Ob2)	51.06	10.27
		Inter (b)	1.12	13.12
			-0.50	13.36
		Inter(u)	2.87	12.55
			1.25	12.15
Step 5- Applying one threshold to the BG ROI of intensity adjusted T2W				
BG ovoid region	T2W-ia	Intra (Ob1)	18.97	5.67
		Intra (Ob2)	19.37	4.95
		Inter (b)	0.12	6.45
			0.31	7.14
		Inter(u)	0.50	4.87
			0.69	6.94

SD: standard deviation; T2W: T2-weighted; ia: image after intensity adjustment; BG: basal ganglia; CS: centrum semiovale; BG ROI: basal ganglia regions of interests; Ob: observer; b: blinded; u: unblinded.

Bland-Altman plots (Bland and Altman, 1986) were used to estimate the agreement within or between observers in Step 2, 3 and 5. Step 2 used multiple thresholds in the both the basal ganglia (BG) and centrum semiovale (CS) regions to assess PVS on the original T2-weighted (T2W) images. Step 3 used multiple thresholds in the restricted two ovoid BG regions to assess PVS on the original T2W images. Step 5 used one threshold in the restricted two ovoid BG regions to assess PVS on the intensity adjusted T2W images. The results were documented as: first measurement from Ob1 (Ob1_1); second measurement from Ob1 (Ob1_2); first measurement from Ob2 when blinded to the slice number (Ob2_1); and second measurement from Ob2 unblinded to the slice number used by Ob1 (Ob2_2).

1. Observer variability in Step 2

Both observers had high intra-observer variability on the PVS volume and count measurements in the BG and CS regions (Figure F1). For PVS volume intra-observer variability, most dots were located between -40 and 40 voxels (voxel: the unit of volume measurement). For the PVS count intra-observer variability, most dots located between -10 and 10 (number of dots). Ob2 tended to measure less than Ob1 in the BG regions, and more in the CS regions for PVS volume and Count measurements. The results from both observers showed that both volume and count obtained in the CS regions had larger SD than in the BG regions (Table F1, F2).

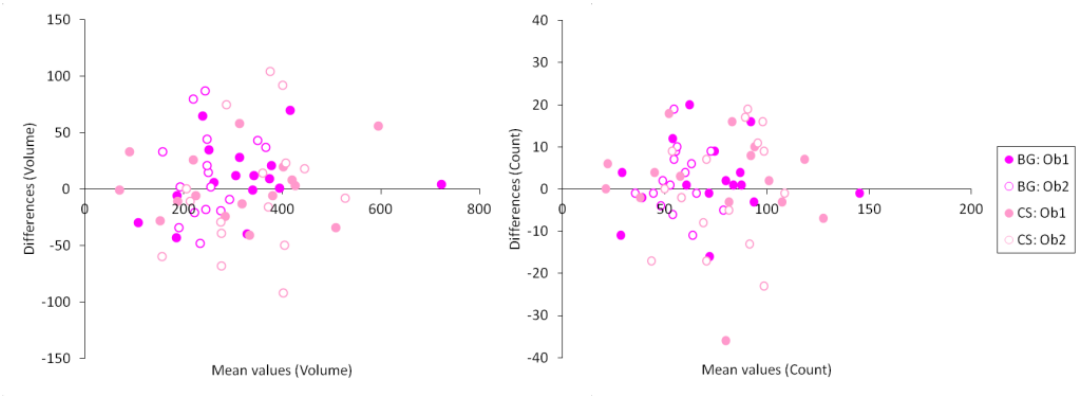

Figure F1 Intra-observer variability in PVS measurements (Step 2). Left: intra-observer variability of PVS volume measurement; Right: intra-observer variability of PVS count measurement.

PVS volume and count measurements in both regions showed high inter-observer variability (Figure F2, Table F1, F2). The discrepancy of the inter-observer difference in PVS volume and number in the CS regions was more scattered than the discrepancy in the BG regions. The situation was the same as observed in the intra-observer variability: there was a systematic bias between observers in differentiating PVS in both the BG and CS regions, and Ob2 tended to measure less than Ob1 in the BG regions, and measure more in the CS regions (Table F1, F2).

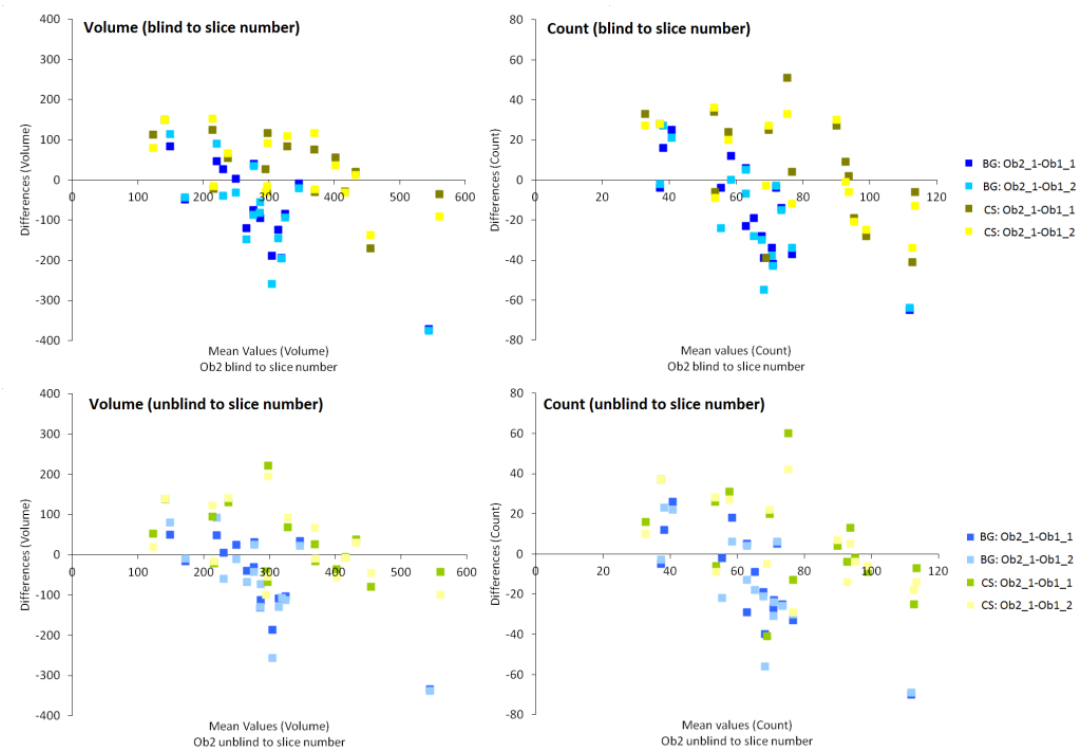

Figure F2 Inter-observer variability in PVS measurements (Step 2). Upper left: inter-observer variability of PVS volume when Ob2 was blinded to the standard slice number chosen by Ob1. Lower left: inter-observer variability of PVS volume when Ob2 was unblinded to the standard slice number chosen by Ob1. Upper right: inter-observer variability of PVS count when Ob2 was blinded to the standard slice number chosen by Ob1. Lower right: inter-observer variability of PVS count when Ob2 was unblinded to the standard slice number chosen by Ob1.

The intra- and inter-observer variability figure (Figure 6.3 in chapter 6) demonstrated that though this method was not effective in picking up the linear-shaped PVS in the CS, it was helpful in picking up the dots in the two ovoid regions

of the BG. In order to diminish the observer variability and increase the consistency, the regions of interest (ROI) were suggested to set specifically to the two BG ovoid regions in later method optimization.

2. Observer variability in Step 3

After restricting the ROI specifically to the two BG ovoid regions, both observers obtained smaller SD and smaller ranges of discrepancy on the measurements of PVS volume and count when compared with measuring the whole BG slice (Figure F3, Table F1, F2). For the PVS volume measurement, after setting the ROI into the two specific ovoid BG regions, the number of cases which had larger differences (>40 voxels or <-40 voxels) was reduced from four to one for Ob1 but stayed the same for Ob2 (five cases). For the PVS count measurement, the number of cases (>10 or <-10) was reduced from five to zero for Ob1 and reduced from three to two for Ob2. The restricted BG ROI helped increase the intra-observer consistency. The discrepancy of measurements from Ob2 was more scattered than Ob1 and might be caused by a learning effect, as Ob1 was more experienced in the PVS measurements than Ob2.

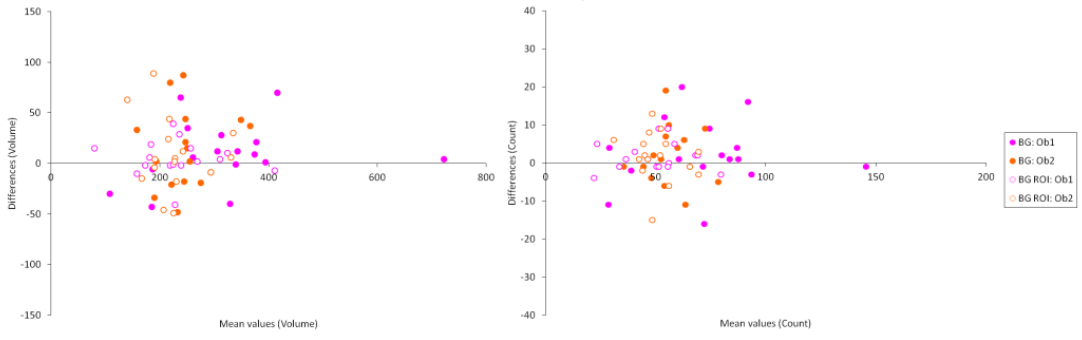

Figure F3 Intra-observer variability of PVS volume and count measurements showing the efficiency of setting ROI into the BG ovoid regions (orange) when compared with the results from Step 2 (pink).

The variability between the two observers was reduced by restricting the measurements to BG ROI, as shown in the aspects of SD and discrepancy of dots (Figure F4 and Table F1, F2). The systematic bias still existed between the two observers in differentiating PVS, Ob2 tended to measure more than Ob1 when the

PVS was small in terms of volume or count, but measured less when the volume was bigger.

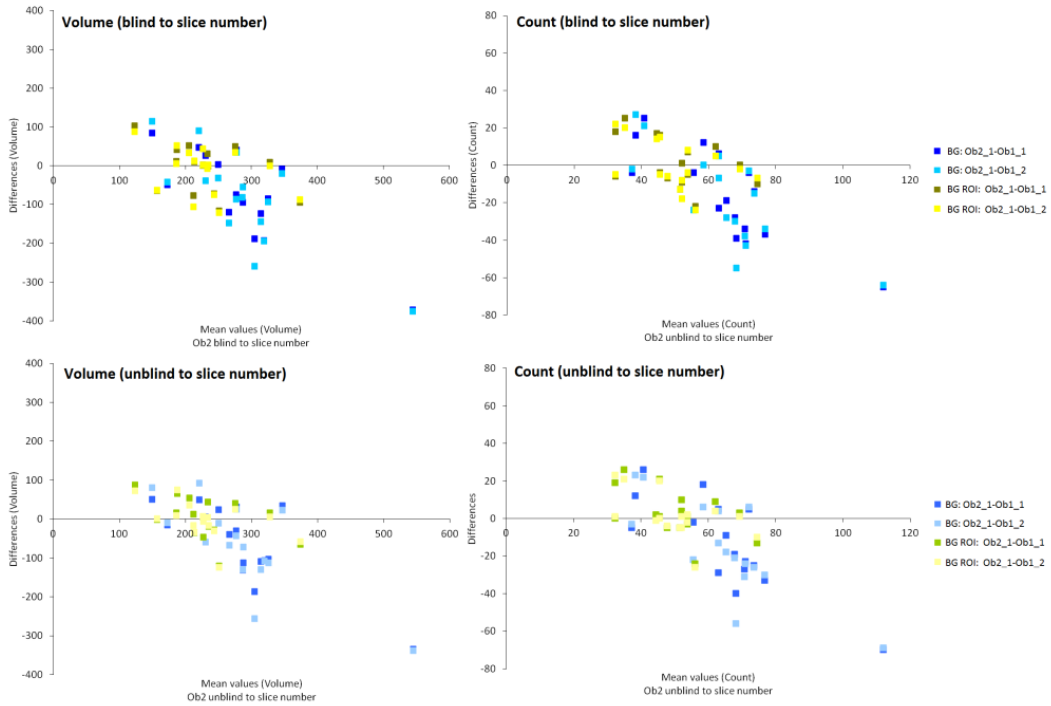

Figure F4 Intra-observer variability of PVS volume and count measurements showing the efficiency of setting ROI into the BG ovoid regions (yellow) when compared with the results from Step 2 (blue). Upper left: inter-observer variability of PVS volume when Ob2 was blinded to the standard slice number chosen by Ob1. Lower left: inter-observer variability of PVS volume when Ob2 was unblinded to the standard slice number chosen by Ob1. Upper right: inter-observer variability of PVS count when Ob2 was blinded to the standard slice number chosen by Ob1. Lower right: inter-observer variability of PVS count when Ob2 was unblinded to the standard slice number chosen by Ob1.

The intra- and inter-observer variability decreased after we restricted ROI, and there were fewer discrepancies in PVS selection (Figure F5).

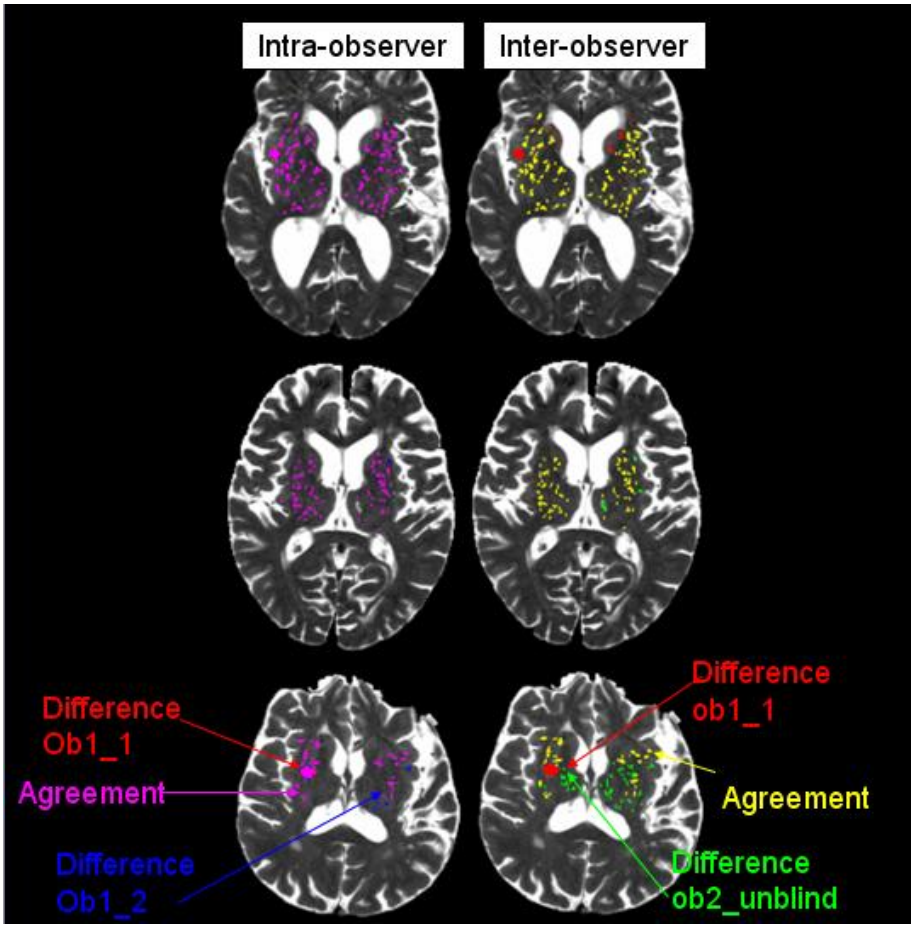

Figure F5 Location of intra- and inter-observer variability in two ovoid regions in the BG regions.

3. Observer variability in Step 5

Both observers obtained much smaller PVS volume and count after applying a single threshold to intensity-adjusted T2W images when compared to applying multiple thresholds to the original T2W images in step 2, and the SD was also smaller (Table F1, F2). The discrepancies of PVS were fan-shaped, suggesting there was no systematic bias in this method, and also suggesting that step 5 was less dependent on observer skills for both PVS volume and count measurements (Figure F6).

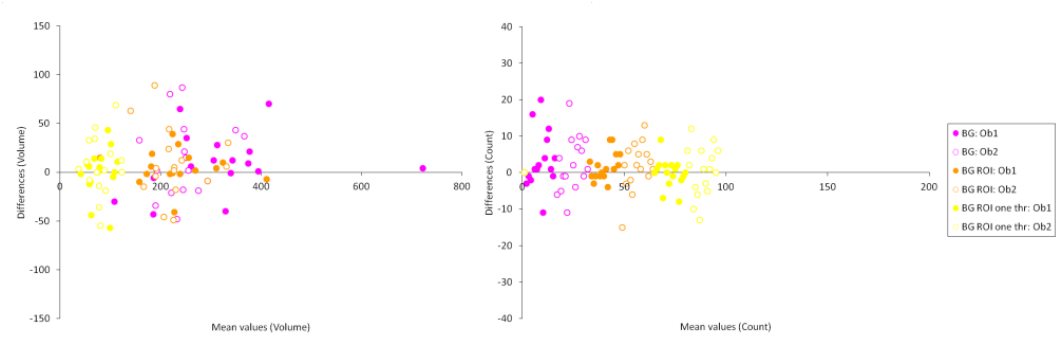

Figure F6 Intra-observer variability comparison of PVS volume and count measurements (step 2: pink; step 3: orange; step 5: yellow).

The inter-observer variability of PVS volume and count was much smaller after applying a single threshold to intensity-adjusted images in step 5 than applying multiple thresholds to the original images in step 2 (Table F1, F2). There was no systematic bias shown by the two fan-shaped discrepancies on the Bland-Altman plots (Figure F7, orange dots).

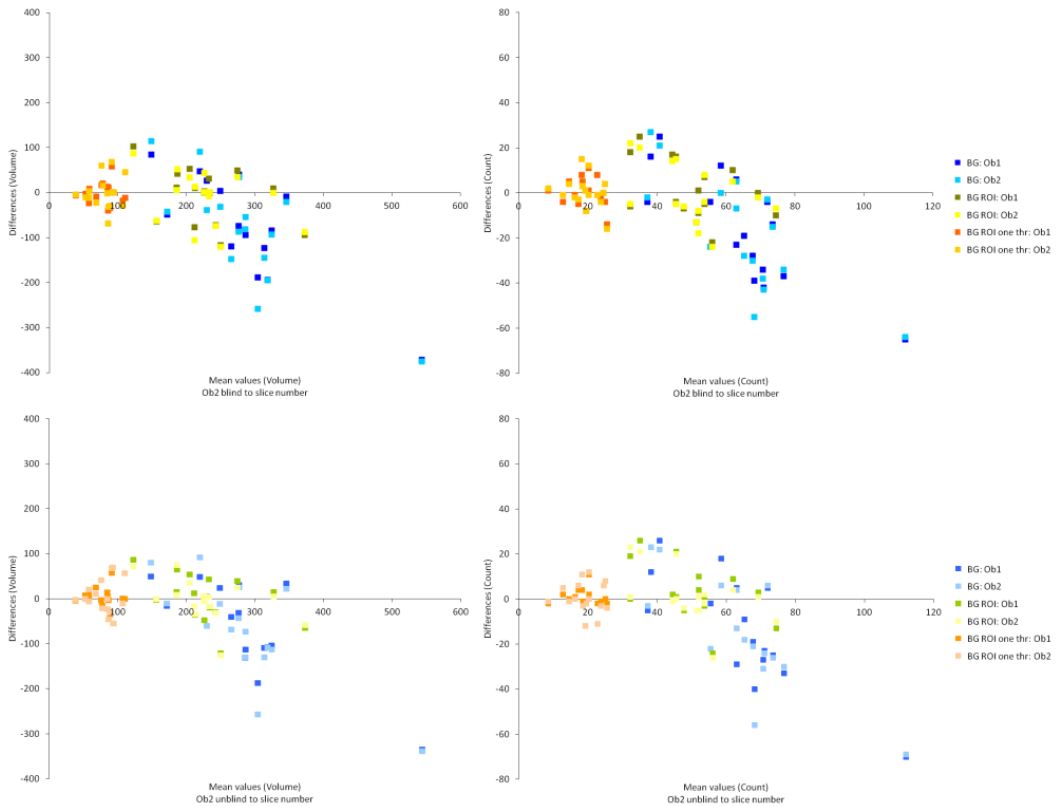

Figure F7 Inter-observer variability comparison of PVS volume and count measurements (step 2: pink; step 3: orange; step 5: yellow).

When restricting ROI to BG ovoid regions, applying one threshold to the intensity-adjusted images (**Figure F8**) increased the observer variability when compared to using multiple thresholds to the original images (**Figure F5**). The accuracy and consistency of measurements was sacrificed by reducing the amount of thresholds. The intra- and inter-observer variability and location of variability suggested that the intensity-adjusted images alone were not enough to reduce the number of thresholds as well as keep the observer consistency. Applying lesion masks and combination with other MR images was considered for further investigation.

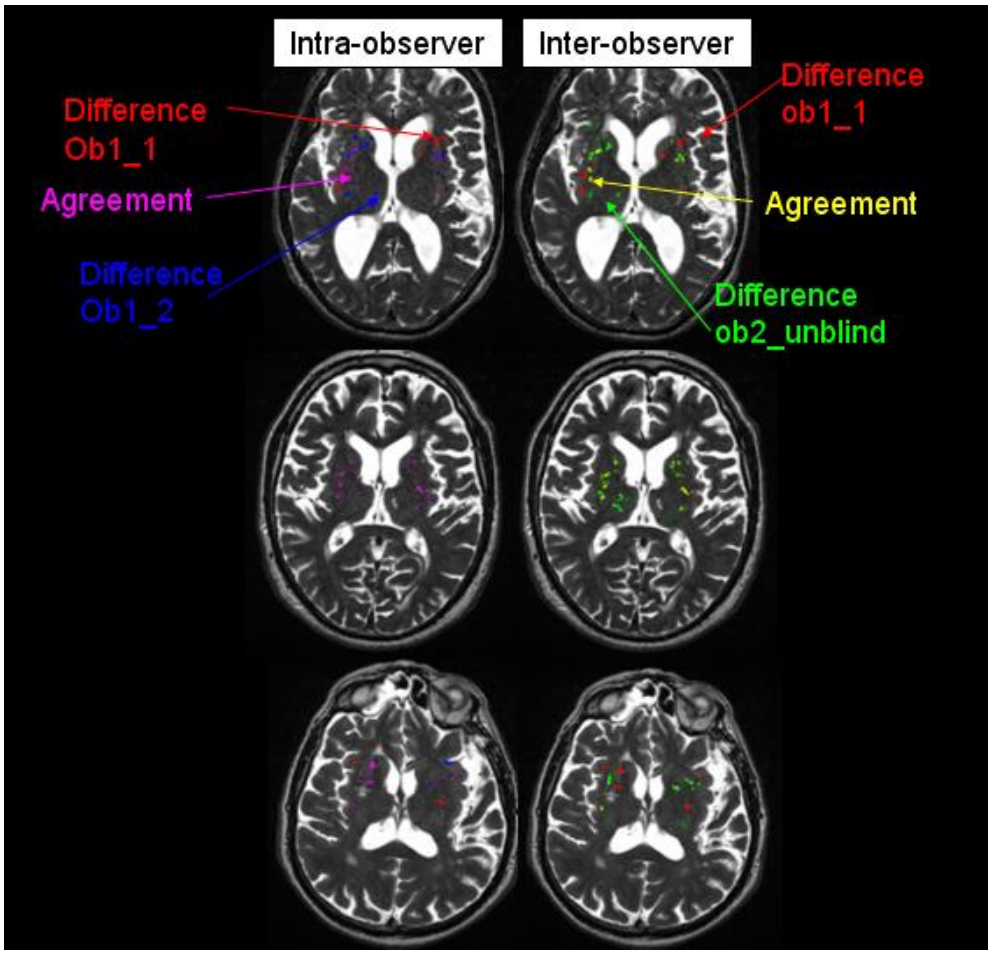

Figure F8 Location of intra- and inter-observer variability in two BG ovoid regions after applying one threshold to intensity-adjusted images.

Appendix (G) Results from unsuccessful steps in the PVS method development and optimization

Step 5-Single threshold in intensity adjusted image

In order to find a best fitting threshold on the intensity adjusted T2W image within BG ROI, for each case, we applied three thresholds. These thresholds ranged from 25% to 54% of maximum intensity value. Then the experienced neuroradiologist chose the best-fitting threshold according to visual comparisons. According to the best-fitting threshold applied and the image characters, we categorized these 16 testing cases into four subgroups into four groups and with an overlapping of the groups (**Figure G1**):

(a) For nine cases, applying one threshold picked up most of the appearing PVS. Within those cases, a threshold of t=25% was suitable for three cases, t=27.5% was suitable for two cases, t=29.5% was suitable for three cases, and t=33% was suitable for one case.

(b) For six cases (threshold range 35.5% to 53%), applying only one threshold missed a large number of PVS when compared with reference, an intensity adjusted T2W image. The missing PVS may be due to the high background signal of the image, which made it difficult for the program to distinguish the PVS from other patchy lesions such as WMH. In addition, PVS that were close to each other were considered as a big 'whole lesion' and excluded by the program because it exceeded the maximum size limit (maximum=12).

(c) Applying only one threshold was not successful in picking up PVS in three cases which had high background signal.

(d) Applying only one threshold was not successful in picking up PVS in two cases which had poor MR scan quality.

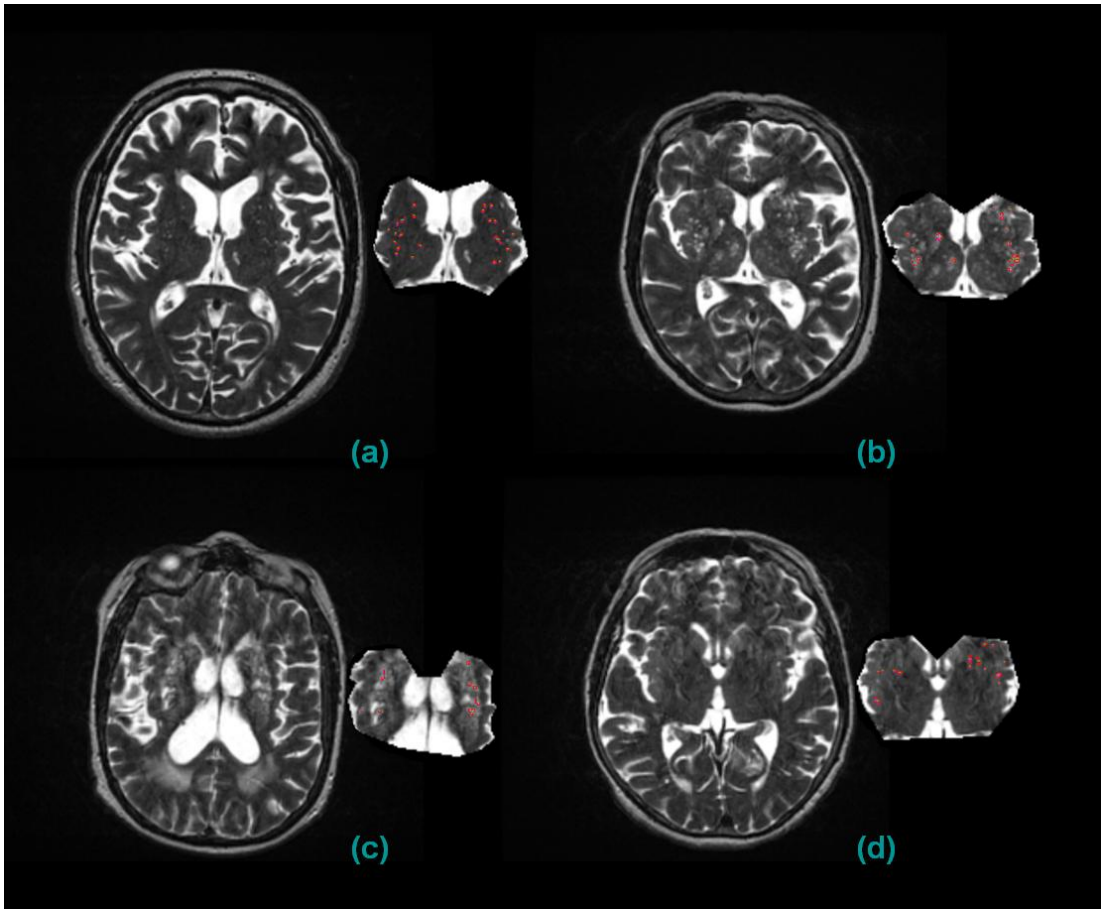

Figure G1 Four groups of cases applying one threshold within in BG ROI in the intensity-adjusted T2W images. (a) Using one threshold was effective in picking up most of the PVS; (b) Using one threshold missed a large amount of PVS; (c) Image with high background signal; (d) Poor MR scan quality image.

Because the range of best fitting threshold varied a lot, for example in group (a) the threshold range was from 25% to 33% and in group (b) it was from 35.5% to 53%, it was take the averaged threshold and applied it for all 16 cases. We selected group (a) to test whether applying the threshold was effective in picking up most of the PVS in the BG ROI in the intensity adjusted T2W images. We applied the averaged threshold in group (a), 29% of the maximum intensity, to all 9 cases in group (a). However, it was not effective and suitable to pick up PVS dots in all 9 cases.

The results suggested applying a single threshold on the intensity adjusted T2W image alone was not enough to find a gold standard threshold or threshold range suitable for all cases. We needed to test the effect of lesion masks and combination of intensity adjusted images.

Step 6- Applying lacune masks

Within the 4 cases had lacunes, there was little overlapping on the location or size between lacunar lesions and PVS (**Figure G2**). Lacune removement did not help improve PVS segmentation. It might possibly be useful for the cases having more overlapping of the location and size between lacunar lesions and PVS.

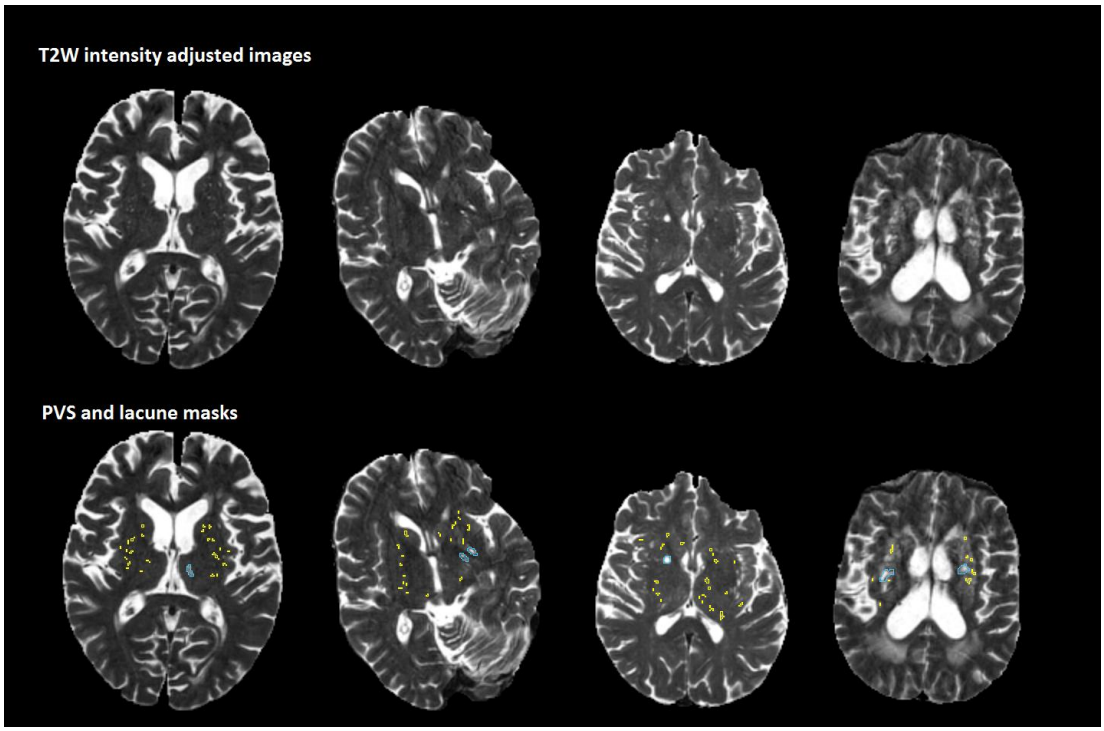

Figure G2 PVS and lacune masks on the four cases had lacunes. PVS mask: yellow; lacune mask: blue.

Step 7-Combination of T2W intensity adjusted image and T1W intensity adjusted image

We tested the effect of combined T2W intensity adjusted image and T1W intensity adjusted image in identifying the PVS computationally. The results showed, compared with T2W image after intensity adjustment, the combined image in the non-colour and colour blend conditions blurred the edges of the PVS lesions, and was not suitable to test the effect of reducing thresholds in the PVS segmentation (**Figure G3**). Thus, this combination was not successful in identify PVS and reduce thresholds.

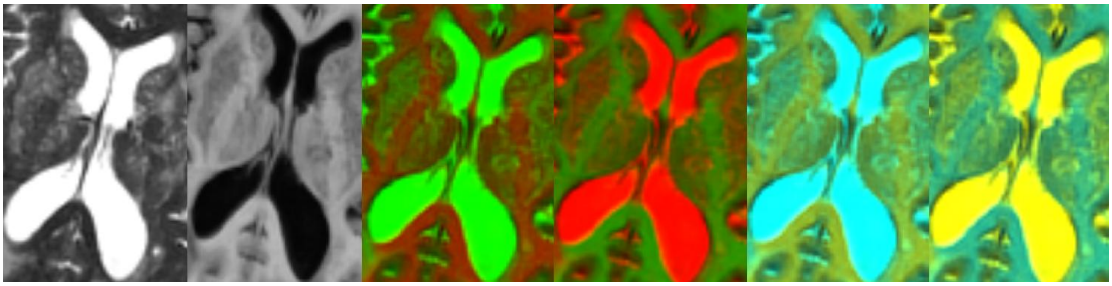

(1) (2) (3) (4) (5) (6)

Figure G3 T2W intensity adjusted image and its combinations with T1W intensity adjusted image in non-colour blend or colour blend conditions. (1) T2W intensity adjusted image; (2) T2W intensity adjusted image combined with T1W intensity adjusted image (non-color blend); (3)-(6) Combined image with colour blend of red and green or yellow and cyan.

Appendix (H) PVS associations

Table H1 Associations between BG PVS count and SVD features visual rating scales (WMH, atrophy and CS PVS) for baseline and follow-ups.

Associations	Coefficient of linear regression	95% CI	CV
Baseline 100 patients			
PWMH Left	2.175	1.176 to 3.174	38.197
PWMH Right	2.128	1.123 to 3.133	38.366
DWMH Left	1.997	1.093 to 2.900	38.103
DWMH Right	1.894	0.973 to 2.816	38.535
Deep Atrophy	1.614	0.732 to 2.495	39.127
Superficial Atrophy	1.774	0.701 to 2.846	39.559
CS Left	0.688	-0.254 to 1.629	41.239
CS Right	0.677	-0.279 to 1.633	41.268
Baseline 46 patients			
PWMH Left	1.642	-0.062 to 3.347	40.793
PWMH Right	1.642	-0.062 to 3.347	40.793
DWMH Left	2.626	1.014 to 4.238	38.097
DWMH Right	2.626	1.014 to 4.238	38.097
Deep Atrophy	2.111	0.315 to 3.908	40.029
Superficial Atrophy	1.241	-0.604 to 3.086	41.648
CS Left	-0.355	-2.002 to 1.292	42.412
CS Right	-0.355	-2.002 to 1.292	42.412
Follow-up 46 patients			
PWMH Left	0.847	-0.700 to 2.394	28.110
PWMH Right	0.841	-0.661 to 2.342	28.097
DWMH Left	1.208	-0.063 to 2.479	27.382
DWMH Right	0.936	-0.386 to 2.258	27.859
Deep Atrophy	0.927	-0.322 to 2.176	27.797
Superficial Atrophy	1.025	-0.462 to 2.512	27.893
CS Left	0.533	-0.893 to 1.958	28.315
CS Right	0.416	-1.027 to 1.860	28.389

CI: confident interval; CV: coefficient of variances; PWMH: periventricular white matter hyperintensities; DWMH: deep white matter hyperintensities; ICV: intracranial volume; CS: centrum semiovale.

Table H2 Associations between BG PVS volume and SVD features visual rating scales (WMH, atrophy and CS PVS) for baseline and follow-ups.

Associations	Coefficient of linear regression	95% CI	CV
Baseline 100 patients			
PWMH Left	0.027	0.015 to 0.039	48.904
PWMH Right	0.027	0.014 to 0.039	48.973
DWMH Left	0.021	0.009 to 0.032	50.234
DWMH Right	0.019	0.007 to 0.030	50.815
Deep Atrophy	0.016	0.005 to 0.027	51.367
Superficial Atrophy	0.013	0.000 to 0.027	52.450
CS Left	0.010	-0.002 to 0.021	52.677
CS Right	0.010	-0.001 to 0.022	52.618
Baseline 46 patients			
PWMH Left	0.014	-0.001 to 0.029	43.158
PWMH Right	0.014	-0.001 to 0.029	43.158
DWMH Left	0.020	0.005 to 0.035	41.592
DWMH Right	0.020	0.005 to 0.035	41.592
Deep Atrophy	0.018	0.002 to 0.034	42.516
Superficial Atrophy	0.008	-0.008 to 0.025	44.278
CS Left	-0.006	-0.020 to 0.009	44.507
CS Right	-0.006	-0.020 to 0.009	44.507
Follow-up 46 patients			
PWMH Left	0.017	0.001 to 0.034	35.172
PWMH Right	0.017	0.001 to 0.033	35.059
DWMH Left	0.015	0.001 to 0.026	35.091
DWMH Right	0.014	0.000 to 0.028	35.318
Deep Atrophy	0.009	-0.005 to 0.023	36.231
Superficial Atrophy	0.012	-0.004 to 0.028	36.061
CS Left	0.008	-0.008 to 0.023	36.489
CS Right	0.008	-0.008 to 0.023	36.538

CI: confident interval; CV: coefficient of variances; PWMH: periventricular white matter hyperintensities; DWMH: deep white matter hyperintensities; ICV: intracranial volume; CS: centrum semiovale.

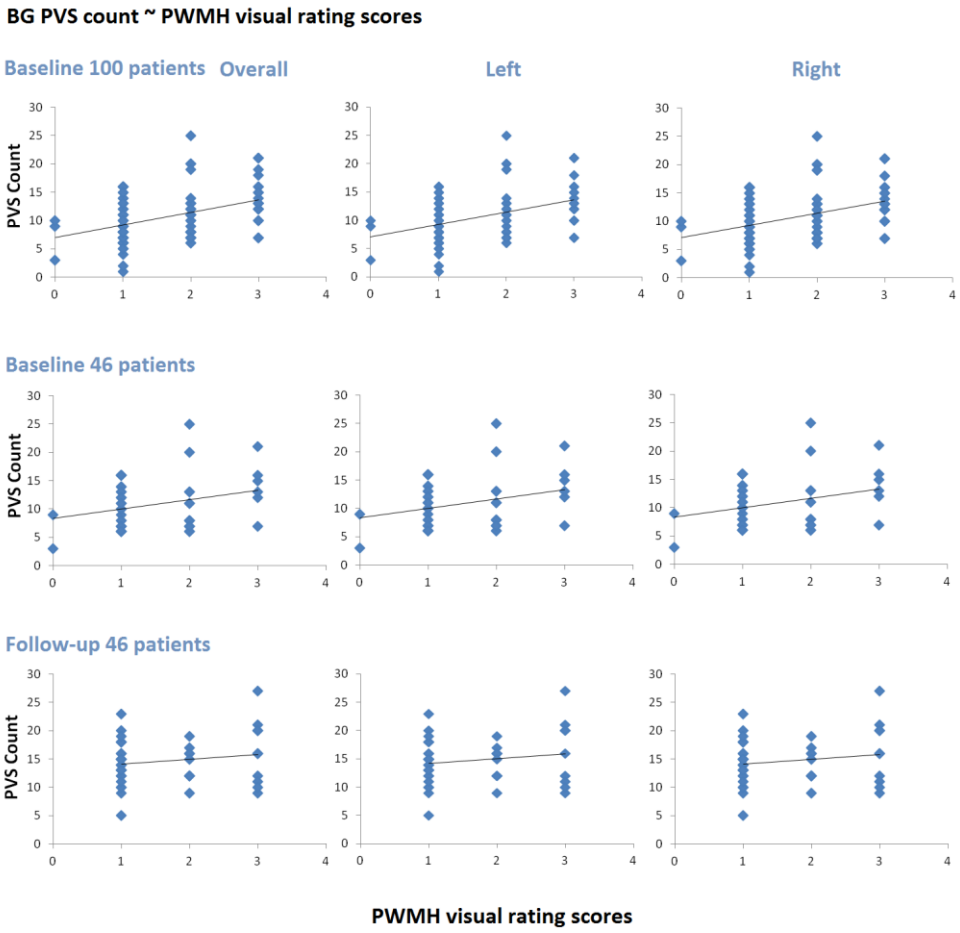

Figure H1 Associations between BG PVS count and PWMH visual rating scores (overall, left and right hemispheres) at baseline and follow-ups.

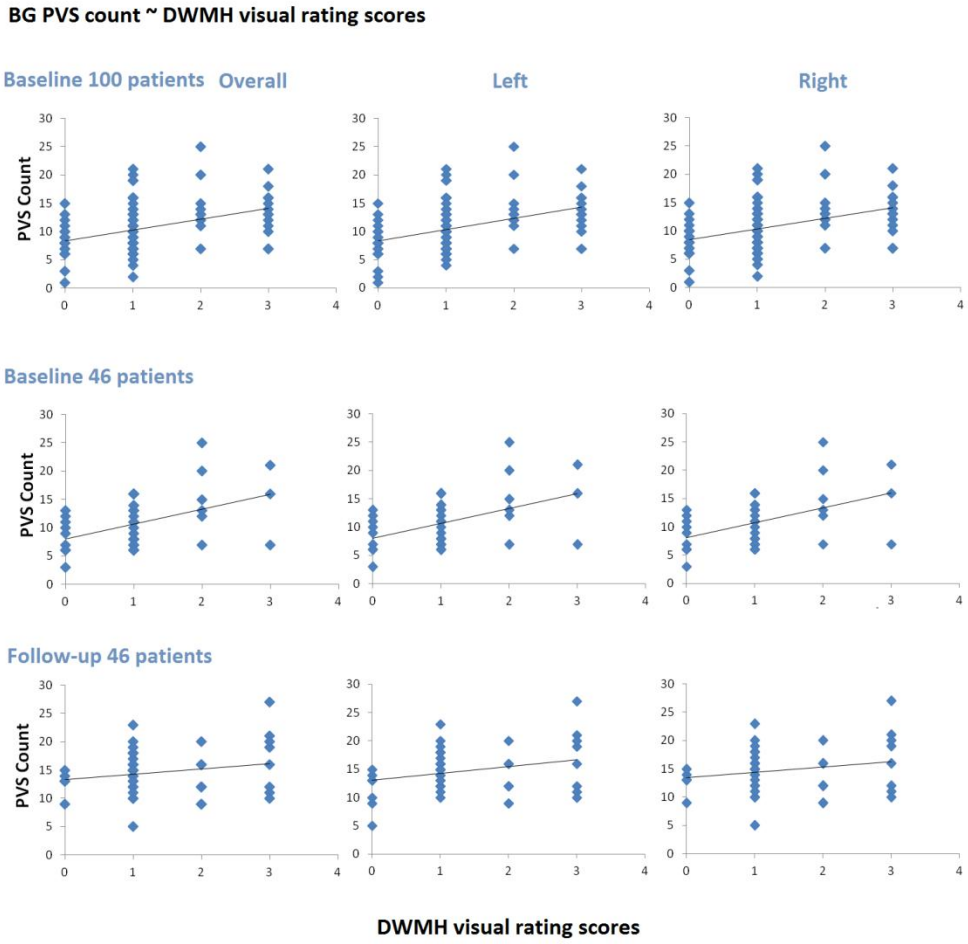

Figure H2 Associations between BG PVS count and DWMH visual rating scores (overall, left and right hemispheres) at baseline and follow-ups.

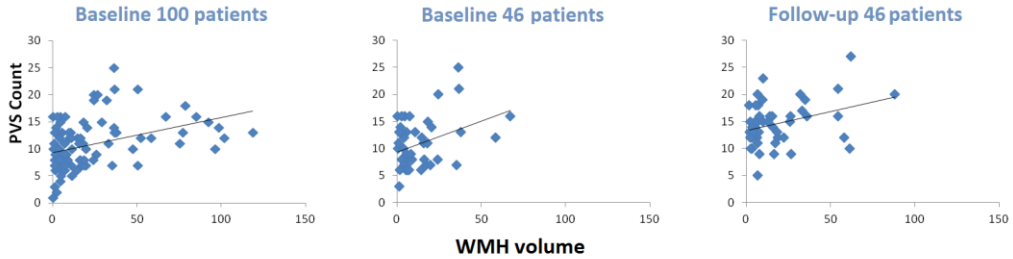

Figure H3 Associations between BG PVS count and WMH volume at baseline and follow-ups.

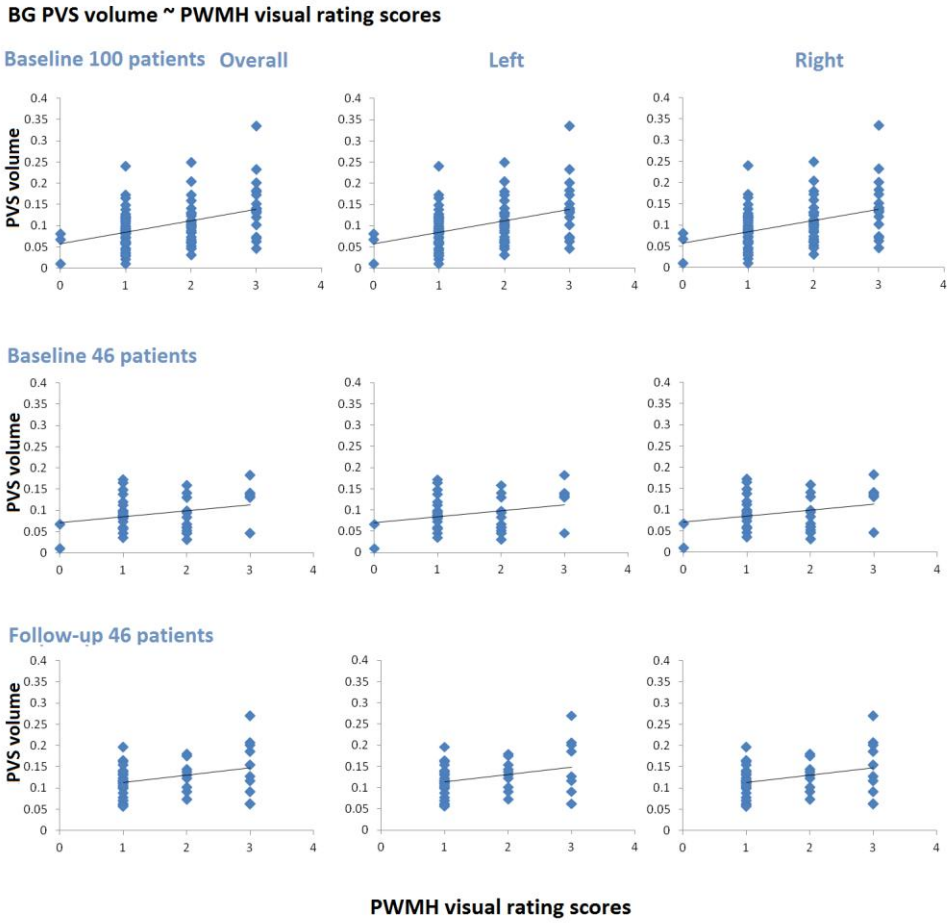

Figure H4 Associations between BG PVS volume and PWMH visual rating scores (overall, left and right hemispheres) at baseline and follow-ups.

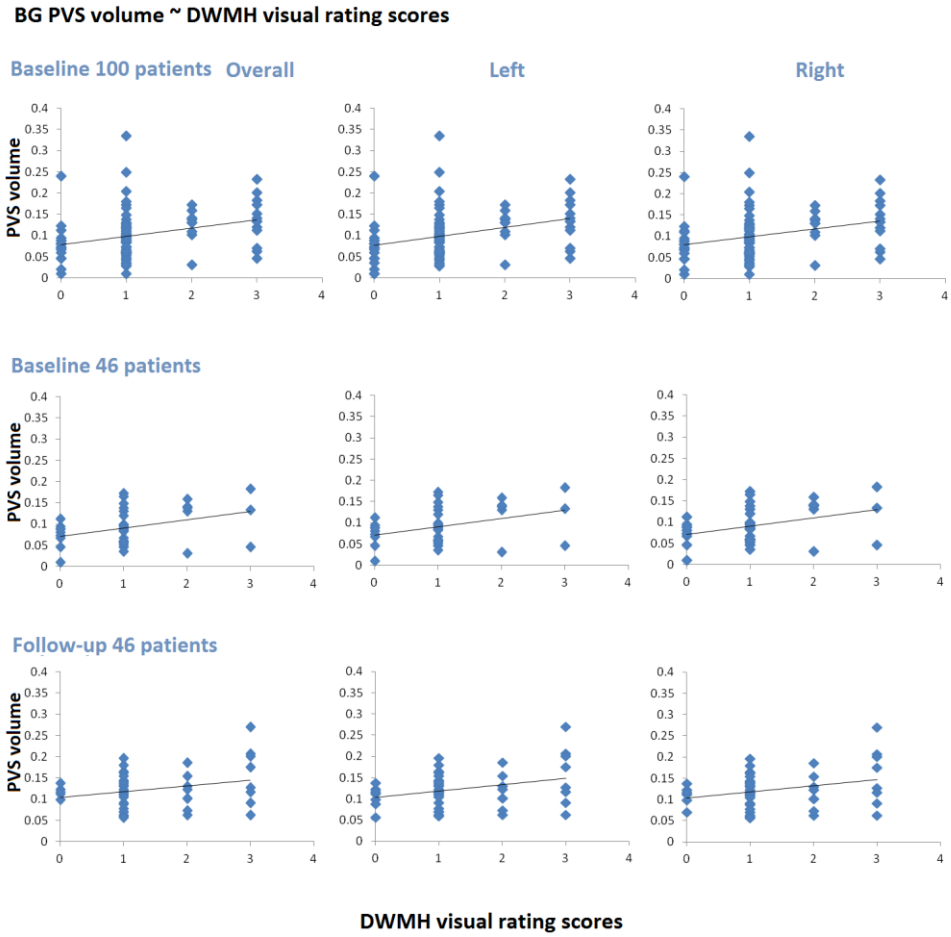

Figure H5 Associations between BG PVS volume and DWMH visual rating scores (overall, left and right hemispheres) at baseline and follow-ups.

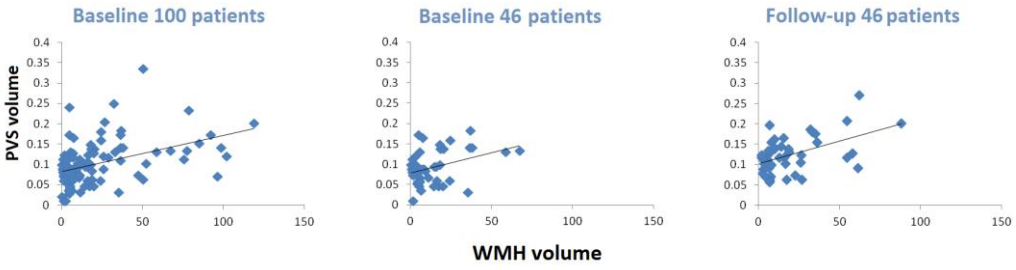

Figure H6 Associations between BG PVS count and WMH volume at baseline and follow-ups.

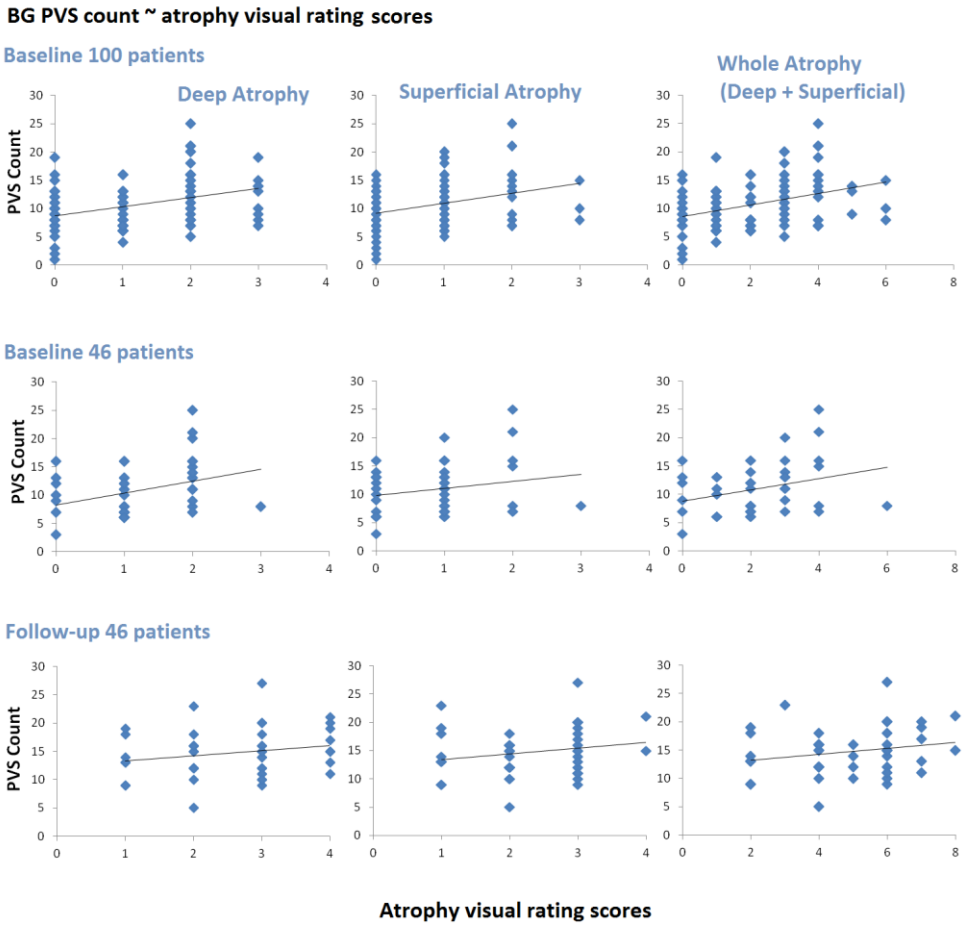

Figure H7 Associations between BG PVS count and atrophy visual rating scores (deep, superficial and whole) at baseline and follow-ups.

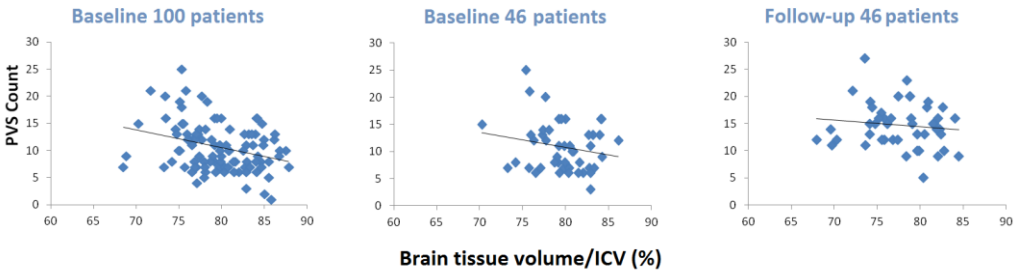

Figure H8 Associations between BG PVS count and brain tissue volume expressed as a percentage of ICV at baseline and follow-ups.

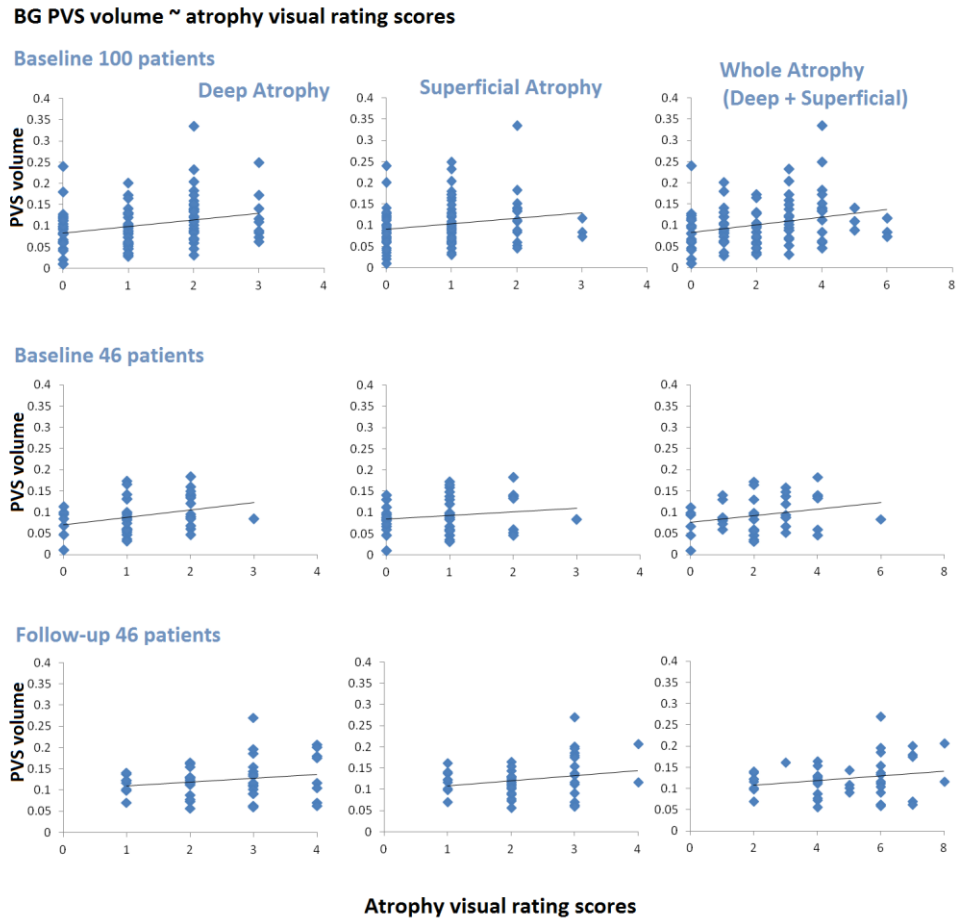

Figure H9 Associations between BG PVS volume and atrophy visual rating scores (deep, superficial and whole) at baseline and follow-ups.

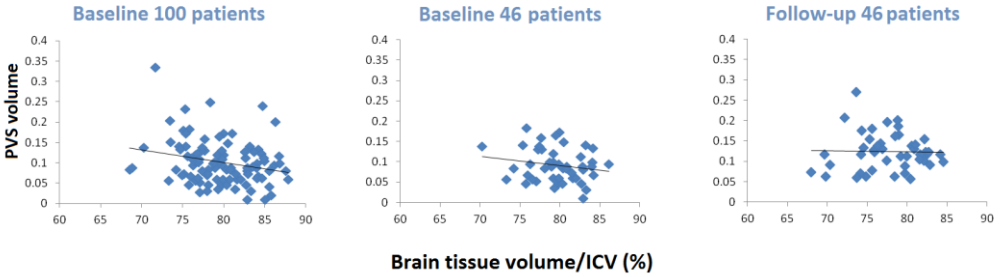

Figure H10 Associations between BG PVS volume and brain tissue volume expressed as a percentage of ICV at baseline and follow-ups.

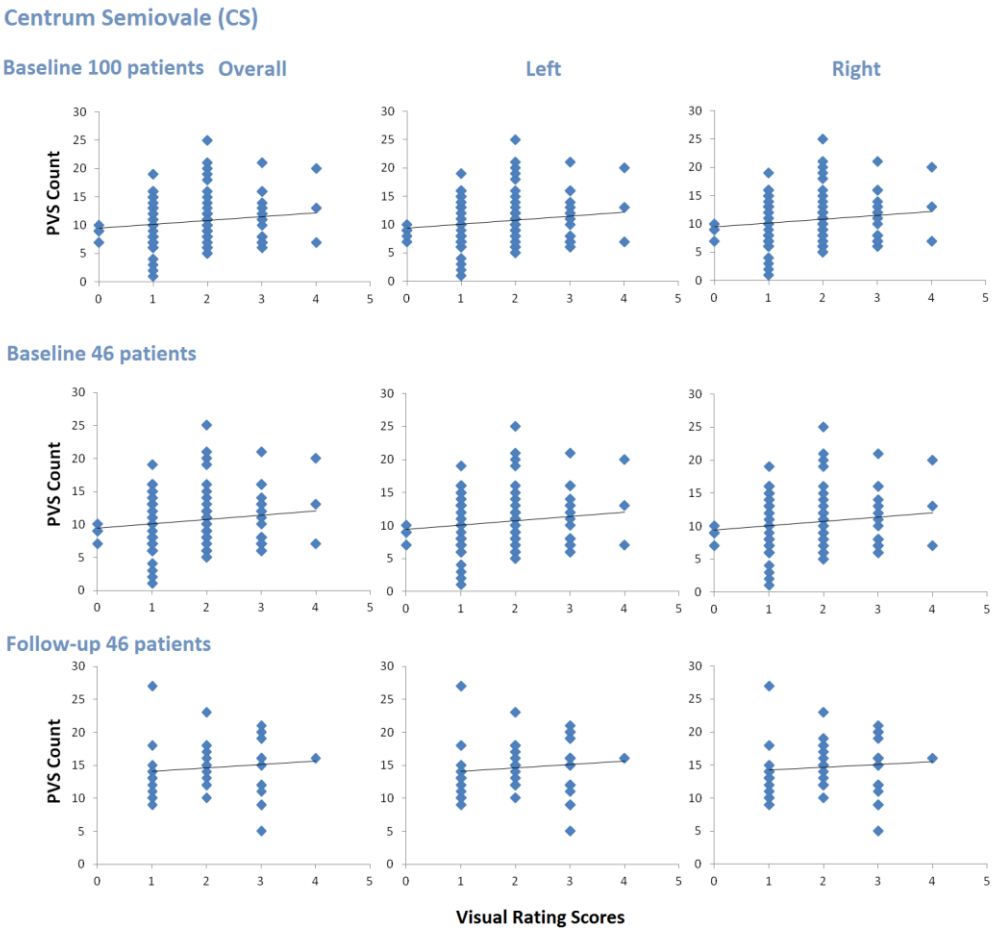

Figure H11 Associations between BG PVS count and CS PVS visual rating scores (overall, left and right hemispheres) at baseline and follow-ups.

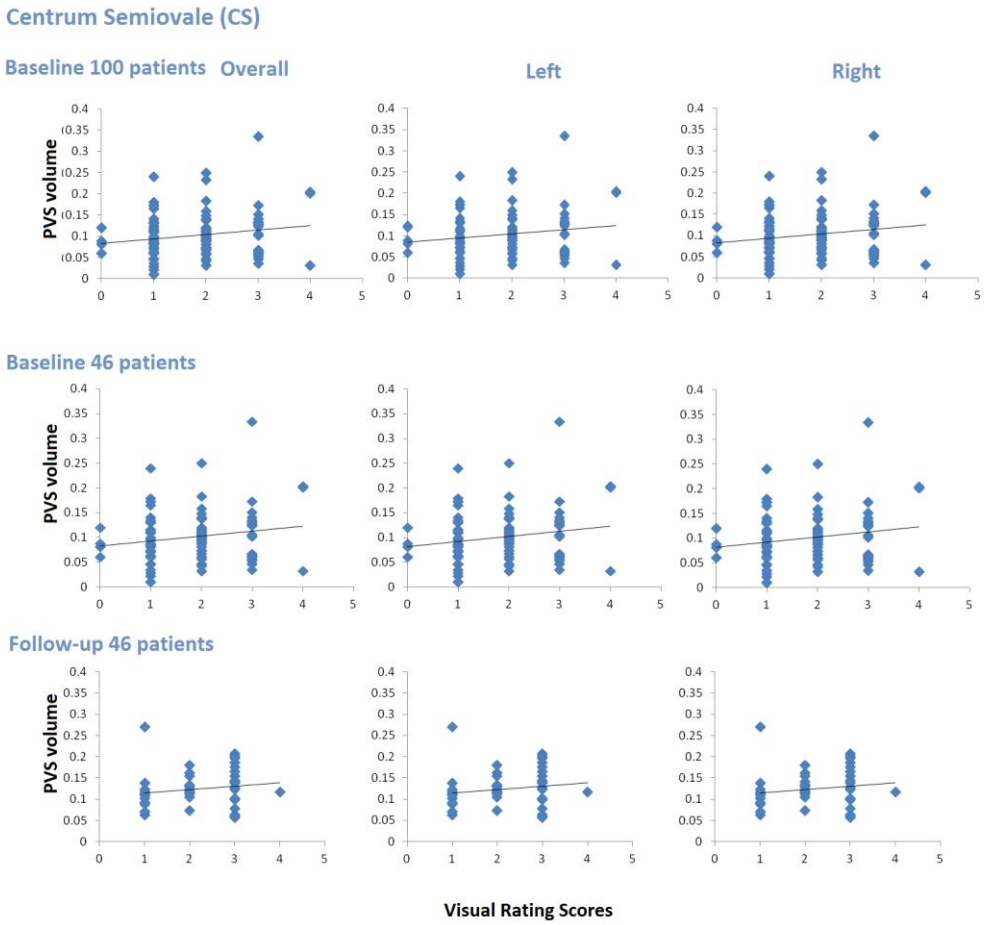

Figure H12 Associations between BG PVS count and CS PVS visual rating scores (overall, left and right hemispheres) at baseline and follow-ups.

Appendix (I) Publications relating to the work of this thesis

1. Wang, X., Valdes Hernandez, M.C., Doubal, F., Chappell, F.M., Wardlaw, J.M., 2012. How much do focal infarcts distort white matter lesions and global cerebral atrophy measures? *Cerebrovasc Dis* 34, 336-342.

2.Wardlaw, J.M., Doubal, F.N., Valdes-Hernandez, M., Wang, X., Chappell, F.M., Shuler, K., Armitage, P.A., Carpenter, T.C., Dennis, M.S., 2013a. Blood-brain barrier permeability and long-term clinical and imaging outcomes in cerebral small vessel disease. *Stroke* 44, 525-527.

3. Hernandez, M.D., Piper, R.J., Wang, X., Deary, I.J., Wardlaw, J.M., 2013. Towards the automatic computational assessment of enlarged perivascular spaces on brain magnetic resonance images: A systematic review. *J Magn Reson Imaging* 38, 774-85.

4. Wang X, Hernandez MCV, Armitage PA, Doubal F, Wardlaw JM. Pilot study to assess white matter lesion progression in longitudinal studies: preliminary findings from The Mild Stroke Study 1. International Society for Magnetic Resonance in Medicine 2010.

5. Wang X, Hernandez MCV, Armitage PA, Doubal F, Wardlaw JM. Effect of infarcts on the assessment of brain atrophy in longitudinal studies. European Stroke Conference 2011.

6. Wang X, Hernandez MCV, Doubal F, Chappell FM, Wardlaw JM. Development and validation of a computational method to quantify perivascular spaces on MRI in cerebral small vessel disease. European Stroke Conference 2013.

7. Wang X, Hernandez MCV, Doubal F, Chappell FM, Wardlaw JM. Computational quantification of perivascular spaces (count and volume) in ischemic stroke patients is associated with white matter hyperintensities and cerebral atrophy. European Stroke Conference 2013.

8. Wang X, Hernandez MCV, Wardlaw JM. Structure and function of perivascular spaces in the brain: a systematic literature analysis. European Stroke Conference 2014.

9. Wang X, Hernandez MCV, Sakka E, Wardlaw JM. Common white matter hyperintensity artefacts on fluid attenuated inversion recovery images: literature review and ischemic stroke patient study. European Stroke Conference 2014.

10. Wang X, Hernandez MCV, Doubal F, Chappell FM, Wardlaw JM. Basal ganglia perivascular spaces are associated with reduced von Willebrand Factor in patients with mild stroke – evidence of cerebral endothelial dysfunction. European Stroke Conference 2014 (Platform presentation).